CIVIL ENGINEERING STUDIES
Illinois Center for Transportation Series No. 13-002
UILU-ENG-2013-2012
ISSN: 0197-9191

EXPERIMENTAL INVESTIGATION OF THE SEISMIC RESPONSE OF BRIDGE BEARINGS

Prepared By
James LaFave
Larry Fahnestock
Douglas Foutch
Joshua Steelman
Jessica Revell
Evgueni Filipov
University of Illinois at Urbana-Champaign

Jerome Hajjar
Northeastern University

Research Report No. FHWA-ICT-13-002

A report of the findings of
ICT-R27-070
Calibration and Refinement of Illinois' Earthquake Resisting System Bridge Design Methodology

Illinois Center for Transportation

May 2013

Technical Report Documentation Page

1. Report No.	2. Government Accession No.	3. Recipient's Catalog No.
FHWA-ICT-13-002		

4. Title and Subtitle	5. Report Date
Experimental Investigation of the Seismic Response of Bridge Bearings	May 2013
	6. Performing Organization Code

7. Author(s)	8. Performing Organization Report No.
James LaFave, Larry Fahnestock, Douglas Foutch, Joshua Steelman, Jessica Revell, Evgueni Filipov, and Jerome Hajjar	ICT-13-002 UILU-ENG-2013-2-12

9. Performing Organization Name and Address	10. Work Unit No. (TRAIS)
Illinois Center for Transportation Department of Civil and Environmental Engineering University of Illinois at Urbana-Champaign 205 N. Mathews, MC 250 Urbana, IL 61801	11. Contract or Grant No. R27-70

12. Sponsoring Agency Name and Address	13. Type of Report and Period Covered
Illinois Department of Transportation Bureau of Materials and Physical Research 126 East Ash St. Springfield, IL 62704	14. Sponsoring Agency Code

15. Supplementary Notes
Volume 1 of 2 submitted for Project ICT-R27-070

16. Abstract
The Illinois Department of Transportation (IDOT) commonly uses elastomeric bearings to accommodate thermal deformations in bridges. These bearings also present an opportunity to achieve a structural response similar to isolation during seismic events. IDOT has been developing an earthquake resisting system (ERS) to leverage the displacement capacity available at typical bearings in order to provide seismic protection to substructures of typical bridges. The research program described in this report was conducted to validate and calibrate IDOT's current implementation of design practice for the ERS, based on experiments conducted on typical full-size bearing specimens, as well as computational models capturing full bridge response. The overall final report is divided into two volumes. This first volume describes the experimental program and presents results and conclusions obtained from the bearing and retainer tests. The experiments described in this volume provide data to characterize force-displacement relationships for common bearing types used in Illinois. The testing program comprised approximately 60 individual tests on some 26 bearing assemblies and components (i.e., retainers). The testing program included (1) Type I elastomeric bearings, consisting of a steel-reinforced elastomeric block vulcanized to a thick top plate; (2) Type II elastomeric bearings, distinct from Type I bearings with a steel bottom plate vulcanized to the bottom of the elastomeric block, and a flat sliding layer with polytetrafluoroethylene (PTFE) and stainless steel mating surfaces between the elastomer and the superstructure; and (3) low-profile fixed bearings. Tests conducted to simulate transverse bridge motion also included stiffened L-shaped retainers, consistent with standard IDOT practice. Tests were conducted using monotonic and cyclic displacement protocols, at compression loads corresponding to a range of elastomer compression stresses from 200 to 800 psi. Peak displacements from initial position ranged from 7-1/2 in. to 12-1/2 in., depending on bearing size. Test rates were generally quasi-static, but increased velocities up to 4 in./sec were used for bearings with PTFE and for a subset of other elastomeric bearings. On the basis of all of the experimental findings, bearing fuse force capacities have been determined, and appropriate shear stiffness and friction coefficient values for seismic response have been characterized and bracketed.

17. Key Words	18. Distribution Statement
Seismic, bridge bearings, isolation, elastomeric bearings, PTFE, fixed bearings, bearing retainers	No restrictions. This document is available to the public through the National Technical Information Service, Springfield, Virginia 22161

19. Security Classif. (of this report)	20. Security Classif. (of this page)	21. No. of Pages	22. Price
Unclassified	Unclassified	72 + appendices	

Form DOT F 1700.7 (8-72) Reproduction of completed page authorized

ACKNOWLEDGMENT, DISCLAIMER, MANUFACTURERS' NAMES

This publication is based on the results of ICT-R27-70, **Calibration and Refinement of Illinois' Earthquake Resisting System Bridge Design Methodology**. ICT-R27-70 was conducted in cooperation with the Illinois Center for Transportation; the Illinois Department of Transportation, Division of Highways; and the U.S. Department of Transportation, Federal Highway Administration.

The research team thanks the ICT staff for their assistance, the Technical Review Panel (TRP) members for their constructive comments, and the IDOT district staff for their assistance with field review and survey.

Members of the TRP are the following:

Daniel Tobias, IDOT (Chair)
Mark Shaffer, IDOT (Co-Chair)
Dan Brydl, FHWA
John Ciccone, IDOT
Patrik Claussen, IDOT
Chad Hodel, WHKS
William Kramer, IDOT
Carl Puzey, IDOT
Kevin Riechers, IDOT

EXECUTIVE SUMMARY

The Illinois Department of Transportation (IDOT) commonly uses elastomeric bearings atop substructures to accommodate superstructure thermal deformations in bridges. These bearings also present an opportunity to achieve a structural response similar to isolation during seismic events. IDOT has been developing an Earthquake Resisting System (ERS) to leverage the displacement capacity available at typical bearings in order to provide seismic protection to substructures of typical bridges. The IDOT ERS is conceptually discretized to three levels of response. At Level 1, bearings reach a fuse capacity, corresponding to the limit of small displacement response and the peak force that can be transmitted from the superstructure to the substructure. At Level 2, bearings are permitted to slide on substructures, provided that peak displacements do not result in unseating of the superstructure. At Level 3, the most severe seismic events are even permitted to induce some inelastic response in substructures and foundations. The research program described in this report was conducted to validate and calibrate IDOT's current implementation of design practice for the ERS, based on experiments conducted on typical full-size bearing specimens, as well as computational models capturing full bridge response.

The overall final report is divided into two volumes. This first volume describes the experimental program and presents results and conclusions obtained from the bearing and retainer tests. The second volume presents the results from non-linear time-history analyses of full bridge models. The experiments described in this volume provide salient data for calibration of Level 1 fuse capacities, as well as appropriate parameters to define sliding responses that were incorporated when investigating Level 2 behavior in the full bridge models. All bearings tested in the experimental program were new bearings, complying with current IDOT specifications. The testing program comprised approximately 60 individual tests on some 26 bearing assemblies and components (i.e., retainers). The testing program included (1) Type I elastomeric bearings, consisting of a steel-reinforced elastomeric block vulcanized to a thick top plate; (2) Type II elastomeric bearings, distinct from Type I bearings with a steel bottom plate vulcanized to the bottom of the elastomeric block, and a flat sliding layer with polytetrafluoroethylene (PTFE) and stainless steel mating surfaces between the elastomer and the superstructure; and (3) low-profile steel fixed bearings. Tests conducted to simulate transverse bridge motion also included stiffened L-shaped retainers, consistent with standard IDOT practice.

The tested elastomeric bearing sizes ranged from 7 in. × 12 in. to 13 in. × 20 in. footprints. Bearing motion was constrained to a vertical plane, with loading imposed by a testing frame consisting of two vertical actuators, each with an axial load capacity of 100 kips and a total stroke of 20 in., and a horizontal actuator with an axial load capacity of 220 kips and a total stroke of 30 in. Simulated gravity load imposed by the vertical actuators corresponded to average compression ranging from 200 to 800 psi on the elastomer footprint for various tests, and was generally controlled to remain approximately constant throughout each individual test. Maximum horizontal displacements for Type I bearings corresponded to 400% shear strain over the total elastomer thickness for each specimen, which ranged from peak cyclic strokes of 15 in. (for 7 in. × 12 in. bearings) to 25 in. (for 13 in. × 20 in. bearings). Displacement rate was increased for tests on Type II bearings and a subset of Type I bearings. The maximum achievable rate varied throughout the testing program, depending on the hydraulic capacity available at the time of the test, with a maximum rate of 4 in./sec. All tests were conducted with the bearing specimen placed on a concrete pad, cast using concrete supplied to match that typically used for bridge structures in Illinois, and with roughened top surfaces per IDOT Standard Specifications.

Type I bearing response in the transverse direction was found to provide a Level 1 fuse capacity of approximately 1.3 to 1.65 times the nominal tension capacity of the anchor used to secure each retainer to the concrete. If bridge response to earthquake motions is primarily limited to shear deformations with few slip cycles, bearing stiffness can be estimated from an adjusted shear modulus, accounting for peak strain and strain rate effects, with a range of approximately 60% to 100% of the supplier's documented value (required to fall between 110 and 150 psi) in the longitudinal bridge direction, and 75% to 105% in the transverse bridge direction. With multiple slip cycles, the response degrades slightly to 45% to 90% for longitudinal motion, and about 50% to 80% for transverse motion. Sliding friction is likely to range from 0.45 at relatively low compression stress, to about 0.25 at moderate and relatively high (for IDOT) compression stress. The initial breakaway coefficient is likely to be about 33% higher than the sliding friction coefficient. Friction resistance is dictated primarily by concrete surface roughness and slip rate, but it also degrades slightly with accumulated slip.

Type II bearing response in the transverse direction was found to provide a Level 1 fuse capacity of approximately 0.85 to 1.1 times the nominal tension capacity of the anchor used to secure each retainer to the concrete. The test data suggest that elastomer stiffness can be bounded in the range of approximately 65% to 100% of the value reported by the bearing manufacturer, with the upper bound likely to be a preferable estimate for elastomer response during a seismic event. The coefficient of friction for PTFE will increase with slip rate during a seismic event. Although a bearing may meet IDOT Standard Specifications, with an experimental friction coefficient less than 0.07 for quasi-static testing, the value will rise to a range of about 0.15 to 0.18 during a seismic event. Type II bearings were found to tolerate large displacements, well over 400% of the total elastomer thickness in some cases, prior to unseating at the sliding interface, but localized damage or unusual mechanical responses tended to emerge at displacements larger than about 200% of the elastomer thickness. The PTFE was likely to incur damage and delaminate for relatively short elastomer heights. Alternatively, the response would not transition smoothly to sliding upon reversal for relatively tall elastomer heights.

For low-profile fixed bearings, although either pintles or anchors could be selected as the critical fusing components in shear, designs with weak anchors (as opposed to pintles) showed better agreement between predicted and observed fusing mechanisms. Level 1 fuse capacity can be reliably estimated from the nominal shear capacity of the anchors, superimposed with friction resistance. The coefficient of friction at the interface of the bottom steel plate and a thin elastomeric leveling pad may be bounded by approximately 0.2 and 0.35. Theoretically, fixed bearings should have identical fuse capacity in any orientation. However, loading in the transverse bridge direction was found to be more susceptible to a reduction in observed capacity as a consequence of installation procedures of concrete anchors. If anchors are accurately cast-in, and the fixed bearing is placed so that the holes in the bottom plate are centered on the anchors, or if excess epoxy is removed at bearing holes for post-installed anchors, then the fuse capacity should be the same regardless of loading direction.

CONTENTS

CHAPTER 1 BACKGROUND

1.1 MOTIVATION FOR RESEARCH PROJECT

In 2008 and 2009, the American Association of State Highway and Transportation Officials (AASHTO) published modernized standards for the design of highway bridges likely to be subjected to earthquake loading. The methods and soil parameters used to determine design earthquake response spectra, along with numerous other aspects of seismic bridge design philosophy, were modified. Most significantly, the design earthquake, previously characterized by a 500-year return period, is now based on a 1000-year return period. These changes have increased the complexity of seismic design and the cost of construction, as well as substantially increasing the population of bridge structures in Illinois requiring seismic design.

In an effort to reduce design and construction costs, while still ensuring structural safety during seismic events, the Illinois Department of Transportation (IDOT) developed an innovative Earthquake Resisting System (ERS) strategy tailored specifically to common bridge configurations and typical earthquake hazards in Illinois. The IDOT ERS is an extension of the seismic isolation bridge design methodology employed in higher seismic regions of the United States, where the substructure and superstructure ideally remain elastic and a fusing mechanism is provided at the interface between the two. Historically, the fusing mechanism has been a seismic isolation device, such as a lead-rubber bearing. These classical isolation systems have typically been used in high seismic regions (such as the West Coast of the United States, as well as Japan and New Zealand), where the additional design and construction costs are justifiable when balanced against the seismic hazard. For bridges outside of high seismic areas, however, some commonly employed structural components, such as steel-reinforced elastomeric bearings, may inherently possess properties that are suitable for an isolation system.

As a result, the concept of quasi-isolation has emerged as an innovative, yet pragmatic, design philosophy for bridges in moderate seismic regions. Typical bridge bearing systems can be designed and detailed to act as fuses, providing the benefit of reduced force demands for the superstructure and substructure, so long as the structural system can be designed to accommodate the concomitant increase in displacements. The IDOT ERS features three distinct levels of fusing and redundancy, namely: Level 1—permit damage and failure of bearing components to allow quasi-isolation; Level 2—provide sufficient seat widths to accommodate sliding of the bearings; and Level 3—permit some modest damage to the substructure, so long as there is no span loss. The overall intent is to provide a cost-effective bridge, with an ERS that limits damage for small seismic events and still prevents span loss during a strong event in the New Madrid Seismic Zone (NMSZ).

Although the Illinois ERS strategy is described in the IDOT Bridge Manual and supported by a Seismic Design Guide (with examples), the theoretical methods used in its development have lacked systematic experimental testing to verify or calibrate some of the fundamental design assumptions. There is also concern that, without refined and improved guidance, designers who are less experienced with seismic design principles could exercise unnecessary conservatism, leading to more expensive designs, or might inadvertently develop designs that are not sufficiently conservative for seismic load effects.

To facilitate full implementation of quasi-isolated seismic design, IDOT and the Illinois Center for Transportation (ICT) sponsored a combined experimental and computational research program at the University of Illinois. The overall research program comprised five primary components, summarized as follows:

1. Conducting full-scale tests of typical bridge bearings used in Illinois, to study how bearings not designed for seismic demands behave when subjected to large displacement demands.
2. Developing numerical models of bridge bearings, validated against test results.
3. Developing numerical models of full bridge systems, which capture all important aspects of non-linear behavior when a bridge is subjected to an earthquake.
4. Conducting parametric studies, using the numerical bridge models, to explore system-level seismic response for a range of representative Illinois bridges.
5. Developing recommendations for seismic design of bridges using the quasi-isolation philosophy.

The research presented in this report should assist IDOT in further developing a consistent bridge design approach that can best balance the requisite structural safety with design methodologies and construction practices appropriate for the state of Illinois.

1.2 REPORT ORGANIZATION

The primary goal of this research was to investigate, validate, and calibrate the IDOT ERS strategy, focusing on the specific seismic hazard and bridge structural characteristics appropriate for Illinois. This report presents the results of laboratory testing of standard bridge bearings and computational modeling of typical IDOT bridge configurations, conducted from 2009 through 2012 in the Department of Civil & Environmental Engineering at the University of Illinois at Urbana-Champaign. The report is divided into two volumes, with the first addressing the experimental program and the second describing the computational bridge modeling. Following is a brief summary of the contents of this (first) volume of the report.

Chapter 1 discusses the motivation for the research, briefly reviews published literature on bridge bearings similar to those used in Illinois, and provides an overview of the state of practice for the design of bridge bearings.

Chapter 2 describes the test setup, specimens, and methods used in the experimental bridge bearing testing program.

Chapter 3 presents test results from the bridge bearing experiments, along with analysis and discussion of the key findings, for Type I elastomeric bearings.

Chapter 4 presents test results from the bridge bearing experiments, along with analysis and discussion of the key findings, for Type II elastomeric bearings.

Chapter 5 presents test results from the bridge bearing experiments, along with analysis and discussion of the key findings, for low-profile fixed bearings.

Chapter 6 summarizes the key results from the experimental program.

1.3 REVIEW OF PUBLISHED BEARING RESEARCH LITERATURE

1.3.1 Type I Bearings: Elastomer Behavior

IDOT Type I bearings comprise a steel-reinforced elastomeric block vulcanized to a thick steel top plate. Elastomeric bearings began to see widespread use in the United States in the late 1950s, first as plain elastomeric pads and then as laminated bearings comprised of steel plates or fiberglass sheets sandwiched between layers of elastomeric material. Today,

IDOT commonly uses steel-reinforced elastomeric bearings on highway bridges because of their modest initial cost, simple installation, and maintenance-free durability.

When properly designed, elastomeric bearings are stiff and strong in the vertical direction to resist gravity loads but are flexible in shear to accommodate movements induced by thermal loads, creep, and shrinkage. The steel shims in reinforced elastomeric bearings restrict bulging of the elastomer and result in higher compression stiffness but have no effect on shear stiffness for a given elastomer height. Thus, compression and shear behavior can essentially be calibrated independently.

1.3.1.1 Elastomer Material Response

Elastomers, specifically neoprene and natural rubber for typical bridge bearings, are somewhat different from materials encountered in highway bridge design applications, requiring consideration of significantly larger strains and more pronounced non-linear behavior than conventional materials such as steel and concrete (Roeder and Stanton 1991). In both compression and tension, elastomer material response is fundamentally non-linear, exhibiting softening and stiffening responses depending on strain level.

Material properties also vary significantly with temperature and load history and, to a lesser extent, with load rate and age (Stanton and Roeder 1982). For example, at temperatures below freezing, the elastomer begins to crystalize, and the shear response stiffens as a function of temperature and exposure time (Roeder et al. 1987; Ash et al. 2002). The load history effect of interest is termed “scragging,” whereby elastomer response softens after the initial load cycle and then stabilizes at a reduced level after several cycles (Roeder et al. 1987; Constantinou et al. 1999). Once unloaded, the initial unscragged elastomer properties are recovered over time. Given the cyclic nature of seismic loading, there is some potential for scragging to influence experimental results, and the test protocols for this research were developed such that scragging effects could be identified and separately quantified.

1.3.1.2 Behavior in Compression and Shear

While elastomeric bearing response is not linear elastic even at small strains, simplified linear relationships are often used because rigorously accounting for material and geometric non-linearities in design applications is simply not practical. Large compression strains cause bearings to follow a non-linear stiffening force-deflection curve, but compression response is roughly linear within the range of bearing pressures typically allowed by bridge design codes (Stanton and Roeder 1983; Mori et al. 1996). Estimates of shear deformation are generally based on simple shear response, and research has verified that this assumption of a constant shear stress distribution is reasonable (Roeder and Stanton 1983).

For service loads, AASHTO limits shear deformation to 50% shear strain, based on bearing fatigue control considerations over a 55-year bearing life span (Roeder and Stanton 1991). In comparison with this service limit state, typical seismic design considers a very different location on the fatigue curve, requiring far fewer cycles to far greater displacements, and it even allows permanent damage to a bearing so long as the failure mode is not critical for the overall structure.

Recognizing that elastomeric bearings can actually sustain much larger shear strains than code limitations would imply, Mori et al. (1999) and Konstantinidis et al. (2008) tested steel-reinforced elastomeric bearings to roughly 200% shear strain. The bearings did not have top or bottom plates, and shear deformation was ultimately limited by roll-over considerations. Mori et al. (1999) observed up to a 50% lift-off of bearing area at 200% shear strain. Similarly, Konstantinidis et al. (2008) concluded that the ultimate displacement capacity was

approximately 150% to 225% shear strain, limited by roll-over of the bearing to the point where the initially vertical face of the bearing lay flush against the horizontal concrete support. The IDOT bearings in this research program were expected to exhibit very different behavior at large shear strains because the elastomer is vulcanized to a thick steel top plate that prevents roll-over, but the existing research demonstrates the potential of elastomeric bearings designed only for thermal loads to "perform extremely well, even under seismic loading conditions" (Konstantinidis et al. 2008).

1.3.1.3 Frictional Response

Existing research on frictional response has focused on slip behavior at service loads, with particular emphasis on "walking" of elastomeric bearings under cyclic thermal loads. Friction resistance has been studied for various combinations of natural rubber and neoprene elastomeric materials, in plain and laminated configurations, with steel, smooth concrete, and rough concrete mating surfaces, and at different compression levels and shearing velocities, producing a broad range of potential friction thresholds (Schrage 1981; Muscarella and Yura 1995; McDonald et al. 2000). In general, the friction coefficient depends on average compressive stress and the rate of lateral displacement (for any particular contacted material), but it does not depend on the bearing shape factor or plan area. Trends in friction coefficient are inversely proportional with compression stress and proportional to shearing velocity (Schrage 1981). Notably, much of the existing experimental work on frictional response was conducted at low velocities and to small displacements; however, the response under seismic loading may be quite distinct from the response under these service-level conditions. Therefore, one focus of this research was to characterize the expected slip behavior of Type I bearings on concrete for multiple cycles to large deformations.

1.3.2 Type II Bearings: PTFE Sliding Behavior

When laminated elastomeric bearings cannot accommodate the required superstructure movements at the service limit state, IDOT details a Type II bearing that incorporates an unfilled PTFE sheet on top of a steel-reinforced elastomeric bearing, creating a sliding interface that allows increased movement capacity. This research sought to quantify the frictional response at these PTFE sheets when subjected to multiple large displacement cycles.

Mokha et al. (1990) and Constantinou et al. (1990) conducted extensive tests of PTFE sliding surfaces for application to base-isolated buildings and bridge structures. Those cyclic tests, of smooth, circular, Teflon sheets against polished stainless steel plates, were conducted at higher bearing pressures (1.0 to 6.5 ksi) than typical for PTFE sheets in Type II IDOT bearings, but they still provide valuable insight into behavioral trends. The coefficient of friction was sensitive to bearing pressure and sliding velocity, decreasing with increasing bearing pressure and increasing markedly with sliding velocity (until plateauing at velocities of 4 to 8 in./sec). At lower bearing pressures, there was a larger difference between the static and sliding coefficients of friction. More recently, Konstantinidis et al. (2008) confirmed these behaviors for a bearing configuration similar to the IDOT Type II steel-reinforced elastomeric bearings, vulcanized to top and bottom plates and topped with two circular unfilled dimpled PTFE discs that mated with a stainless steel sliding surface. However, in contrast to the large displacement tests in this research program, those PTFE disks were always in full contact with the stainless steel sliding surface.

1.3.3 Fixed Bearing Behavior

IDOT low-profile fixed bearings feature a rectangular “masonry” plate anchored to the concrete substructure and mated with the curved face of a sole plate that is attached to the superstructure. Under service loads, the low-profile fixed bearings allow a slight rotation about the transverse axis of the bearing, by virtue of the curved sole plate, while pintles prevent “walking” of the sole plate. Under seismic loading, failure is expected to occur either by shear failure of the anchor bolts or shear failure of the pintles, but very little documentation of fixed bearing behavior was found in the literature.

Research by Mander et al. (1996) is the only known source of relevant experimental data, presenting results for tests of three low-profile fixed bearings retrieved from an in-service slab-on-girder bridge. In those tests, the use of large, high-strength anchor bolts ensured a pintle failure mode. The longitudinal and transverse cyclic behavior was similar, with hysteresis typified by elasto-plastic behavior with strain hardening. Under a longitudinal monotonic push to pintle yielding, the sole plate was forced up the side of the pintles and off the masonry plate.

Given the dearth of existing data, this research will significantly expand the understanding of fixed bearing behavior in seismic events. The testing protocols in this research investigated both anchor-bolt and pintle-controlled failure modes, and large displacement tests captured the sliding response of a fixed bearing assembly after failure of the steel components.

1.4 STATE-OF-PRACTICE REVIEW

In conventional (i.e., thermal expansion) applications, steel-reinforced elastomeric bearings must be designed to resist loads and accommodate movement at the service and strength limit states. Failure of a bearing is generally due to gradual deterioration over many cycles rather than by sudden failure under a single load, and the AASHTO specifications are written with an eye toward controlling compressive stress, uplift, buckling, and fatigue over the design life of a bearing.

The AASHTO specifications allow two distinct methods for elastomeric bearing design. Both methods require bearings to be checked to ensure satisfactory performance at limit states governed by compression stress, combined compression and rotation, externally applied shear, buckling stability, and reinforcing. Method A is the older, simpler, and more conservative method. This design approach allows shear modulus to be approximated from hardness measurements. Method B, by comparison, requires laboratory testing to verify shear modulus, but it compensates for the additional material testing with less stringent stress and deformation limits. This method is the more rigorous of the two, and it requires significantly more effort on the part of the designer, but it may result in a bearing that uses less material.

The criteria employed by IDOT for elastomeric bearings are summarized below and generally align with AASHTO Method A:

- The total elastomer height must be at least twice the total expected movement for a Type I bearing, effectively limiting elastomer shear strain to roughly 50% in order to control bearing fatigue. The elastomer height requirement is relaxed to equal the total movement for a Type II bearing in recognition of the slip displacement capacity available at the PTFE surface
- The width of the bearing parallel to the direction of movement must be at least three times the total elastomer height in order to ensure stability of the bearing under service loads.

- The average bearing compression stress from dead load must be between 200 and 500 psi.
- The average compression stress from dead load plus live load (without impact) must be between 200 and 800 psi, which is more conservative than the AASHTO criteria, which would allow up to 1250 psi average bearing compression stress.

IDOT has augmented these provisions with tabular and graphical design aids that incorporate the design parameters and limitations, which simplifies the elastomeric bearing selection process for ordinary highway bridges.

CHAPTER 2 EXPERIMENTAL RESEARCH PROGRAM

2.1 TEST SETUP

2.1.1 Testing Frame

The tests were performed in the Newmark Structural Engineering Laboratory at the University of Illinois using the customized experimental apparatus shown in Figure 2.1, which was designed to reflect field conditions for the full-scale bridge bearing test specimens. Vertical loading was imposed on a bearing using a pair of 100 kip capacity actuators reacting against a steel frame that was secured to the laboratory strong floor with pre-tensioned anchors. The use of a pair of actuators allowed the loading beam to remain level while the vertical load was maintained at a specified target, regardless of the lateral displacement of the bearing. The loading beam was constrained to move in a plane by fabricating and installing steel channel braces to extend from the loading frame columns to flat plates welded to the sides of the beam. Concrete pads were cast to simulate typical bridge substructures, including a brushed finish as specified by IDOT (IDOT 2012b), to ensure that the frictional response at the elastomer-to-concrete substructure interface represented expected field conditions. The concrete test pads were secured to the strong floor using ten pre-tensioned anchors around the perimeter of the pad.

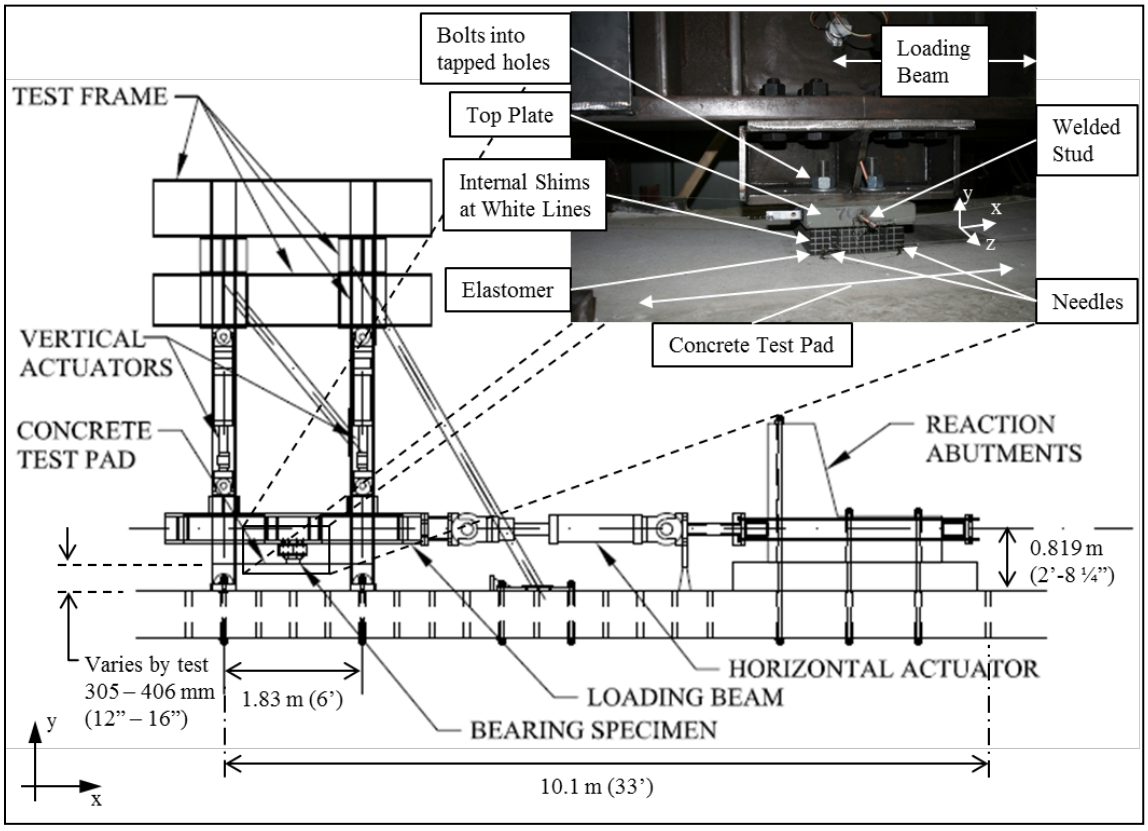

Figure 2.1. Test setup evaluation.

The primary objective of the testing program was to characterize the structural performance and behavior of typical bridge bearings used in Illinois when subjected to large lateral deformations during seismic events. The bearings investigated in this experimental program

included Type I and Type II elastomeric bearings and low-profile fixed bearings, as shown in Figure 2.2. On the basis of preliminary systems analyses of full bridges, in conjunction with a review of literature documenting previous tests of similar elastomeric bearings (Stanton and Roeder 1982; Roeder et al. 1987; Kulak and Hughes 1992; Mori et al. 1999; Konstantinidis et al. 2008), a maximum shear strain target of 400% was selected for the testing program. Equivalent shear strain (ESS) was chosen as a simple measure of displacement that could consistently be applied to all elastomeric bearings in the test program. ESS is the shear strain that would have developed at a given displacement if no slip had occurred (i.e., total top plate displacement divided by total height of rubber).The stroke requirement for the horizontal actuator was therefore governed by the displacement at 400% ESS for the largest bearing in the testing program. The Type I 13c bearings have five layers of 5/8 in. elastomer, for a total height of rubber (h_{rt}) of 3-1/8 in. and an associated 400% ESS of 12-1/2 in. A 30 in. stroke, 220 kip capacity actuator was employed to provide the required 25 in. total horizontal displacement capacity for fully reversed cyclic testing.

2.1.2 Bearing Attachments

An example of the initial state of a Type I bearing prior to application of lateral load is shown in the photo inset of Figure 2.1. The top steel plate was bonded to the elastomer by vulcanization during bearing manufacture. The elastomeric bearings were secured to a built-up steel fixture, which represented a bridge girder. The fixture was mounted under the test frame loading beam with sixteen 1 in. diameter A325 bolts, and the top plate of an elastomeric bearing specimen was attached to the bottom of the fixture with four 1 in. diameter threaded steel studs into tapped holes in the bearing top plate (for most bearings) and eight studs for 13c bearings. This attachment method for the bearing top plates is consistent with bridge construction in Illinois, except that the threaded steel studs are typically only 3/4 in. diameter in practice (IDOT 2012a). The stud size was increased to ensure that the studs and surrounding material would remain elastic and that horizontal displacement would occur only through shear deformation of the elastomer and/or slip at selected sliding interfaces within or below the bearing (and not between the top plate and the loading beam). For each fixed bearing test, the top plate of the bearing specimen was welded to the underside of the steel fixture, according to standard practice for Illinois bridges (IDOT 2012a).

As shown in the photo inset of Figure 2.1, horizontal lines were drawn on the sides of the elastomer to indicate the locations of the internal shims, and vertical lines were added to form a grid to aid in visualization of shear deformations for elastomeric bearings. Longitudinal tests of Type I bearings were performed without any positive horizontal restraint at the simulated substructure interface. For tests of Type II bearings or fixed bearings, as well as for tests involving Type I retainers, threaded steel anchors were embedded in the concrete pad with Hilti HY150 epoxy and a nominal 9 in. embedment depth. Nuts were installed at embedded anchors with a calibrated torque wrench. In most cases, the installation torque was the maximum recommended by Hilti, although some tests were performed at half the maximum value to explore whether this parameter had a significant influence on response.

2.1.3 Instrumentation

Common sensor instrumentation for all tests included axial load cells and displacement transducers for each of the three actuators, a vertically oriented cable-extension position transducer (also called a “string potentiometer,” or “string pot”) to measure the vertical position of the loading beam relative to an objective reference frame outside the test setup

(to avoid including deformations of the loading frame), and an inclinometer mounted to the side of the loading beam. Two 5 in. string pots were used to identify whether (relative) slip occurred at the top plate of the bearing. Absolute bearing displacements were measured by attaching two 50 in. and four 25 in. string pots to the bearings.

The two 50 in. string pots were attached to studs welded onto the bearing top plate for the Type I and Type II bearing tests and to the built-up steel fixture that interfaced between the bearing and the loading beam for the fixed bearing tests. The four 25 in. string pots were attached near the bottom corners of the bearing using needles inserted in the elastomer and by welded studs for Type I and fixed bearing tests, respectively. For Type II bearings, two of the 25 in. string pots were attached to each of the middle and bottom steel plates. All these arrangements permitted calculation of relative displacements between bearing components. When retainers were included in the bearing configuration, four additional 10 in. string pots were attached to each retainer, with two attachment points each at the top and bottom. Two linear variable differential transformers (LVDTs) were also mounted to the sides of each retainer to fully capture their “roll-over” motions. An array of six linear strain gages was installed at each out-of-plane built-up channel brace. Five linear strain gages were also installed on each long side of the fixed bearing bottom plates for longitudinal tests. Strain gage rosettes were installed on each side of each retainer stiffener to capture the multi-axial stress state acting through those components, and four rosettes were also installed at the top surface of each fixed bearing specimen.

2.2 TEST SPECIMENS

The three IDOT bearing types investigated as part of the experimental program are illustrated in Figure 2.2 . All these bearing types were tested in both longitudinal and transverse configurations. Side retainers were included in transverse tests of Type I and Type II bearings.

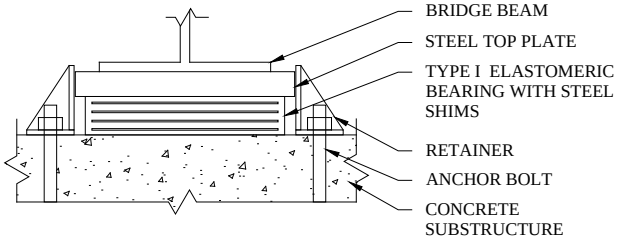

Type I Bearing

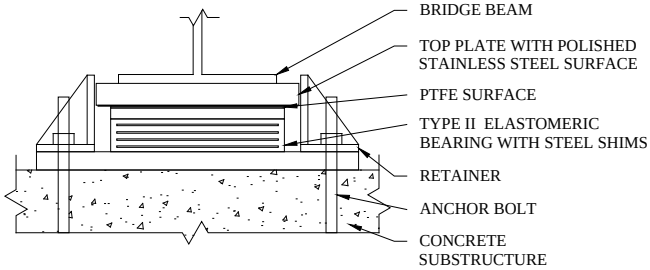

Type II Bearing

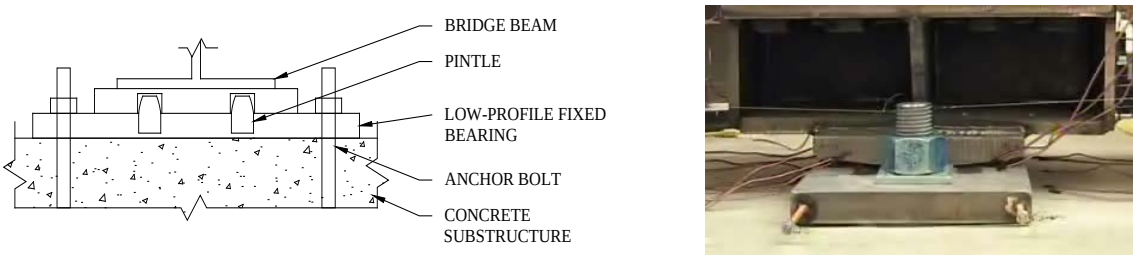

Low-Profile Fixed Bearing

Figure 2.2. Longitudinal (left) and transverse (right) direction views for examples of the IDOT bearings included in the testing program.

A broad overview of the scope of the testing program is given in Table 2.1, with more detailed information provided in Table 2.2.and Table 2.3. (Test specimen Alt Fuse 3 was designed as a unique component, with response and performance characteristics significantly different from typical IDOT bearing components. Results obtained for Alt Fuse 3 are therefore shown and discussed in detail in Appendix D, separate from the main body of the report.) The full testing program included more than 60 individual tests, with four sizes each of Type I and Type II elastomeric bearings and two designs of fixed bearings. Tests were performed on ten individual Type I bearing specimens (including five pairs of standard retainers, plus one pair of modified retainers), six Type II bearing specimens (including four pairs of retainers), four fixed bearing specimens, and four single retainer specimens (with no bearing present).

Table 2.1. Summary of Tested Specimens

Specimen		Test Type		
		Monotonic	**Cyclic**	**Simulated EQ**
Type I	7c	L	L, T	L, T
	9c	--	T	--
	11b	--	T	--
	13c	L	L, T	--
Type II	7c	L	L, T	--
	9a	--	L, T	--
	11a	T	T	--
	13a	--	L, T	--
Fixed		--	L, T	--
Single Retainer	7c	T	T	--
	13c	T	T	--
Alt Fuse		--	T	--

L = longitudinal; T = transverse (includes retainers for Type I and II)

Table 2.2. Test Matrix for Original Testing Program

Specimen	Test	Orientation		Protocol			Rate		Vert Load	Anchor Bolt	
	ID	Long	Trans	Mono	Cyclic	Sim EQ	QS	ISR	(psi)	Grade	Dia. (in)
Type I 7c Tests	1	X		X (-)			X		500		
	2	X		X (-)			X		500		
	3	X		X (-)			X		500		
	3x1	X		X (+)			X		500		
	3x2	X		X (+)			X		375		
	3x3	X		X (+)			X		200		
	3x4	X		X (+)			X		500		
	3x5	X		X (+)				X	500		
	3x6	X		X (+)			X		500		
	3x7	X		X (+)			X		500		
	4	X			X		X		200		
	4x1	X			X		X		800		
	5	X			X		X		500		
	5x1	X			X			X	500		
	15		X		X		X		500	36	3/4
	20	X				X	X		500		
	21		X			X	X		500	36	3/4
Type I 13c Tests	8	X			X		X		385		
	8x1	X		X (+)			X		385		
	8x2	X		X (+)				X	385		
	14		X		X		X		385	36	1 1/4
7c Retainer Tests	6		X	X (-)			X		--	36	3/4
	7		X		X		X		--	36	3/4
13c Retainer Tests	11		X	X (-)			X		--	36	1 1/4
	12		X		X		X		--	36	1 1/4
Type II 7c Tests	9	X		X (-)			X		500	36	3/4
	9x1	X			X		X		500		
	9x2	X			X		X		500		
	9x3	X			X		X		500		
	9x4	X			X			X	500		
	9x5	X			X		X		500		
	10	X			X			X	500	36	3/4
	13		X		X			X	500	36	3/4
Fixed Bearing Tests	16	X			X		X		(42 kip)	36	3/4
	17		X		X		X		(42 kip)	36	3/4
	18	X			X		X		(42 kip)	105	1 1/2
	19		X		X		X		(42 kip)	105	1 1/2

Table 2.3. Test Matrix for Testing Program Extension

Specimen	Test	Orientation		Protocol			Rate		Vert Load	Anchor Bolt	
	ID	Long	Trans	Mono	Cyclic	Irregular	QS	ISR	(psi)	Grade	Dia. (in)
Type I 9c	Ext1		X		X		X		500	36	1
Type I 11b	Ext2		X		X		X		500	36	1 1/4
Type II 9a	Ext3-1		X		X		X		500	36	1
	Ext3-2		X		X			X	500		
	Ext3-3	X			X		X		500	36	1
Type II 11a	Ext4-1	X			X		X		500	36	1 1/4
	Ext4-2	X			X		X		500		
	Ext4-3	X			X			X	500		
	Ext4-4	X		X (-)			X		500		
	Ext4-5	X				X	X		500		
	Ext4-6	X				X	X		500		
	Ext4-7	X			X		X		500		
	Ext4-8	X			X			X	500		
Type II 13a	Ext5-1		X		X		X		385	36	1 1/4
	Ext5-2		X		X			X	385		
	Ext5-3	X			X		X		385	36	1 1/4
Alt Fuse 1	Ext6		X		X		X		385	36	1 1/4
Alt Fuse 2	Ext7		X		X		X		385	36	1 1/4
Alt Fuse 3	Ext8		X		X		X				

2.2.1 Type I Bearings

IDOT size 7c and 13c bearings were selected to bracket a range of commonly used Type I bearings and were considered representative of bearings used at abutment and pier locations, respectively. All elastomeric bearings were furnished by Tobi Engineering, Inc., in Glenview, Illinois. Dimensions of the test specimens conformed to standards used by IDOT, as specified in their Bridge Manual (IDOT 2012a). According to documentation supplied by the manufacturer, the elastomer used for the bearings was composed of polyisoprene (natural rubber) that met the AASHTO thermal requirements of Grade 3. Specifications for bearings supplied to IDOT require a Shore A hardness of 55 ± 5, which corresponds to a range of estimated shear moduli from 95 to 200 psi, according to AASHTO (2012); all the bearing specimens satisfied this hardness requirement. The manufacturer reported a hardness of 54.3 and a shear modulus (according to ASTM D4014, Annex A [2007]) of 124 psi for the elastomer used in the bearing specimens.

Transverse response of Type I bearings was studied by conducting both single retainer tests and complete bearing assembly tests. Threaded anchor diameters and dimensions of the retainers were specified to provide a design fuse capacity equal to 20% of dead load, in accordance with the ERS guidelines, and to conform to standard details found in the IDOT Bridge Manual (IDOT 2012a) in effect at the start of the project (2008). Designs assumed F1554 Gr 36 steel and an average dead load of 500 psi acting on the elastomer area (for bearings other than 13c) and 385 psi for 13c bearings. Anchor diameters provided for each test are shown in Table 2.2 and Table 2.3.

2.2.2 Type II Bearings

Type II bearings were also furnished by Tobi Engineering, Inc. Each Type II bearing contained three steel plates (in addition to the internal elastomer reinforcing shims). The upper two plates met at a sliding interface with stainless steel on the upper plate and Teflon on the middle plate. The middle and lower plates were vulcanized to a reinforced elastomeric bearing, similar to a Type I bearing. Documentation supplied by the bearing manufacturer indicated that mating surfaces at the sliding interface conformed to IDOT requirements (IDOT 2012b). With particular reference to factors influencing sliding characteristics, the stainless steel was furnished with a Type 2B finish, and the Teflon static coefficient of friction at 500 psi average pressure was 0.065 (compared with the IDOT specified maximum of 0.07).

Anchor and retainer sizes and installation methods for the Type II bearings were similar to those used for Type I bearings of the same size, with the retainer height increased to account for the increased height of the top plate. All tests had anchors installed to secure the bottom plate to the concrete pad, but retainers were not installed for the longitudinal tests in order to prevent interference with string pot attachments.

2.2.3 Fixed Bearings

Fixed bearings were tested to evaluate their longitudinal and transverse response for two design cases: (1) anchor bolt-controlled and (2) pintle-controlled. These bearings were designed and tested based on the typical demands for the most common Type I bearing case of the experimental program: simulated gravity load of 42 kips and peak cyclic displacements of ±7.5 in. The smallest pintle size available was 1-1/4 in. diameter, which was anticipated to provide a fuse capacity significantly in excess of the nominal target of 20% of dead load, even if Gr 36 material was used. Therefore, the distinguishing characteristic between anchor bolt-controlled and pintle-controlled cases was the size and grade of steel anchors. The anchor bolt-controlled case used two 3/4 in. diameter Gr 36 anchors, whereas the pintle-controlled case used two 1-1/2 in. diameter Gr 105 anchors. Bearings for the anchor bolt-controlled cases were supplied by Industrial Steel Construction, Inc., for which documentation indicated that the plates and pintles were M270 Gr 36. For the pintle-controlled case, the bearings, consisting of M270 Gr 36 top and bottom plates and A588 press-fit pintles, were supplied by D. S. Brown, and the 1-1/2 in. diameter F1554 Gr 105 threaded anchors were supplied by J. H. Botts, Inc. In all cases, the top plate was welded to the steel test fixture bolted to the underside of the loading beam, and the bottom plate was located on the concrete pad to match the press-fit pintles with the holes provided in the bottom of the top plate.

2.3 TEST PROCEDURE

A variety of tests were performed to simulate either longitudinal or transverse motion of a bridge superstructure. Parameters for each test are summarized in the testing matrix shown in Table 2.2 and 2.3. For clarity, the tests are organized by specimen type, with chronological test order then indicated by the Test ID. Test IDs with an appended *x1*, *x2*, etc. (or *−1*, *−2*, etc.) indicate that multiple tests were performed on the same bearing. The Orientation field states whether the bearing was tested in a longitudinal or transverse configuration. For Type I and Type II bearings, all transverse tests included side retainers. The Anchor Bolt field indicates the nominal anchor bolt grade and diameter employed, for tests where this is pertinent.

2.3.1 Testing Control Overview

All three actuators were driven in position control during the experiments. Each actuator was accompanied by a controller to interpret feedback from the internal sensors and update command signals to regulate the flow of oil, thereby driving the piston to prescribed target positions. For all tests, each controller was fed an external waveform, which was then converted internally by the controller to position commands for the attached actuator. The overall testing control objectives, however, were to displace the bearings to prescribed horizontal position targets while maintaining a constant simulated vertical gravity load. To achieve this, real-time feedback was read from sensors attached to the specimen and load frame during a test, the displaced configurations of actuators were evaluated and used to resolve the forces into horizontal and vertical components, and the vertical load was determined from the combination of actuator vertical force components and loading beam weight. The horizontal actuator command was adjusted to account for discrepancies between current horizontal position and the target value, and, similarly, the vertical actuator commands were adjusted to provide more or less vertical load as required to maintain the simulated gravity load near the target value for the test. Thus, slow “quasi-static” (QS) tests were conducted by supplying external waveform commands to each actuator according to a mixed-mode control algorithm. Tests performed at an increased strain rate (ISR) employed a pre-defined sequence of command signals for all the actuators, based on bearing response to actuator commands obtained from a previous similar QS test.

2.3.2 Displacement Protocols

The Protocol field indicates whether a test was monotonic, cyclic, or based on a simulated earthquake record (or, in some instances, “irregular”), and the Test Travel field indicates the maximum travel of the top plate for that particular test, in units of ESS (where 100% = 1). Directionality of monotonic tests is indicated with a (+) or (−) per the x-coordinate defined in Figure 2.1.

The displacement record used for fully reversed longitudinal cyclic testing of Type I bearings, shown in Figure 2.3(a), was determined based on a review of pre-qualification and characterization tests used for seismic isolation bearings (Shenton 1996; HITEC 1996; AASHTO 2010). The initial stages included seven cycles each to 25% and 50% shear strain, followed by three cycles each at 100%, 200%, 300%, and 400% ESS. The additional cycles at the lower strain levels were imposed to investigate any effect of scragging (i.e., degradation in stiffness resulting from multiple imposed cycles of strain) that may have developed in elastomer material response.

When retainers were included for transverse tests, a number of initial cycles were added to the beginning of the record, bounded by force targets rather than displacement targets—three cycles at each of 25%, 50%, and 70% of the estimated fuse force capacity of the retainers. The record then transitioned to the standard displacement-based targets, starting at the next higher target than the initial force-based targets had required. Testing protocols for the fixed bearings generally followed the same procedure as for Type I 7c bearings, with displacement targets matching the 7c ESS targets. In contrast to the Type I protocol, however, only three displacement cycles were performed for 25% and 50% ESS levels, with displacement targets then gradually stepped up in increments of approximately 5% from 25% to 50% and 50% to 100% of a corresponding Type I 7c bearing’s rubber thickness.

The Type II bearing tests that included retainers for the transverse direction followed a protocol similar to the Type I bearing testing protocol including retainers. Mokha et al. (1990) have shown that Teflon slip resistance varies significantly for increasing velocities until a

plateau is reached at about 4 in./sec. Consequently, for both longitudinal and transverse orientations, the Type II bearings were also tested at higher strain rates than used for typical Type I bearing tests, in order to capture the velocity dependence of the Teflon sliding surface response. Because Type II bearing response was anticipated to be more significantly affected by velocity (rather than peak displacement), the typical Type II test protocol included only five pre-slip cycles at 25% and 50% ESS and then transitioned immediately to a sequence of twelve maximum displacement cycles. The maximum displacement target was limited to 200% ESS for the ISR test in the longitudinal orientation with the 7c, but it was held at 400%, similar to corresponding Type I's, in the transverse direction. The longitudinal maximum displacement was set to a lower value than for the transverse tests, based on observations of response from initial quasi-static cyclic tests up to 400% ESS. For the 9a, 11a, and 13a bearings in the testing program extension, the peak displacement was set so that the exposed portion of the Teflon would account for no more than about 20% of the total area. The maximum displacement target for ISR tests on Type II bearings, in terms of ESS, therefore varied among bearing specimens, with typical values of 200% but increasing to 250% for the 13a bearing and to 400% for the 7c bearing in the transverse orientation. The time required to perform each ISR test varied slightly, depending on the combination of peak ESS, rubber thickness for individual bearings, and available peak oil flow rate at the time of the test. The protocol for the 9a bearing is provided in Figure 2.3(b) as a representative example for the general form and approximate time required for ISR tests on Type II bearings.

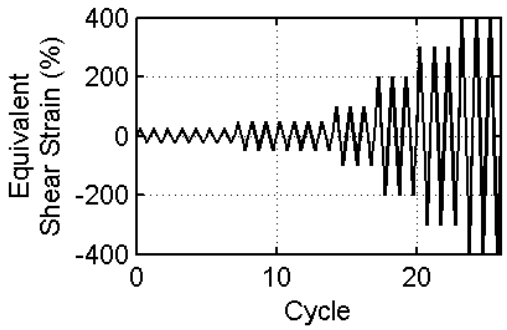

(a) For Type I bearings

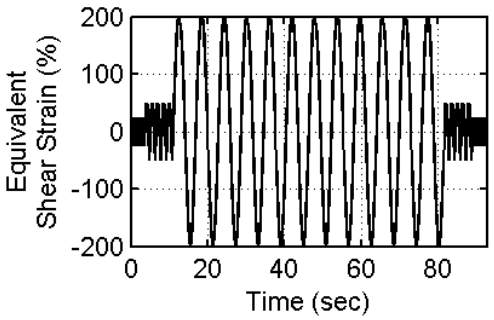

(b) For the Type II 9a bearing

Figure 2.3. Cyclic testing protocols.

The two simulated earthquake tests used displacement records obtained from an OpenSees model of the prototype bridge (discussed separately in Volume 2 of this report). Elastomeric bearing and anchor bolt properties in the OpenSees model were calibrated to match the expected performance of the test specimen. Bearing shear modulus was obtained from pre-tests of three fully reversed cycles to ±100% ESS, and coefficients of friction were estimated from a single reversed slip cycle to ±200% ESS. Retainer properties for the transverse test were based on data from Test 15, a transverse cyclic test of a Type I 7c bearing with side retainers. The displacement protocols obtained from OpenSees are shown in Figure 2.4.

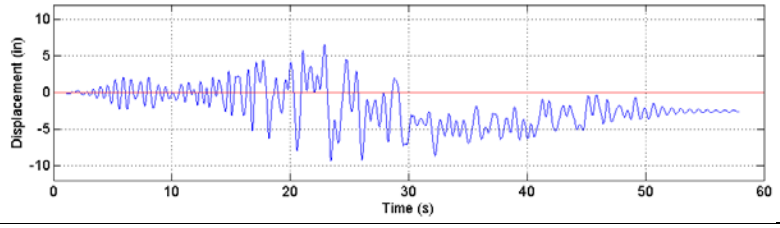

Bridge	SsC15T1F
Ground Motion	Pa06
Scale Factor	1.75
Bearing	Abut 1 Exterior Brg

(a) Longitudinal simulated earthquake displacement time history and OpenSees information

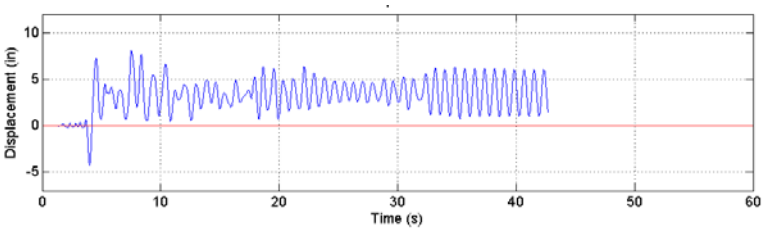

Bridge	SsC15T1F
Ground Motion	Pa01
Scale Factor	1.00
Bearing	Abut 1 Interior Brg

(b) Transverse simulated earthquake displacement time history and OpenSees information

Figure 2.4. Displacement protocol for simulated earthquake tests.

2.3.3 Test Rate

The Rate field in Table 2.2 and Table 2.3 indicates whether a test was quasi-static (QS) or was performed at an increased strain rate (ISR) to investigate sensitivity in response characteristics to velocity demands. QS tests were performed by dividing the displacement record into substeps equal to 1% of total rubber height, h_{rt} (also referred to as effective rubber thickness [ERT] in the IDOT Bridge Manual). The vertical force on the bearing varied by as much as ±2 kips from the target during vertical control iterations of QS tests. The velocity of the top plate was determined by the time required to sample signals and perform calculations between substep iterations, and it was generally low relative to the hydraulic capacity of the testing equipment. For example, the average velocity for Test 3-1 was approximately 0.0027 in./sec, or about 0.14% shear strain per second.

For ISR tests, the command signals from a previous quasi-static test were used to define the signals corresponding to converged states. Those signals were then mapped to a sinusoidal waveform on a compressed timeline so that the bearing travel would meet a target velocity. Target velocities for ISR tests were selected based on the available hydraulic capacity of the testing setup and ranged from 0.6 to 2.5 in./sec, or 32% to 80% shear strain per second. Although the velocities considered are smaller than expected for seismic demands, the ISR tests do provide some insight into potential rate effects. Prior research (MRPRA 1980) shows that a strain rate dependency exists for natural rubber with respect to shear modulus, but that the shear modulus is more significantly influenced by peak shear strain than by strain rate. More recent research by Konstantinidis et al. (2008) agrees with this finding, showing a relatively minor influence of strain rate, which was overshadowed by the influence of peak shear strain. Ideally, strain rates for such a testing program would reach those expected for large seismic events, but peak strain demand and capturing the behavior of the bearings when subjected to large cycles with slip were judged in this study to be even more significant for characterizing the bearings' behavior during large earthquakes.

The simulated earthquake records were also conducted at increased strain rates, but they differed from the typical ISR tests in that a previous slow test was not available from which to determine the appropriate command signals for the converged states of horizontal position and vertical load. To overcome this lack of information, pre-tests were conducted to map vertical loads to command signals for the actuators at 1 in. horizontal position increments. The OpenSees displacement and vertical force records were then mapped to an expanded timeline so that the maximum velocity would be 4 in./sec, and the command signals were interpolated for combinations of position and vertical load, at steps of 10 milliseconds. This approach was intended to account for deformations in the loading frame associated with a range of vertical load levels and positions while only subjecting the bearing to vertical loads within typical service load and deformation limits (therefore avoiding

any unnecessary shear deformation or sliding prior to conducting the actual test, beyond the minimal amount imposed to characterize bearing stiffness and friction for the OpenSees model).

2.3.4 Vertical Load

Standard IDOT designs are required to maintain an average compression stress of between 200 and 800 psi on the elastomer plan area because of gravity load (IDOT 2012a). Accordingly, the compression levels selected for the tests, shown in the Vertical Load field, fall within this range. In the initial phase of each test, prior to imposing shear displacements on the specimen, the bearing was first subjected to a vertical loading/unloading/reloading cycle to obtain data for the compression stiffness of the specimen and also to pre-load the bearing with the target simulated gravity load before applying lateral displacements. For typical monotonic and cyclic QS tests, the control algorithm sought to maintain the simulated gravity load to be constant within a tolerance throughout the duration of the test. This was also the objective for typical ISR tests, where the commands supplied to the actuators were obtained from previous QS tests, during which the simulated gravity load had been held approximately constant. The earthquake simulation tests were unique in that the OpenSees model accounted for vertical load variation induced during the time history response of the bridge. The force record from OpenSees was employed, accordingly, for each earthquake simulation test to vary vertical actuator commands throughout the time history.

CHAPTER 3 TYPE I BEARING EXPERIMENTAL RESULTS

3.1 QUASI-STATIC MONOTONIC LONGITUDINAL TEST RESULTS

Monotonic tests were performed, for movement in the longitudinal bridge direction, on two Type I bearings (a 7c and a 13c), to explore the fundamental shear deformation and sliding characteristics for elastomeric bearings with positive connections to superstructures but only frictional restraint at substructures. For the Type I 7c bearing, these monotonic tests (1 through 3x7) were conducted on a bearing that was new for Test 1, whereas for the Type I 13c, a monotonic test (8x1) was conducted after cyclic testing. Tests were typically performed to a maximum equivalent shear strain (ESS) of 400%, which equates to 7-1/2 in. for a Type I 7c bearing, or 12-1/2 in. for a Type I 13c bearing. The observed constitutive horizontal force-displacement responses are shown in Figure 3.1 in terms of kips and inches, and non-dimensionally in Figure 3.2 in terms of the ratio of horizontal to vertical force and ESS. The non-dimensional plot provides insight into the shear strain level at which slip initiates, as well as into the coefficients of friction that characterize the response of the bearings.

Detailed response characteristics for the individual tests are provided in Appendix A. The effective apparent shear stiffness is the measured linear stiffness from the initiation of the test until a deviation of the response from linear shear strain to a sliding response. Effective apparent shear modulus is the shear modulus associated with the measured shear stiffness, determined according to

$$G_{eff} = \frac{K_{h,eff}\, ERT}{A} \frac{1000\, lb}{1 kip} \qquad \text{(Eq. 3-1)}$$

where

$K_{h,eff}$ = Effective apparent shear stiffness, kips/in.

ERT = Effective Rubber Thickness, in.

A = Nominal plan area of elastomer ($W_e * L_e$), in^2

The shear characteristics are noted as “effective” and “apparent” because they do not in general represent fundamental material properties. In addition, they are not reflective of the exact shape of the shear response curve, which will exhibit a sequence of stiff, softened, and secondary stiffening segments rather than truly linear elastic behavior. However, these effective apparent values are expected to be more valuable than fundamental material properties when constructing complete bridge models, which are anticipated to employ simplified linear elastic components to represent Type I elastomeric bearings. An effective linear shear modulus of approximately 75 to 80 psi appears to be reasonable for large shear strain response, sufficient to induce slip at approximately 150% to 225% shear strain at average compression stresses of 200 to 500 psi, respectively.

Mean slip resistance is the measured resisting force during sliding, averaged over the sliding travel during a given test. The coefficients of friction are determined from the ratio of horizontal to vertical force at each data point during slip, with the mean value determined with respect to slip travel, similar to the slip resistance value. A peak friction coefficient of

about 0.35 and a typical sliding coefficient of about 0.3 appear to be reasonable general assumptions for Type I sliding response observed from the monotonic tests.

General trends observed in the monotonic tests were that the shear stiffness tended to degrade with repeated tests, even when allowing approximately 24 hours to recover from scragging in the elastomer. The decrease in stiffness with succeeding tests is suspected to be the result of chamfering of the leading edge of the elastomer through abrasion against the concrete surface. It was also observed that the apparent shear modulus tends to decrease with increasing shear strain. Close inspection of the shear response reveals that there is an initial, relatively stiff branch, followed by a softened shear stiffness that remains approximately linear up to slip. The larger the shear strain at slip, the less the initial stiffening branch contributes to the two-point linear shear stiffness estimate. Lastly, tests with varying average compression stress confirmed that the coefficient of friction is an inversely related function of the imposed compression. This can be observed in a comparison of Figure 3.1 and Figure 3.2 where Test 3x3, with the least compression stress, had the lowest force level of slip resistance but the highest coefficient of friction after normalizing the slip resistance by the imposed compression.

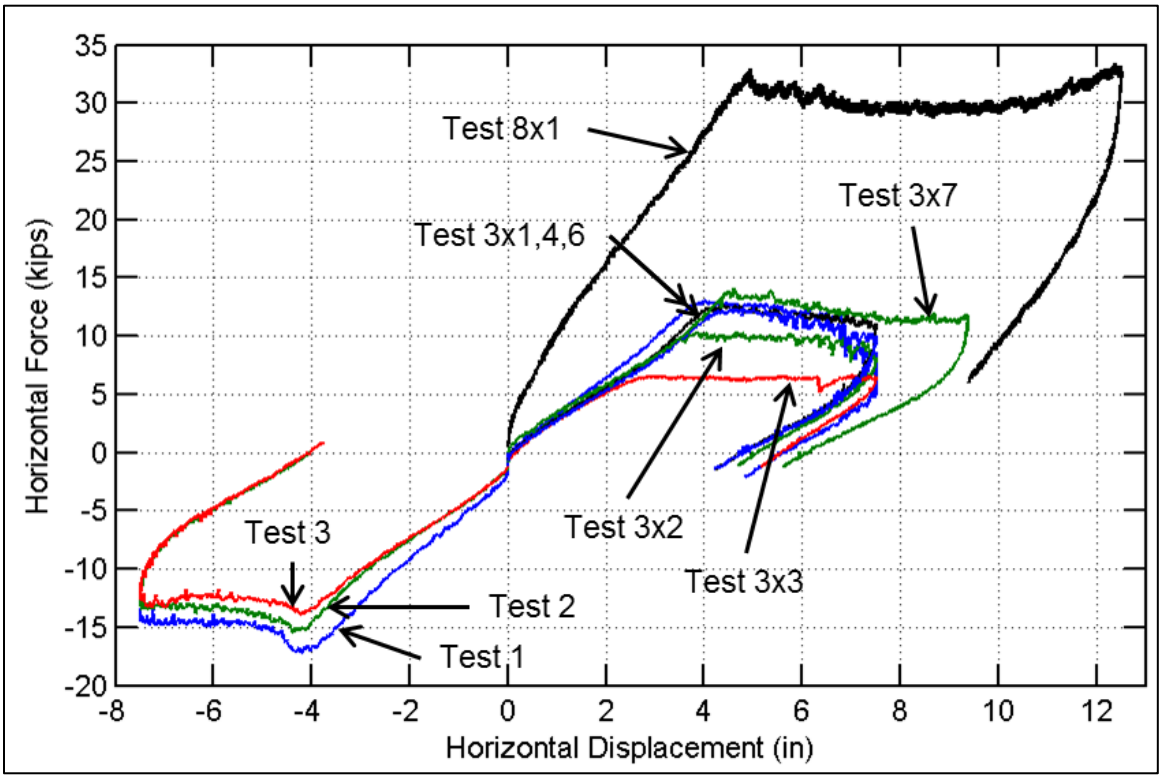

Figure 3.1. Monotonic Type I force versus displacement, longitudinal orientation.

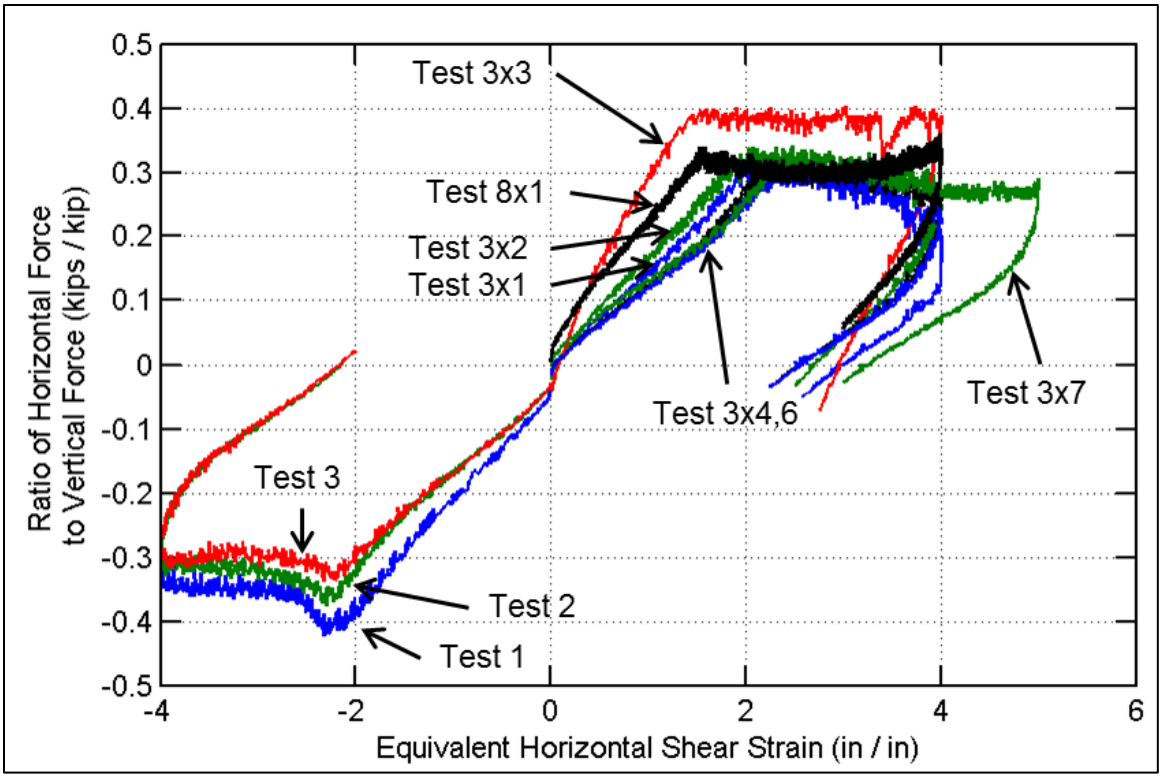

Figure 3.2. Non-dimensional monotonic Type I constitutive response, longitudinal orientation.

3.2 QUASI-STATIC CYCLIC LONGITUDINAL TEST RESULTS

Cyclic tests, following the protocol described in Section 2.3.2, were used to study two Type I 7c bearings and one Type I 13c bearing subject to simulated longitudinal bridge excitation. The results of the cyclic tests are shown in Figure 3.3 through Figure 3.6 The three cyclic 7c tests are overlaid in Figure 3.3, showing the progression from primarily sliding with a compression load of 200 psi in Test 4, to a more non-linear shear response with a compression load of 800 psi in Test 4x1 (where “x1” indicates reuse of the bearing specimen from the previous Test 4). The bearings exhibited a shear response over a range of approximately ±100% shear strain at 200 psi compression, increasing to approximately ±250% shear strain at 800 psi compression. The 13c results are overlaid on the 7c results in Figure 3.4. The general form of the response is similar to the 7c data, but the magnitude of the forces and displacements are larger because of larger elastomer plan area and total thickness.

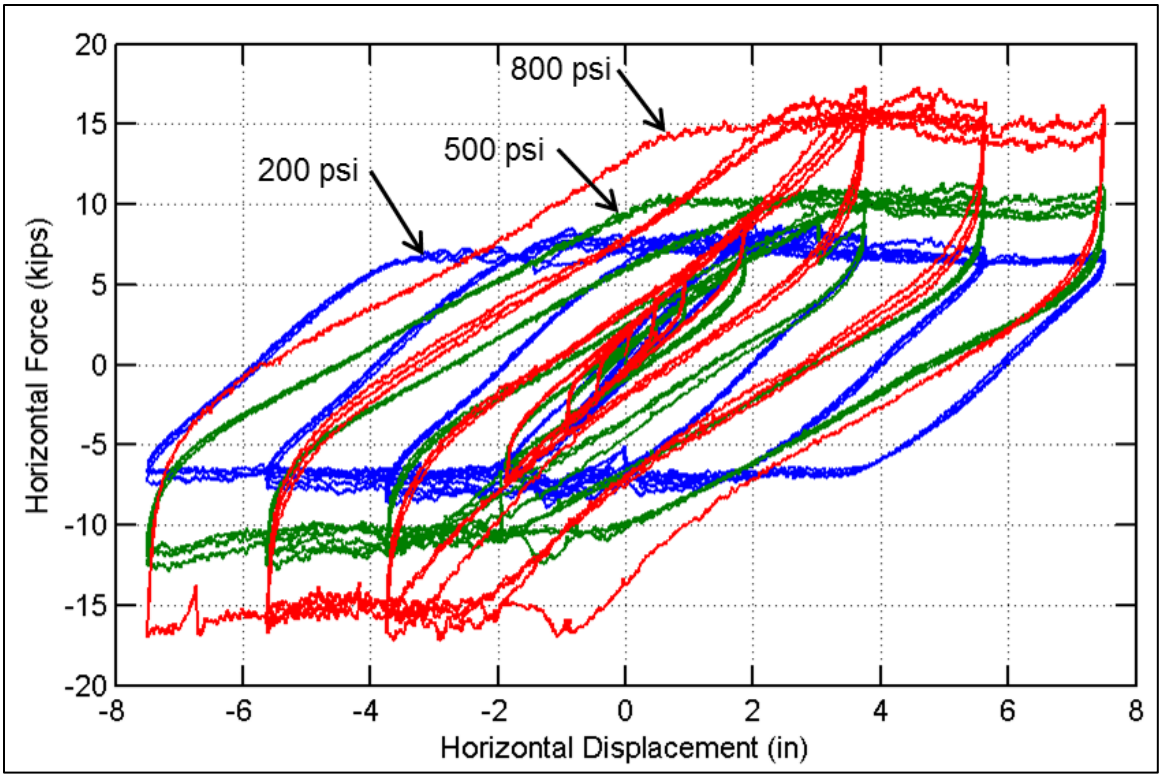

Figure 3.3. Cyclic Type I 7c force versus displacement, longitudinal orientation.

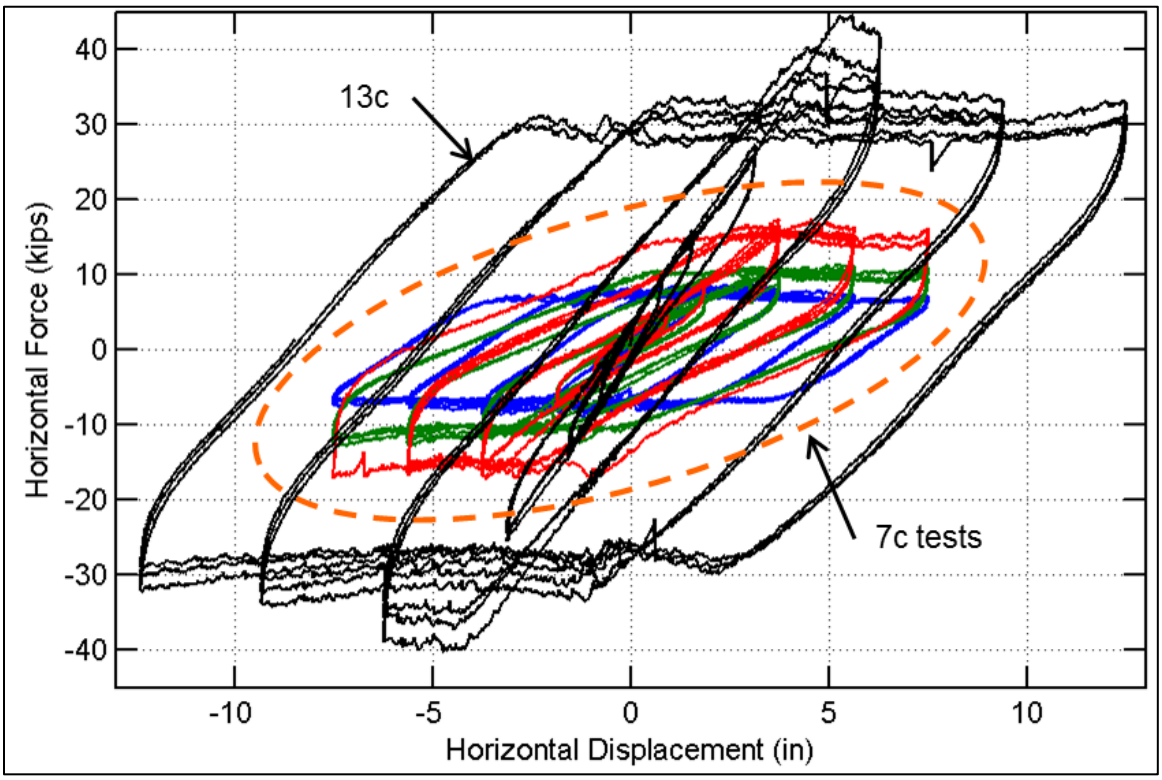

Figure 3.4. All quasi-static cyclic Type I tests, force versus displacement, longitudinal orientation.

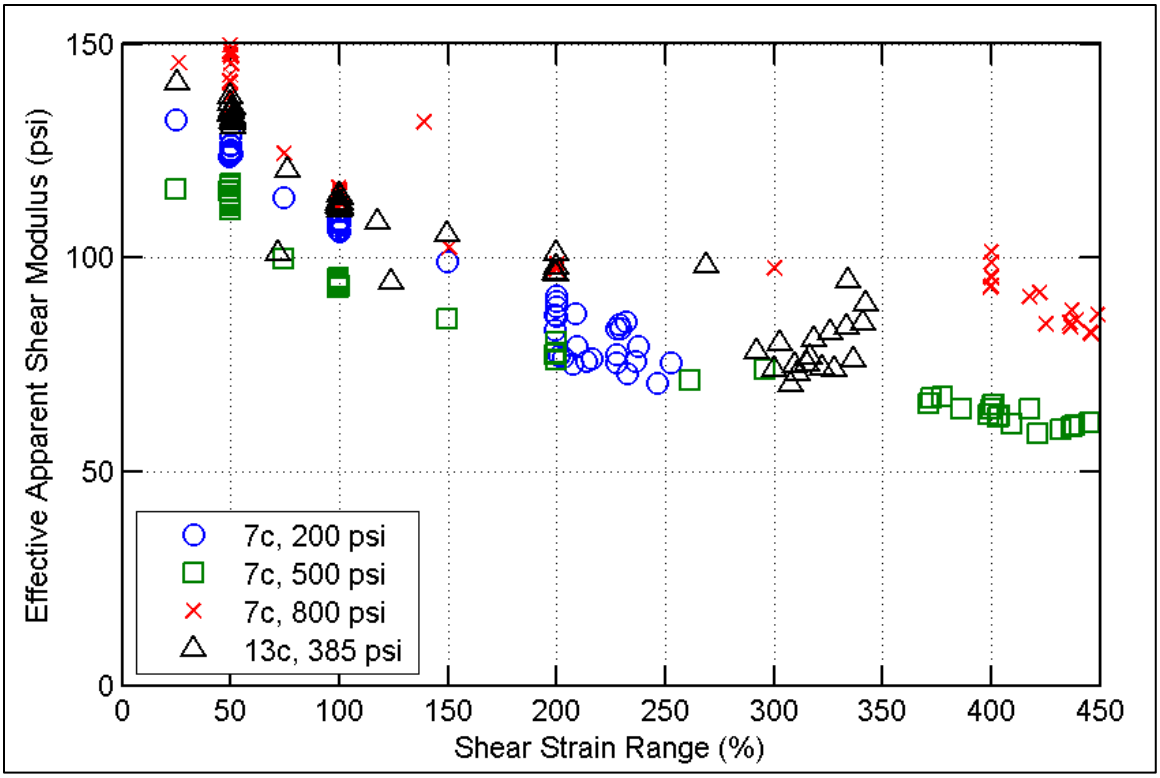

Figure 3.5. Variation of Type I effective apparent shear modulus with shear strain range.

A significant decrease in shear stiffness was correlated with the shear strain range for the individual ramps during a test. For the initial ramps of the tests, with imposed shear strain ranges of about 50% (from −25% to +25%), the effective apparent shear modulus ranged from about 110 to 150 psi, including both scragged and unscragged conditions during seven reversed cycles of shear displacements. These results agree with the data supplied by the bearing manufacturer, which indicated that the shear modulus obtained from ASTM D4014, Annex A, was 124 psi. As mentioned previously in the monotonic testing section, the constitutive response consists of an initial, relatively stiff branch that results in increased apparent linear shear moduli for small strains. As the shear strain demands increase, the initial stiff branch becomes progressively more overshadowed by the softened secondary stiffness. Consequently, shear moduli assumed for modeling parameters to reflect high strains should be significantly reduced from the values stipulated in the testing data of bearing suppliers. The ratio of apparent shear moduli to the manufacturer's reported value for the data shown in Figure 3.5 ranges from a maximum of around 0.8 to a minimum of about 0.5 for ramps that transition to sliding.

Non-dimensional results are provided in Figure 3.6, where, consistent with the monotonic test observations, the observed sliding friction is sensitive to the imposed compression load, and the coefficient of friction is inversely related to the applied compression. Friction coefficients were calculated at 5% ESS increments for sliding segments of longitudinal tests, yielding the data presented in Figure 3.7. These data are essentially an extraction of only the sliding segments from Figure 3.6. The inverse relation of compression load and friction resistance can be seen most clearly in the abrupt shift from Test 4, which had an average compression stress of 200 psi, to Test 4x1, performed on the same bearing as Test 4 but with an average compression of 800 psi. There is also a slight degradation in friction resistance with accumulated slip travel, seen most clearly for Test 4, which had long sliding

segments because of a relatively light average compression of 200 psi on the elastomer area, and for Test 8, which had relatively large peak displacements in the testing protocol corresponding to increased elastomer thickness (with maximum displacement demands of ±12-1/2 in., compared with ±7-1/2 in. for the other tests shown).

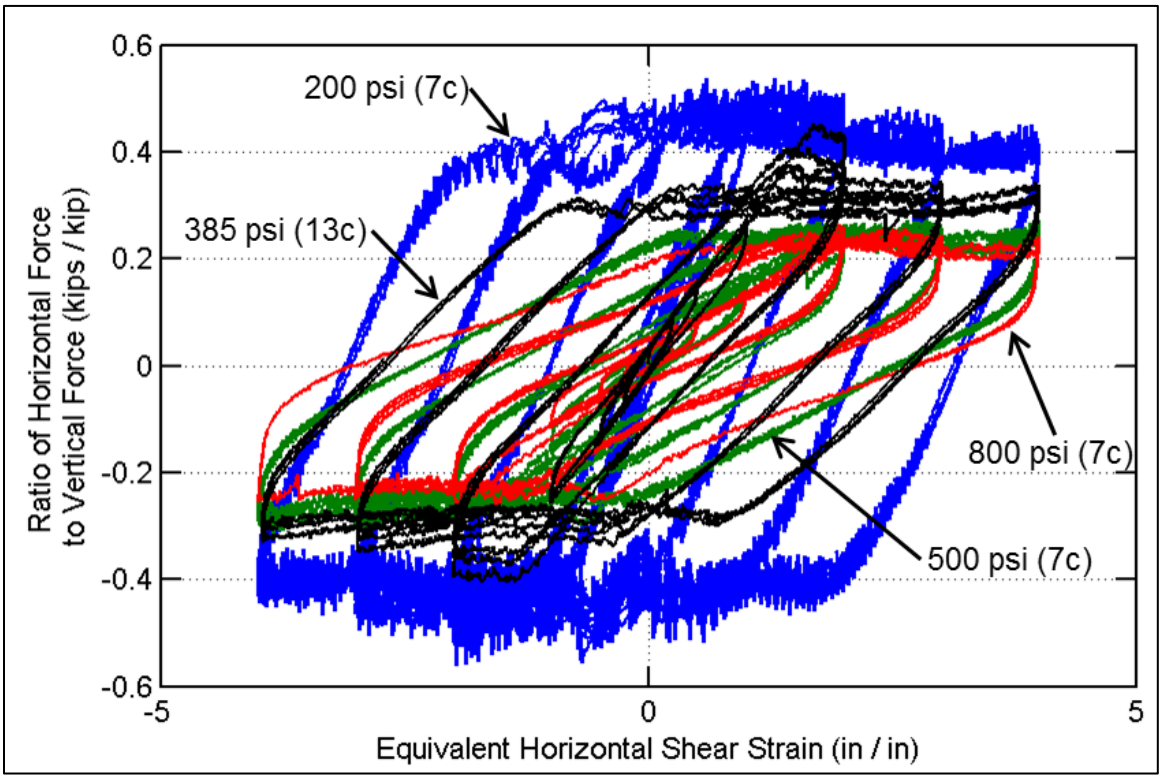

Figure 3.6. Non-dimensional cyclic Type I constitutive response, longitudinal orientation.

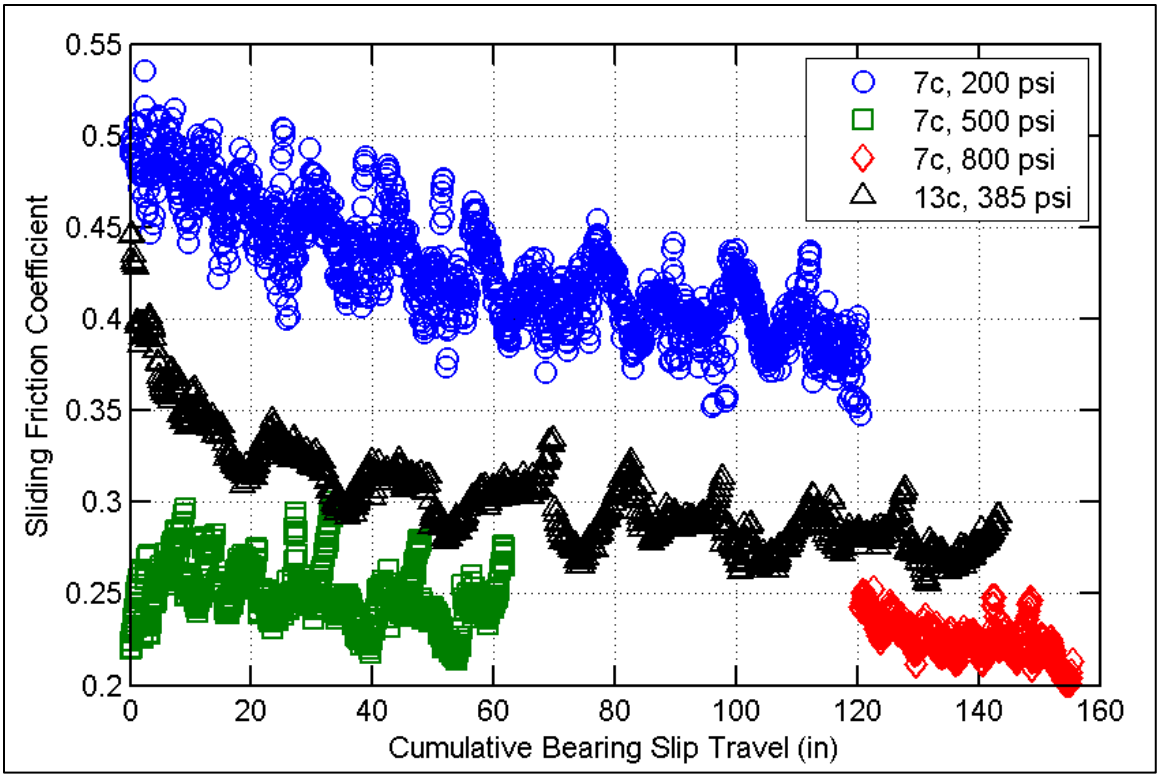

Figure 3.7. Variation of sliding friction coefficient with cumulative Type I bearing slip for longitudinal tests.

Effective damping values for a range of peak cyclic shear demands are shown in Figure 3.8, where the damping was estimated according to the Guide Specification for Seismic Isolation Design (AASHTO 2010). The two-branch shear stiffness response of the bearings also influences the effective damping observed as a function of peak cyclic ESS. At low levels of shear strain, the initial stiffened branch significantly increases the available damping of the bearing, in conjunction with the applied load. Relatively heavily loaded bearings exhibited effective damping up to nearly 20% of critical for cycles with peak shear strains of 25%. As strain increases, the effective damping is reduced as the linear stiffness converges toward the secondary shear stiffness, and the initial stiffened branch becomes a less significant influence on the overall response. The effective damping converged to approximately 5-10% for all loading cases with peak shear strains of about 100%. Beyond 100%, sliding will initiate at a shear strain limit depending on the applied load. The effective damping then begins to increase dramatically when the response includes sliding, as indicated with hollow markers in the figure (as opposed to filled markers indicating shear deformation only).

For large seismic events, the estimated damping evaluated according to AASHTO (2010) would primarily reflect the energy dissipation associated with sliding of the bearings on the substructure. However, based on results obtained from the simulated earthquake test for the longitudinal bridge direction, the hysteretic component of the elastomer material response contributed about 20% of the total energy dissipation, which would normally be neglected when using an elastic-perfectly plastic constitutive model for bearing response. This proportion was determined by evaluating the total energy dissipated during the experiment and deducting the portion associated with slip. The stated value may even somewhat underestimate the hysteretic component for this test, because the longitudinal earthquake simulation experiment was also influenced by significant fluctuations in vertical load for the

bearing, in some cases causing the bearing to briefly lift off from the concrete surface, and these instances would be perceived as slip in the data.

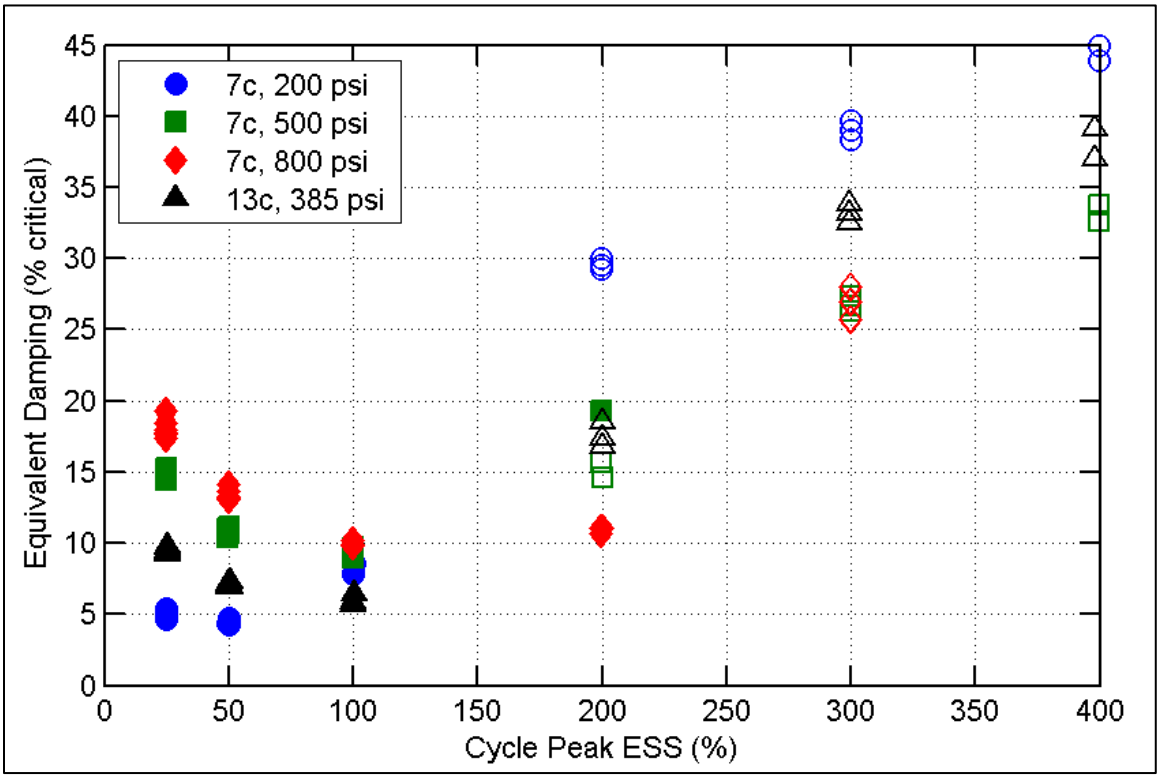

Figure 3.8. Variation of effective damping with peak shear strain for Type I longitudinal orientation tests.

3.3 INCREASED STRAIN RATE INFLUENCE ON TYPE I BEARING RESPONSE

Two monotonic tests and one cyclic test were performed at an increased strain rate (ISR) on Type I bearings. In each case, a quasi-static (QS) test was performed first, and the converged states of the actuator command signals were mapped to a sinusoidal displacement record on a compressed timeline, such that the peak horizontal velocity during the ISR test would make use of the full hydraulic capacity of the actuator pump and control system available at the time of the test. For the tests investigating the longitudinal response of Type I bearings, the hydraulic capacity limited the maximum velocity to approximately 0.7 in./sec. The monotonic test results are shown in Figure 3.9, in terms of force and displacement, and in Figure 3.10 in a non-dimensional form. The cyclic test force-displacement results are shown in Figure 3.11, with a non-dimensional plot available in Appendix A. In each figure, the previous QS test is included for comparison. In all cases, the effective shear modulus and maximum friction increased as strain rate increased. The data for the monotonic tests are summarized in Table 3.1 and Table 3.2, and the trends of effective shear modulus with shear strain range for similar QS and ISR cyclic tests are shown in Figure 3.12.

.

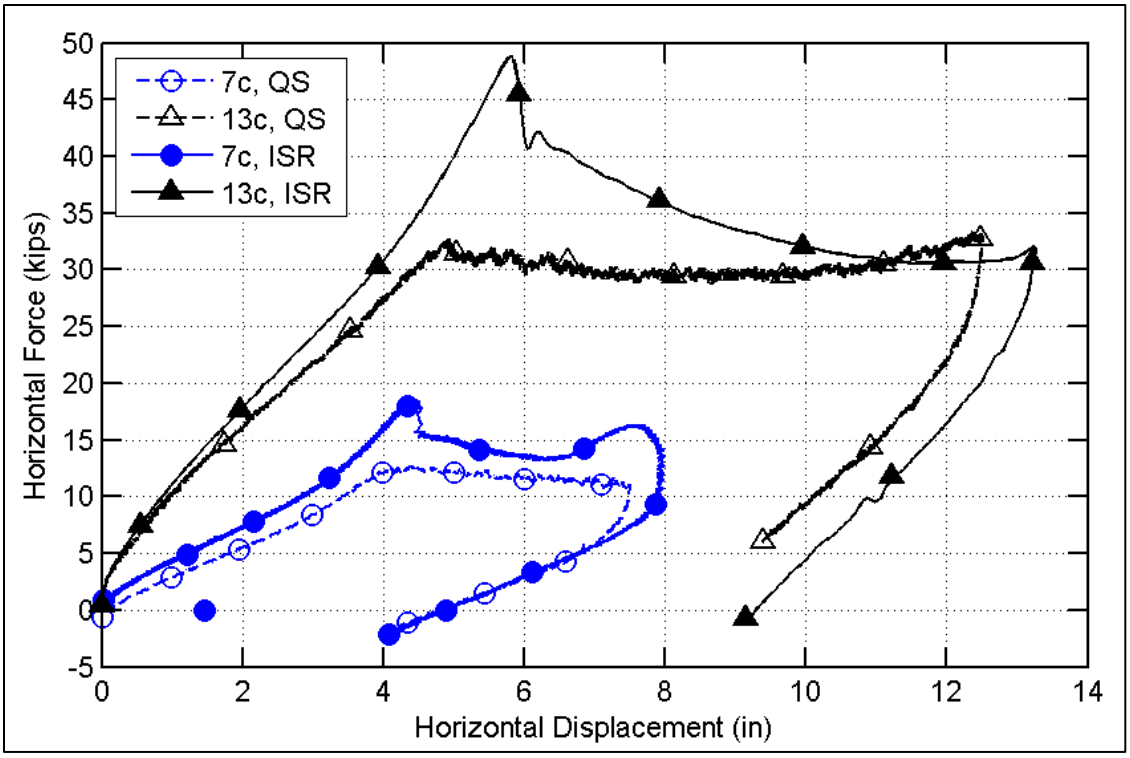

Figure 3.9. Monotonic Type I force versus displacement, longitudinal orientation, with increased strain rate.

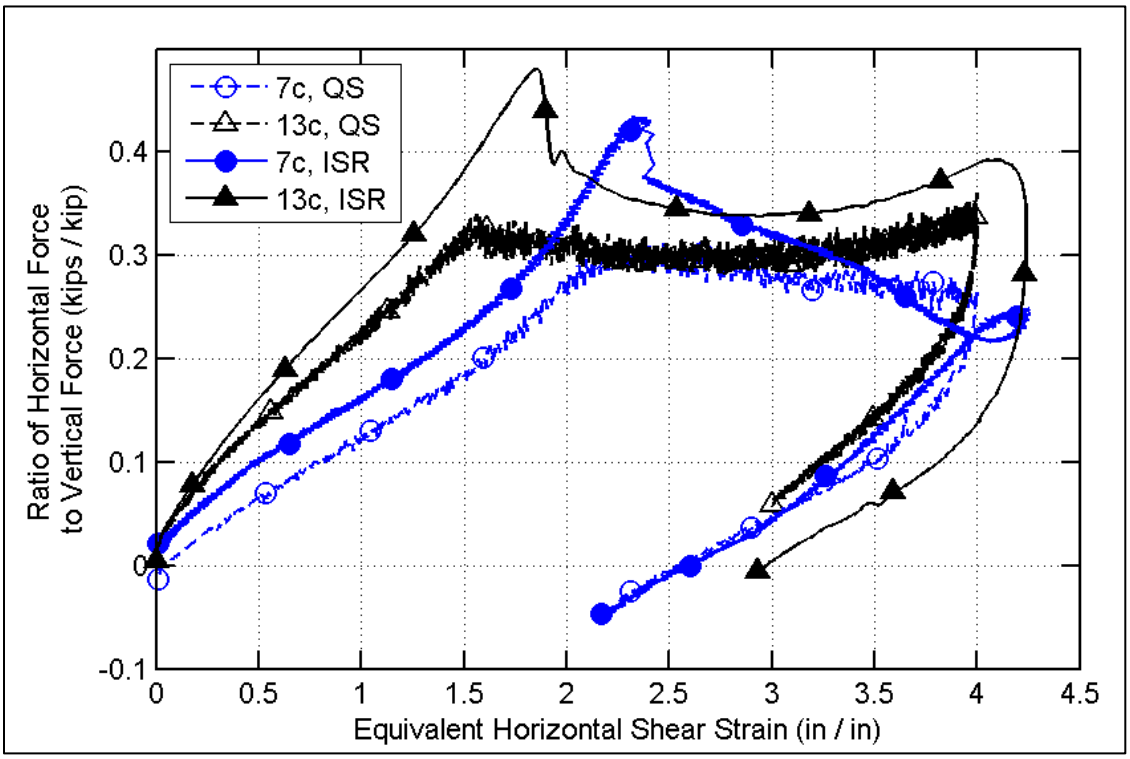

Figure 3.10. Non-dimensional monotonic Type I constitutive response, longitudinal orientation, with increased strain rate.

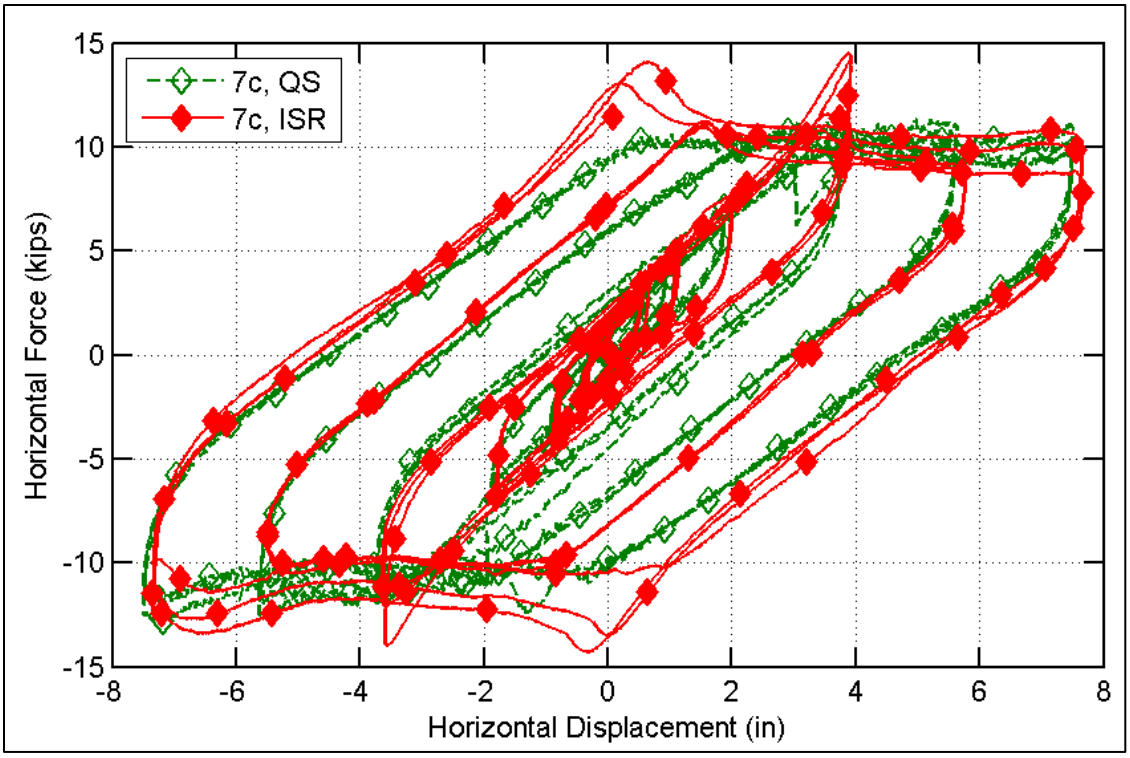

Figure 3.11. Cyclic Type I force versus displacement, longitudinal orientation, with increased strain rate.

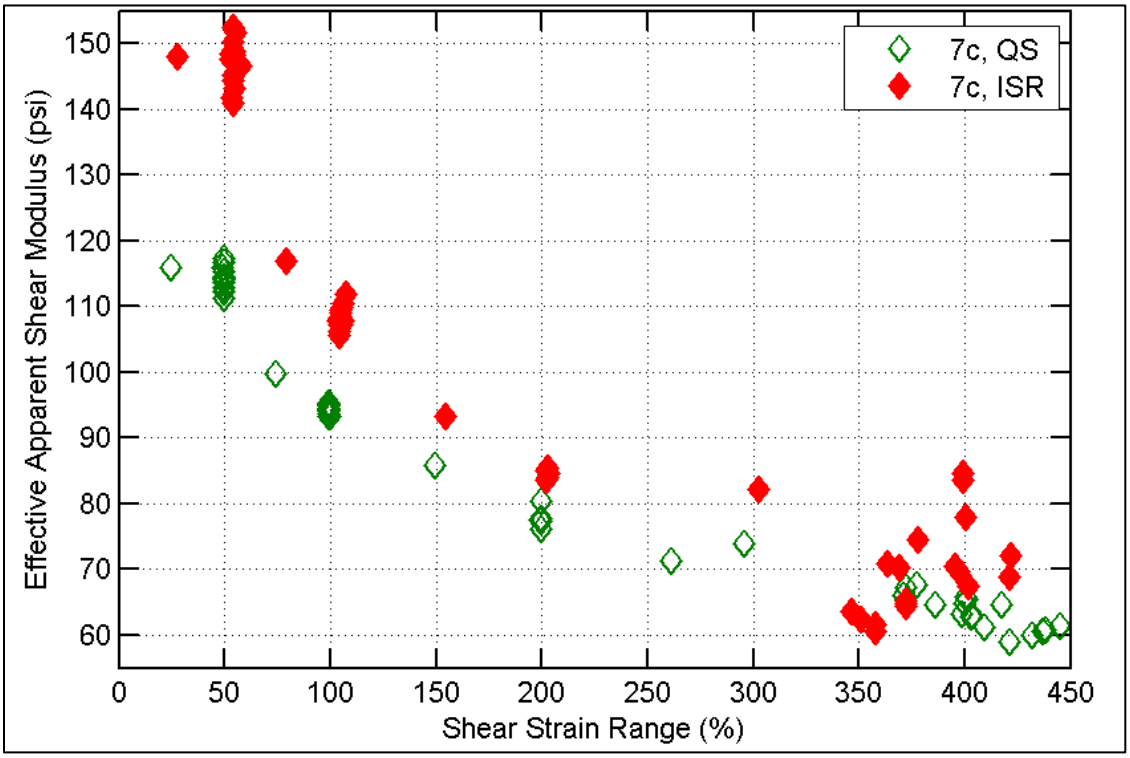

Figure 3.12. Variation of effective apparent shear modulus with shear strain range for Type I quasi-static vs. increased strain rate cyclic tests.

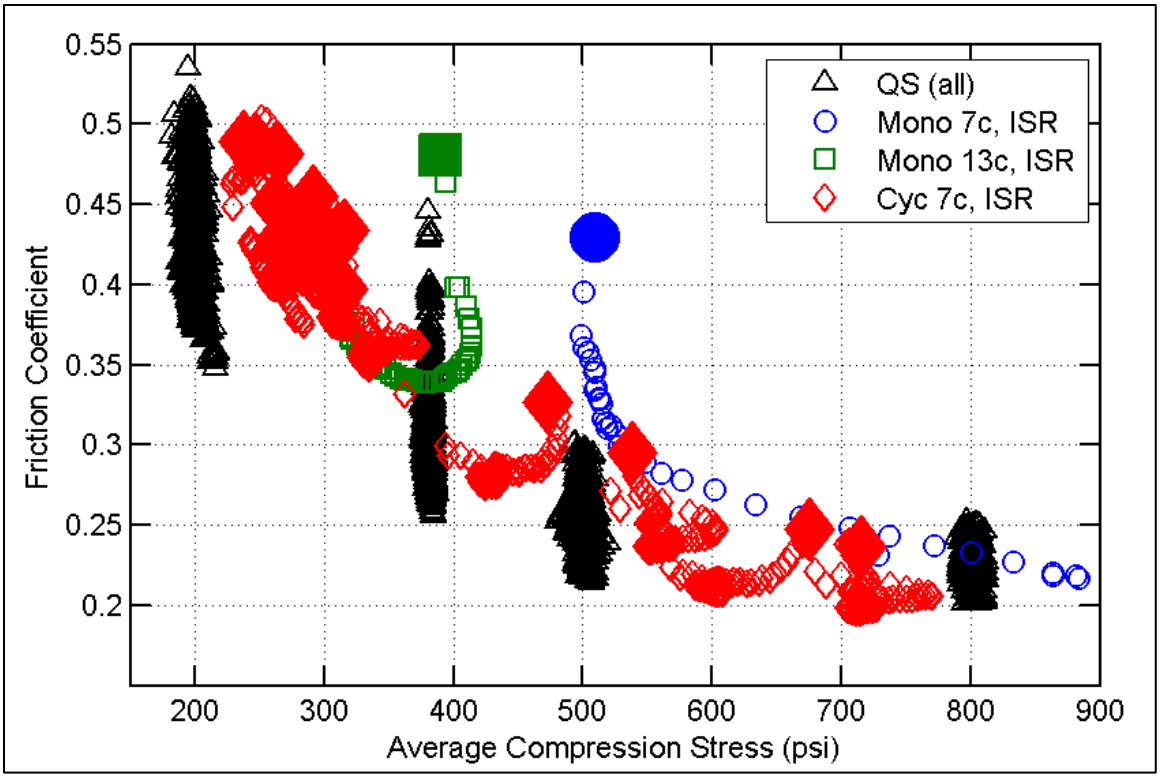

Figure 3.13. Variation of friction coefficient with average compression stress for Type I longitudinal tests.

Table 3.1. Comparison of Quasi-Static vs. Increased Strain Rate: Effective Apparent Linear Shear Modulus (psi) for Monotonic Tests

	QS	ISR	% diff
7c	71.8	87.2	21.4%
13c	79.0	100.4	27.1%

Table 3.2. Comparison of Quasi-Static vs. Increased Strain Rate: Peak Friction (Breakaway) Coefficient for Monotonic Tests

	QS	ISR	% diff
7c	0.31	0.43	38.0%
13c	0.36	0.48	33.9%

Observed friction resistance varied significantly during the ISR tests because the testing apparatus was following a pre-defined sequence of position commands for the individual actuators rather than iteratively measuring bearing position and load and adjusting to within convergence tolerances, as had been done for QS tests. As a result, the data clearly show the influence of compression stress on friction resistance. Data from the ISR tests are presented together with QS data in Figure 3.13. All QS test data are shown using the same marker type and color. The QS data presented in Figure 3.13 are the same as those presented in Figure 3.7, with the range of friction coefficients observed for individual

compression levels caused by repeated cyclic slip travel. For the ISR tests, the breakaway coefficients of friction are indicated with enlarged and in-filled markers.

The sliding friction observed during ISR tests appears to agree reasonably well with the sliding friction observed during QS tests. The QS tests tended to gradually transition to a sliding response, with the elastomer crawling slowly along the concrete to relieve the internal stresses in the elastomer. The crawling was more rapid and pronounced for higher elastomer shear strains so that pauses in tests would correlate to rapid relief of shear strain through sliding for a few seconds, with much slower crawling of elastomer on concrete for the remainder of the pause. On the basis of these observations, it is recommended that the friction coefficients observed during QS tests be regarded as more representative of sliding friction coefficients, while breakaway coefficients should be anticipated to be higher than the values observed during QS tests.

3.4 SINGLE RETAINER TEST RESULTS

A pair of Type I single retainer tests was performed for both 7c and 13c retainers. For each retainer size, a first test was performed to characterize the monotonic pushover response, and a second test was performed on a new retainer to characterize the loading/unloading/reloading response. Results of these tests are presented in terms of force and displacement in Figure 3.14. The force-displacement response is also provided in Figure 3.15, with the horizontal axis adjusted to account for the total height of rubber of the associated bearing.

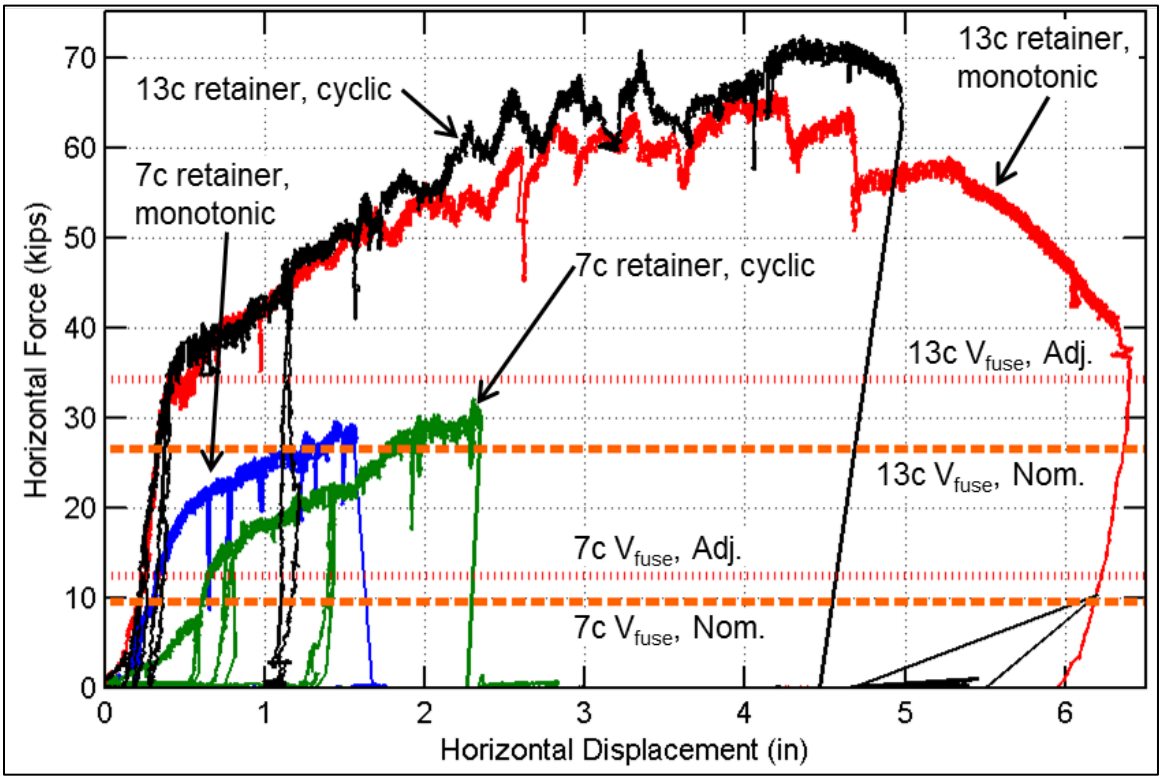

Figure 3.14. Horizontal force versus displacement for single retainer tests.

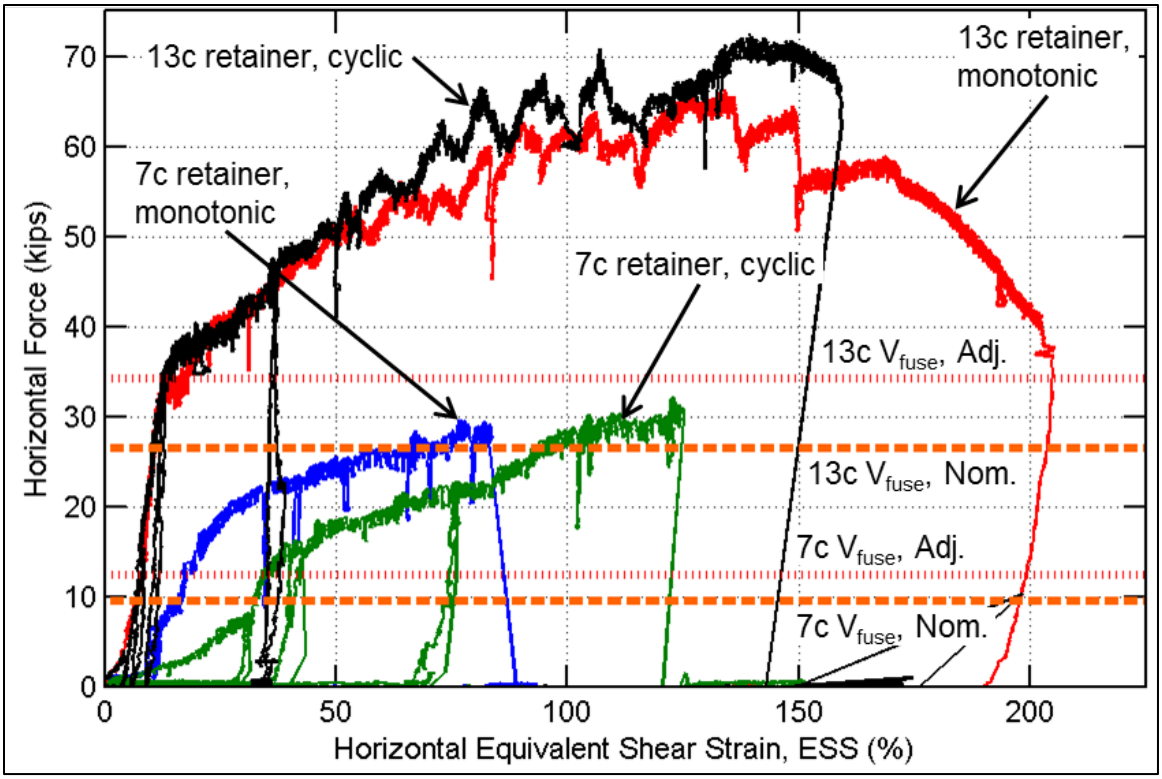

Figure 3.15. Horizontal force versus equivalent shear strain of associated bearing size for single retainer tests.

Both Figure 3.14 and Figure 3.15 include horizontal lines to indicate the predicted capacity of the retainers (V_{fuse}, Nom.) according to current design practice in the IDOT Bridge Manual (2012a) and adjusted to account for the strength of the supplied material (V_{fuse}, Adj.). The anchors were specified as F1554 Gr 36, but tension tests performed on the material revealed that the strength was actually close to Gr 55. (The mean of the observed ultimate tension strength values obtained from the tension tests is shown in the shaded cells in the Adjusted column of Table 3.3.) Regardless, even with an adjustment for material strength, the current equation used for retainer design is seen to significantly underestimate the actual fuse capacity of the retainers.

The predicted and observed fuse capacities are summarized in Table 3.3. In the table, the peak horizontal force carried by the retainer is identified as V_{fuse}, with calculated values in the Nominal and Adjusted columns, and experimentally obtained values in the Observed column. The Overstrength Ratio in the Observed column is the ratio of the observed to the nominal V_{fuse}. The last field in the Observed column is a normalized V_{fuse} capacity, presented as the ratio of the observed horizontal force capacity to the theoretical maximum tension capacity of the anchor, calculated as N_{sa} according to Appendix D of the American Concrete Institute's *Building Code Requirements for Structural Concrete* (ACI 2011) so that

$$N_{sa} = nA_{se,N} f_{uta} \qquad \text{(Eq. 3-2)}$$

where

n = Number of anchors, equal to 1 for all retainers

$A_{se,N}$ = Effective cross-sectional area of a single anchor (in^2), taken equal to 0.8 times the nominal cross-sectional area of the anchor to account for threads

f_{uta} = Ultimate tensile stress of an anchor (ksi), taken equal to the F_u value in the Adjusted column

Table 3.3. Summary Data for Single Retainer Tests

Test ID	Description	Nominal			Adjusted		Observed		
		Fu (ksi)	Dia. (in)	V_{fuse} (kips)	Fu (ksi)	V_{fuse} (kips)	V_{fuse} (kips)	Overstrength Ratio	$\frac{V_{fuse}}{N_{sa}}$
6	T1 7c Single Ret	60	0.75	9.5	73.26	11.7	29.6	3.10	1.14
7		60	0.75	9.5	73.26	11.7	32.1	3.36	1.24
11	T1 13c Single Ret	60	1.25	26.5	69.37	30.6	66.3	2.50	0.97
12		60	1.25	26.5	69.37	30.6	72.5	2.73	1.06

The single retainer tests were performed without a bearing installed to support a simulated gravity load, and the control program did not impose vertical load constraints during the test. Consequently, a vertical load was induced as the retainer was pushed over. The magnitude of the vertical reaction was found to be significant, especially in the case of the 13c retainers. A plot of the data recorded for the induced vertical load is provided in Appendix A. It should be noted that the induced vertical reactions suggest the bearing may lift off of the concrete surface as the retainer is pushed over.

3.5 QUASI-STATIC CYCLIC TRANSVERSE TEST RESULTS

Tests were performed on a range of Type I bearing sizes to characterize their transverse response, including the influence of the bearing on the pushover response of the retainer, as well as the post-fusing influence of the remnants of concrete anchors at retainers. The sizes evaluated in the experiments were 7c, 9c, 11b, and 13c. Additionally, two modified retainer designs were also evaluated, using the 13c bearing specimen that had previously been subjected to longitudinal bridge motion testing.

3.5.1 Comparison of Transverse vs. Longitudinal Orientation Response

Transverse and longitudinal responses of similar Type I bearings are compared in Figure 3.16 and Figure 3.17. In both cases, the shear stiffness is higher in the transverse orientation when compared with the results obtained from the longitudinal test orientation. The variation in effective apparent shear modulus is shown in Figure 3.18, corresponding to the test results presented in Figure 3.16 and Figure 3.17. In Figure 3.18, marker shapes correspond to test orientation, with circular markers for longitudinal tests and triangular markers for transverse tests. Markers are hollow for the smaller 7c bearing, and in-filled for the larger 13c bearing. The triangular markers tend to fall above the circular markers, while maintaining a similar degradation in stiffness with increasing shear strain demand.

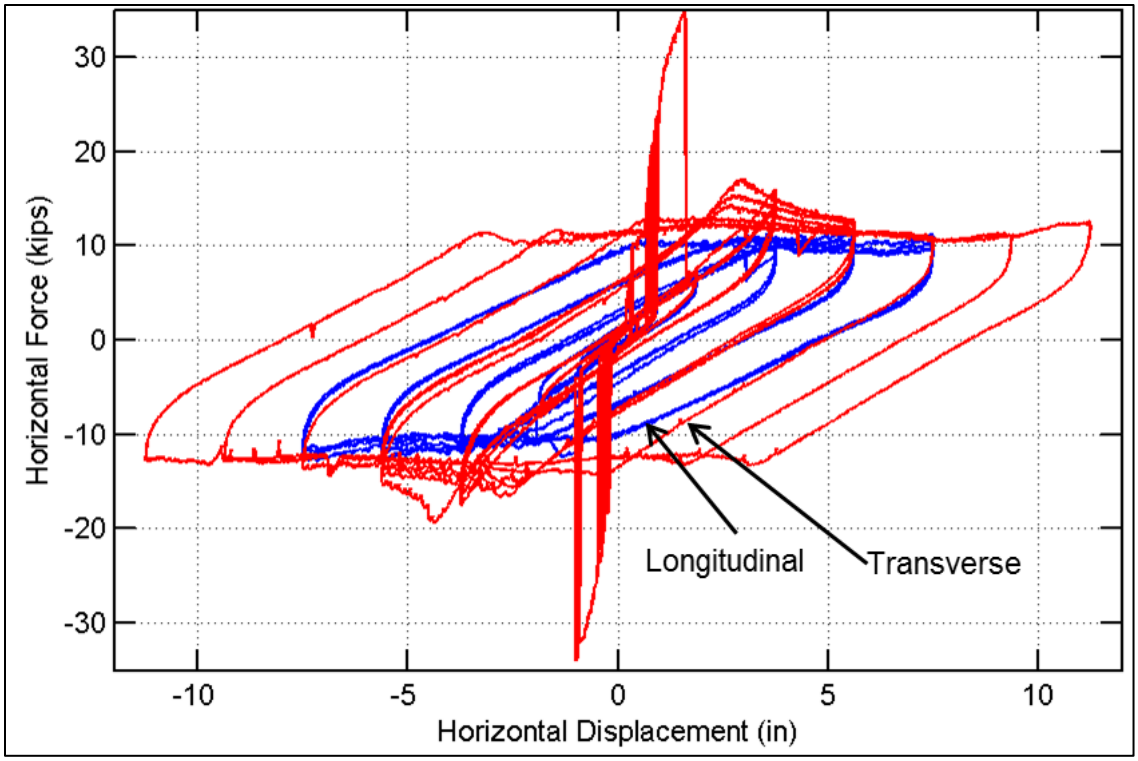

Figure 3.16. Force versus displacement of Type I 7c bearings in longitudinal and transverse orientations.

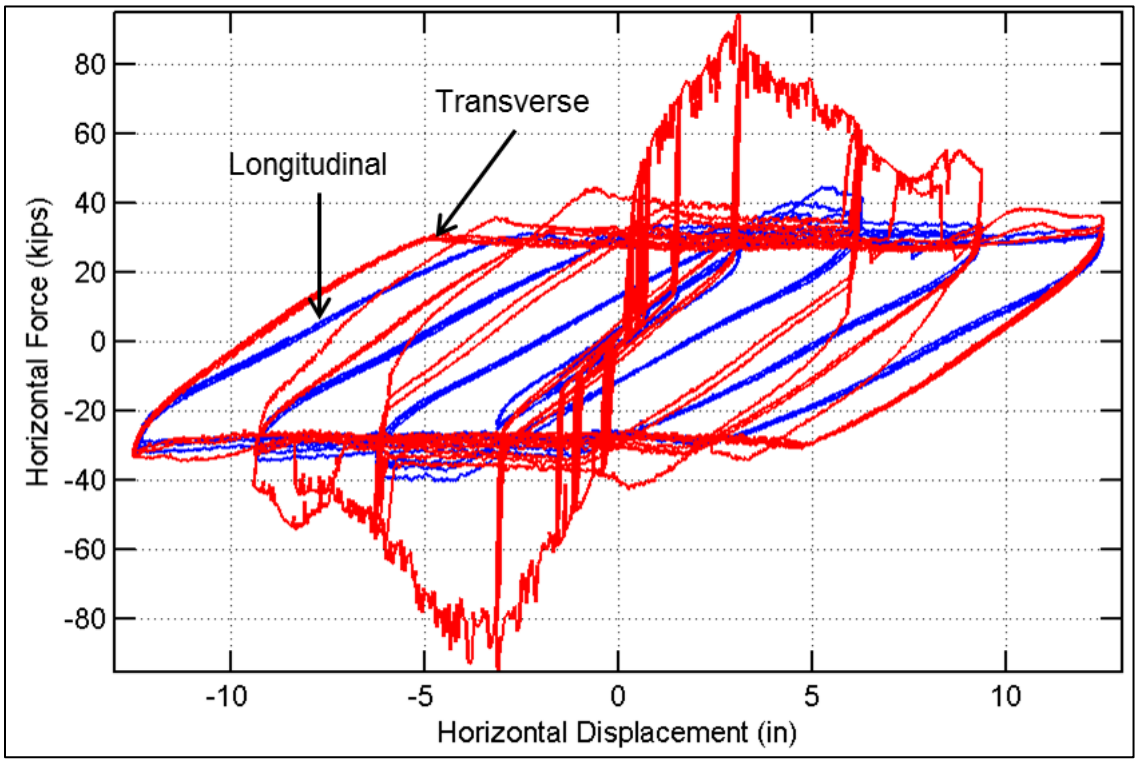

Figure 3.17. Force versus displacement of Type I 13c bearings in longitudinal and transverse orientations.

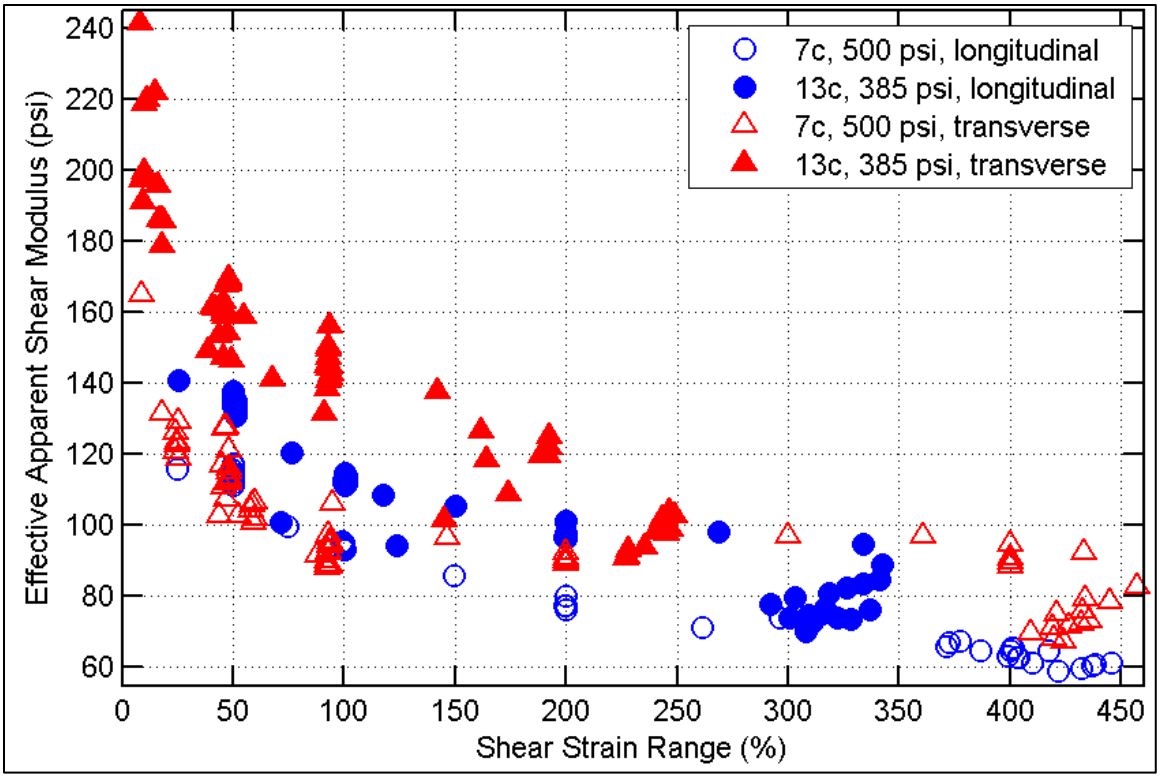

Figure 3.18. Effective apparent shear modulus for Type I bearings in longitudinal and transverse orientations.

The discrepancy between observed shear stiffness responses for alternate orientations is likely a result of the relative significance of trailing edge curling and leading edge abrasion chamfering between the two cases. Curling is restrained by rotational stiffness of the combined elastomer and shims, and the increased depth in the transverse orientation is expected to reduce curling by affording greater flexural stiffness. Furthermore, while penetration from the outer edge of the area influenced by leading edge abrasion should be similar in the two cases, the proportionate influence on the bearing is greater for the bearing in the longitudinal direction than for the transverse direction. Another commonality in the two figures is the relatively minor influence of anchors following fusing. The increases in resistance when the bearings are traveling over the remnants of the failed anchors are slight in both cases.

3.5.2 General Force-Displacement Response

The most striking difference in the responses of the bearing cases in the previous section was foreshadowed in the single retainer tests. Those tests had previously shown the different apparent ductility of the different retainer sizes, primarily afforded by excessive stress and crushing of concrete at the toe of the Type I 13c retainers, and a subsequent transformation of the mechanical demands induced in the steel anchors. For 7c retainers, the anchors developed a combined tension and shear stress state at the concrete surface after the initial deformations required to plant the toe securely into the concrete. The 13c retainers, on the other hand, drove the toe more deeply into the concrete, and the steel anchor deformation was primarily influenced by a combination of flexure/tension rather than the shear/tension observed for the 7c retainers. The response was further complicated with the elastomeric bearing installed because the elastomer came in contact with the heel of the

overturning retainer. Consequently, in the early cycles, the retainer was loaded by the top steel plate of the bearing driving against the initially vertical face of the retainer, but in later cycles for the 13c bearing, the top steel shim of the reinforced elastomer became the primary means of delivering horizontal load to the retainer. The evolution of these response characteristics is described in more detail in Appendix A for individual bearing/retainer sizes.

3.5.2.1 Bearings Without Lift-Off

The 7c and 11b bearings did not experience significant lift-off from the concrete when driving against retainers. Both bearings were tested with an applied vertical load corresponding to 500 psi on the elastomer footprint. The observed fuse capacity ranged from 0.80 to 0.89 times the applied vertical load, and the failure mechanism was a combined tension/shear failure of the anchor at elastomer shear strains ranging from 53% to 85%. The overall response was dominated by an abrupt rupture of the anchor with an immediate transition to a stable hysteretic sliding response (similar to that observed in the longitudinal orientation). Test results for both bearings are shown in Figure 3.19.

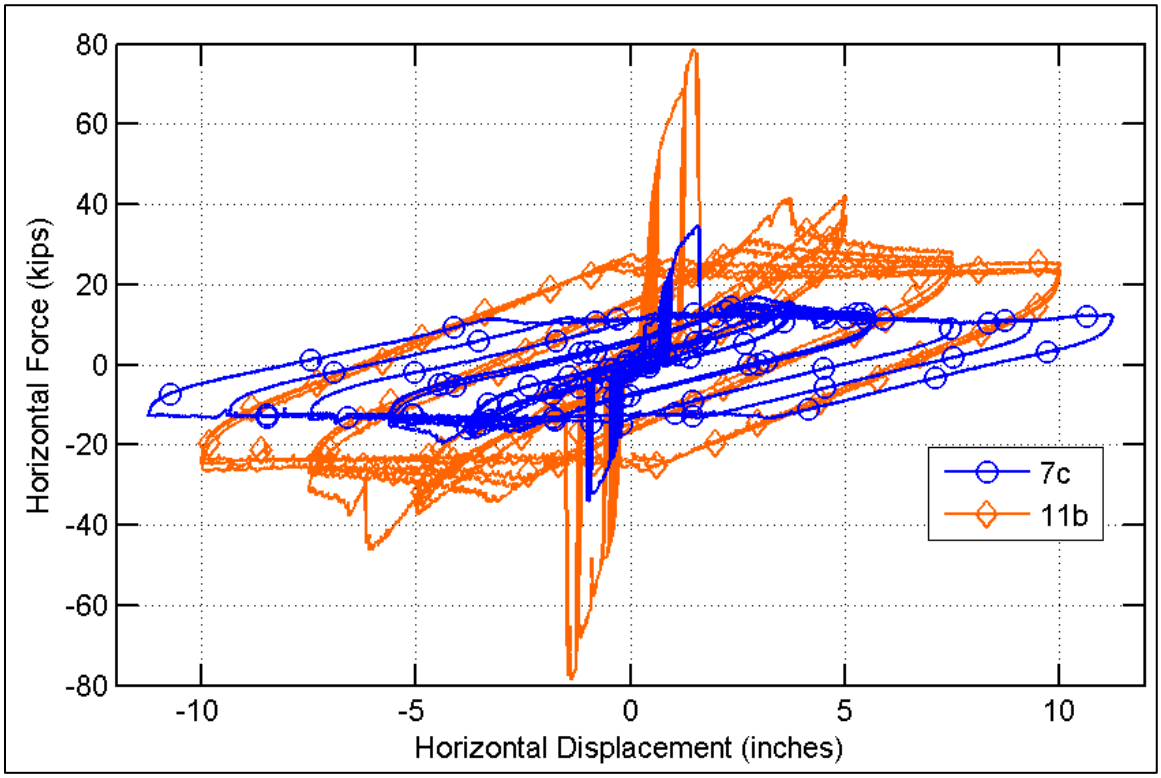

Figure 3.19. Force versus displacement of Type I bearings without lift-off in transverse orientation.

3.5.2.2 Bearings with Lift-Off

The 9c and 13c bearings experienced lift-off when driving against retainers such that the elastomer was raised up off of the concrete surface. Applied vertical load corresponded to 500 and 385 psi on the elastomer footprint for the 9c and 13c bearings, respectively. The observed peak force capacity ranged from 0.94 to 0.98 times the applied vertical load. The transition to sliding response was more complex for these bearings than for bearings without lift-off. The 9c bearing exhibited abrupt fusing of retainer anchors at about −66% and +86% elastomer shear strains, but the retainers continued to influence the response even after the

anchors had ruptured because the toe had been driven deeply into the concrete prior to anchor failure. Consequently, the first excursions to ±200% ESS included secondary effects with the bearing lifting off of the concrete and the retainer digging a shallow trough in the top surface of the concrete. The 13c bearing did not exhibit an abrupt anchor failure until the second cycle to peak displacements of ±300% ESS. The anchor was deformed significantly in flexure in addition to tension and shear, and the interaction between the bearing elastomer and the retainer heel was more pronounced than for the 9c bearing. Test results for both bearings are shown in Figure 3.20.

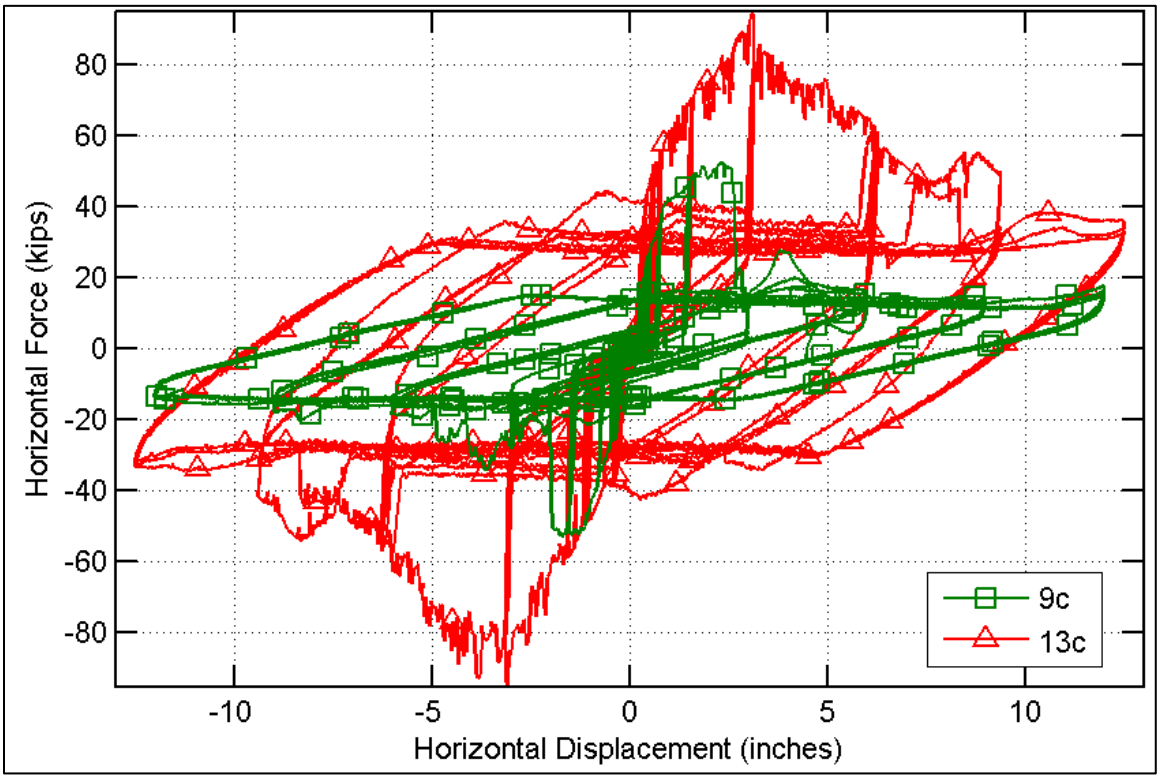

Figure 3.20. Force versus displacement of Type I bearings with lift-off in transverse orientation.

3.5.3 Modified Retainer Designs

The complications involved in the response, and the reliability of the anticipated performance, of a bearing such as the 13c, as tested, led to consideration of alternate retainer designs aiming to achieve a cleaner fusing response, closer to what had been observed with the 7c bearings. The primary characteristic desired to be modified was the crushing of the concrete observed at the toe for the 13c. All retainers were 8 in. long in the longitudinal bridge direction. The 7c retainers had total base width of 4 in. in the transverse bridge direction, a distance from the center of the anchor hole to the toe of 1-7/8 in., and a total elastomer height (total thickness of rubber and shims) of 2-1/4 in. The 13c retainers, on the other hand, had a base width slightly wider, at 4-3/4 in., and a distance from the center of the anchor hole to the toe of 2-3/8 in., but the total elastomer height was 3-7/8 in. On the basis of an evaluation of the previous test data, an estimate of approximately 8 in. total base width was calculated to be required to ensure that concrete crushing would be minimal. Consequently, alternate retainers were fabricated with the same height, length, and plate thicknesses as the original 13c retainers and with the same distance from the vertical face to

the center of the anchor hole but with extended base widths. One retainer was fabricated with an 8 in. base width, and the other was fabricated with a 6 in. base width.

Data for the tests with the alternate retainer designs are shown in Figure 3.21, where the 8 in. base width retainer was mounted on the (+) side and the 6 in. base width retainer was mounted on the (–) side. The results generally agree with the expected performance, although the 6 in. retainer appeared more ductile than anticipated by continuing to dig a trough in the concrete after anchor failure until the testing equipment reached its peak displacement range. The 8 in. retainer provided a fuse capacity of 0.90 times the vertical load, and the anchor ruptured at about 67% shear strain. The 6 in. retainer provided a fuse capacity of 1.11 times the vertical load, achieving the peak capacity at about 100% shear strain. The observed behavior resembled the original 13c response with the 6 in. retainer and the original 7c response with the 8 in. retainer, thereby validating the design expectations for the two options.

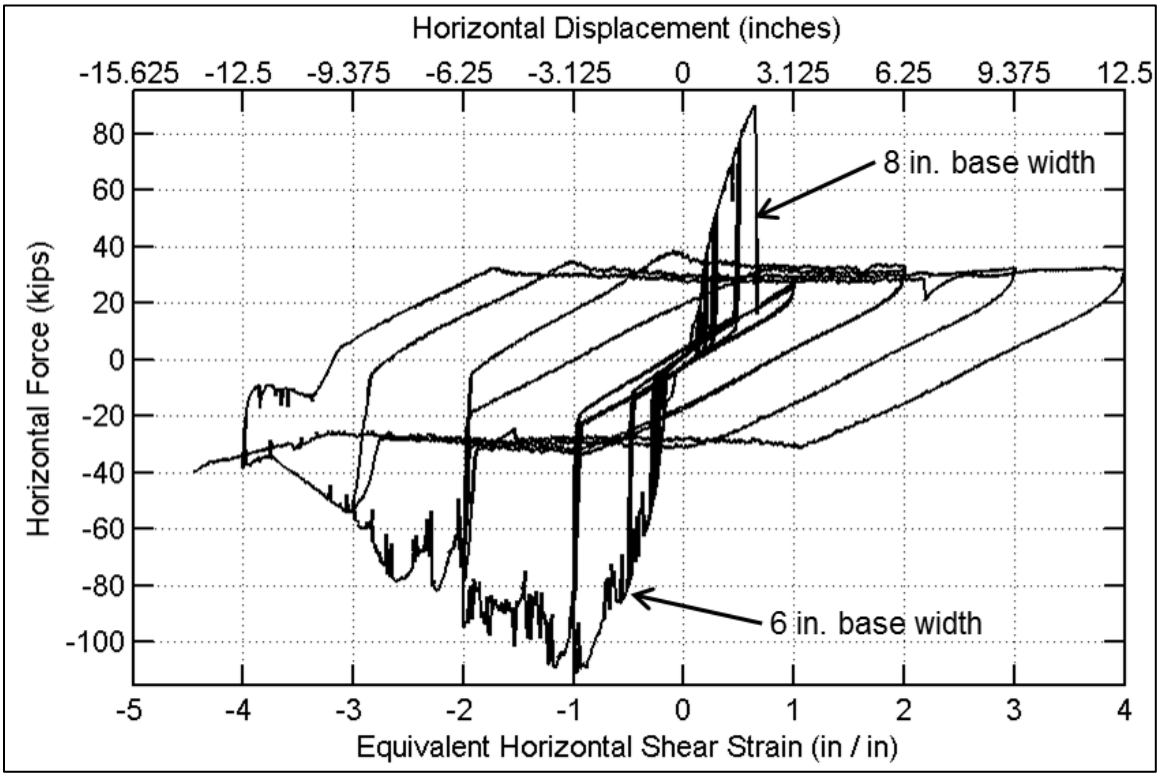

Figure 3.21. Force versus displacement of Type I 13c bearing with modified retainer designs for transverse orientation.

3.5.4 Summary of Response Characteristics

This section is provided to extract and summarize data from the full Type I bearing cyclic responses shown in the previous sections.

3.5.4.1 Fuse Force Capacity

Fuse force capacity is defined as the actual peak force observed during the experiments for each bearing assembly, including contributions of the elastomeric bearing and resistance developed at retainer toes during overturning. Summary fuse capacity data are presented in Table 3.4 for the quasi-static transverse tests. In the table, the nominal capacities correspond to current estimates published in the IDOT Bridge Manual, assuming that Gr 36

material was used for the anchors (as was requested from the bearing supplier). For the first set of bearings, tension tests indicated that the material was likely rejected Gr 55 and consequently had higher capacity than anticipated. The adjusted fuse capacities account for material strength obtained from uniaxial tension testing of representative material samples (shown in the shaded cells of the table). The observed fuse capacities, V_{fuse}, report the maximum force level observed during the test, which implicitly includes the contribution of the elastomer to the total shear resistance and therefore reflects the load per bearing that should be anticipated for design of substructures to ensure capacity protection during a major seismic event. As for the single retainer tests, the observed fuse capacity is also supplied as a normalized value relative to the nominal tension capacity of the anchor, N_{sa}. The observed fuse capacity was generally about 1.1 to 1.4 times the ultimate tension capacity of the anchor. Although the failure mechanism was a result of shear and flexural demands in addition to tension, the contributions of elastomer shear in the bearing and, more significantly, the shear resistance as the retainer toe is driven against and into the concrete surface, produce a total resistance in excess of the maximum that could have been estimated using the anchor strength alone.

Table 3.4. Summary Data for Type I Transverse Fuse Capacities

Test	Description	Nominal			Adjusted		Observed		
		Fu (ksi)	Dia. (in)	V_{fuse} (kips)	Fu (ksi)	V_{fuse} (kips)	V_{fuse} (kips)	Overstrength Ratio	$\frac{V_{fuse}}{N_{sa}}$
15	T1 7c Trans	60	0.75	9.5	73.26	11.7	34.8	3.65	1.34
		60	0.75	9.5	73.26	11.7	33.9	3.56	1.31
Ext 1	T1 9c Trans	60	1	17.0	74.38	21.0	52.3	3.08	1.12
		60	1	17.0	74.38	21.0	52.7	3.11	1.13
Ext 2	T1 11b Trans	60	1.25	26.5	70.35	31.1	78.5	2.96	1.14
		60	1.25	26.5	70.35	31.1	78.5	2.96	1.14
14	T1 13c Trans	60	1.25	26.5	69.37	30.6	94.1	3.55	1.38
		60	1.25	26.5	69.37	30.6	94.2	3.56	1.38
Ext 6	T1 13c Trans	60	1.25	26.5	69.37	30.6	114.6	4.32	1.68
Ext 7	Alternate Designs	60	1.25	26.5	69.37	30.6	91.3	3.44	1.34

3.5.4.2 Friction Resistance

Calculations of friction resistance extracted from the sliding segments of each transverse test are shown in Figure 3.22. As for the longitudinal tests, each data point represents an average of the slip resistance observed over a 5% ESS slip displacement increment. The previous trend of degrading resistance with accumulated travel is repeated in the test data for the transverse orientation tests. The tests were performed only with loads of 385 and 500 psi average compression stresses, so there is not a clear discrepancy observed between tests with significantly varying simulated gravity loads, as there was for the longitudinal tests. The longitudinal results indicated that friction coefficients may be about 0.25 for a gravity load corresponding to 500 psi average compression on the elastomer, but a similar condition in terms of bearing size and load in the transverse orientation indicated that 0.3 to 0.35 may be more appropriate. There are natural variations in both the surface condition of the elastomer and, especially, the surface roughness of the concrete, and so such a variation is not unexpected. In general, the results suggest that estimates for earthquake scenarios with large sliding displacement travel demands could assume about 0.25 for a friction coefficient, but the maximum

sliding force that could be transmitted by sliding friction could be estimated with a friction coefficient of about 0.4 to 0.45.

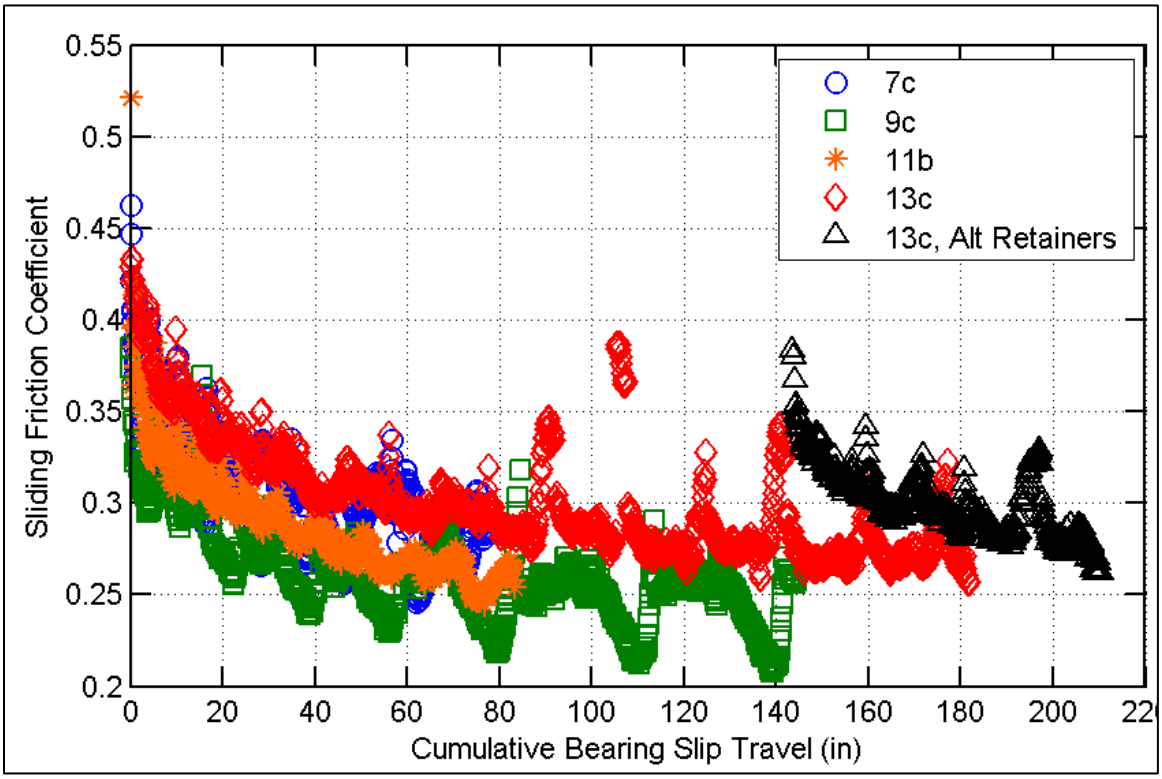

Figure 3.22. Variation of sliding friction coefficient with cumulative bearing slip for Type I transverse tests.

3.5.4.3 Equivalent Damping

Similar to the damping data presented for the longitudinal tests in Figure 3.8, effective damping values for transverse tests are shown in Figure 3.23, where the damping was again estimated according to the Guide Specification for Seismic Isolation Design (AASHTO 2010). As with the longitudinal orientation, the damping values are seen to increase significantly at large displacements, when sliding has initiated. Contrary to the longitudinal tests, there are many additional data points clustered in the small displacement range for the transverse tests because of the nine initial force-based cycles (three each at 25%, 50%, and 70% estimates of retainer force capacity). These low-displacement damping values are noticeably lower than similar values for longitudinal motion, typically falling at or below 5% in the transverse direction, compared with 10% to 20% in the longitudinal direction. The trend of these early transverse cycles is shown in Figure 3.24. The transverse damping values for small displacements reflect the increased force capacity and effective stiffness, coupled with a pinched hysteresis, prior to fusing of the retainers.

The pinching effects are also seen in Figure 3.24 with the pattern of decreased damping at cycles following the first excursions to new displacement demands. Specifically, cycles 1, 4, and 7 for the initial 25%, 50%, and 70% force-based cycles, and cycles 10 and 17 for the initial 25% and 50% ESS displacement-based cycles, exhibit higher damping than the succeeding cycles at equal displacement demands. By cycle 24, the first 100% cycle, retainers have typically failed and the bearing response is transitioning to a sliding response similar to that observed with longitudinal orientation tests. Although retainer failure occurs

during the second 300% cycle (cycle 31) for Test 14 with a 13c bearing, the retainer has been pushed so far that there is significant sliding required for the bearing to travel between the retainers. The combination of degraded retainer force capacity and large cyclic peak displacement results in relatively low effective stiffness compared with the cyclic hysteretic energy dissipation, and the overall response at 200% and 300% displacement levels is therefore less dominated by pinching effects.

The transverse simulated earthquake test offered additional insights into anticipated energy dissipation. As with the longitudinal case, the data indicated that a portion of the dissipated energy should be attributed to the hysteretic response of the elastomer material. Focusing on the portion of the test after the second retainer had failed, so that the response could be entirely characterized by elastomer shear and sliding on the concrete surface, the total energy dissipated was more than 300% above that predicted from sliding in the corresponding OpenSees model (at only the bearing under consideration). For this portion of the test, the hysteretic elastomer material contribution accounted for about 50% of the total energy dissipated in the experiment. Additionally, the bearing experienced multiple small slippages, so the total sliding energy in the experiment was about twice the anticipated sliding energy dissipation from the corresponding OpenSees analysis. When the full test is evaluated, the corresponding OpenSees model indicates that about 55% of the total energy for the full earthquake record is expended prior to fusing of the retainers, but the large post-fusing energy dissipation in the experiment reduced the pre-fusing portion to about 25% of the total energy.

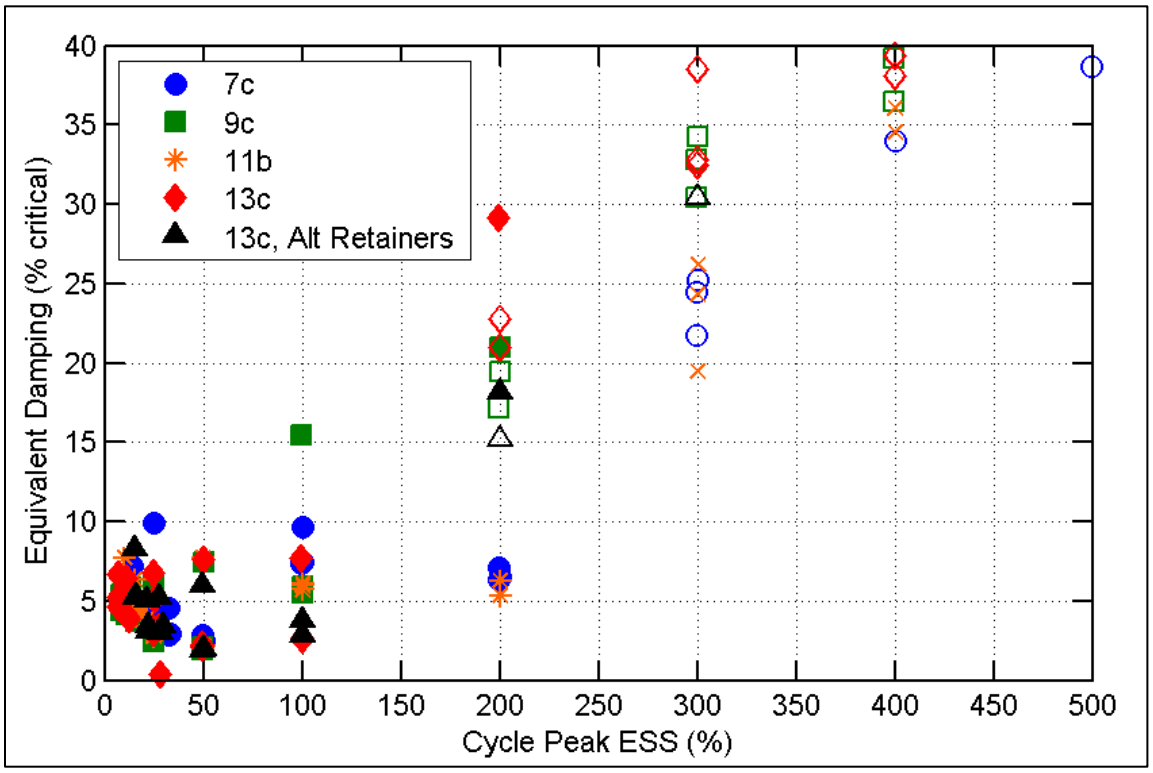

Figure 3.23. Variation of effective damping with peak shear strain for Type I transverse orientation tests.

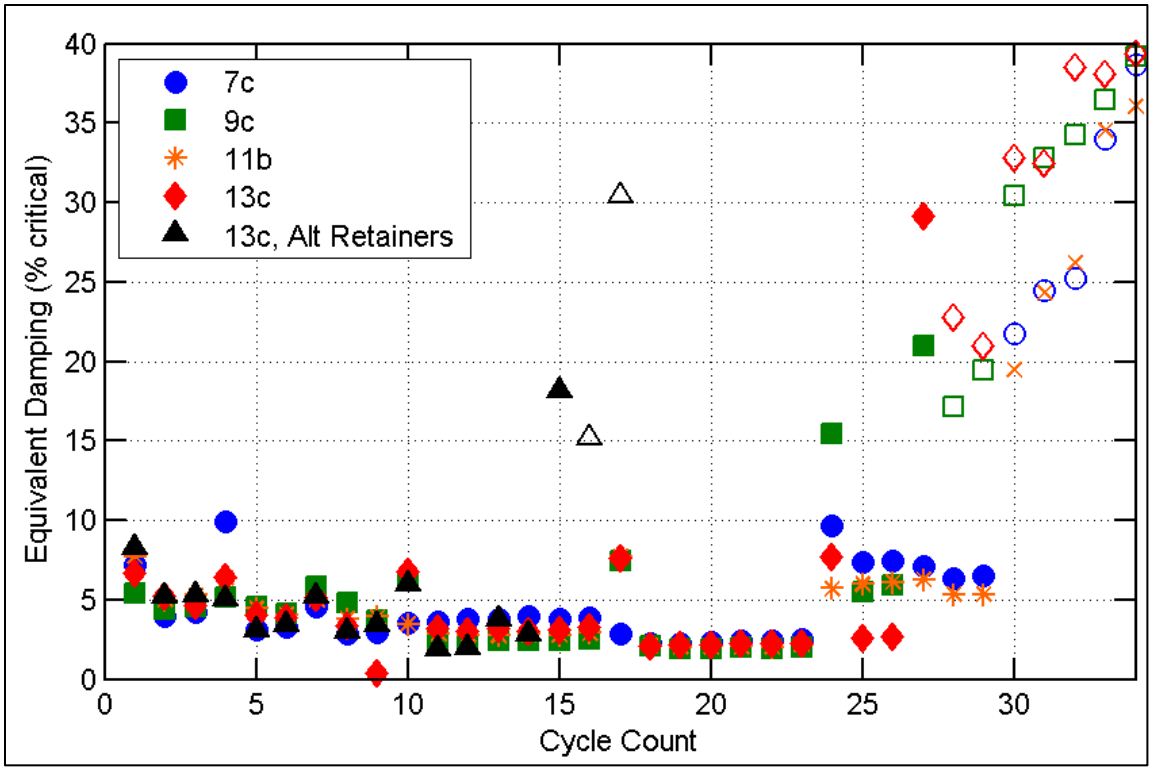

Figure 3.24. Variation of effective damping with cycles for Type I transverse orientation tests.

CHAPTER 4 TYPE II BEARING EXPERIMENTAL RESULTS

4.1 TRANSVERSE RESPONSE WITH RETAINERS

Tests were performed with retainers installed for each Type II bearing size listed in Chapter 2. A plot of the transverse force-displacement response for all Type II bearings with retainers is shown in Figure 4.1. Corresponding fuse capacities are summarized in Table 4.1. As in the Type I bearing results sections, fuse force capacity is defined here as the actual peak force observed during the experiments for each bearing assembly, including contributions from the elastomeric bearing and resistance developed from friction between retainer toes and “masonry” (bottom) steel plates. The fuse capacities are presented with nominal, adjusted (in shaded cells to indicate observed values from ancillary tension tests), and observed quantities. The observed capacities were lower than those observed for Type I’s but were higher than initial estimates from IDOT design equations. The difference in capacity between Type I and Type II bearings is primarily due to the condition at the retainer toes. Toes of Type I bearings are driven down and into the concrete of the substructure through overturning. Type II retainers stand on top of masonry plates instead of being placed directly on concrete. When horizontal load is applied, the retainer toe slips off the edge of the steel plate, and resistance is provided primarily through shear strength at the threaded anchor, with a minor contribution from friction between the retainer and the masonry plate. Summary data for the friction response observed during the transverse Type II tests with retainers are presented in Table 4.2. The values are consistent with expected properties for sliding of PTFE on stainless steel. The maximum permissible friction coefficient, according to IDOT Standard Specifications (2012b), is 0.07, and the mean friction values conform to this limit, although the initial friction break-off coefficient is slightly higher than the specified limit.

Table 4.1. Summary Data for Type II Transverse Fuse Capacities

Test	Description	Nominal			Adjusted		Observed		
		Fu (ksi)	Dia. (in)	V_{fuse} (kips)	Fu (ksi)	V_{fuse} (kips)	V_{fuse} (kips)	Overstrength Ratio	$\frac{V_{fuse}}{N_{sa}}$
13	T2 7c Trans	60	0.75	9.5	73.26	11.7	18.2	1.91	0.70
		60	0.75	9.5	73.26	11.7	22.5	2.35	0.87
Ext 3x1	T2 9a Trans	60	1	17.0	74.38	21.0	40.0	2.36	0.86
		60	1	17.0	74.38	21.0	37.6	2.21	0.80
Ext 4x1	T2 11a Trans	60	1.25	26.5	70.35	31.1	53.9	2.04	0.78
		60	1.25	26.5	70.35	31.1	58.0	2.19	0.84
Ext 5x1	T2 13a Trans	60	1.25	26.5	70.35	31.1	59.7	2.25	0.86
		60	1.25	26.5	70.35	31.1	56.8	2.14	0.82

Table 4.2. Summary Data for Friction Response of Type II Tests with Retainers

	7c	9a	11a	13a	Avg
Max Friction	0.102	0.099	0.088	0.109	0.100
Mean Friction	0.057	0.072	0.069	0.072	0.067

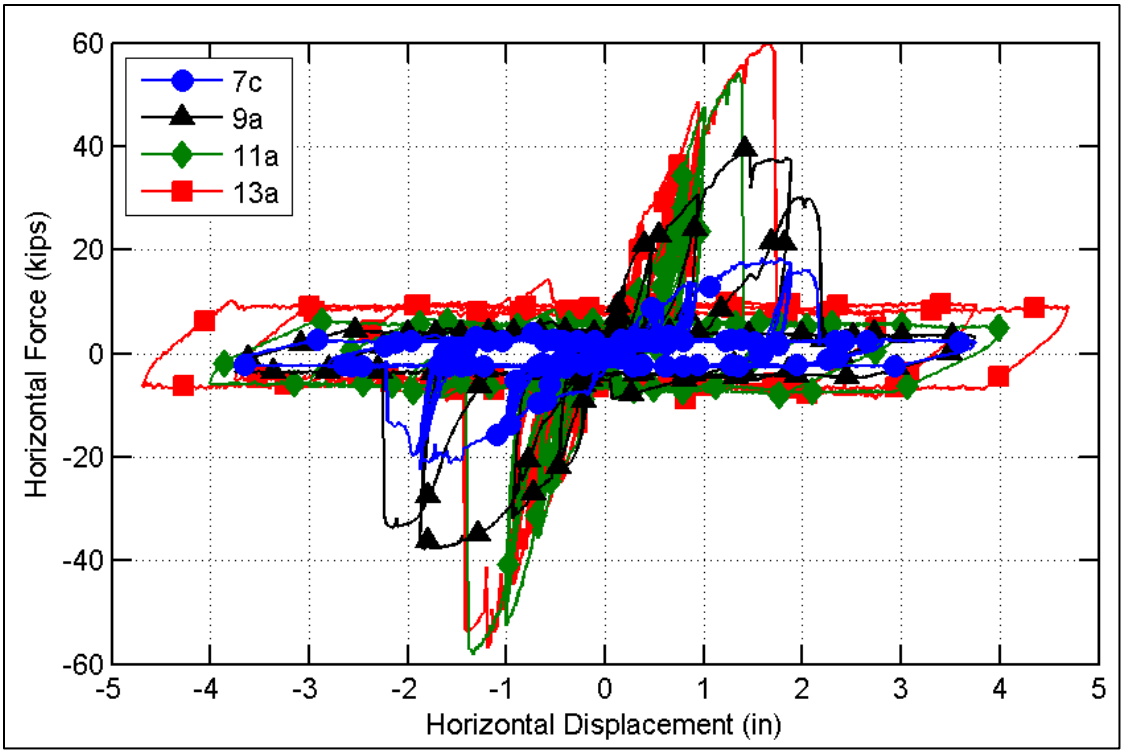

Figure 4.1. Force versus displacement response for transverse Type II bearings with retainers.

4.2 PTFE INCREASED STRAIN RATE RESPONSE

It has been well established that the sliding response of PTFE is significantly influenced by slip rate. Mokha et al. (1990) demonstrated that the friction resistance of PTFE-on-stainless steel sliding surfaces increased with velocity until reaching a plateau in the range of 4 to 8 in./sec. The experiments performed for this testing program were conducted at the highest velocities available, as limited by the hydraulic capabilities of the test setup. The vertical actuator positions were the only control mechanism for the simulated gravity load during ISR tests, with signals defined using the command input recorded from a previous QS test. The time-varying bearing deformed configuration was therefore slightly different between QS and ISR tests as a result of rate dependency of stiffness and slip characteristics. Furthermore, synchronization of the horizontal actuator with the vertical actuators was imperfect because of discrepancies in hydraulic characteristics (servovalves, hydraulic service manifolds, hoses) and control loop tuning parameters. The result of these discrepancies was a larger variation in simulated gravity load for ISR tests than had been enforced during QS pre-tests. In addition to variation in vertical force, the stress at the sliding interface varied continuously throughout each test to maintain equilibrium as the top and bottom plate slid relative to one another.

4.2.1 General Force-Displacement Response

4.2.1.1 Type II 7c, Longitudinal Orientation

ISR tests were performed on two Type II 7c bearings with a longitudinal orientation, indicated in Figure 4.2 showing normalized experimental results, as 7c [1] and 7c [2]. (A similar plot showing actual forces and displacements is available in Appendix B.) The

longitudinal orientation tests were limited to 200% ESS, based on observed response of the bearings extending to larger displacements during other QS tests. Slip rates for the QS pre-tests of each bearing were about 0.07 to 0.08 in./sec. For the first bearing (7c [1]), one ISR test was performed with a sequence of five cycle sets of sinusoidal top plate translation, at magnitudes of 25%, 50%, 200%, 150%, 100%, 50%, and 25% ESS. The ISR test for 7c [1] was performed with a target peak velocity of 2.5 in./sec at the top plate. The slip of the middle plate relative to the top plate increased the observed peak velocity slightly, to 2.78 in./sec. The two 7c [2] bearing ISR tests followed the standard Type II ISR protocol indicated in Chapter 2 (twelve cycles at the peak displacement, bounded by five cycles each of 25% and 50% at the beginning and end of the test). The first test was performed at a target of 2.5 in./sec, resulting in an observed maximum slip rate of 2.62 in./sec, and the second test was performed at a target of 3.0 in./sec, resulting in an observed maximum slip rate of 3.70 in./sec.

The target vertical load, which was imposed on the bearings prior to initiating the ISR horizontal top plate motion, was 42 kips. The imposed load varied between 36.4 and 48.2 kips for the 7c [1] ISR test, 33.1 and 51.9 kips for the 7c [2] ISR test with a target peak velocity of 2.5 in./sec, and 33.3 and 74.6 kips for the 7c [2] ISR test with a target peak velocity of 3.0 in./sec. The average normal stress was about 0.7 ksi on the PTFE surface at the start of each test. Varying load and contact conditions resulted in a range of average stresses. Calculations performed using the individual actuator loads indicate that the average stress values ranged from about 0.55 ksi up to more than 8 ksi for the 7c [1] bearing and up to an estimated 28 ksi for the 7c [2] bearing. The high stress values were observed as spikes when the direction of motion reversed at the peak displacement, causing the compression contact stress to redistribute so that the vertical reaction was shifted toward the interior of the PTFE and the edge of the top plate. The spikes dissipated quickly subsequent to the initiation of sliding at the PTFE surface.

4.2.1.2 Type II 7c, Transverse Orientation

Two ISR tests were performed on a single Type II 7c bearing with a transverse orientation. The force versus displacement response is shown in a non-dimensional form in Figure 4.3. (A similar plot showing actual forces and displacements is available in Appendix B.) The transverse orientation tests were extended to 400% ESS because the peculiar behaviors observed for the 7c in the longitudinal orientation were not present in the transverse orientation. The transverse direction did, however, exhibit its own variation of unusual behavior that had not been observed in the longitudinal orientation, in that the PTFE was more susceptible to delamination at large displacements. There was slight damage observed at the PTFE during the QS pre-test, and roughly half of the PTFE was torn away and pushed off of the middle plate during the first ISR test (target peak velocity of 2.5 in./sec). The remaining PTFE was removed during the first few peak displacement cycles of the second ISR test (target peak velocity of 3.0 in./sec) so that most of those cycles experienced steel-on-steel sliding rather than PTFE on steel.

Slip rates for the QS pre-test were again about 0.07 in./sec. The ISR tests followed the standard Type II ISR protocol indicated in Chapter 2. The first test was performed at a target of 2.5 in./sec, resulting in an observed maximum slip rate of 3.14 in./sec, and the second test was performed at a target of 3.0 in./sec, resulting in an observed maximum slip rate of 4.60 in./sec. The target vertical load was 42 kips, but the imposed load varied between 24.3 and 46.5 kips for the ISR test with a target peak velocity of 2.5 in./sec, and 13.8 and 78.6 kips for the ISR test with a target peak velocity of 3.0 in./sec. The progressive delamination and destruction of the PTFE sheet prevents reliable estimation of stresses throughout each

test. Estimates from the QS pre-test, when the PTFE was mainly intact, indicate that the average stress was approximately 7.6 ksi. If the stress state is assumed to be a triangular distribution, then the peak stress may have been in excess of 15 ksi, with a contact length of about 1 in. at the interface between the PTFE and stainless steel.

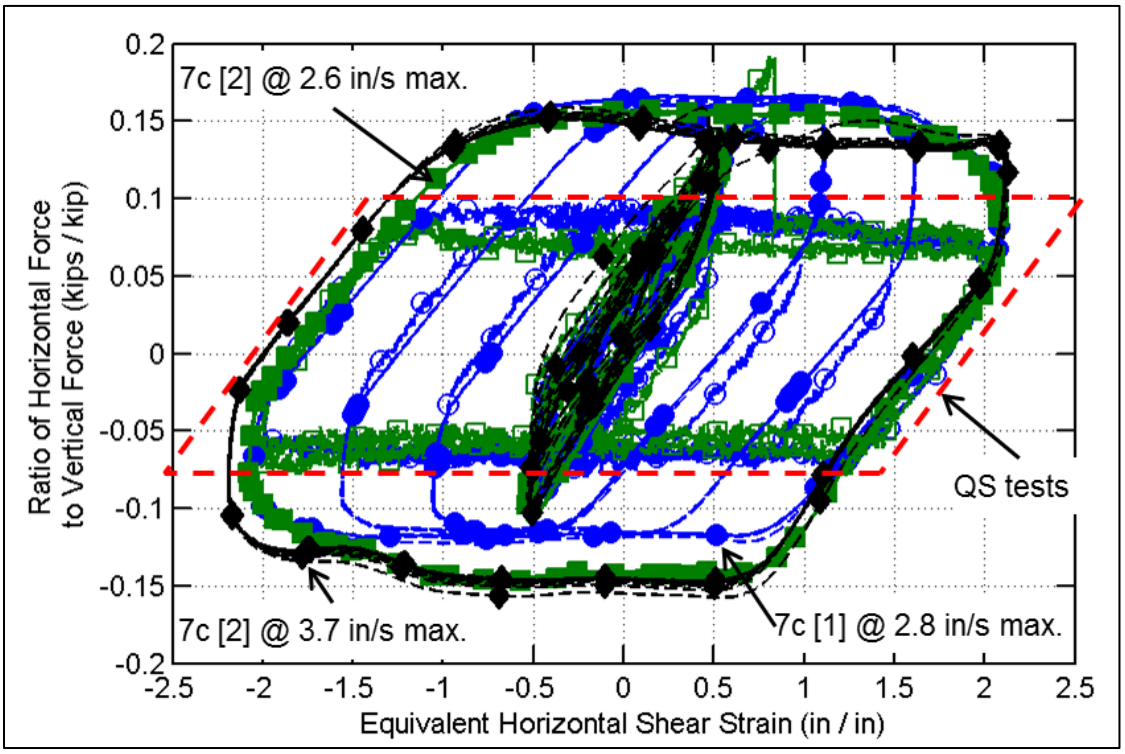

Figure 4.2. Non-dimensional Type II 7c constitutive response, longitudinal orientation.

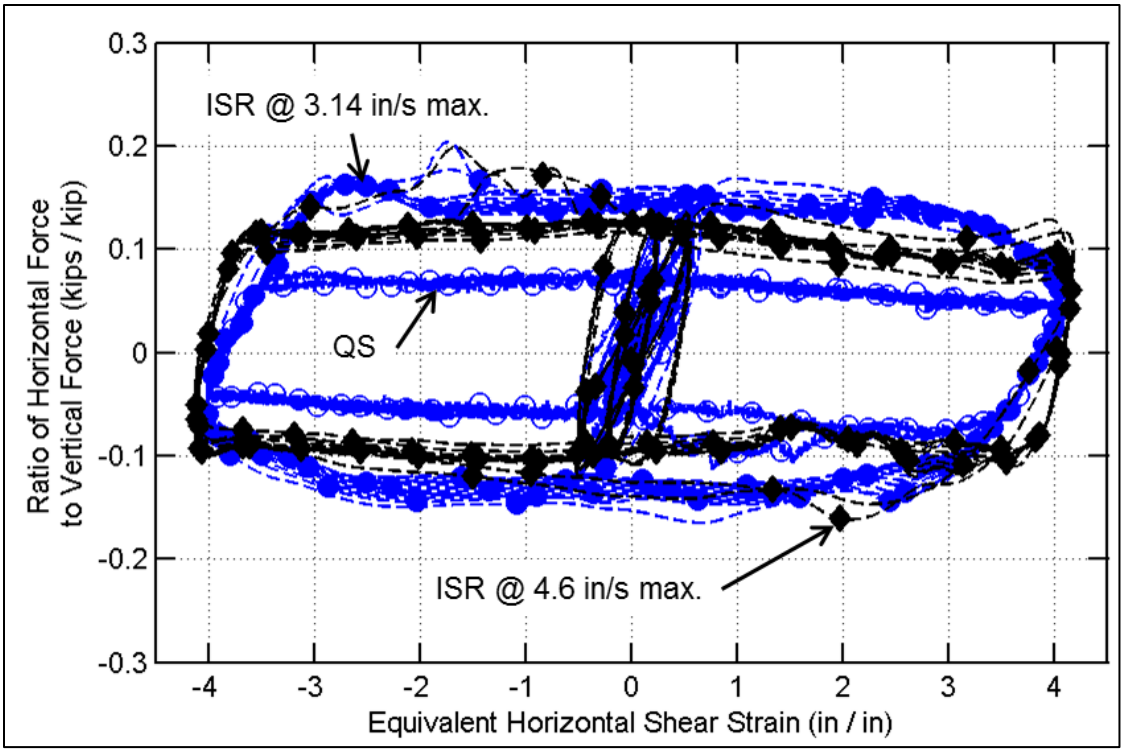

Figure 4.3. Non-dimensional Type II 7c constitutive response, transverse orientation.

4.2.1.3 Type II 9a/11a/13a, Transverse Orientation

One ISR test was performed on each of the Type II 9a, 11a, and 13a bearings with a transverse orientation, in each case subsequent to a previous test to determine fuse capacities of the bearings with retainers installed. Non-dimensional response is shown in Figure 4.4 for all three bearing sizes, including both QS and ISR responses. (Additional plots of actual force versus displacement and associated non-dimensional response are provided in Appendix B.) Each of the "a" height Type II bearings was subjected to multiple tests, and the PTFE ISR response was limited to moderate displacements in an effort to preserve the PTFE surface for subsequent tests. Consequently, the peak displacement demand was limited to 200% to 250% ESS rather than the 400% that had been used for the 7c and resulted in severe damage to the PTFE sheet. Slip rates for the QS pre-test were about 0.04 to 0.10 in./sec. These ISR tests followed the standard Type II ISR protocol indicated in Chapter 2, performed to a target of 4.0 in./sec, resulting in observed maximum slip rates ranging from 3.86 to 4.18 in./sec. The target vertical load corresponded to 500 psi average compression on the elastomer footprint for 9a and 11a bearings, and 385 psi for the 13a bearing. The imposed load varied between 85% and 128% of the target load during the ISR tests. The average compression stress acting on the PTFE ranged from 95% to 131% of the initial load during the QS tests, with the higher stresses corresponding to peak displacements when the top plate slid far enough to expose part of the PTFE layer and reduce the available contact area. The range of average stress broadened to 84% to 149% of the initial load during the ISR tests.

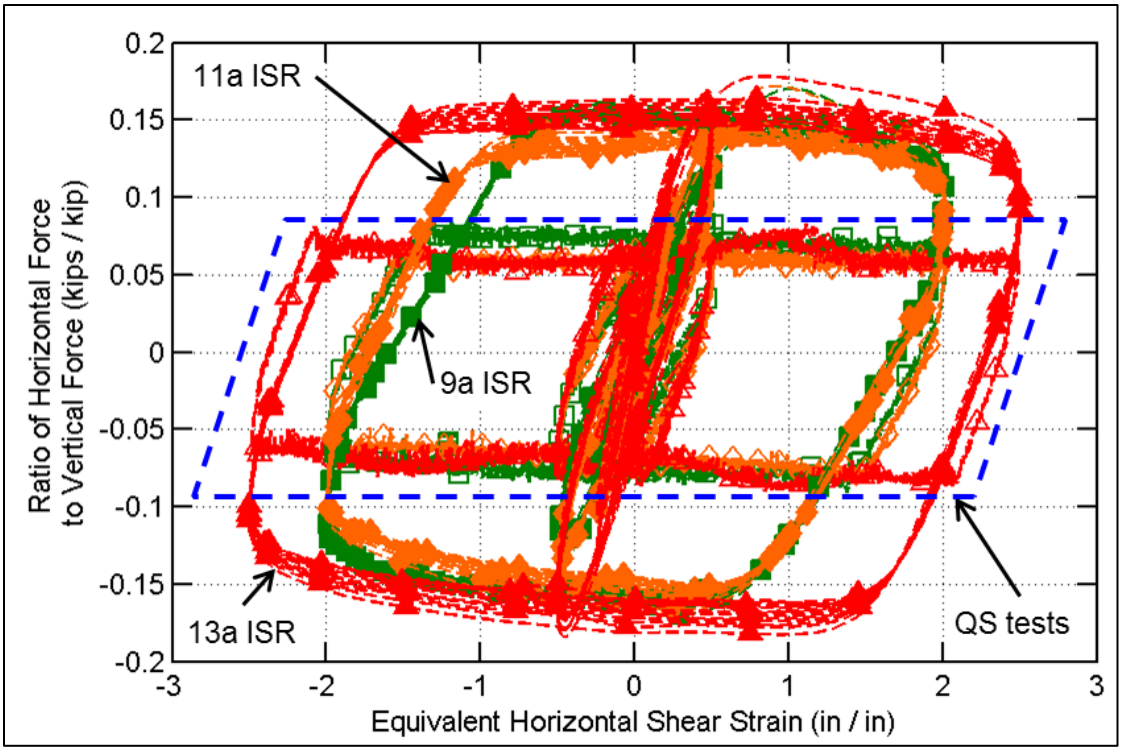

Figure 4.4. Non-dimensional Type II 9a/11a/13a constitutive response, transverse orientation.

4.2.2 Summary of Response Characteristics

4.2.2.1 Shear Stiffness

The elastomeric components of the Type II bearings exhibited a rate-sensitive response to shear loading. Linear stiffness is presented for individual ramps in QS and ISR tests for longitudinal 7c tests and transverse 9a, 11a, and 13a tests in Figure 4.5 and Figure 4.6, respectively. In both figures, the shear modulus for similar shear strain ranges is higher for the ISR relative to the QS tests, by approximately 20% and 45% for the 7c and “a” height bearings, respectively, at a shear strain range of about 50%. The “a” height bearings are more likely to be representative of the pure rate effect, whereas additional geometric effects influence the 7c bearing response. Coincidentally, the unadjusted shear modulus obtained from QS testing appears to be a reasonable estimate of the shear modulus at an increased strain rate because the PTFE friction also increases with strain rate. Consequently, the strain demand also increases with increasing strain rate, and the linear shear modulus is inversely related to strain demand. The net effect appears to be a balancing of stiffening and softening influences for the elastomeric compound used in the bearing specimens at the rates employed for the experimental program.

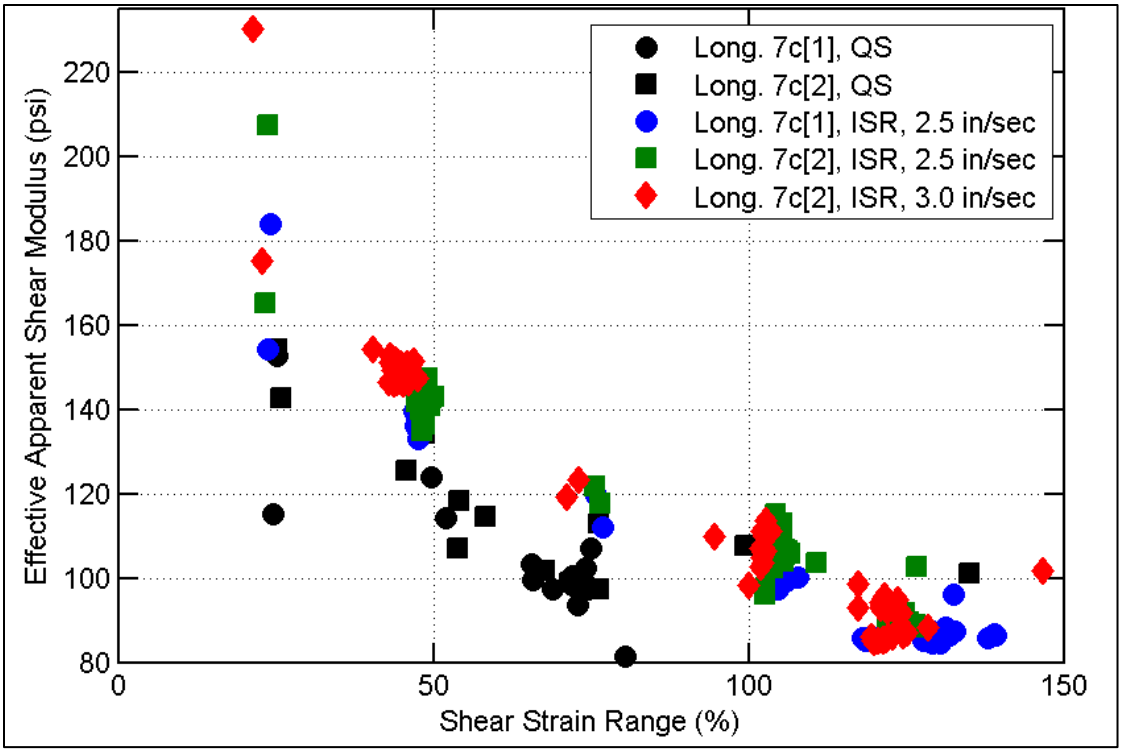

Figure 4.5. Effective apparent shear modulus for Type II 7c, longitudinal orientation.

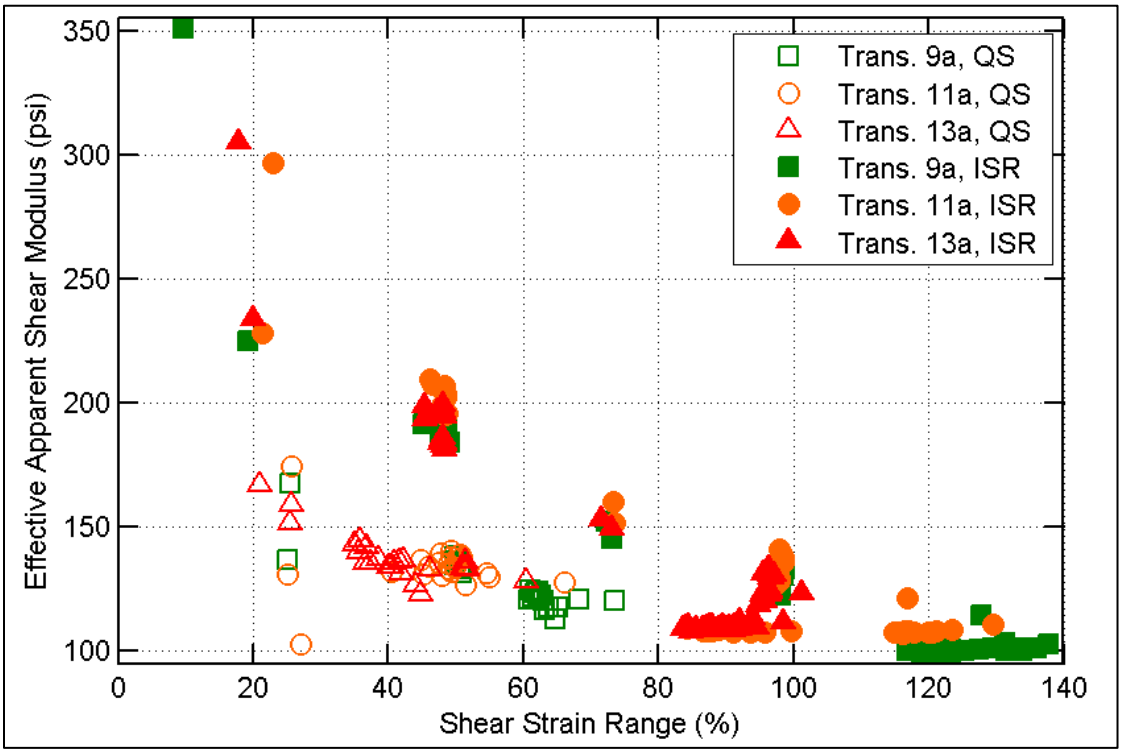

Figure 4.6. Effective apparent shear modulus for Type II 9a, 11a, 13a, transverse orientation.

4.2.2.2 Friction Resistance

Calculations of friction resistance extracted for sliding segments of Type II 9a, 11a, and 13a ISR tests are shown in Figure 4.7. Each data point represents an average of the slip resistance observed over a 5% ESS slip displacement increment. The dominant feature, as seen in the previous constitutive plots, is a marked increase in friction resistance at the PTFE sliding interface for ISR versus QS tests. The coefficient of friction increases with instantaneous velocity within the individual ISR tests, and it also exhibits significant inherent variability.

Aggregated summary friction data for the ISR versus QS tests are provided in Table 4.3. As for the force versus displacement plots, "[#]" denotes individual bearings of identical design. The Rate field includes some entries with "(#)", where two ISR tests were run sequentially on the same bearing. The numbers correlate to the testing sequence, with the first test being the slower (2.5 in./sec target max velocity) test. The mean friction coefficient for all QS tests is 0.069, and the mean for the ISR tests is 0.14. The range of two standard deviations for the ISR tests would be bracketed by (0.11, 0.17) at a 10% c.o.v., or by (0.084, 0.20) at a 20% c.o.v.

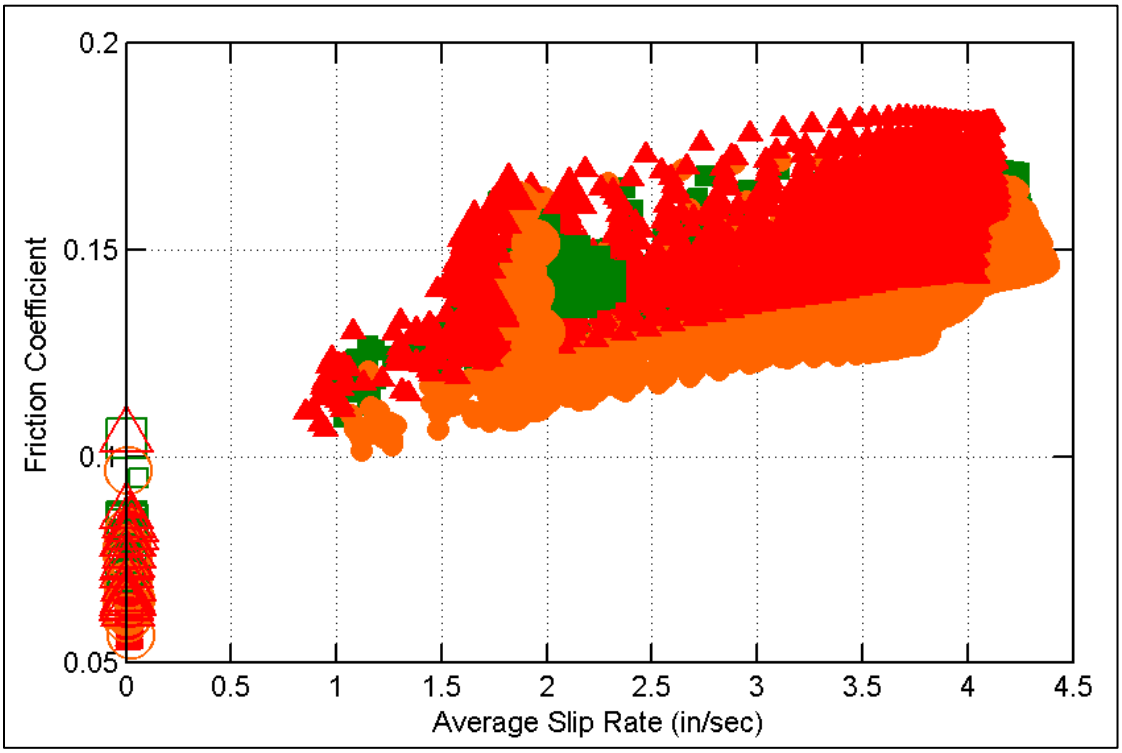

Figure 4.7. Friction coefficients for Type II 9a, 11a, and 13a, transverse orientation.

Table 4.3. Friction Response Summary Data for Type II ISR vs. QS Tests

Specimen	Orientation	Rate	Friction		
			Mean	c.o.v.	% Diff (ISR vs QS)
7c [1]	Long	QS	0.076	15%	
7c [2]	Long	QS	0.065	15%	
7c [2]	Trans	QS	0.064	18%	
9a	Trans	QS	0.074	5%	
11a	Trans	QS	0.064	9%	
13a	Trans	QS	0.068	11%	
7c [1]	Long	ISR	0.135	17%	77%
7c [2]	Long	ISR (1)	0.142	9%	117%
7c [2]	Long	ISR (2)	0.140	6%	115%
7c [2]	Trans	ISR (1)	0.132	14%	106%
9a	Trans	ISR	0.148	7%	99%
11a	Trans	ISR	0.137	9%	113%
13a	Trans	ISR	0.154	8%	124%

4.3 LARGE DISPLACEMENT RESPONSE WITH SMALL MIDDLE PLATE ROTATION

Tests were performed to large displacements with 7c and 11a bearings in a transverse orientation, and 9a and 13a in a longitudinal orientation, which resulted in small middle plate rotations. These bearings were tested with progressively increasing peak displacement cycles, until the PTFE layer was delaminated or otherwise damaged by the top plate.

4.3.1 Type II 7c, Transverse Orientation

Tests were performed to a maximum of 400% ESS on two Type II 7c bearings with a transverse orientation, indicated in Figure 4.8 as 7c [2] and 7c [3]. Bearing 7c [2] was used to perform a QS pre-test and two longitudinal 7c ISR tests described in the previous section and therefore is identified with a (4) to indicate how many tests in total had been performed on the specimen. The bearing was set in a transverse orientation and run with a series of cycles increasing by 50% ESS at each iteration, to the maximum of 400%. No delamination or other severe damage was observed during Test 7c [2] (4). The old 7c [2] bearing was then removed and replaced with a new bearing, 7c [3]. This bearing was subjected to a QS pre-test with the intent of using the test data to supply the commands for a subsequent ISR test. There were no intermediate cycles between the 50% and 400% displacement targets. Upon reversal from the first excursion at +400%, a ripple of delamination was observed on the PTFE sheet. During the second excursion, roughly half of the PTFE sheet on the (–X) side of the bearing had been delaminated in the previous cycle, and the now delaminated PTFE sheet was pinched and plastically deformed. These effects are the reason for the slight increase in horizontal resistance between +200% and +300% ESS. The 7c [3] bearing was then replaced with the previously used 7c [2] bearing, and the same QS pre-test was performed, yielding the data identified as 7c [2] (5). The PTFE was pinched slightly, and small segments of the PTFE sheet were clipped free from the main sheet by the leading edge of the top plate. This is reflected in the constitutive response with a slight increase and abrupt drop to the typical sliding resistance upon reversal from +400% at a horizontal

displacement of approximately +75% ESS (about +1.75 in.). Bearing 7c [2] and the data from Test 7c [2] (5) were used as the QS pre-test for the transverse 7c ISR tests described in the previous section, which experienced removal of about half of the PTFE on the (–X) side during the first ISR test, and removal of the remainder of the PTFE during the second ISR test.

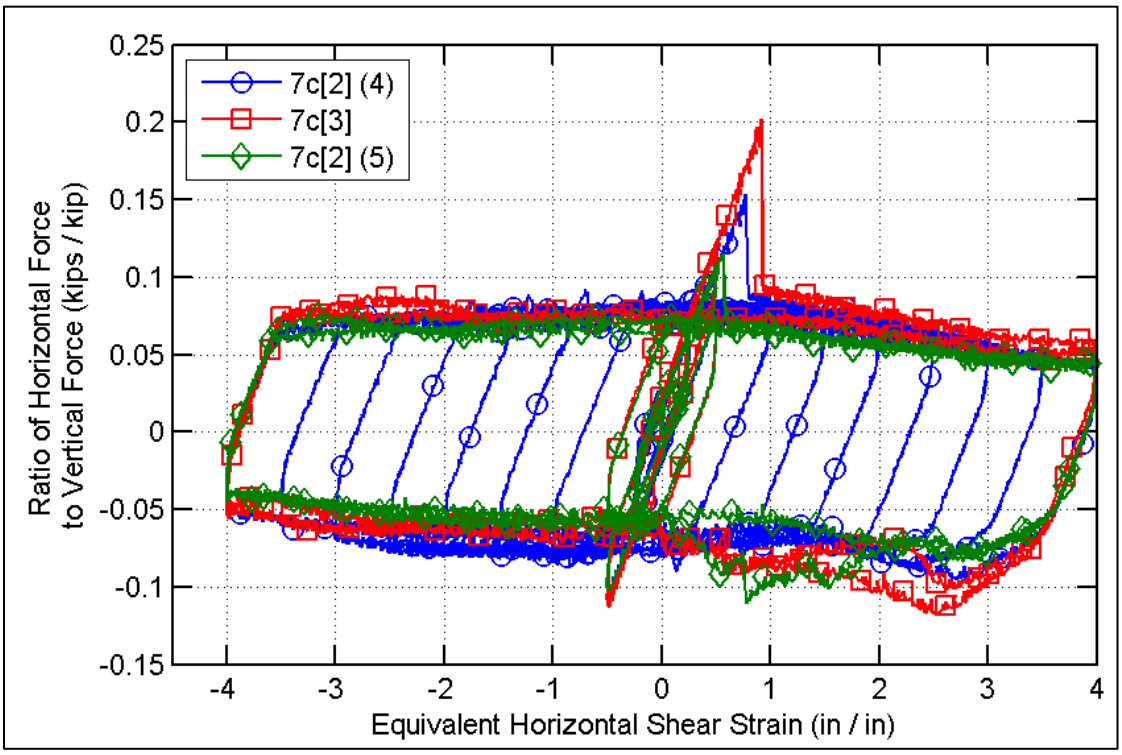

Figure 4.8. Non-dimensional Type II 7c constitutive response, transverse orientation.

4.3.12 Type II 9a, Longitudinal Orientation

Subsequent to the tests performed on the Type II 9a (one test with retainers and a QS pre-test/ISR test pair without retainers) in the transverse orientation, the bearing was turned on the concrete pad and tested to large displacements in a longitudinal orientation. The resulting non-dimensional friction-ESS data are presented in Figure 4.9. The cycles increased at 25% ESS increments up to 250% ESS, and at 50% increments beyond that level. Although no obvious burrs were noted at the weld line connecting the stainless steel plate to the thick top plate, the visible evolution of damage to the PTFE sheet and corroborating evidence in the force-displacement response indicates that a burr or similar localized effect did exist. Damage initiated at a top plate displacement of slightly more than +2 in. (about +125% to +150%) and became more pronounced with each cycle. Up to the 350% cycle, the response transitioned back to typical sliding as the top plate returned from +X to −X displacements. In the 400% cycle, a large portion of the PTFE sheet became pinched between the top and middle plates, causing the horizontal force to increase to almost three times the typical sliding resistance, until the PTFE sheet tore and the middle plate slid freely under the top plate. PTFE damage continued to worsen, and the +450%, −450%, and final excursions exhibited increased sliding resistance, including periodic stick-slip of the steel-on-steel interface.

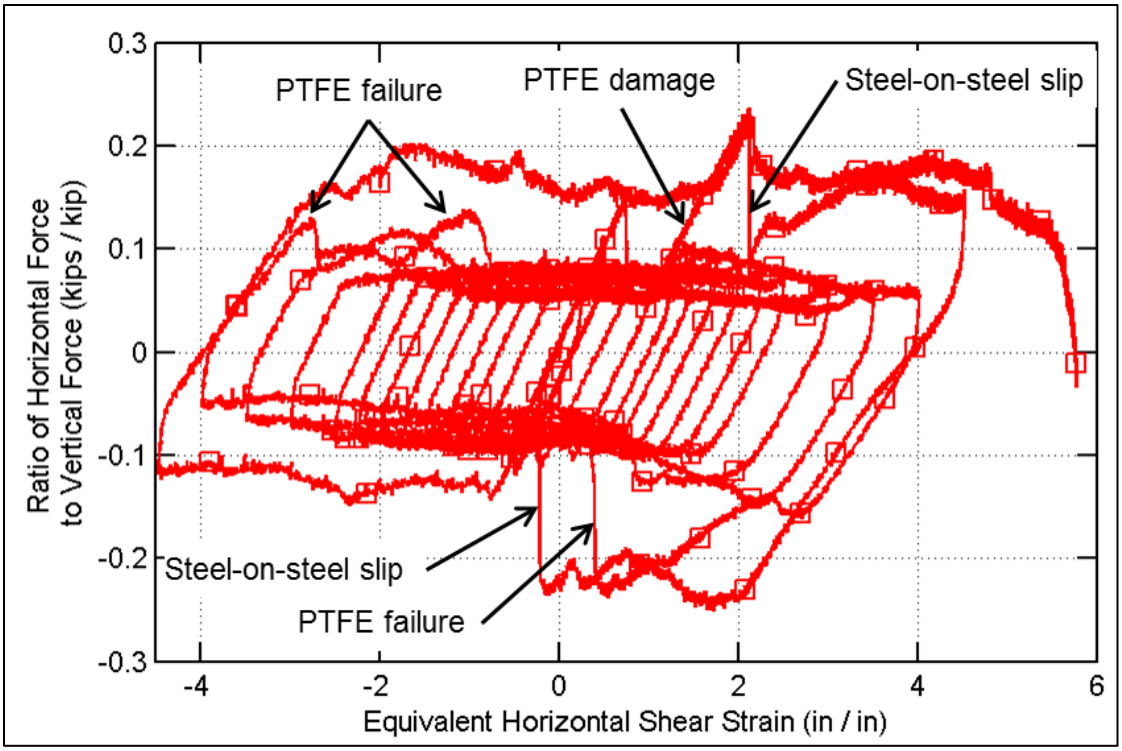

Figure 4.9. Non-dimensional large displacement response of Type II 9a, longitudinal orientation.

4.3.3 Type II 11a, Transverse Orientation

Multiple subsequent “irregular” tests were performed on the Type II 11a specimen in a transverse orientation. The results of several of these tests are presented in terms of non-dimensional friction versus ESS in Figure 4.10. The tests are identified according to their chronological sequence in the figure legend. Test (2) was the QS pre-test performed to define control signals for the ISR test, described in the previous section. Test (3) was a repetition of Test (2), after having performed the ISR test, showing that the performance of the PTFE was not significantly degraded as a result of the ISR test. Test (4) was performed in two segments in order to achieve unseating in the transverse direction. The top plate was initially driven in the (–X) direction to a distance of 14 in., but the test was terminated at that point and the bearing was unloaded to prevent saturation of the control signal to the horizontal actuator (15 in. max.). A second component of the test was appended by initiating the test with an initial 8 in. offset in the (–X) direction. Test (4) appeared to cause plastic flexural distortion in the middle plate at incipient unseating, with the middle plate bent over the supporting reinforced elastomer block.

Test (5) was conducted to investigate the performance of the PTFE when subjected to reversing cycles at large displacements, and it consisted of a series of increasing peak demand excursions in the (+X) direction, to a maximum of +8 in. (+400% ESS). The returning phase of each cycle was truncated when typical sliding resumed. No damage to the PTFE was apparent up to the 250% ESS excursion. At the 300%, 350%, and 400% excursions, there was visible damage to the PTFE sheet at the (−X) side of the middle plate. The damage was manifested in the force-displacement response as a slight increase in apparent friction coefficient to about 0.1, up from the typical value of 0.06 to 0.07. A second component of Test (5) was performed by driving the top plate through a single half-cycle,

from 0 in. to +11.25 in. (+562.5%) and returning to 0 in. This was the physical limit of the stroke of the horizontal actuator, relative to the zero position of the 11a bearing. The (–X) half of the PTFE sheet was torn away from the (+X) half, causing the apparent coefficient of friction to increase to approximately 0.12 when the bearing returned to an ESS of approximately 380%.

A series of tests, collectively referred to as Test (6), were performed subsequent to Test (5) to finish removal of the PTFE sheet from the (+X) half, but they are not shown in the figures. Test (7) was performed after complete removal of the PTFE, and it represents the sliding response of the resulting steel-on-steel surface. For the most part, the sliding response exhibits a relatively low apparent coefficient of friction between 0.07 and 0.11. The exception is the reversal at a displacement of +10 in. (+500% ESS). The localized increase in horizontal resistance is likely an artifact of the previous unseating test [Test (4)] and the resulting convex upper surface of the middle plate, with a peak at about the quarter point of the plate length in the (–X) direction. Once the top plate reaches the local maximum of the plastically curved middle plate, the middle plate slides under the top plate and returns to a more typical sliding response.

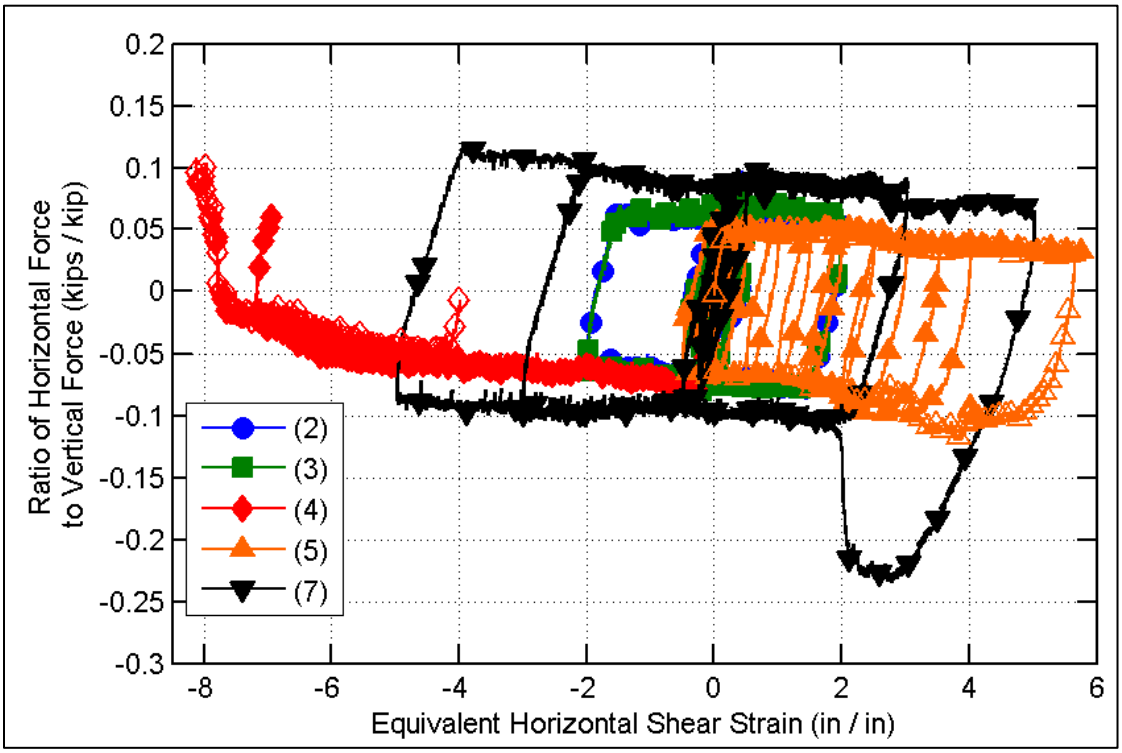

Figure 4.10. Non-dimensional large displacement response of Type II 11a, transverse orientation.

4.3.4 Type II 13a, Longitudinal Orientation

Similar to the Type II 9a, the Type II 13a bearing was turned on the concrete pad and tested to large displacements in a longitudinal orientation subsequent to the three transverse orientation tests. The resulting non-dimensional friction-ESS data are presented in Figure 4.11. Also similar to the Type II 9a longitudinal test, the cycles increased at 25% ESS increments up to 250% ESS and at 50% increments beyond that level. The bearing exhibited consistent sliding response for increasing peak displacement demands up to about 300% ESS, with an average apparent sliding coefficient of friction of 0.06. From 300% ESS

to 500% ESS, the (+X) excursions began to induce rotations at the middle plate, with apparent friction resistance increasing to about 0.13 from the typical sliding friction of about 0.06. The effect was much less pronounced in the (–X) direction, with the apparent friction resistance increasing to only about 0.08. Finally, the cycles with peak displacements of 550% and 600% ESS included severe delamination and damage to the PTFE sheet and resulted in complete removal of the PTFE from the middle plate. Apparent friction reached approximately 0.15 to 0.16 when the PTFE was delaminating and tearing.

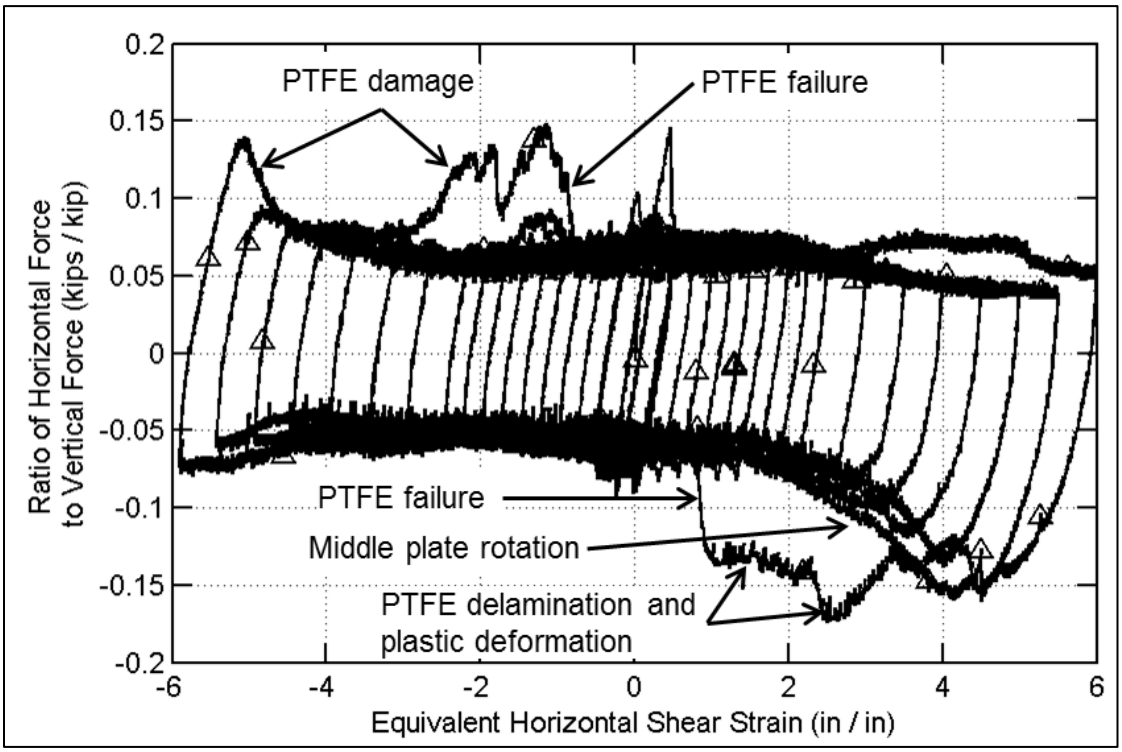

Figure 4.11. Non-dimensional large displacement response of Type II 13a, longitudinal orientation.

4. 4 LARGE DISPLACEMENT RESPONSE WITH SIGNIFICANT MIDDLE PLATE ROTATION

The combination of elastomer height and relatively short bearing length in the direction of motion for the longitudinal orientation of Type II 7c bearings led to significant rotations of the middle plate about a horizontal transverse axis for large top plate displacements. Three sequential tests performed with a single bearing exhibited the characteristic response to be expected for such bearing configurations, as shown in Figure 4.12. The test data shown were obtained for tests performed on the 7c [1] bearing prior to the ISR tests shown in previous sections (recall that the QS and ISR tests for 7c [1] were indicated as tests (4) and (5)). Test 7c [1] (1) was a monotonic loading/unloading sequence in the (–X) direction, limited to a peak displacement of −350% ESS. Test 7c [1] (2) included cycles with peak displacements of 25%, 50%, 100%, 200%, and 400% ESS. The sliding response was consistent at displacements up to 200% ESS, but when the displacement increased to 400% ESS, the eccentric load applied to the middle plate elicited significant flexural deformation in the elastomer. The rotational deformations also permitted the top plate to drop in elevation. Consequently, when the direction of motion was reversed at ±400% ESS, the top plate drove against the middle plate and upper portion of elastomer rather than

relieving the prior elastomer pure shear and sliding back toward the initial position on the PTFE. Equilibrium required that the top plate rise when traveling back to the initial position, and eventually the top plate rose high enough that the middle plate could rotate back to level and slide under the top plate, as in the initial configuration. Test 7c [1] (3) was carried out to explore the evolution of the transition from the level middle plate configuration at 200% ESS to the rotated middle plate configuration at 400% ESS. The test was terminated prior to reaching 400% ESS because the top plate unseated by sliding off of the middle plate at about +350% ESS. In all cases, the peak force for large displacements corresponded to an apparent coefficient of friction of about 0.15 to 0.18. These values were similar to or higher than the maximum static friction coefficients for bearing 7c [1], which were themselves unusually high (in the range of 0.12 to 0.16).

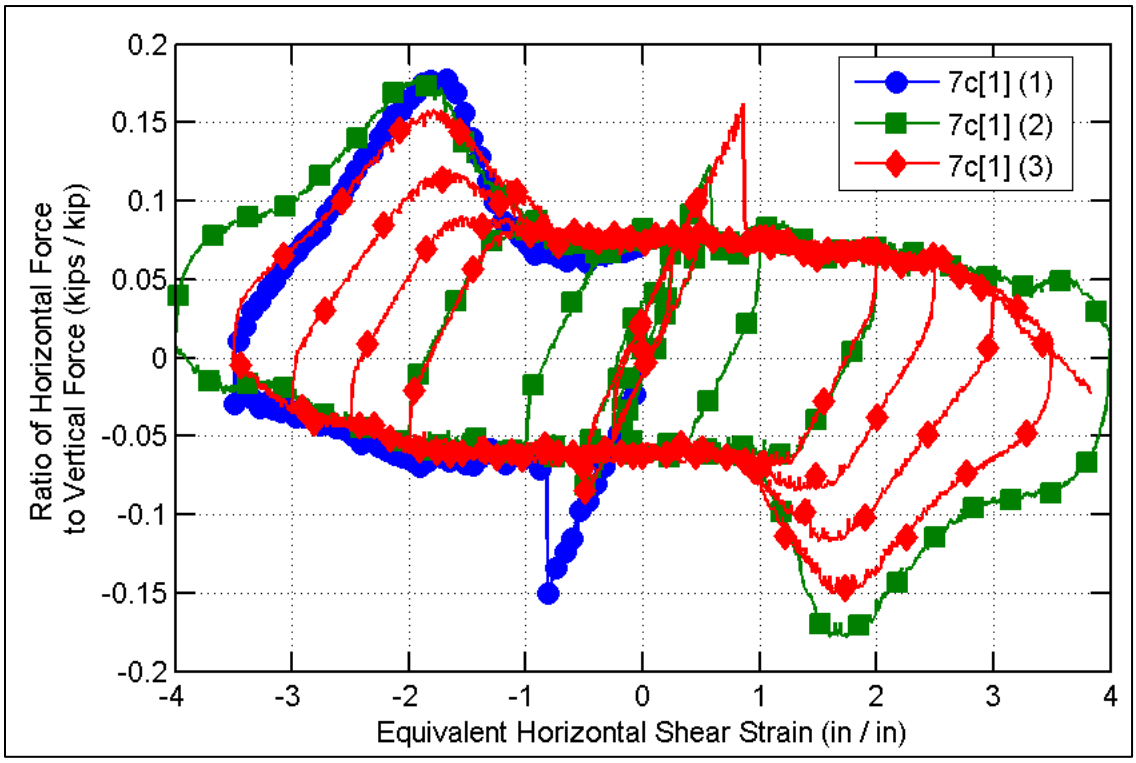

Figure 4.12. Ratio of horizontal to vertical force versus equivalent shear strain response for Type II elastomeric bearings, longitudinal orientation.

4.5 LARGE DISPLACEMENT RESPONSE WITH UNSEATING AT PTFE

Four tests were performed to unseating of Type II bearings at the sliding interface between the top and middle plates. Three of the four tests were performed on a longitudinal orientation. If a Type II bearing unseats in the longitudinal direction, the consequences may not be catastrophic for the bridge because the bottom flange can fall on the middle plate (although impact and concentrated loads would need to be considered for a bridge girder, especially if the design had required web stiffeners at the bearing support location). Each of the longitudinal unseating tests was also tested to ultimate strength with reversal post-unseating, to investigate the behavior and capacity of the bearing in the unseated configuration.

4.5.1 Type II 7c, Longitudinal Unseating

The force versus displacement results obtained from the Type II 7c longitudinal unseating test (7c [1] (6)) are shown in Figure 4.13, together with the results from the last large displacement longitudinal test (see Appendix B) for comparison. The test consisted of a single ramp to unseating in the (−X) direction at approximately −400% ESS, followed by reversal in the (+X) direction. The peak load during reversal was limited by rupture of one of the concrete anchors when the top plate had returned to approximately −100% ESS. When one of the anchors ruptured, the bottom plate rotated on the concrete surface. The remaining anchor restrained the bottom plate so that it could not slide freely on the concrete. Consequently, the rotated configuration of the elastomeric block was forced to resist a disproportionate load at the side nearer to the remaining anchor. The elastomer began to shear internally, resulting in shear capacity degradation starting around −20% ESS.

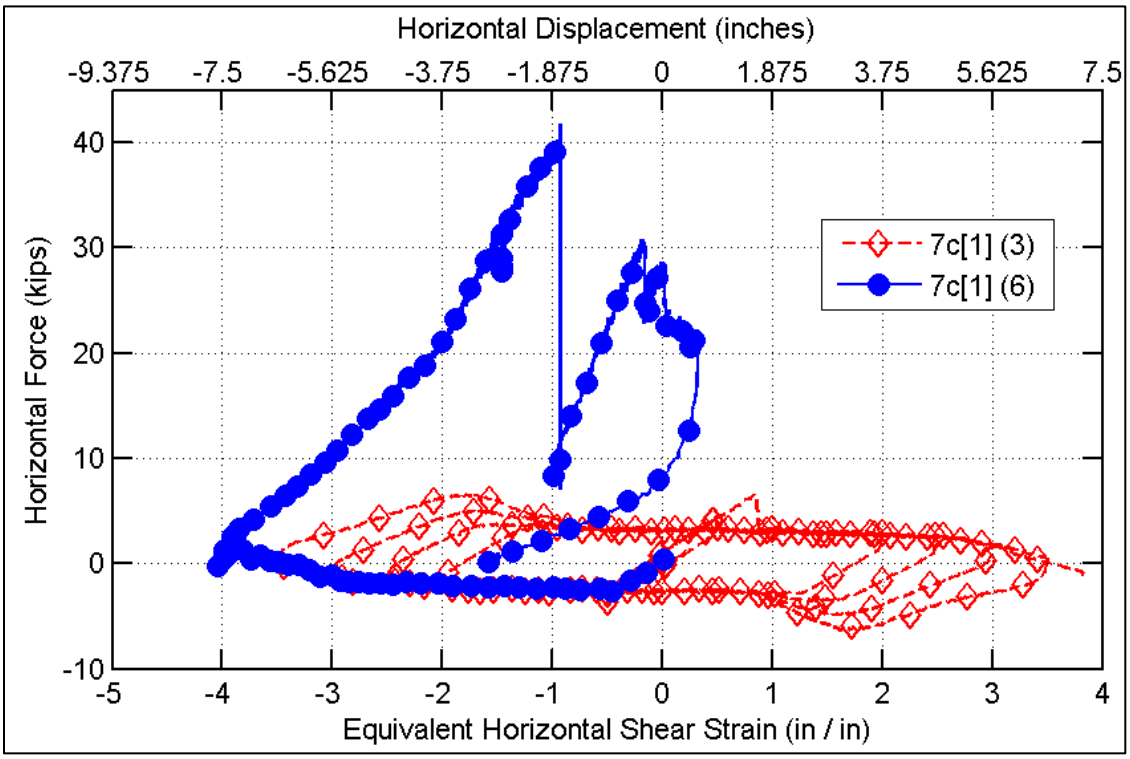

Figure 4.13. Force versus displacement for unseating and reversal with Type II 7c bearing, longitudinal orientation.

4.5.2 Type II 9a, Longitudinal Unseating

The complete force versus displacement results obtained from the Type II 9a longitudinal unseating test (9a (4)) are shown in Figure 4.14. A portion of this test data has already been noted in a previous section (see also Appendix B), but the plotted data had been truncated so that the initial sliding and evolution of PTFE damage and removal could be seen more clearly. This test was driven to unseating after the PTFE had been fully removed with cycles up to 450% ESS. Unseating occurred at about +575% ESS, and the top plate was driven back against the elastomer block. The initial stiffness of the response from about +575% to about +375% represents the shear stiffness of the full height of the elastomer block. Initially, the edge of the steel fixture to which the top plate was anchored pressed against the middle plate, but at about +375% ESS, the steel fixture slid forward and over the middle plate until the side of the middle plate and the upper portion of the elastomer block were constrained against the underside of the steel fixture and the side of the top plate. The top plate then

drove against the elastomer directly, but the effective height of the elastomer was reduced by the height of the top plate, causing an apparent increase in stiffness. The peak load during reversal was limited by rupture of one of the concrete anchors when the top plate had returned to approximately −200% ESS. Similarly to the 7c unseating test, the resulting displacement of one side of the bottom plate on the concrete created a stress concentration, and the elastomer began to shear internally, resulting in shear capacity degradation starting around −100% ESS.

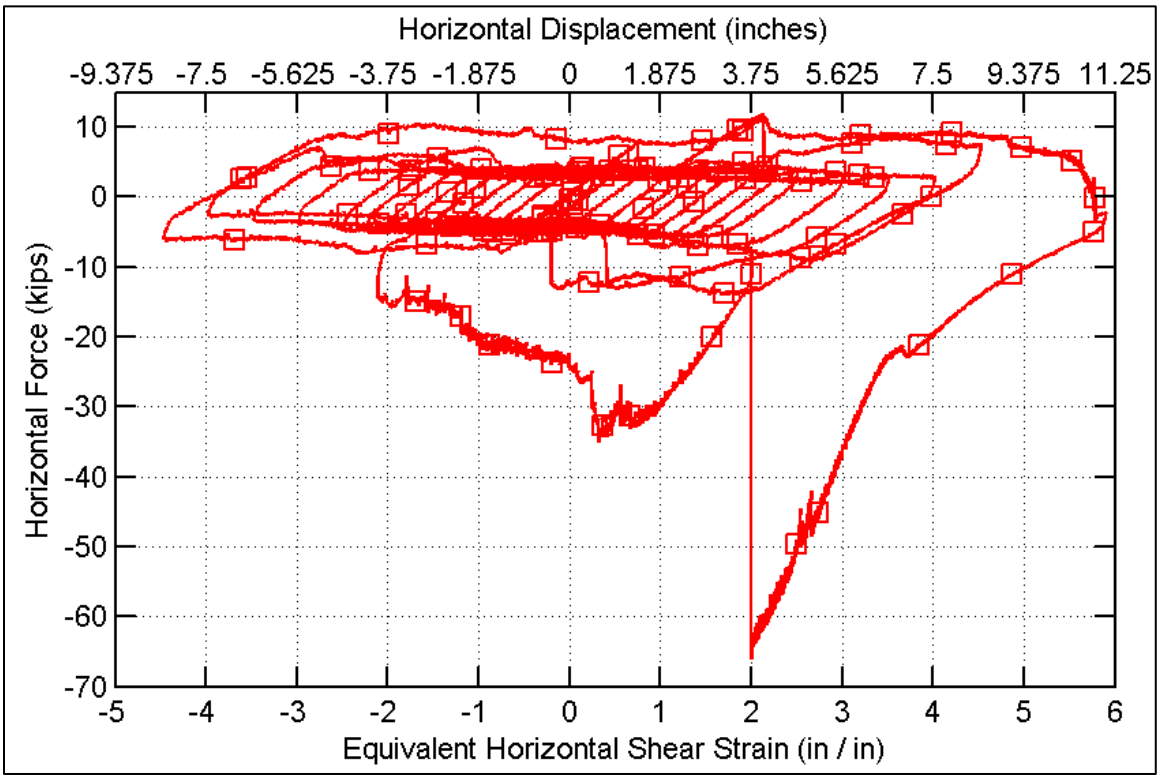

Figure 4.14. Force versus displacement for unseating and reversal with Type II 9a bearing, longitudinal orientation.

4.5.3 Type II 13a, Longitudinal Unseating

This longitudinal unseating test was run separately from the cyclic test to investigate PTFE damage and failure, using a +8 in. offset for the initial position. The data for the unseating test (13a (5)) are shown in Figure 4.15, together with the data obtained from the previous cyclic longitudinal test (13a (4); also see Appendix B). Test 13a (5) was driven to unseating with a monotonic ramp in the (+X) direction after the PTFE had been fully removed with cycles up to 600% ESS in the previous 13a (4) test. Unseating occurred at about +725% ESS, and the top plate was driven back against the elastomer block. The top plate thickness was 2-1/2 in. compared with the combined height of 3 in. for the reinforced elastomer block and middle plate, so the shear transmitted from the top plate passed through only about 1/2 in. of elastomer to reach the bottom plate. For this reason, the response is stiffer immediately after unseating when compared with the shear stiffness observed during 13a (4) at reversals between sliding segments. The peak load occurred at about +585% ESS, when one of the anchors ruptured. This ESS value is based on the full elastomer height, but with only 1/2 in. effective, the adjusted estimated shear strain in the elastomer between the top and bottom plates is approximately 525% to displace from +725% to +585% ESS

relative to the initial zero position centered on the bearing. Unique to this test, the resulting stress concentration was not sufficient to initiate rupture in the elastomer, and the second anchor failed at approximately +550% ESS relative to the initial zero position. The bearing was then free to slide on the concrete, and the slip segment with a resistance of about 32 kips (approximate sliding friction coefficient of 0.32 with vertical load of 100 kips) is representative of the subsequent sliding mechanism.

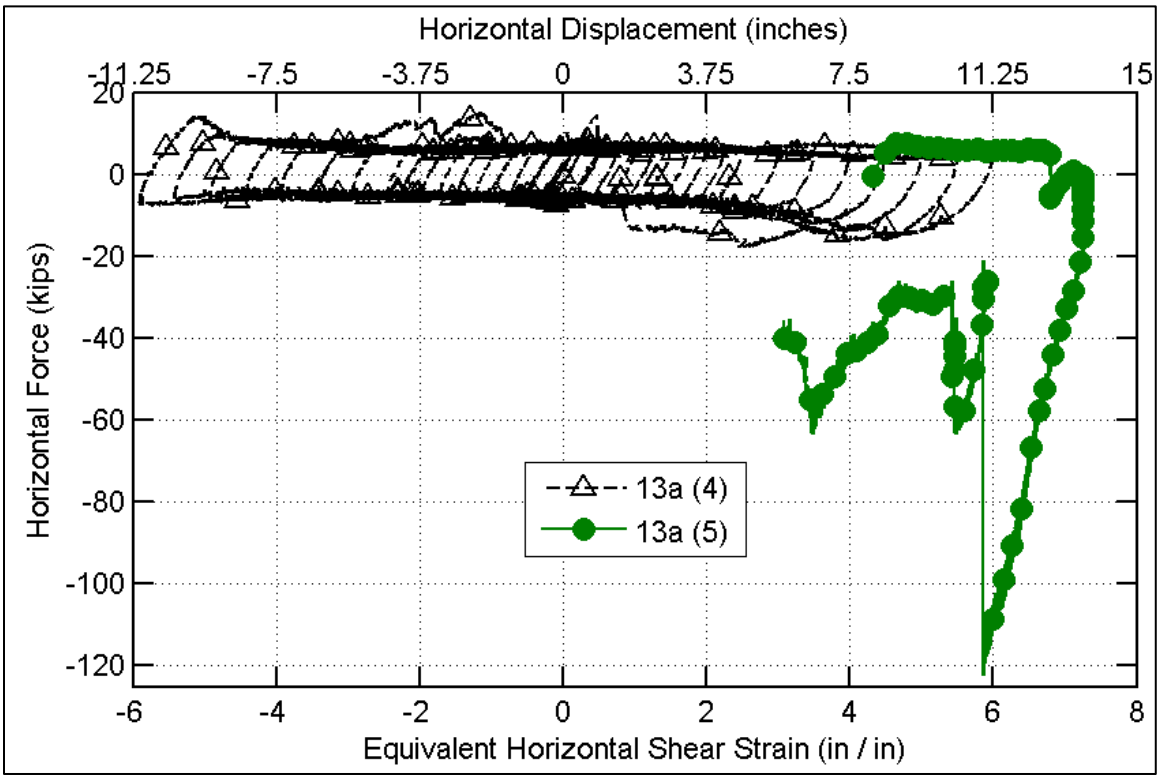

Figure 4.15. Force versus displacement for unseating and reversal with Type II 13a bearing, longitudinal orientation.

4.5.4 Summary of Unseating Test Characteristics

Summary values for the Type II bearing unseating tests are provided in Table 4.4. The first fields list the displacements at which instability and unseating occur. Instability is the first instance at which the calculated horizontal load crosses zero (i.e., where an external horizontal force is required to act in the opposite direction from the current displacement direction to maintain equilibrium with simulated vertical load and mechanical forces developed in the deformed elastomer). Values are provided in terms of both absolute displacement and ESS. For Type II bearings, the nominal displacement capacity is 100% ESS, according to the IDOT Bridge Manual (IDOT 2012a). All limits for instability are far in excess of the nominal displacement capacity for the respective bearings. Plate overlap is determined according to the measured relative positions of the top and middle plates. For 7c and 9a bearings, the values represent the combination of the PTFE overlap and the tapered edge of the middle plate (1 in. for 7c, 1-1/2 in. for 9a). The shaded cell for the 13a is an approximate value, determined visually from video capture during the experiment and examination of the specimen after the test. The top plate experienced a slight slip from the etched region where the PTFE had been applied, and it caught on the tapered edge of the middle plate at the instability limit. The value shown represents the overlap of the top plate

on the tapered edge of the middle plate during the deformation from the instability limit to unseating. The peak loads are the recorded maximum values at incipient failure of the first anchor for each test, and the maximum average shear stress is determined by dividing the peak load by the nominal elastomer area.

Table 4.4. Summary Data for Type II Unseating Tests

Test	Displacement to:				Plate Overlap at Unseating (in.)	Peak Load (k)	Max. Avg. Shear Stress (ksi)
	Instability		Unseating				
	Dx (in.)	ESS (%)	Dx (in.)	ESS (%)			
7c[1] (6)	6.2	330	7.4	395	1.7	40.3	0.48
9a (4)	10.8	575	10.8	578	1.9	64.4	0.60
11a (5)	15.4	772	16.2	812	0.28		
13a (4)	12.7	680	13.6	724	0.875	122.2	0.47

CHAPTER 5 LOW-PROFILE FIXED BEARING EXPERIMENTAL RESULTS

5.1 GENERAL FORCE-DISPLACEMENT RESPONSE

5.1.1 Weak Anchor Tests

Two steel low-profile fixed (LPF) bearing specimens with design capacities limited by their steel anchors to the concrete were tested, one each in a longitudinal and transverse orientation. The fusing behavior for the fixed bearings with capacities limited by weak anchors is shown in Figure 5.1. Sliding response for the full test to large displacements is shown in Figure 5.2, with the horizontal load normalized by the vertical load on the vertical axis. (Plots of individual fixed bearing response may be found in Appendix C.) The general response obtained for the weak anchor tests is consistent with expectations based on basic mechanics considerations and corroborated in Mander et al. (1996). In both orientations, the response is a combination of sliding friction and mechanical shear resistance provided by the anchors. Observations of the anchor rupture surfaces following the tests showed that the fractures were planar pure shear failures at the top of the concrete surface. A stable hysteretic response was obtained in each orientation for large sliding displacements.

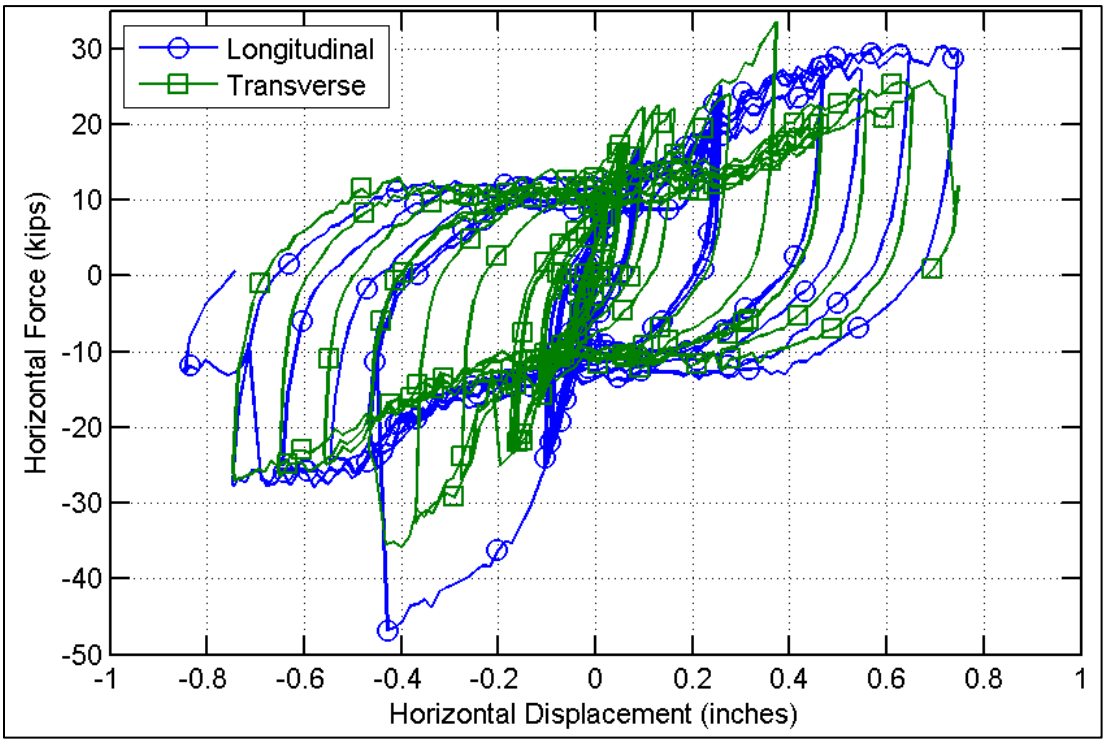

Figure 5.1. Force versus displacement response to a fully fused state, for weak anchor LPF tests.

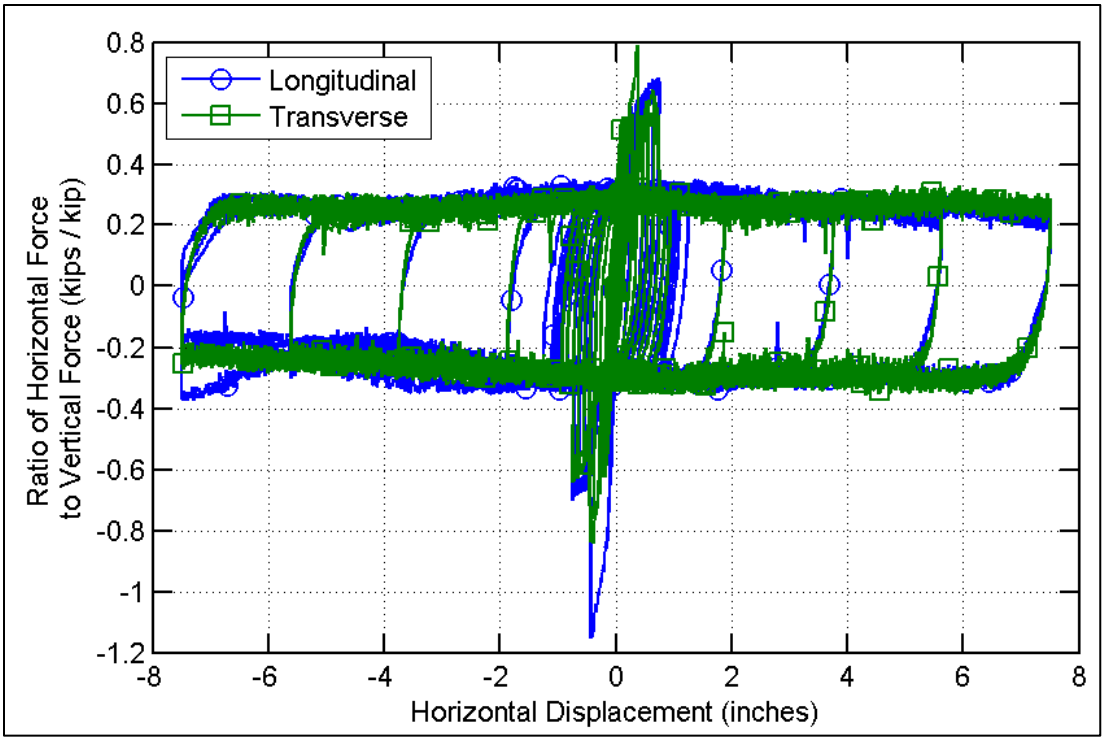

Figure 5.2. Ratio of horizontal to vertical force versus displacement response for complete weak anchor LPF tests.

5.1.2 Weak Pintle Tests

Two tests, one each in the longitudinal and the transverse direction, were performed on fixed bearings for which the pintles were intended to be the ultimate fuse component. Fusing behavior is shown in Figure 5.3 and sliding response at large displacements is shown in Figure 5.4, with the horizontal load normalized by the vertical load on the vertical axis. (Plots of individual bearing response may be found in Appendix C.) The response observed for the weak pintle cases is significantly more complicated than for the weak anchors cases, and neither orientation exhibited the intended ultimate behavior (fractured pintles and intact concrete anchors). In the transverse weak pintle case, both of the anchors failed while the pintles remained intact, although plastically deformed. It appeared that concrete crushed locally around the high-strength anchors and that the concrete damage extended outward from the anchors and downward with succeeding cycles. Rupture surfaces of the anchors were approximately 2 to 2-1/2 in. below the surface of the concrete pad, and rupture occurred at bearing displacements in the range of 1 to 1-1/2 in. in each direction. The crushed concrete led to mechanical demands on the anchors analogous to those on driven piles in soil, with a combination of shear and flexure. Even after the anchors had failed, they continued to influence the response, with each new displacement level exhibiting a clear increase in shear resistance above typical sliding resistance, as remnants of the anchors that extended below the masonry plate were dragged through undamaged concrete.

For the longitudinal orientation of the weak pintle case, the masonry plate appeared to rotate about the axis passing through both anchors (a roll-over response in the longitudinal direction of the bridge). This mechanism induced tension in the anchors in addition to the anticipated shear demands. Meanwhile, the rounded tops of the pintles, oversized holes in the sole plate, and curved bottom surface of the sole plate all permitted relative rotation of the sole and masonry plates without inducing significant demands in the pintles beyond

direct shear. Consequently, the peak force capacity was determined by the anchors rather than the pintles, and the first rupture occurred at about −1.6 in. Following the failure of one of the anchors, the masonry plate pivoted about the remaining anchor while the sole plate was restrained from rotating by the loading beam, causing the pintles to resist a couple in addition to direct shear. Because of these mechanical demands, the pintle nearer to the remaining anchor eventually failed, at a displacement of about −2.75 in. With only one anchor and one pintle remaining, the rotation of the masonry plate became more pronounced, and the cyclic protocol was foregone in favor of a monotonic ramp to fail the remaining pintle, which finally occurred at approximately −8 in.

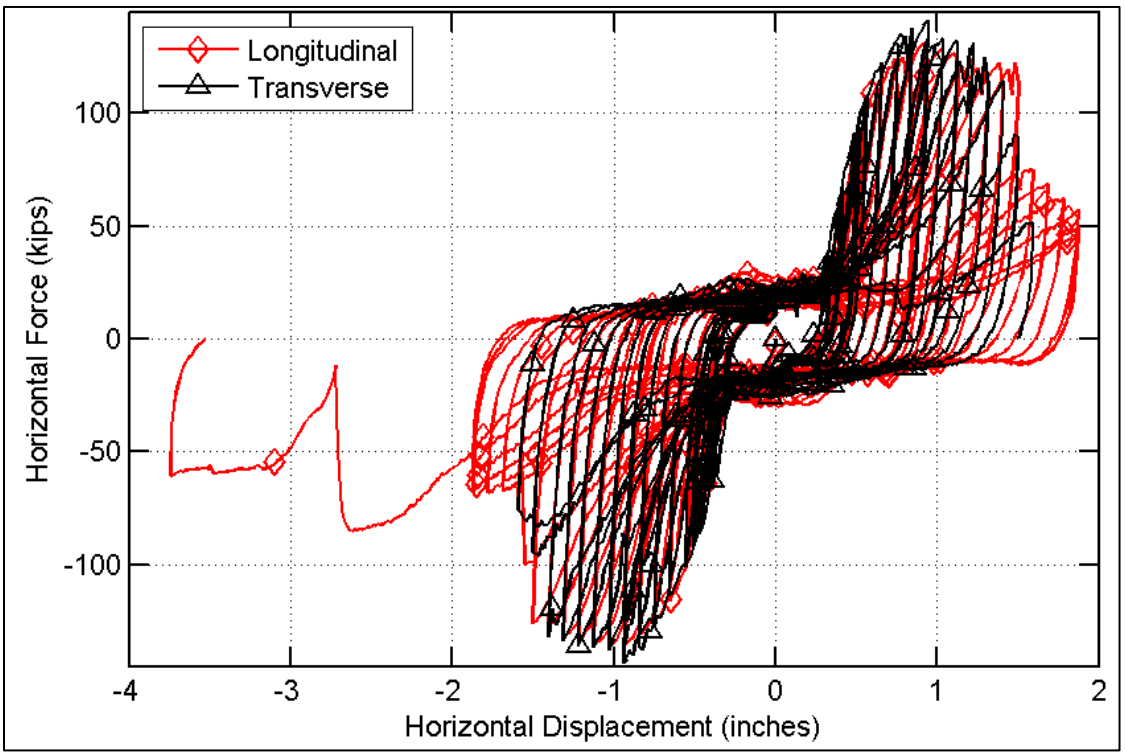

Figure 5.3. Force versus displacement response to a fully fused state, for pintle-controlled LPF tests.

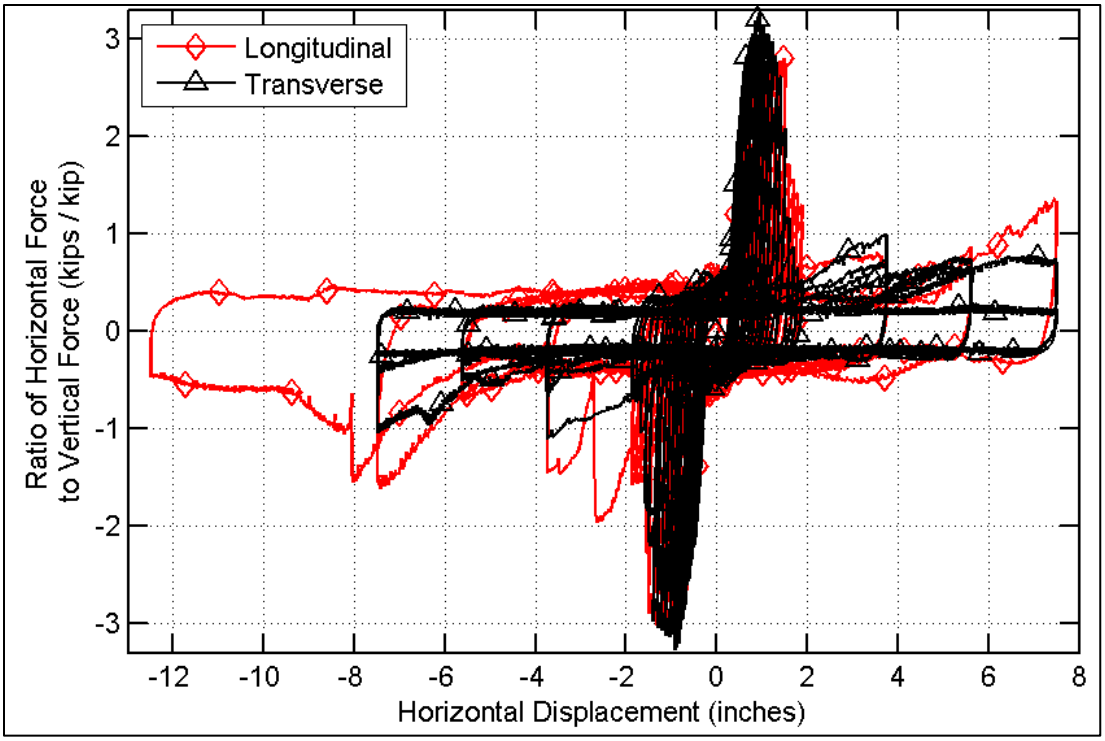

Figure 5.4. Ratio of horizontal to vertical force versus displacement response for complete pintle-controlled LPF tests.

5.2 SUMMARY OF LPF BEARING RESPONSE CHARACTERISTICS

5.2.1 Nominal Fuse Capacity Estimate

The nominal fuse capacity, V_{fuse}, for steel fixed bearings can be estimated according to

$$V_{fuse} = \mu N + n\phi 0.6 F_u A_b \qquad \text{(Eq. 5-1)}$$

where

μ = Coefficient of friction

N = Normal (gravity) load applied to bearing (kips)

n = Number of load transfer elements at a shear plane

ϕ = Strength reduction factor

F_u = Ultimate tensile stress of load transfer elements (ksi)

A_b = Effective cross-sectional area of a load transfer element (in^2)

Fuse capacity calculations described in the IDOT Bridge Manual (2012a) typically assume that friction is negligible (i.e., set $\mu \approx 0$). The strength reduction factor, ϕ, used when calculating the estimated capacity, is taken here as unity rather than the 0.75 used in the

nominal anchor capacities to reflect combined loading at retainers. The factor of 0.6 is included in the equation to convert the tension capacity to shear capacity. Additionally, a factor of 0.8 is included within the A_b term when evaluating threaded steel anchors, to account for the reduced area at the threads, compared with a factor of 1 for pintles to reflect that the full nominal area is effective in shear. With the assumption of $\mu \approx 0$, fuse capacities may be estimated, as summarized in Table 5.1, by using only the second term of Eq. 5-1 for each shear transfer plane (pintles between top and bottom plates, or anchors between bottom plate and concrete).

Table 5.1. Summary Data for Fixed Bearing Estimated Fuse Capacities

Fuse Case	Weak Anchors		Weak Pintles	
Fuse Element	Anchors	Pintles	Anchors	Pintles
ϕ	1			
n (elements)	2			
Diameter (in)	3/4	1 1/4	1 1/2	1 1/4
Thread Adj.	0.8	1	0.8	1
A_b (in^2)	0.35	1.23	1.41	1.23
Limit State	Rupture	Yield	Yield	Rupture
F_y or F_u (ksi)	73	*36*	120	**82**
V_{fuse}, est. (kips)	31	*53*	204	**120**

Table 5.1 shows (in italics) the yield capacities of elements that are not intended to be critical for each case, estimated using lower bounds of material yield strength for the specified material. The anticipated fuse capacity for the weak anchors test was determined using a material strength obtained from coupon tests of the anchor material (shown in the shaded cells of the table). The coupon tests indicated that the yield and ultimate tensile strengths were approximately 50 and 73 ksi, respectively. Accounting for the relatively high anchor material strength, the anchors were still expected to control the weak anchor tests' fuse capacities, at about 59% of the lower bound of the minimum pintle yield capacity.

Documentation supplied by the bearing manufacturer indicated that, although M270/Gr 36 (A709) material had been used for the sole and masonry plates, the material used for the pintles was M222 (A588), with an average ultimate tensile strength of 81.6 ksi (according to the mill report). This average value from the mill report was used when calculating the estimated fuse capacity for the pintles in the weak pintle tests (shown in bold). Coupons matching the anchors supplied for the weak pintle experiments were tested, and they exhibited yield and ultimate tensile strengths of approximately 120 and 143.5 ksi, respectively. Consequently, using mill report data for the pintles and coupon test data for the anchors, the estimated fuse capacity based on pintle shear strength was 120 kips, or about 59% of the estimate for pure shear yielding of the anchors for the weak pintle cases.

5.2.2 Friction Resistance

Contrary to the typical assumption of negligible friction, the observed influence of sliding resistance on fixed bearing response was significant relative to the influence of the steel fuse components (and, in particular, for the weak anchor cases). Mean values of sliding

force (determined from segments where the response does not indicate that the steel anchors are active in resisting shear), together with bracketed minimum and maximum values, and corresponding apparent friction coefficients when normalized by the target vertical load of 42 kips, are shown in Table 5.2 for the individual tests.

Table 5.2. Fixed Bearing Friction Resistance

Fuse Case		Weak Anchors		Weak Pintles	
Orientation		Long	Trans	Long	Trans
Sliding Force (kips)	*Min*	*7.6*	*7.6*	*9.4*	*4.7*
	Mean	**11.6**	**11.4**	**16.3**	**8.5**
	Max	*15.5*	*15.1*	*23.2*	*11.9*
μ	*Min*	*0.18*	*0.18*	*0.22*	*0.11*
	Mean	**0.28**	**0.27**	**0.39**	**0.20**
	Max	*0.37*	*0.36*	*0.55*	*0.28*

Sliding occurred at the interface of the masonry steel plate and the elastomeric leveling pad in all cases, although for the weak pintle cases the sliding response was complicated by crushing of concrete near the anchors. In the transverse orientation for weak pintles, in particular, the thin elastomeric pad was torn and ground into multiple pieces as the fractured anchor remnants were dragged through the concrete. Considering the dependency of the weak pintle test results on various mechanisms causing concrete damage, the values obtained for the weak pintle cases should be considered less reliable than the values for the weak anchor tests.

5.2.3 Observed Fuse Capacity

Calculations to compare observed and estimated fuse force capacities, accounting for the influence of friction, are provided in Table 5.3. Peak Force is the maximum absolute value of shear resistance obtained during each individual test. This force is reduced by the sliding resistance values shown in Table 5.2, and then compared with the estimated nominal capacity obtained from Eq. 5-1 (when neglecting friction), to obtain the percent difference of the observed capacity relative to the estimated nominal fuse capacity.

Table 5.3. Fixed Bearing Steel Component Resistance

Fuse Case		Weak Anchors		Weak Pintles	
Orientation		Long	Trans	Long	Trans
Peak Force (kips)		46.7	35.7	136	143
Steel Capacity (kips)	*Max*	*39.1*	*28.1*	*126.8*	*138.6*
	Mean	**35.2**	**24.4**	**120.0**	**134.8**
	Min	*31.2*	*20.7*	*113.1*	*131.4*
V_{fuse}, est. (kips)		31	31	120	120
% Difference @:	*Max*	*26%*	*-10%*	*6%*	*15%*
	Mean	**13%**	**-22%**	**0%**	**12%**
	Min	*1%*	*-34%*	*-6%*	*9%*

The longitudinal weak anchor test data indicates a range of estimated steel component capacity that bracketed the estimated fuse capacity that was determined when neglecting friction. Higher sliding friction is more likely to be representative of the response with anchors intact. The friction resistance observed in the excursions limited to peak displacements of 1 in. after rupture of both anchors averaged approximately 13 kips, suggesting that the steel contribution at fusing was likely about 33.7 kips, or about 8.6% higher than estimated from coupon tests. The transverse results did not provide a bracketed range for the estimated steel component contribution that would agree with the estimated available capacity. The likely cause of the difference between the longitudinal and transverse tests lies with the installation procedure. The anchors were drilled and epoxied into the concrete pad using HILTI HY-150 injected epoxy with the masonry plate in place. In both tests, one of the anchors was inadvertently installed with an excess of epoxy, resulting in epoxy being pushed upward to fill the space between the anchor and the hole in the masonry plate. For the longitudinal test, there was sufficient space around the other bolt and the pintles so that the bottom plate could rotate slightly in plan and engage both anchors. For the transverse test, however, the anchor with excess epoxy had to carry the full shear load (in excess of friction) until deforming sufficiently to close the gap at the other bolt hole. Consequently, one of the bolts was carrying a disproportionate share of the total shear when the peak capacity was achieved for this bearing, and the full strength of the other bolt was not realized, resulting in an observed capacity noticeably less than the estimated nominal strength. The strengths for the weak pintle cases are surprisingly close to the nominal value, but considering that neither orientation exhibited the intended mechanism corresponding to the estimated nominal strength, this outcome must be considered coincidental. Although it may be possible to proportion a fixed bearing to achieve reliable fusing response from pintle fracture, results from this experimental program indicate that anchor bolt fracture is the most reliable and predictable fusing mechanism.

CHAPTER 6 SUMMARY AND CONCLUSIONS

6.1 FUSE CAPACITY

6.1.2 Type I Bearing Retainers

Fuse force capacity has been defined as the actual peak force observed during the experiments for each bearing assembly, including contributions from the elastomeric bearing and resistance developed at retainer toes during overturning. Fuse capacities observed from the bearing and retainer tests were consistently higher than calculated estimates obtained per the current IDOT Bridge Manual (2012a). The discrepancy was strongly pronounced for transverse bridge response of Type I elastomeric bearings, with "overstrength" ratios (of observed experimental to computed nominal capacity) of approximately 3 to 3.5. For retainers at elastomeric bearings, the current Bridge Manual applies a ϕ factor of 0.75 to the pure *shear* capacity (60% of tension capacity) of steel anchors to approximately account for combined tension and shear loading. Determining estimated capacity solely from a reduced shear capacity of a steel anchor neglects two significant sources of resistance: the influence of vertical load carried by the retainer, and shear resistance at the retainer toe. The vertical load acting on the face of the retainer creates a moment demand counter to the overturning effect of the horizontal load, which reduces the amount of tension the anchor must carry to resist overturning. The shear at the toe is present for both Type I and Type II bearings, but it is more pronounced for Type I's, with the toe driving into concrete instead of sliding off the edge of a steel plate.

Furthermore, the Bridge Manual follows typical engineering practice of assuming minimum strength for specified material grades, but actual strength is unlikely to fall at the minimum threshold of acceptability for the specified material grade. For example, material supplied as Grade 36 is required to have tensile strength within the range of 58 to 80 ksi, and the tensile strength of the steel supplied for experiments was approximately 70 to 75 ksi. This led to a further increase in the capacity of the retainers. Finally, the elastomer itself will carry a small amount of shear as the bearing deforms to drive against the retainer. The combined effect of these influences resulted in observed (experimental) transverse strength equal to approximately 1.1 to 1.4 times the *tension* strength (which is itself 5/3 times the shear strength) of the anchor for Type I bearings. These coefficients are based on the actual strength of the supplied anchors, so when using minimum capacity for the specified material grades, their range increases to about 1.3 to 1.65 (of the tensile strength).

6.1.2 Type II Bearing Retainers

Transverse fuse capacities observed during testing for Type II bearings were lower than in Type I bearings, with overstrength ratios typically falling between 2.1 to 2.4. The primary difference between Type I and Type II retainers is the boundary condition at the toe. Type II bearing retainers are able to provide shear resistance based on friction only where the retainer is sliding off the edge of the bearing bottom plate, rather than being driven into concrete (as is typically the case for Type I retainers). A pure shear assumption corresponds more closely to observed strength for Type II bearings (as opposed to in Type I bearings). Observed capacity values were approximately 0.7 to 0.9 times the *tensile* strength, where a value of more like 0.6 would correspond to the pure shear capacity. These coefficients are based on the actual strength of the supplied anchors, so when minimum capacity is used for the specified material grades, the range increases to about 0.9 to 1.1.

6.1.3 Low-Profile Fixed Bearings

Overstrength ratios for the tested low-profile fixed bearings were higher than unity but to a lesser extent, with values of about 1.1 to 1.5. Fixed bearing capacity estimation can be improved by including frictional resistance in calculations of fuse capacity, which is neglected in the current version of the Bridge Manual. When experimentally comparing the two design options (weak anchors versus weak pintles), the anchors were found to provide a more reliable fusing mechanism, with less influence from the concrete. To maximize reliability of fixed bearings with weak anchors, the conditions at each anchor should be maintained as similar as is feasible (e.g., cast-in anchors and locate the bottom plate with holes centered on the anchors, or clean excess epoxy from anchors if post-installed).

6.2 SHEAR RESPONSE

6.2.1 Influence of Elastomer Compound

Shear response is a complex characteristic for elastomeric bearings, with multiple competing and counteracting influences from boundary and loading conditions. Apparent shear stiffness for both Type I and Type II bearings has been found experimentally to be influenced by peak strain demand and strain rate effects. Elastomer compounds are available for specialty applications offering a range of stress-strain characteristics. At one extreme, low-damping elastomers provide a response that is practically linear for a range of shear strains encompassing the anticipated structural demands. At the other extreme are high-damping elastomers, which have an initially high stiffness that transitions to a softened response, creating a source of hysteretic energy dissipation under cyclic loading. Bearing specifications used by IDOT do not explicitly require any particular damping characteristics.

One of the primary means of introducing higher damping characteristics to elastomers is by the addition of carbon black. According to the bearing supplier, carbon black was added to the bearings supplied for the experiments, consistent with the supplier's standard manufacturing practice, to achieve a target range of shear stiffness. Consequently, although the bearings are not specifically required to provide damping or intentionally manufactured to provide high-damping characteristics, the means of achieving a desired stiffness coincidentally resulted in tests exhibiting bilinear stress-strain response typical of high-damping bearings.

With a bilinear stiffness, the apparent linear stiffness will depend on the peak imposed shear strain. The softened stiffness branch becomes an increasingly dominant characteristic proportionately with maximum shear strain demand. For quasi-static tests, the observed stiffness at service-level strains (≤50% shear strain) was reasonably consistent with values reported by the manufacturer, but the apparent stiffness decreased as strains were increased to levels anticipated for seismic demands. Counteracting this effect, elastomer response exhibits some limited strain rate dependency so that stiffness increases with increasing strain rate. The strain rate sensitivity was found to be relatively more significant at low levels of strain demand.

6.2.2 Type II Bearing Response

For Type II bearings, slip at the PTFE interface limits the shear strain demand imposed on the elastomer. The experimental data indicate that the shear strain demand at increased strain rates will exceed the range typically permitted for service loading, resulting in reduced apparent stiffness, but this reduction is partially offset by stiffening of the elastomer associated with the increased strain rate. For seismic scenarios, the test data suggest that

the Type II bearing elastomer stiffness can be bounded in the range of approximately 65% to 100% of the value reported by the bearing manufacturer, with the lower values corresponding to lower strain rates at peak displacement cycles. The upper bound is likely to be a reasonable estimate for elastomer response during a seismic event, considering that the strain rate during an earthquake will almost certainly be higher than the maximum testing capability for the experiments.

6.2.3 Type I Bearing Response

For Type I bearings, the boundary condition at the bottom of the elastomer block introduces additional aspects of complexity to the mechanical response. At the bottom surface of Type I bearings is a simple contact interface of elastomer and concrete, as opposed to the fully bonded interface of elastomer and steel provided in Type II bearings. This boundary condition leads to three separate softening effects observed during the tests. First, the slip surface for Type I bearings is at this interface of elastomer and concrete instead of at the PTFE and stainless steel interface for Type II's. The slip force is higher between elastomer and concrete, so the Type I elastomer experiences greater shear force, greater shear strain, and a reduced apparent stiffness. Second, the shear and associated flexure in the elastomer cause the trailing edge to curl away from the concrete surface, reducing the surface area over which the shear traction acts on the bottom of the bearing. Consequently, the bottom layer of elastomer is only partially effective in resisting shear. Finally, when displacements are sufficient to induce slip at the concrete surface, abrasion of the elastomer on the concrete will remove a portion of the leading edge of the elastomer, further reducing the area available to resist shear.

Two aspects of elastomer response contribute stiffening effects, counteracting these softening effects. First, although elastomer material response softens at moderate strains (up to about 100% to 150%), the ultimate behavior of the elastomer exhibits significant stiffening prior to material rupture. Experimental slip tended to initiate at about 125% shear strain for relatively small vertical compression stresses of 200 psi. The slip threshold increased to about 200% for 500 psi but reached only about 250% for 800 psi. At the higher compression levels, the load-displacement response showed a slight stiffening branch. The net effect of the stiffening branch is to level off the effective apparent linear shear stiffness so that all bearing load levels converge to similar minima for an apparent linear shear stiffness prior to slip. Lastly, the Type I bearings exhibited strain rate sensitivity in the elastomer response, similar to the Type II bearings, but the effect tended to be overshadowed by other influences at the high strain demand levels that would be expected during an earthquake.

One final aspect that affects Type I bearings is a dependency on orientation of applied loading (longitudinal versus transverse bridge direction). The elastomer itself is not inherently sensitive to the direction of loading, and the bearings are short enough that stability effects are not significant. However, to the extent that curling of the trailing edge and loss of effective contact area through abrasion of the leading surface influence the response, the longitudinal orientation of bearing response tends to show higher apparent sensitivity to peak strain demand and incidence of slip with lower stiffness relative to similar tests conducted with a transverse orientation.

The elastomers exhibited sporadic variability between bearings that had nominally been constructed with identical materials and methods. Results were generally consistent for the transverse tests, but they varied more significantly for the bearings used for longitudinal tests. On the basis of the test data, bounding estimates for the effective shear modulus of Type I bearings at high strains are about 60% to 100% of the bearing supplier's documented

value for longitudinal motion and about 75% to 105% for transverse motion. These estimates are provided assuming that there will be few slip cycles. Also, these ranges have been adjusted to include a relative increase of 5% at the lower bound and 30% at the upper bound to approximate the influence of strain rate. With multiple slip cycles, the response degrades so that the ranges would fall to about 45% to 90% for longitudinal motion and about 50% to 80% for transverse motion.

6.3 SLIDING RESPONSE

6.3.1 Type I Bearings

For Type I bearings, sliding occurred between the reinforced elastomer block and the top surface of the concrete substructure. The experimental friction response of Type I bearings was influenced by several factors. Friction response of elastomers follows a non-linear inverse relationship with normal compression stress at the sliding interface (Schrage 1981). The roughness of the finished concrete surface contributes to the initial slip, but friction resistance degrades with increasing accumulation of slip as a small portion of the elastomer is transferred to the surface voids through abrasion, effectively smoothing the surface over the duration of an earthquake. Variation with accumulated slip appeared to be less significant than that resulting from applied compression and initial roughness of the concrete surface. Lastly, the sliding response also exhibited marked increases of initial breakaway friction coefficient when a bearing was subjected to an increased strain rate. The sliding friction observed during quasi-static tests appears to correlate reasonably well with kinetic friction during tests conducted at increased strain rates. The quasi-static friction coefficient (μ_{QS}) can be estimated according to

$$\mu_{QS} = 0.18 + \frac{54}{\sigma} - \frac{\sum \delta_{u_{slip}}}{3900} \qquad \text{(Eq. 6-1)}$$

where

σ = Average compression stress (psi)

$\sum \delta_{u_{slip}}$ = Total accumulated slip (in.)

The initial coefficient has been calibrated to the most common surface roughness used during the tests (a classification of 3 or 4 according to the International Concrete Repair Institute [ICRI] concrete surface profile [CSP] chips [ICRI 1997]), and yields a range of estimated sliding coefficients of approximately 0.45 to 0.25 from 200 to 800 psi average compression, respectively. The tests conducted at increased strain rates suggest that the breakaway slip coefficient may be approximately 33% higher than the sliding coefficient.

Type I bearings were seen to be remarkably resilient when subjected to extensive sliding cycles. No delamination was evident at the shims or at the thick top plate, although the leading edge of the bottom shim was exposed by abrasion during the cyclic test of a 7c bearing at 800 psi average compression. It is challenging to establish an upper bound of friction for Type I bearings that might precipitate a delamination at the reinforced elastomeric block because only a peel test is required for IDOT standard specifications, which does not capture the true shear rupture limit at the bond between elastomer and steel plates. However, the unseating tests performed on Type II bearings provide some insight into the

vulcanized bond strength between the elastomer and steel elements. Shear rupture of the elastomer occurred only for the unseated Type II bearings when one anchor failed, resulting in a rotated configuration for the bottom plate on the concrete and causing a stress concentration at one corner of the elastomer. The calculated shear stresses for the unseated Type II bearings suggest that the coefficient of friction would likely need to reach a value higher than unity in order to pose a threat of elastomer delamination for Type I bearings. All observed friction between elastomer and concrete was limited to values less than 0.55, even for unusually rough concrete surfaces, so it is unlikely that delamination would occur for Type I bearings as currently specified and fabricated, even when accounting for amplification from strain rate effects.

6.3.2 Type II Bearings

For Type II bearings, sliding occurred between PTFE and a stainless steel mating surface, although for large displacements the PTFE would become delaminated and progressively removed from the middle plate until sliding occurred between two steel surfaces. Generally, limited sliding of the top plate sufficient to partially expose the PTFE did not lead to damage of the PTFE surface during testing. Only one bearing, the Type II 9a, appeared to include a surface deformity at one location along the weld line connecting the stainless steel to the top plate large enough to damage the PTFE surface.

Similarly to the interaction of elastomer on concrete, the coefficient of friction at the PTFE surface is sensitive to compression stress and sliding rate. The coefficient of friction is required to be less than 0.07 according to IDOT Specifications (2012b), but during an earthquake, the PTFE sliding resistance will increase as a result of the slip rate. For the Type II 9a, 11a, and 13a bearings, the coefficient of friction at instantaneous slip rates greater than 3 in./sec ranged from about 0.12 to 0.18.

6.3.3 Low-Profile Fixed Bearings

For the low-profile fixed bearings, a thin elastomeric leveling pad was installed between the bottom steel plate and the top surface of the concrete substructure. Sliding ultimately occurred between the bottom steel plate and this elastomeric leveling pad in all test cases. For the preferred case of fusing anchors and intact pintles, the sliding coefficient of friction may be bounded approximately by 0.2 and 0.35.

REFERENCES

American Association of State Highway and Transportation Officials (AASHTO). 2010. *Guide Specifications for Seismic Isolation Design, 3rd Edition*, Washington, D.C.

American Association of State Highway and Transportation Officials (AASHTO). 2012. *LRFD Bridge Design Specifications*, Washington, D.C.

Ash, C., J. Schwartz, M. Aschheim, N. Hawkins, and B. Gamble. 2002. *Evaluation of Elastomeric Bearings for Seismic Design*. Final Report, ITRC FR 99-4. Urbana, IL: University of Illinois at Urbana-Champaign, November.

ASTM International (ASTM). 2007. *Standard Specification for Plain and Steel-Laminated Elastomeric Bearings for Bridges, Designation: D 4014-03*, West Conshohocken, PA.

ASTM International (ASTM). 2008. *Standard Test Methods for Tension Testing of Metallic Materials, Designation: E 8-08*, West Conshohocken, PA.

American Concrete Institute (ACI). 2011*. Building Code Requirements for Structural Concrete (ACI 318-11) and Commentary*. American Concrete Institute, June.

Constantinou, M.C., A . Mokha, and A. Reinhorn. 1990. "Teflon bearings in base isolation II: Modeling." *Journal of Structural Engineering* 116(2):455–474.

Highway Innovative Technology Evaluation Center (HITEC). 1996. *Guidelines for the Testing of Seismic Isolation and Energy Dissipating Devices*, American Society of Civil Engineers, Reston, VA.

Illinois Department of Transportation (IDOT). 2012a. *Bridge Manual*. Springfield, IL.

Illinois Department of Transportation (IDOT). 2012b. *Standard Specification for Road and Bridge Construction*, Springfield, IL.

International Concrete Repair Institute (ICRI). 1997. Concrete Surface Profile Chips, http://www.icri.org//bookstore/launchCatalog.asp?ItemID=PC.

Konstantinidis, D., J.M. Kelly, and N. Makris. 2008. *Experimental Investigations on the Seismic Response of Bridge Bearings*, Earthquake Engineering Research Center, Report No. EERC 2008-02, College of Engineering, University of California, Berkeley, CA.

Kulak, R.F., and T.H. Hughes. 1992. "Mechanical tests for validation of seismic isolation elastomer constitutive models." In *DOE Facilities Programs, Systems Interaction, and Active/Inactive Damping,* C.-W. Lin et al., eds., ASME Publication PVP Vol. 229, 41–46.

Ma, X., E. Borchers, A. Pena, H. Krawinkler, S. Billington, and G. Deierlein. 2011. Design and Behavior of Steel Shear Plates with Openings as Energy Dissipating Fuses, John A. Blume Earthquake Engineering Center, Report No. 173, Department of Civil and Environmental Engineering, Stanford University, Stanford, CA.

Malaysian Rubber Producers' Research Association (MRPRA). 1980. *Natural Rubber Engineering Data Sheet: EDS 16*, Malaysian Rubber Research and Development Board Organization, England.

Mander J.B., D.K. Kim, S.S. Chen, and G.J. Premus. 1996. *Response of Steel Bridge Bearings to Reversed Cyclic Loading*. Report NCEER-96-0014, State University of New York at Buffalo, Buffalo, NY

McDonald, J., E. Heymsfield, and R.R. Avent. 2000. “Slippage of neoprene bridge bearings.” *Journal of Bridge Engineering* 5(3):216–223.

Mokha, A., M. Constantinou, and A. Reinhorn. 1990. “Teflon bearings in base isolation I: Testing.” *Journal of Structural Engineering* 116(2):438–454.

Mori, A., A.J. Carr, N. Cooke, and P.J. Moss. 1996. “Compression behaviour of bridge bearings used for seismic isolation.” *Engineering Structures* 18(5):351–362.

Mori, A., P.J. Moss, N. Cooke, and A.J. Carr. 1999. “The behavior of bearings used for seismic isolation under shear and axial load.” *Earthquake Spectra* 15(2):199–224.

Muscarella, J.V., and J.A. Yura. 1995. *An Experimental Study of Elastomeric Bridge Bearings with Design Recommendations.* Research Report No. 1304-3, Center for Transportation Research, Bureau of Engineering Research, The University of Texas at Austin, Austin, TX.

Roeder, C.W., and J.F. Stanton. 1983. “Elastomeric bearings: State-of-the-art.” *Journal of Structural Engineering* 109(12):2853–2871.

Roeder, C.W., and J.F. Stanton. 1991. “State-of-the-art elastomeric bridge bearing design.” *ACI Structural Journal* 88(1):31–41.

Roeder, C.W., J.F. Stanton, and A.W. Taylor. 1987. *Performance of Elastomeric Bearings*. National Cooperative Highway Research Program 298. Washington, D.C: Transportation Research Board.

Schrage, I. 1981. *Anchoring of Bearings by Friction.* Special Publication SP70-12, American Concrete Institute (ACI), Detroit, MI, 197–215.

Shenton, H.W. 1996. *Guidelines for Pre-Qualification, Prototype and Quality Control Testing of Seismic Isolation Systems*, National Institute of Standards and Technology (NIST), Gaithersburg, MD.

Stanton, J.F., and C.W. Roeder. 1982. *Elastomeric Bearings Design, Construction, and Materials*. National Cooperative Highway Research Program 248. Washington, D.C: Transportation Research Board, National Research Council.

Stanton, J.F., and C.W Roeder. 1983. “Elastomeric Bridge Bearings Specifications: Review of the Present and Proposals for the Future.” *ACI Journal Proceedings* 80: November 1.

APPENDIX A SUPPLEMENTARY TYPE I BEARINGS EXPERIMENTAL RESEARCH RESULTS

A.1 QUASI-STATIC MONOTONIC LONGITUDINAL TEST RESULTS

Response characteristics for the individual tests are summarized in Table A.1. All tests except Test 1 included a controlled unloading ramp from peak displacement. The observed characteristics of the loading and unloading ramps are provided on separate rows of the table. The effective apparent shear stiffness is the measured linear stiffness from the initiation of the test until a deviation of the response from linear shear strain to a sliding response. The linear shear strain range indicates the range from the start of a ramp either to the end of the ramp, or to the initiation of slip, and corresponds to the displacement range used to determine the effective apparent shear stiffness. Effective apparent shear modulus is the shear modulus associated with the measured shear stiffness. The coefficients of friction are determined from the ratio of horizontal to vertical force at each data point during slip, with the mean value determined with respect to slip travel, similarly to the slip resistance value.

Table A.1. Summary Data for Quasi-Static Longitudinal Monotonic Type I Bearing Tests

Test ID	Effective Apparent Shear Stiffness	Mean Slip Resistance	Effective Apparent Shear Modulus	Coefficient of Friction		Linear Shear Strain Range
	k / in	kips	psi	peak	mean sliding	%
1	4.21	14.5	94	0.42	0.35	215
2	3.40	13.2	76	0.38	0.31	220
	3.74	0.0	84	0.00	0.00	186
3	3.03	12.6	68	0.34	0.30	223
	3.57	0.0	80	0.00	0.00	200
3x1	3.40	12.3	76	0.32	0.29	212
	3.87	0.0	86	0.00	0.00	143
3x2	2.93	9.7	65	0.34	0.31	196
	3.26	0.0	73	0.00	0.00	150
3x3	2.61	6.4	58	0.40	0.38	144
	3.29	0.0	73	0.00	0.00	125
3x4	3.22	11.8	72	0.31	0.28	214
	3.82	0.0	85	0.00	0.00	174
3x6	3.00	11.2	67	0.30	0.27	228
	3.34	0.0	75	0.00	0.00	175
3x7	3.09	12.2	69	0.34	0.29	239
	3.44	0.0	77	0.00	0.00	200
7c mean @ 500 psi	3.47	12.5	77	0.34	0.30	202
8x1	6.57	30.5	79	0.36	0.31	158
	8.75	0.0	105	0.00	0.00	99

A.2 INCREASED STRAIN RATE INFLUENCE ON TYPE I BEARING RESPONSE

Figure A.1 shows the non-dimensional form of the force-displacement response for a cyclic test.

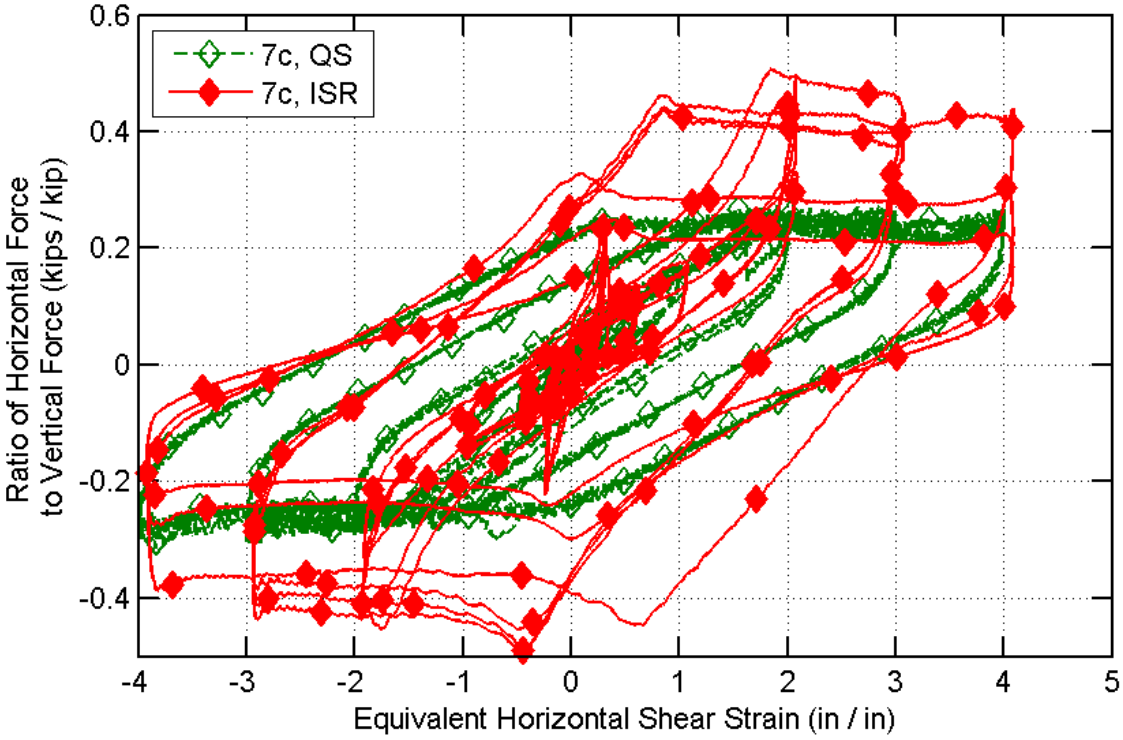

Figure A.1. Non-dimensional cyclic Type I constitutive response, longitudinal orientation, with increased strain rate.

A.3 SINGLE RETAINER TEST RESULTS

The force-displacement responses obtained from the single retainer tests are provided in Figure A.2 with the horizontal axis adjusted to account for the total height of rubber of the associated bearing. Single retainer tests were performed without a bearing installed to support a simulated gravity load, and the control program did not impose vertical load constraints during the test. Consequently, a vertical load was induced as the retainer was pushed over. The magnitude of the vertical reaction was significant, especially in the case of the 13c retainers. Data recorded for the induced vertical load is presented in Figure A.3. Note that the 13c retainers were designed to correspond to a dead load of 100 kips on the 13c bearing, so the induced vertical reactions suggest that the bearing will lift off of the concrete surface as the retainer is pushed over.

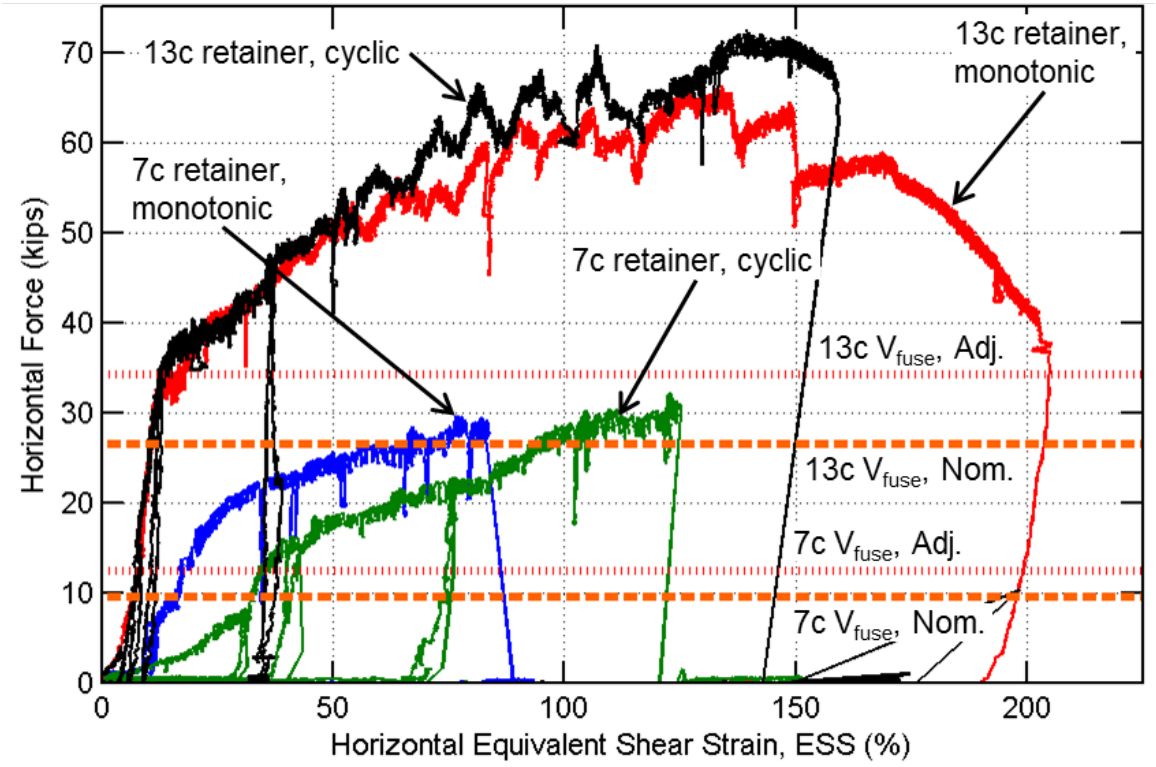

Figure A.2. Horizontal force versus equivalent shear strain of associated bearing size for single retainer tests.

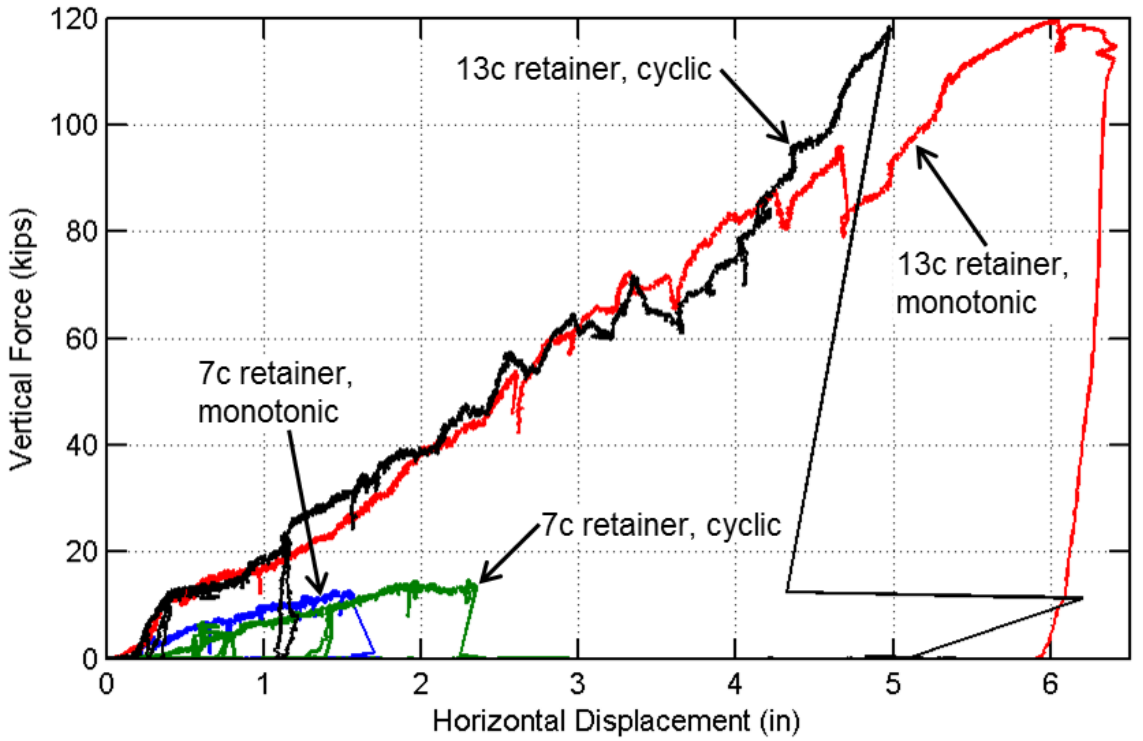

Figure A.3. Vertical force versus displacement for single retainer tests.

A.4 QUASI-STATIC CYCLIC TRANSVERSE TEST RESULTS

A.4.1 General Force-Displacement Response

Individual test results for each bearing size are provided in Figure A.4 through Figure A.7.

A.4.1.1 7c Bearing

Test results for the smallest bearing, a 7c according to IDOT nomenclature, are shown in Figure A.4. With a vertical load of 42 kips (corresponding to 500 psi), the fuse capacity was 0.83 and 0.80 times the vertical load in the (+) and (-) directions, respectively, well in excess of the target capacity of 0.2 times the vertical load. In the (+) direction, the retainer contributed additional resistance up to about 85% shear strain, compared to about 53% shear strain in the (-) direction. The discrepancy reflects an additional amount of travel required in the (+) direction to fully engage the retainer. Such discrepancies are representative of realistic effects to be expected in the field, where anchors may be slightly different distances from the sides of the bearing, the holes in retainer bases may not be identically centered on the anchors, and the retainer may not be perfectly aligned parallel to the bearing face.

Regardless of the slight discrepancies in the two directions, the overall response is dominated by an abrupt rupture of the anchor, followed by a transition to a stable hysteretic sliding response similar to that observed in the longitudinal orientation. Investigation of the rupture planes for the anchors showed that the anchors failed near the concrete surface, leaving small indentations in the surface where the bearing would travel for large displacement demands. The testing protocol was modified for this bearing to investigate what effect the failed anchors would have on the bearing, because the original record, limited to 400% ESS, would only take the edge of the bearing near the anchor installation positions, but would not force the bearing to travel over any protruding post-fusing remnants of the anchor that might extend above the concrete, or a crater or crushed concrete depression (if such existed). Therefore, the final two cycles of the testing protocol were increased from 400% to 500% and 600%. The results show that there are only slight increases in the resistance when the bearing travelled over the remnants of the anchors.

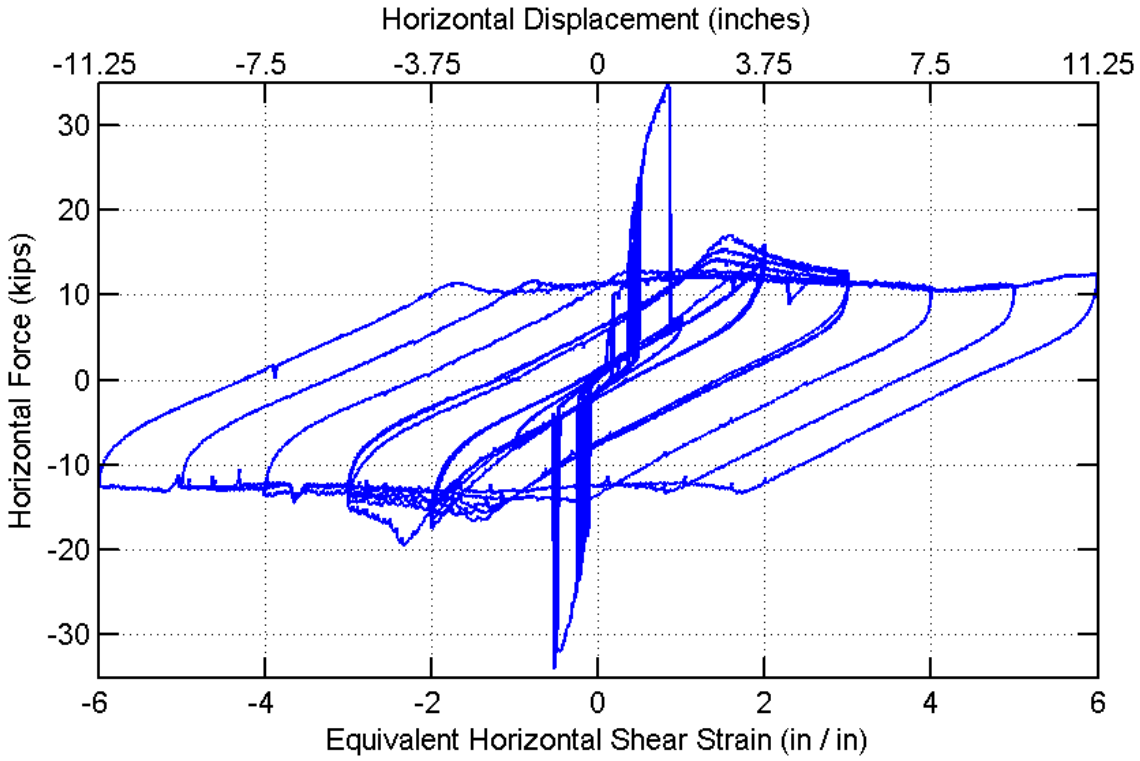

Figure A.4. Force versus displacement of Type I 7c bearing for transverse orientation.

A.4.1.2 9c Bearing

Results of the transverse Type I 9c bearing test are shown in Figure A.5. The fuse capacities in the two directions were very similar, at 0.97 and 0.98 times the vertical load. The (+) direction was again more ductile, with anchor rupture occurring at about 86% shear strain, compared to about 66% in the (-) direction. Although the increases in fuse capacity and ductility to anchor rupture were only slightly higher than for the 7c, the behavior shortly after anchor rupture was markedly different. For the 7c, the toes of the retainers only planted into the concrete sufficiently to engage the full stiffness of the bearing / anchor / retainer assembly, and the retainer was kicked away from the bearing upon anchor rupture, leaving the bearing free to slide unobstructed. For the 9c, the toe planted more deeply into the concrete, and even after the anchor ruptured, the retainer was left standing, and tilted forward. In the (-) direction, the retainer was not as severely rotated as in the (+) direction, and the bearing pushed the retainer along the top surface of the concrete so that the toe dug a small trough in the concrete surface. The influence of this mechanism is seen in the secondary peaks that developed in the response plot between the anchor failure and -200% ESS.

In the (+) direction, the secondary peak is also a consequence of more severe toe embedment than had been observed for the 7c, but the physical mechanism was quite different. Because the toe had planted so deeply in the (+) direction, the retainer was not immediately kicked out with the anchor rupture, and when the bearing drove to a new peak displacement, the retainer acted as a strut and carried the bearing so that the elastomer was entirely lifted off of the concrete. This is seen in the data with the secondary peak in the (+) direction starting at about 100% shear strain. The resulting mechanical arrangement was sufficient to induce a residual lateral force acting between the uppermost steel shim and the rotated heel of the retainer when the cycle reversed and the bearing was set back down on

the concrete, causing the retainer to kick out from the bearing when the lateral load was sufficient to overcome the vertical load that had not yet transferred back to the elastomer from the retainer. In both the (+) and (-) directions, these unusual mechanical responses were resolved after only one cycle, and the response transitioned to the typical stable sliding response exhibited by the transverse 7c and the longitudinal tests for the remaining cycles.

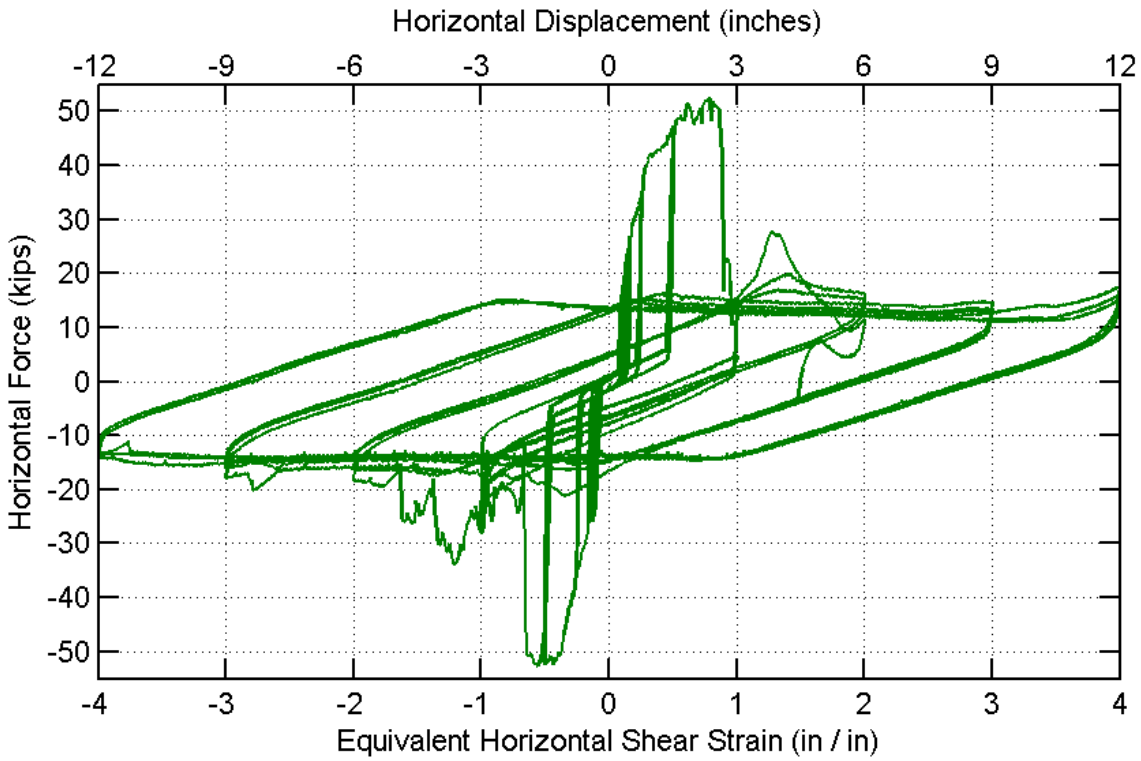

Figure A.5. Force versus displacement of Type I 9c bearing for transverse orientation.

A.4.1.3 11b Bearing

Results of the transverse Type I 11b bearing test are shown in Figure A.6. With a vertical load of 88 kips corresponding to 500 psi, the fuse capacity was similar for the two directions, at 0.89 and 0.87 times the vertical load in the (+) and (-) directions, respectively. Similar to the 7c and 9c bearings, the anchor ruptures occurred during the transition from 50% to 100% shear strain demand, at 63% shear strain for the (+) direction, and 59% shear strain for the (-) direction. The transition to a stable sliding hysteresis was purely a result of steel anchor failure, similar to the behavior observed with the 7c bearing, without complications introduced by excessive penetration of the retainer toes into the concrete. The concrete surface was slightly rougher than for other Type I bearing tests. For other tests, the roughness of the surface was estimated at about CSP 2 or 3, using International Concrete Repair Institute (ICRI, 1997) Concrete Surface Profile (CSP) chips. For the 11b bearing test, however, the concrete surface was approximately 4 or 5. The increased surface roughness is likely the dominant influence which led to a relatively high maximum friction coefficient of 0.53 in the (-) direction and a subsequent value of 0.48 in the (+) direction upon reversal. As the elastomer was ground against the roughened concrete surface, the surface imperfections were progressively in-filled with elastomeric material freed from the main bearing block by abrasion, and the frictional resistance converged to a proportion of approximately 25% to 30% of the vertical load, similar to other Type I bearing tests.

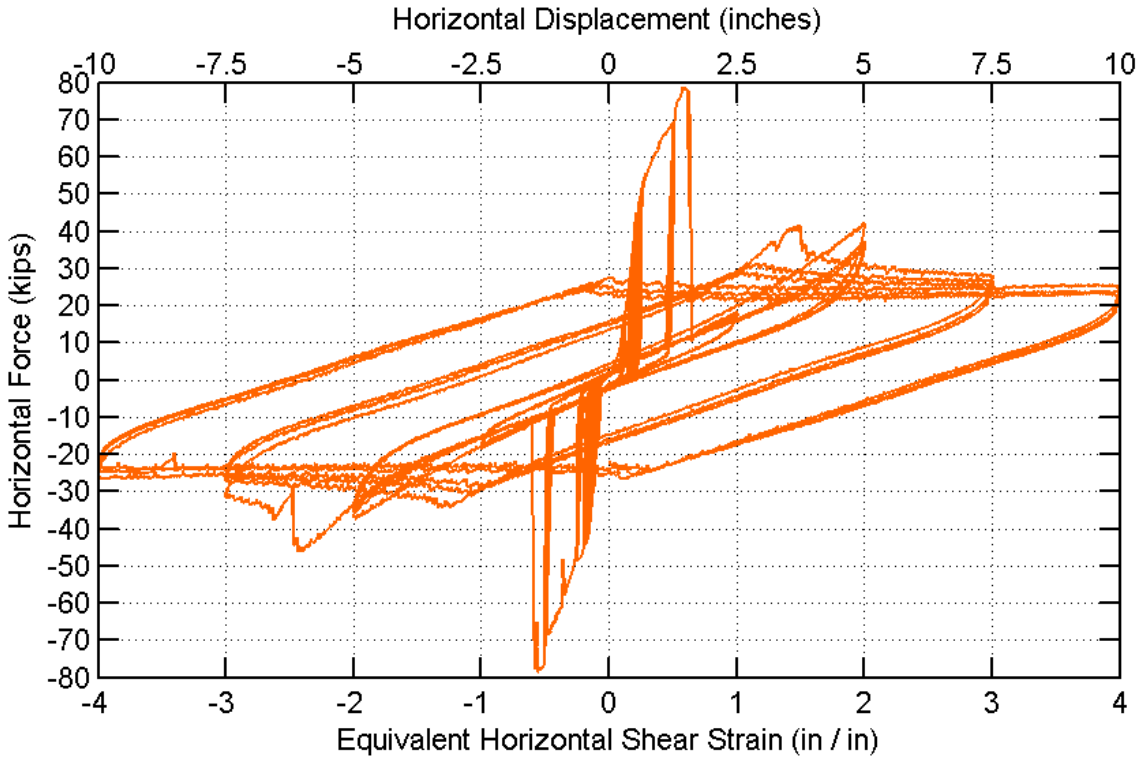

Figure A.6. Force versus displacement of Type I 11b bearing for transverse orientation.

A.4.1.4 13c Bearing

The largest bearing tested was a 13c, which resulted in the hysteretic response shown in Figure A.7. This test was performed with a vertical load of 100 kips (385 psi), to ensure that the experiment would not damage the testing equipment. As with the 9c, the fuse capacities were nearly identical at 0.94 times the vertical load in each direction. As the single retainer tests had predicted, the response was far more ductile for the 13c than with the smaller bearings and retainers. Peak fuse capacity was achieved at about 100% shear strain in each direction, but the anchors did not rupture until the second 300% ESS cycle, after surviving the first full +/- 300% ESS cycle.

The mechanical response of the retainers was much different for the 13c than for the 7c or 9c. In the case of the 13c, crushing of the concrete at the retainer toe was so extreme that the retainer and the upper portion of the anchor were bent over almost perpendicular to the initial configuration. The mechanical interactions of the bearing and retainers became highly complex as the test evolved. In the early-to-moderate stages of the retainer response, the primary difference compared to the previous tests was that the bearing tended to partially lift off of the concrete. The effect was not as severe as the 9c initial +200% excursion, but it was sufficient to allow the base of the bearing to slip forward as the vertical load reduced and the corresponding friction restraint diminished between the elastomer and concrete.

The effect was also most pronounced for the first excursion to a new peak displacement, and so each set of three cycles at +/- 200% and +/- 300% ESS displacement demand is characterized by an initial cycle which appears to stiffen and slide more early than the following cycles at the same displacement level. In the repeated cycles, the bearing does not lift off of the concrete as it approaches the peak demand, and so the reversal is

characterized by first unloading the shear deformation that had been required to initiate sliding, as is typical. For the first cycle, however, that deformation had been relieved as the bearing was partially lifted off of the concrete.

Another mechanism that developed during this test, which could not have been predicted or anticipated with a single retainer test, was how the bearing interacted with the retainer at large displacements. When the retainer was bent over severely and the toe was driven into the concrete, the bearing contacted the retainer by driving the upper steel shim against the heel of the retainer, instead of by driving the thick top plate against the initially vertical face of the retainer. Investigations of the contact areas on the bearing after the test showed that the elastomer had been permanently damaged by plastic deformations in the shims, and cracks and permanent bulges in the surface of the elastomer.

The fracture surface for the 13c bearing anchors was close to the nut, rather than deep in the concrete as had been observed from the single retainer test. Consequently, the bearing traveled over the remnant of the bent-over anchor during the +/- 400% cycles. There was a noticeable increase in the sliding resistance in those ranges of displacement demand, up to about 33% more than typical sliding resistance, but the increase diminished rapidly with repeated cycles. Examination of the bearing after the test showed that the bottom layer of elastomer had been torn and the lowest steel shim had been permanently bent to curve over the anchor remnant.

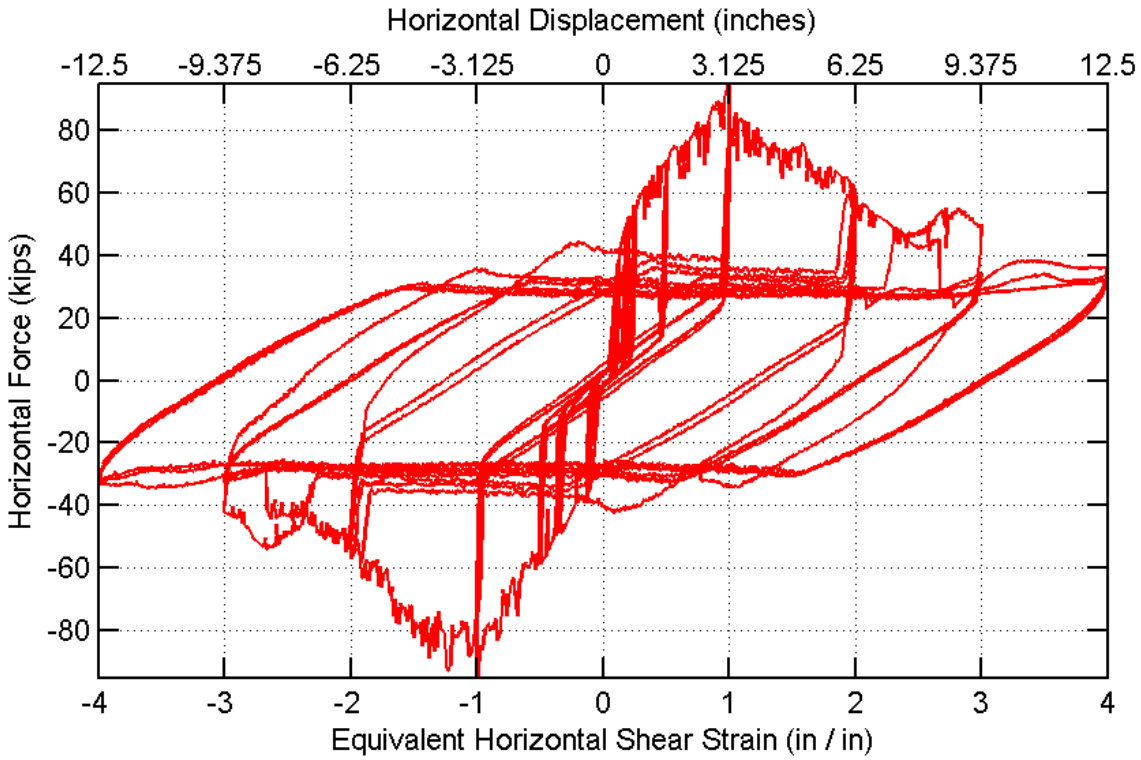

Figure A.7. Force versus displacement of Type I 13c bearing for transverse orientation.

APPENDIX B SUPPLEMENTARY TYPE II BEARINGS EXPERIMENTAL RESULTS

B.1 TRANSVERSE RESPONSE WITH RETAINERS

Figure B.1 through Figure B.4 show plots of the force-displacement response for each of the Type II bearings with retainers.

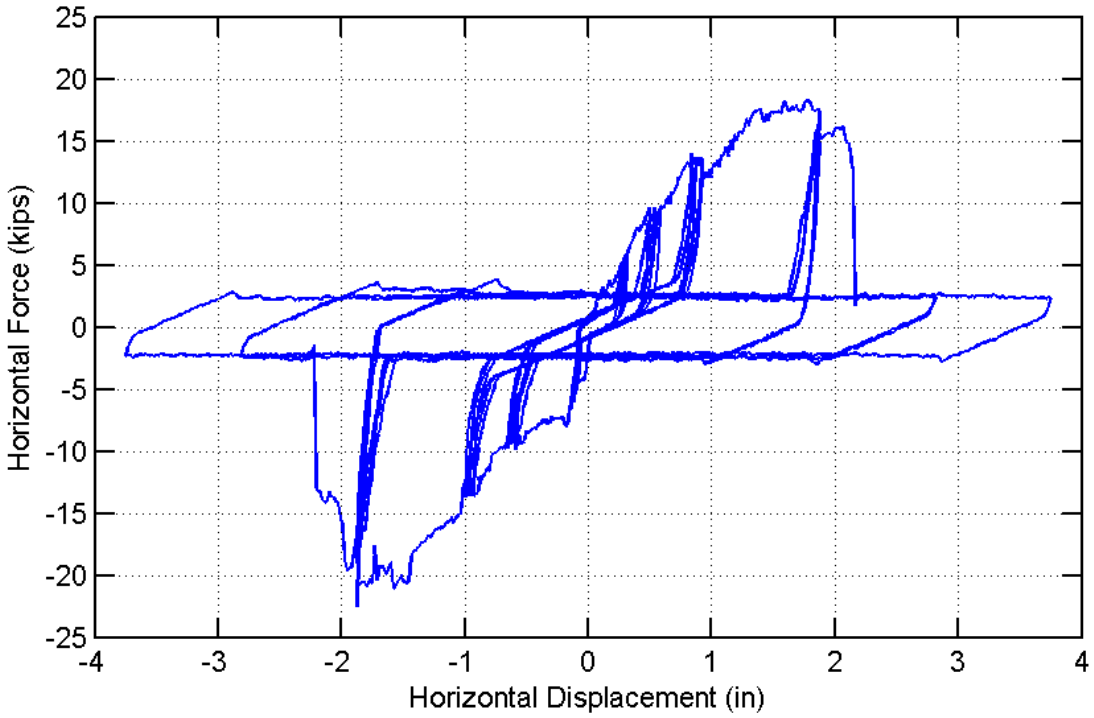

Figure B.1. Force versus displacement response for transverse Type II 7c with retainers.

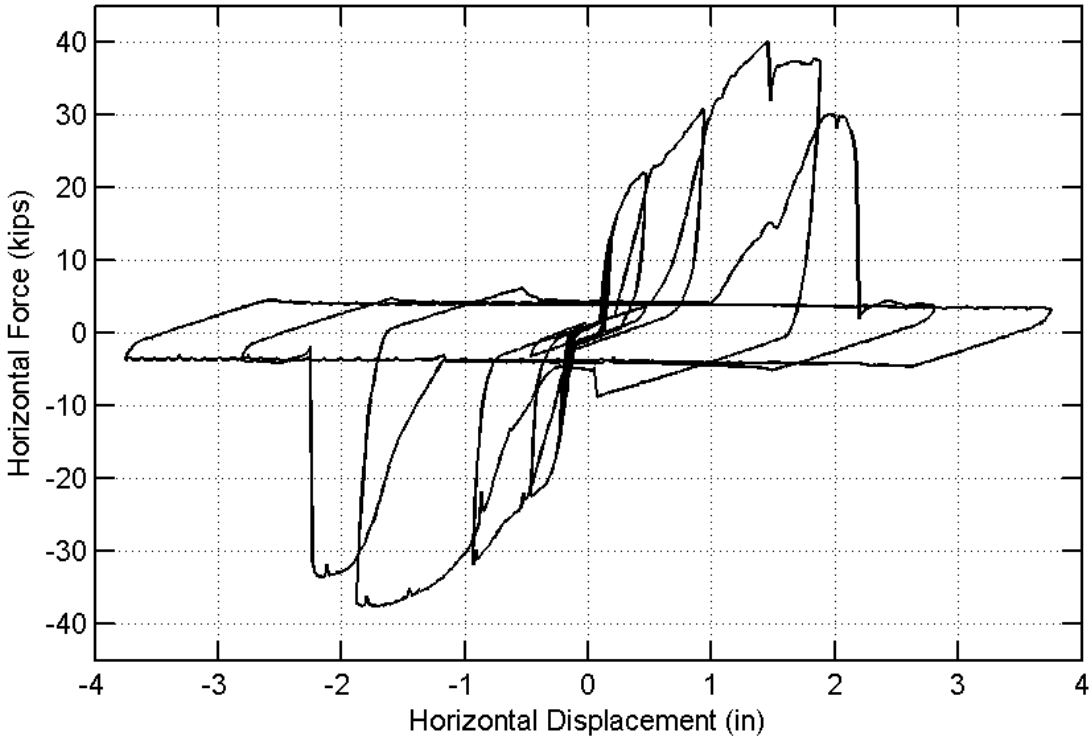

Figure B.2. Force versus displacement response for transverse Type II 9a with retainers.

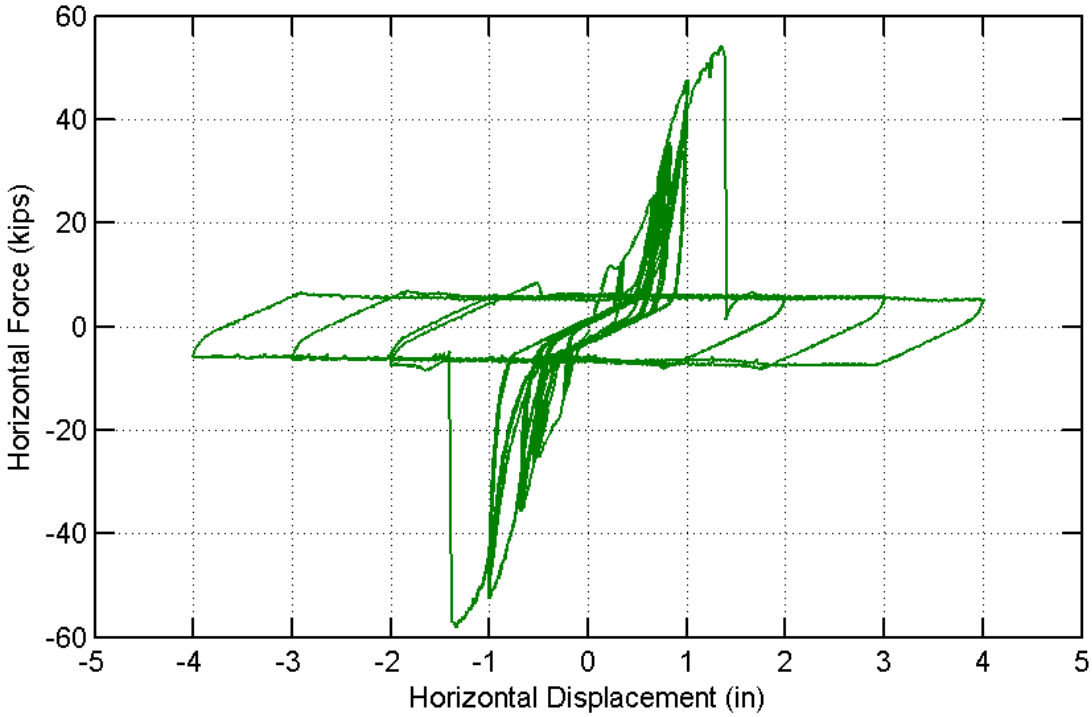

Figure B.3. Force versus displacement response for transverse Type II 11a with retainers.

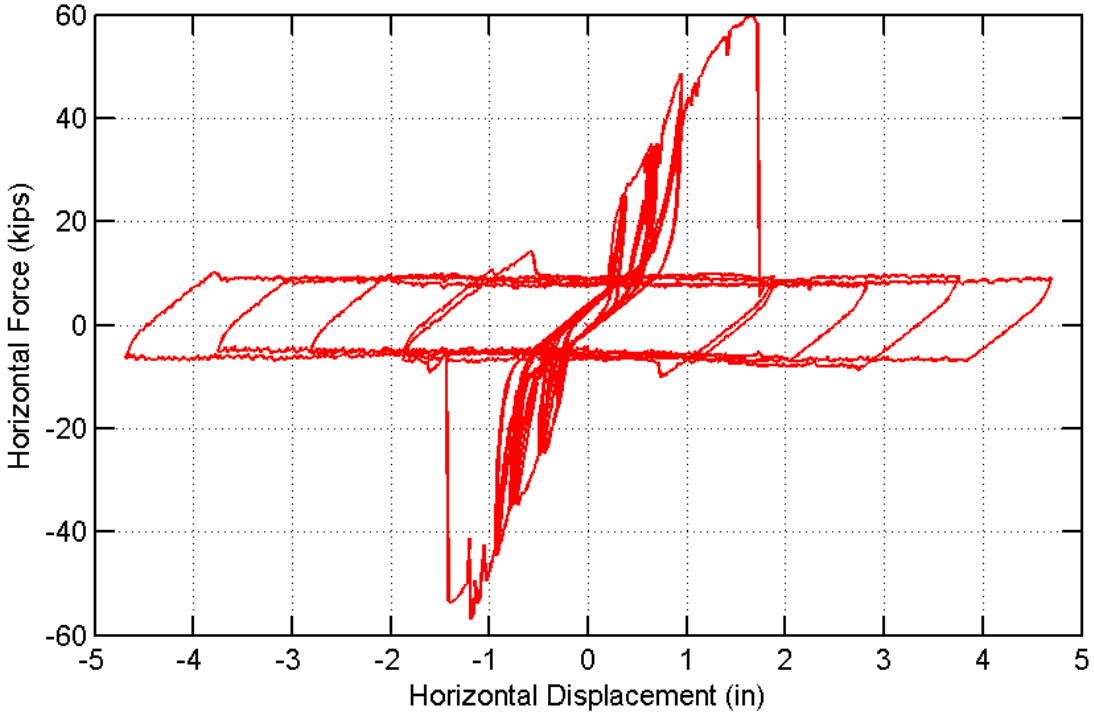

Figure B.4. Force versus displacement response for transverse Type II 13a with retainers.

B.2 PTFE INCREASED STRAIN RATE RESPONSE

B.2.1 General Force-Displacement Response

B.2.1.1 Type II 7c, Longitudinal Orientation

Force-displacement test results for ISR tests performed on two Type II 7c bearings with a longitudinal orientation are shown in Figure B.5.

.B.2.1.2 Type II 7c, Transverse Orientation

Force-displacement test results for ISR tests performed on a single Type II 7c bearing with a transverse orientation are shown in Figure B.6.

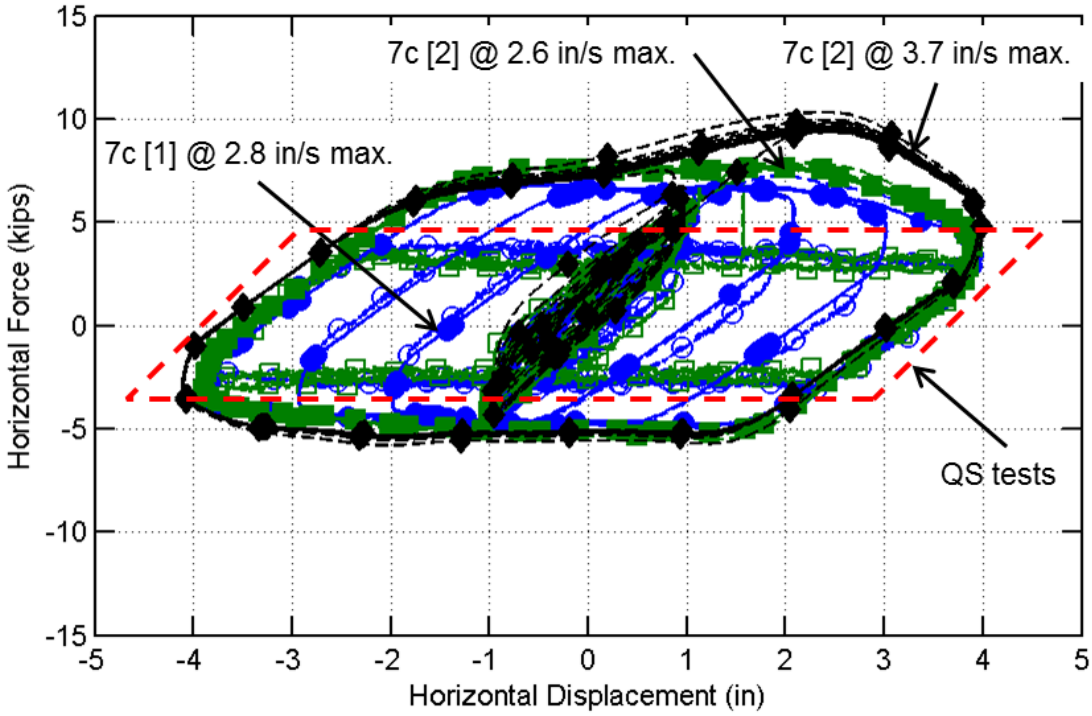

Figure B.5. Type II 7c force vs. displacement response, longitudinal orientation.

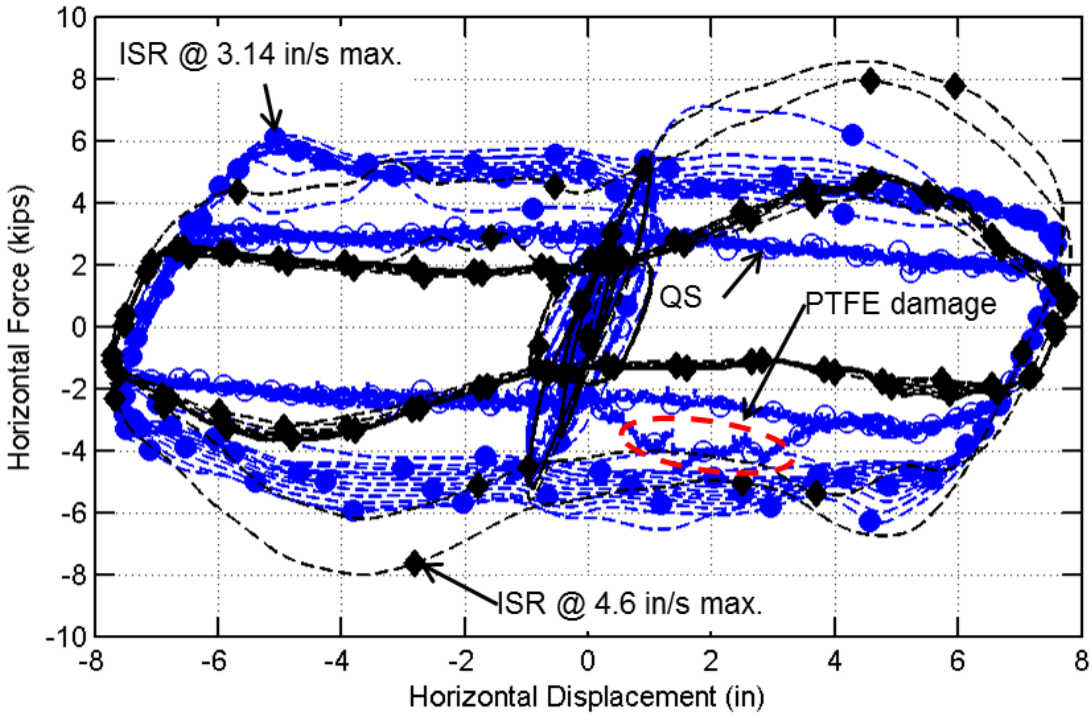

Figure B.6. Type II 7c force vs. displacement response, transverse orientation.

B.2.1.3 Type II 9a, Transverse Orientation

One ISR test was performed on a single Type II 9a bearing with a transverse orientation. The force versus displacement response is shown in Figure B.7 and in a non-dimensional form in Figure B.8. The “a” height Type II bearings were subjected to multiple tests, and the PTFE ISR response was limited to moderate displacements in an effort to preserve the PTFE surface for subsequent tests. Consequently, the peak displacement demand was limited to 200% ESS, rather than the 400% that had been used for the 7c and had resulted in severe damage to the PTFE sheet. Slip rates for the QS pretest were about 0.04 in. / sec. The ISR test followed the standard Type II ISR protocol indicated in Chapter 2, and the test was performed at a target of 4.0 in. / sec, resulting in an observed maximum slip rate of 4.18 in. / sec. The target vertical load was 54 kips, and the imposed load varied between 46.9 and 69.1 kips for the ISR test. The average normal stress was about 0.75 ksi on the PTFE surface at the start of each test, and estimates of the average stress values ranged from about 0.71 ksi up to 0.98 ksi for the QS pretest, and from about 0.66 ksi up to 1.12 ksi for the ISR test.

B.2.1.4 Type II 11a, Transverse Orientation

One ISR test was performed on a single Type II 11a bearing with a transverse orientation. The force versus displacement response is shown in Figure B.9 and in a non-dimensional form in Figure B.10. Similar to the Type II 9a test, the peak displacement demand was limited to 200% ESS to preserve the PTFE sheet. Slip rates for the QS pretest were about 0.08 in. / sec. The ISR test followed the standard Type II ISR protocol indicated in Chapter 2, and the test was performed at a target of 4.0 in. / sec, resulting in an observed maximum slip rate of 3.86 in. / sec. The target vertical load was 88 kips, and the imposed load varied between 74.4 and 105 kips for the ISR test. The average normal stress was about 0.69 ksi on the PTFE surface at the start of each test, and estimates of the average stress values ranged from about 0.66 ksi up to 0.85 ksi for the QS pretest, and from about 0.58 ksi up to 0.93 ksi for the ISR test.

B.2.1.5 Type II 13a, Transverse Orientation

One ISR test was performed on a single Type II 13a bearing with a transverse orientation. The force versus displacement response is shown in Figure B.11 and in a non-dimensional form in Figure B.12. Similar to the Type II 9a test, the peak displacement demand was limited to 250% ESS to preserve the PTFE sheet. Slip rates for the QS pretest were about 0.10 in. / sec. The ISR test followed the standard Type II ISR protocol indicated in Chapter 2, and the test was performed at a target of 4.0 in. / sec, resulting in an observed maximum slip rate of 4.06 in. / sec. The target vertical load was 100 kips, and the imposed load varied between 89.9 and 114 kips for the ISR test. The average normal stress was about 0.50 ksi on the PTFE surface at the start of each test, and estimates of the average stress values ranged from about 0.48 ksi up to 0.62 ksi for the QS pretest, and from about 0.45 ksi up to 0.67 ksi for the ISR test.

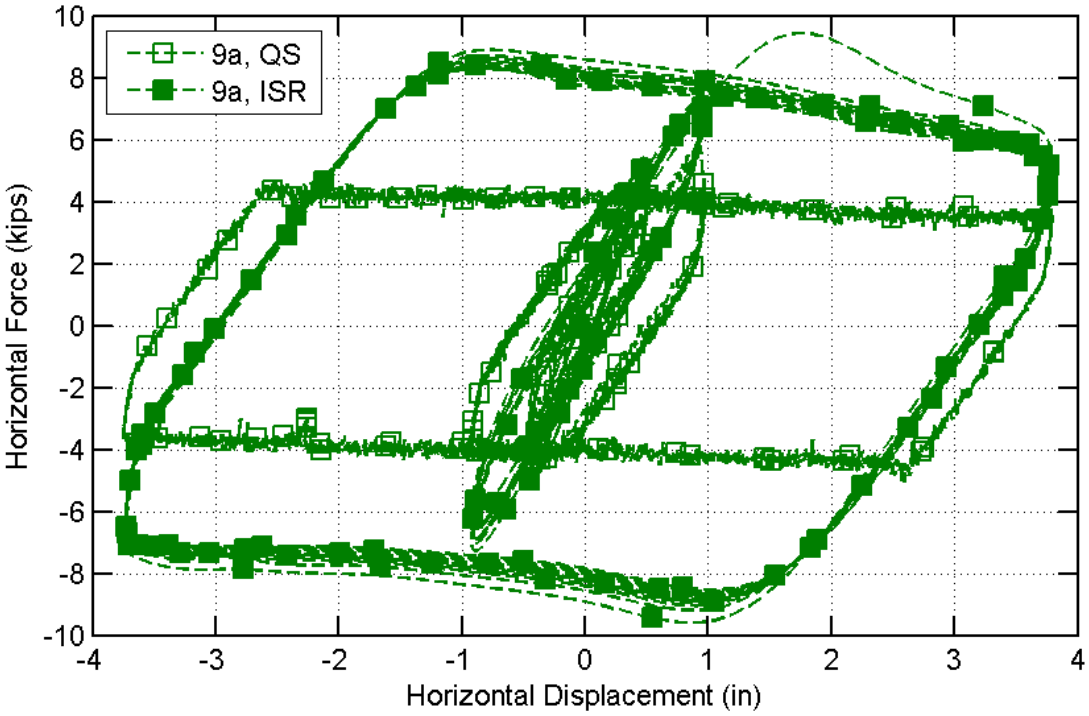

Figure B.7. Type II 9a force vs. displacement response, transverse orientation.

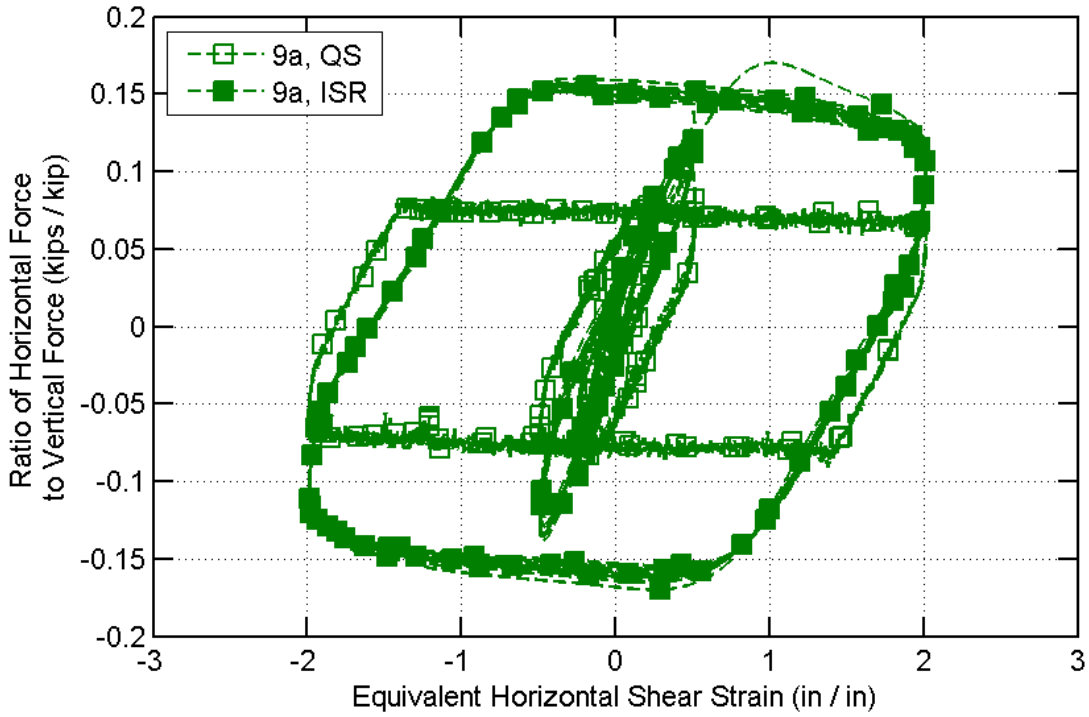

Figure B.8. Non-dimensional Type II 9a constitutive response, transverse orientation.

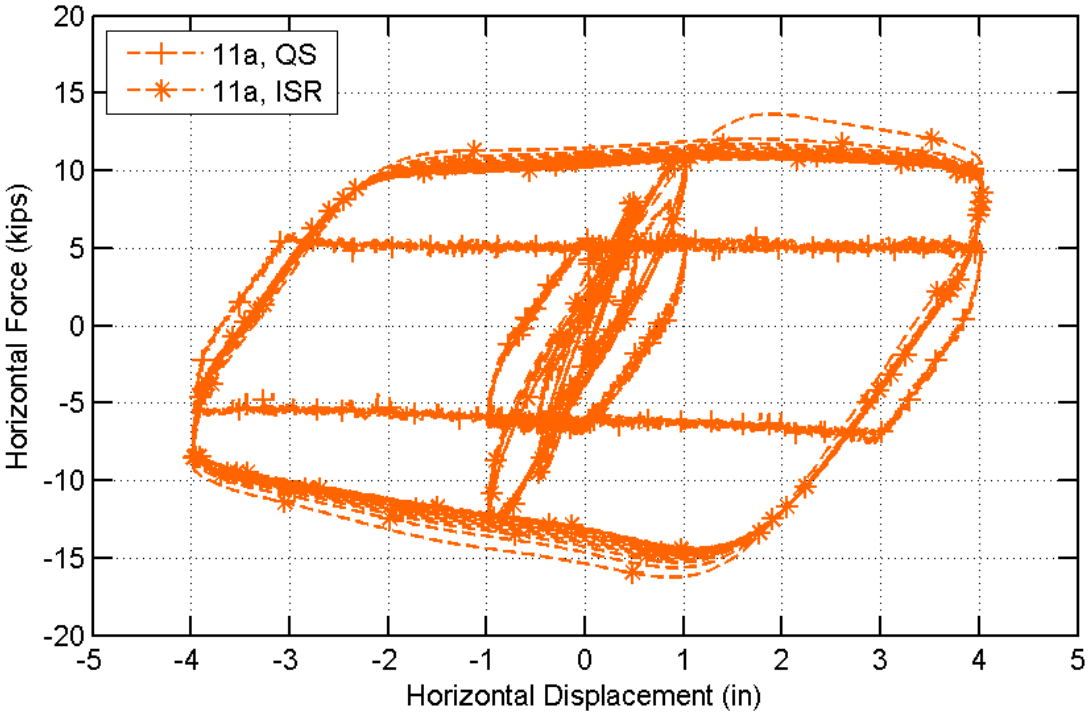

Figure B.9. Type II 11a force vs. displacement response, transverse orientation.

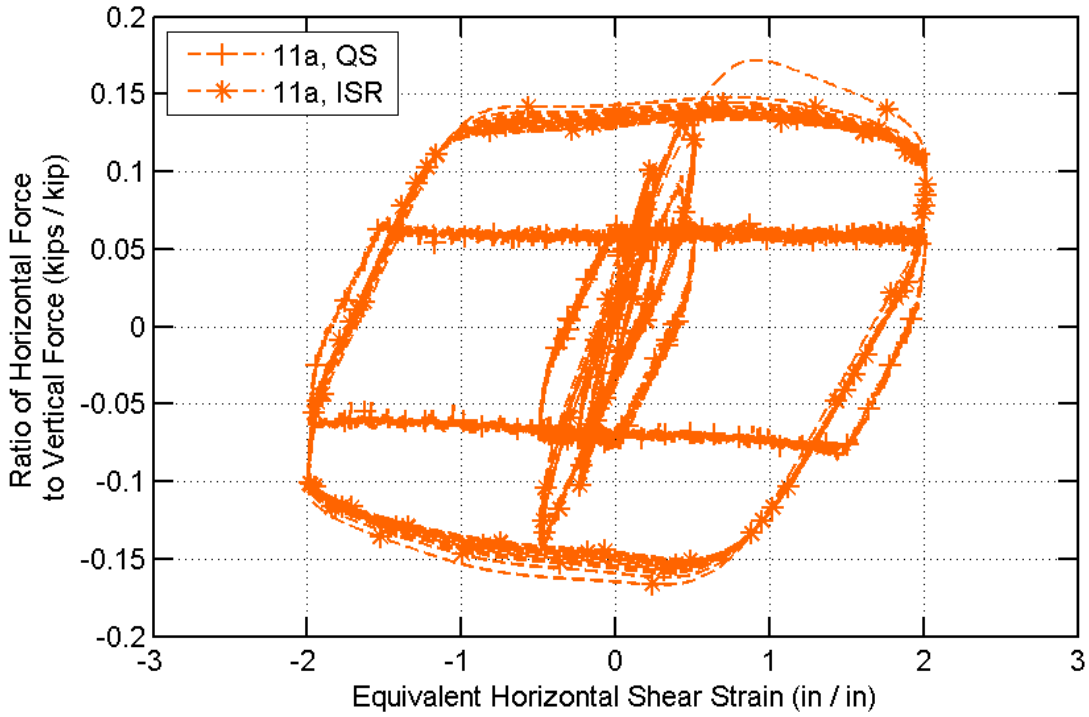

Figure B.10. Non-dimensional Type II 11a constitutive response, transverse orientation.

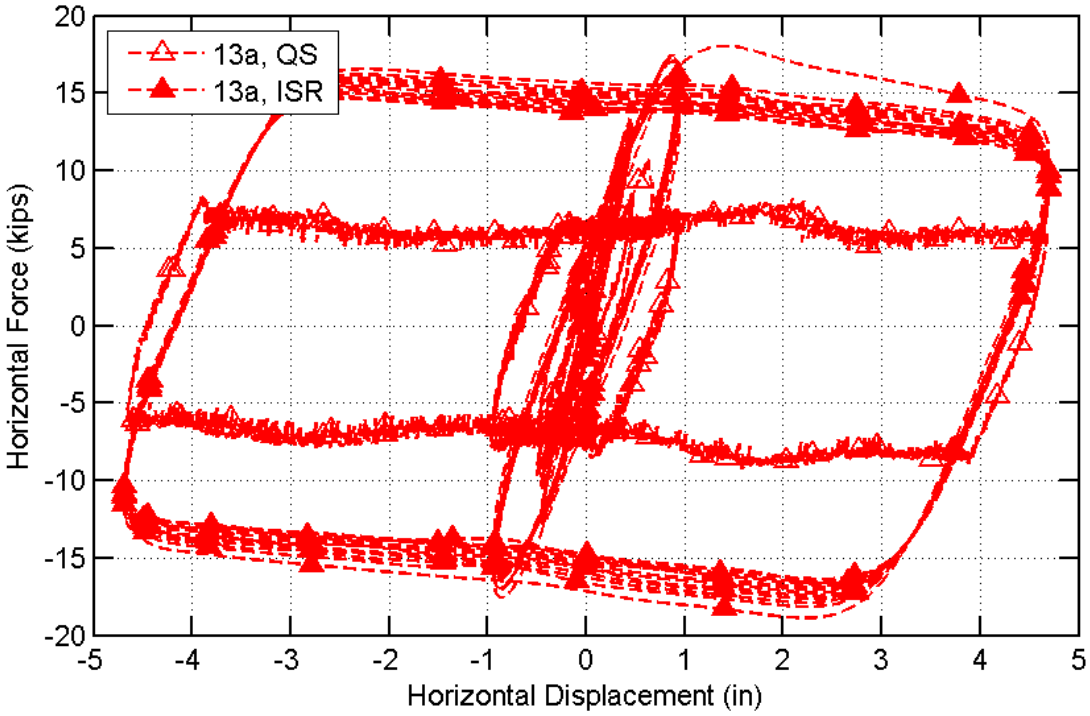

Figure B.11. Type II 13a force vs. displacement response, transverse orientation.

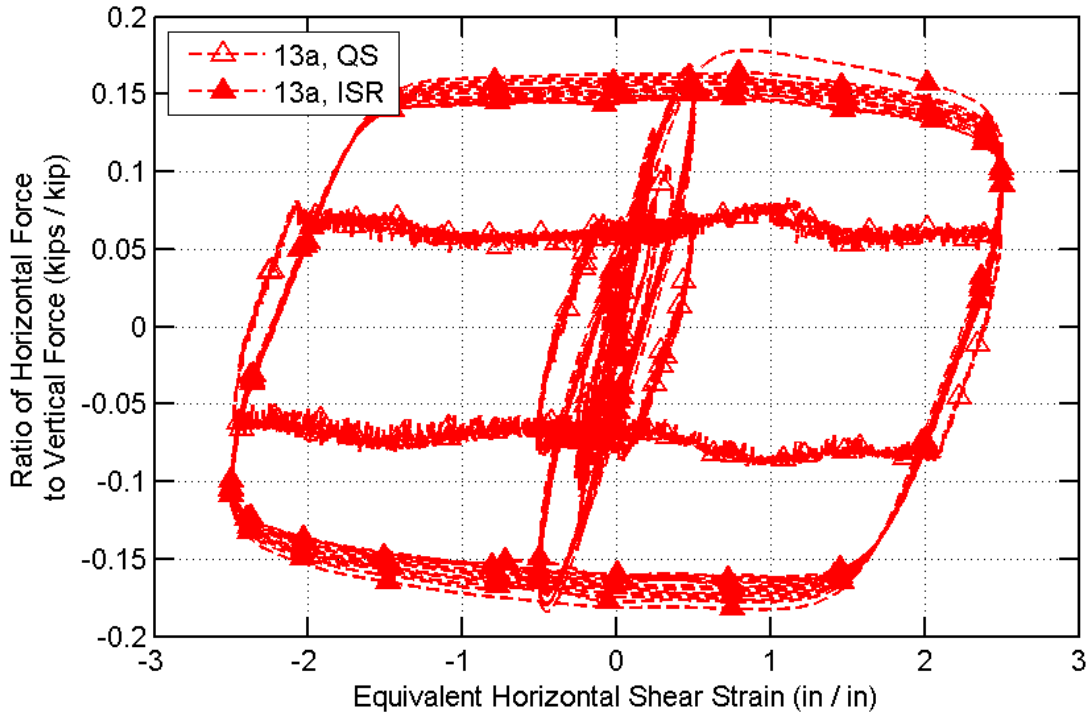

Figure B.12. Non-dimensional Type II 13a constitutive response, transverse orientation.

B.3 LARGE DISPLACEMENT RESPONSE WITH SMALL MIDDLE PLATE ROTATION

B.3.1 Type II 7c, Transverse Orientation

Force-displacement responses obtained from tests performed to a maximum of 400% ESS on two Type II 7c bearings with a transverse orientation are shown in Figure B.13.

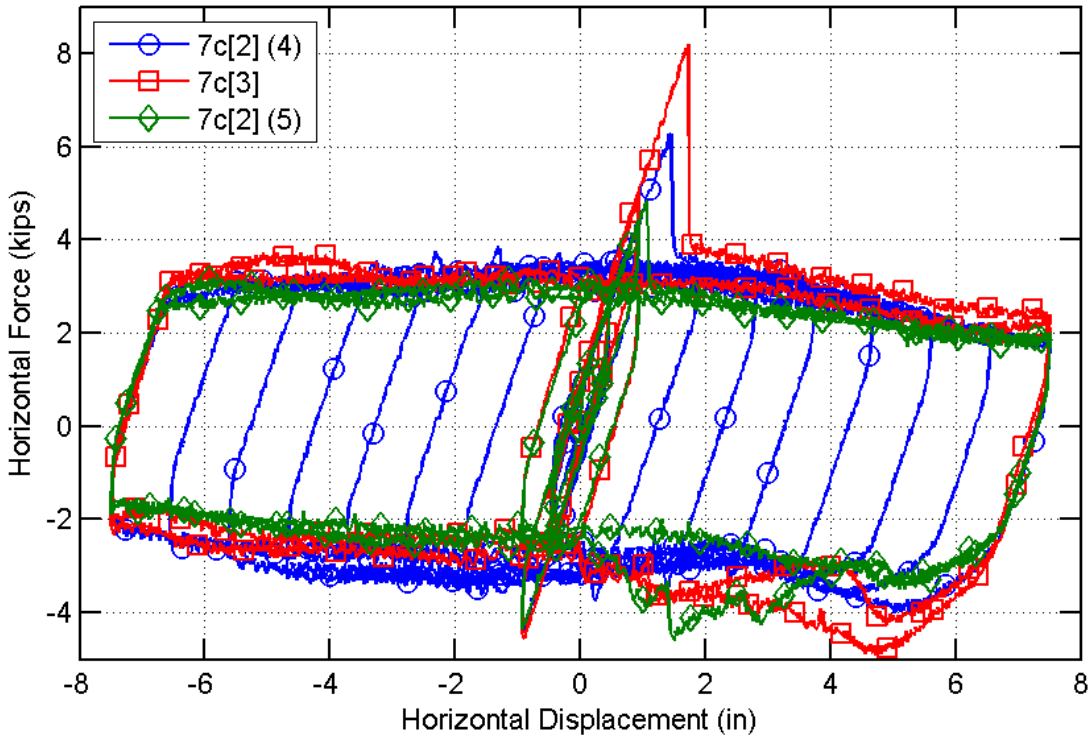

Figure B.13. Type II 7c force vs. displacement response, transverse orientation.

B.3.2 Type II 9a, Longitudinal Orientation

Force-displacement data are presented in Figure B.14 corresponding to the friction-ESS data shown in the report for large displacement response of a Type II 9a bearing in a longitudinal orientation.

B.3.3 Type II 11a, Transverse Orientation

Force-displacement data are presented in Figure B.15 corresponding to the friction-ESS data shown in the report for large displacement response of a Type II 11a bearing in a transverse orientation.

B.3.4 Type II 13a, Longitudinal Orientation

Force-displacement data are presented in Figure B.16 corresponding to the friction-ESS data shown in the report for large displacement response of a Type II 13a bearing in a longitudinal orientation.

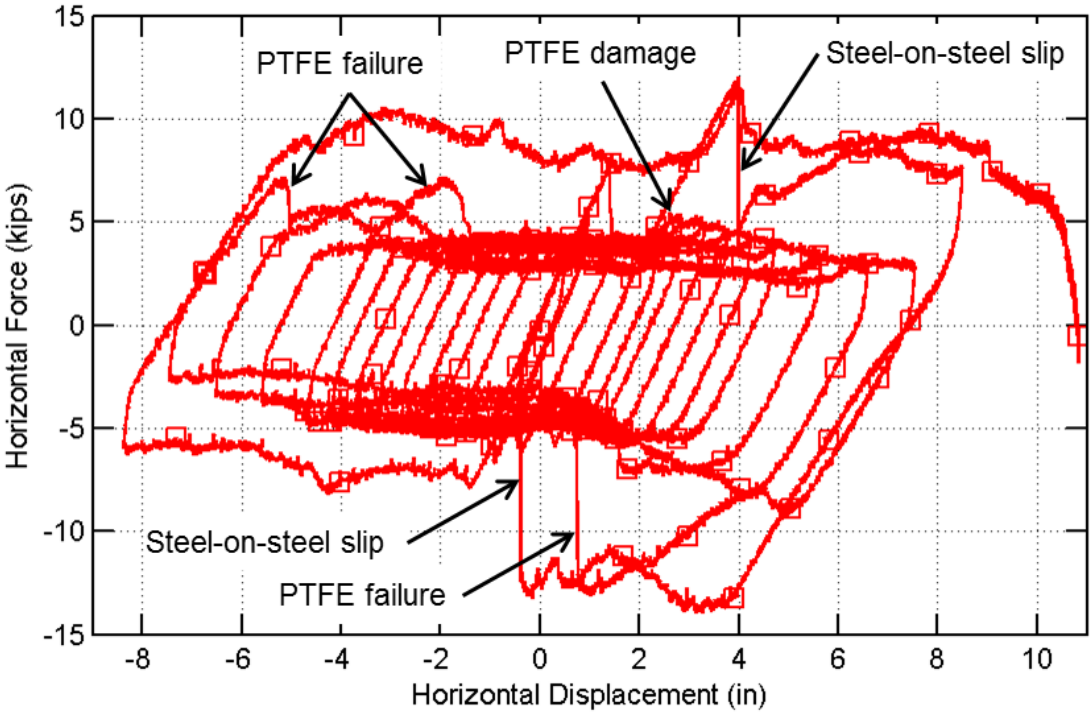

Figure B.14. Large displacement response of Type II 9a, longitudinal orientation.

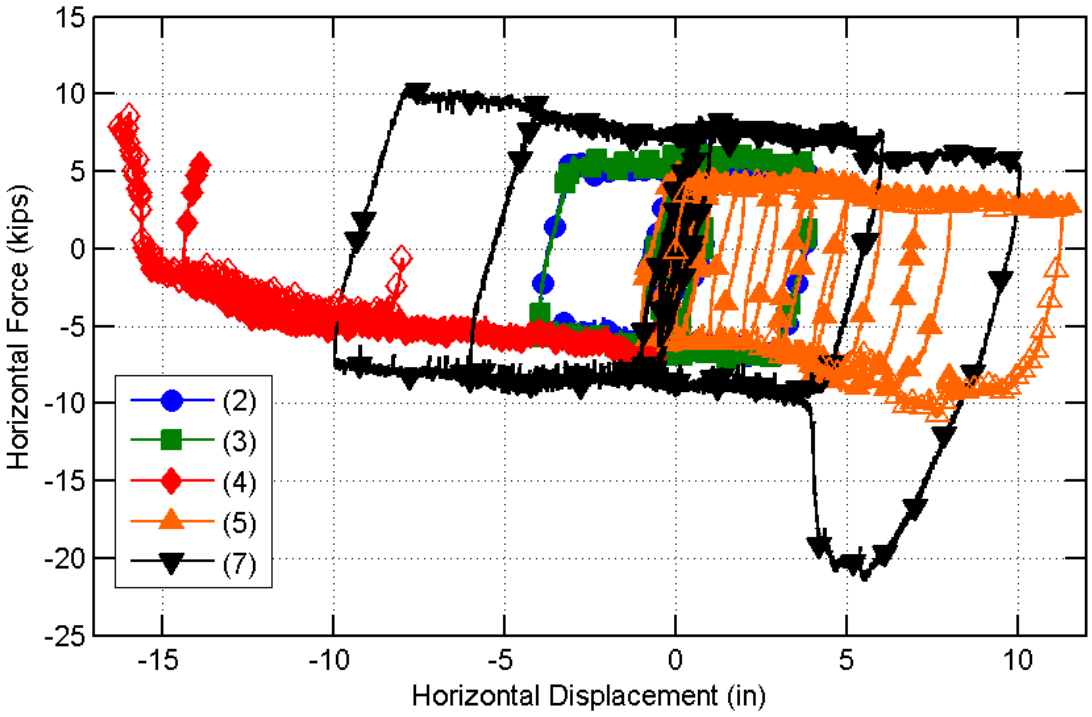

Figure B.15. Large displacement response of Type II 11a, transverse orientation.

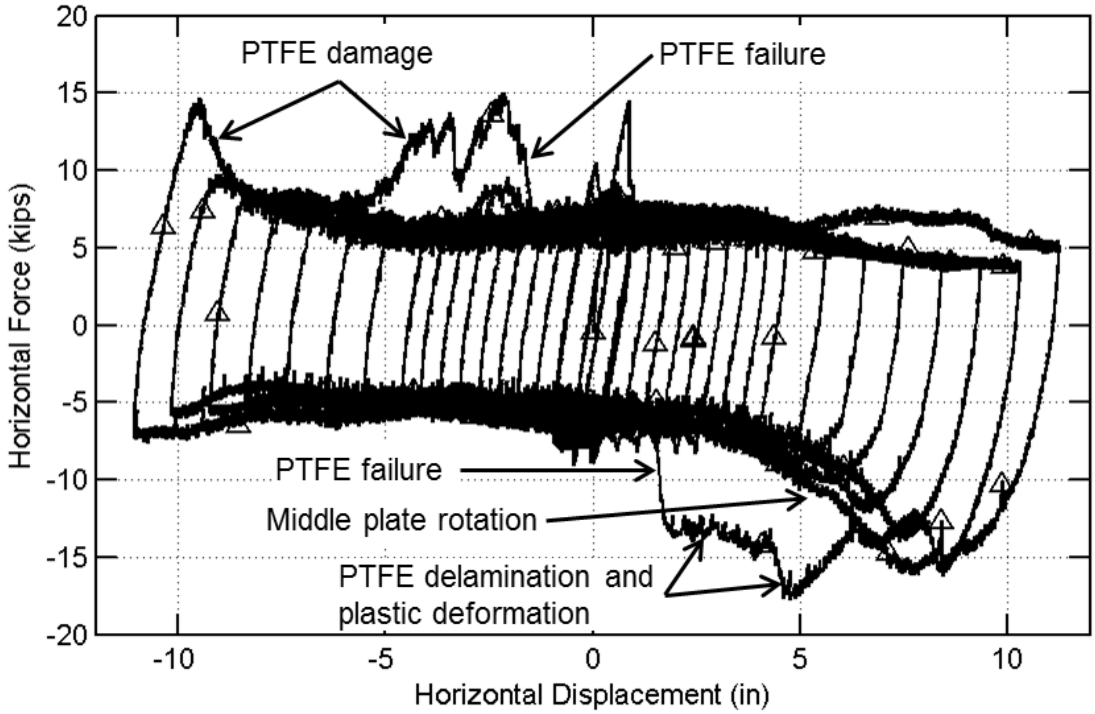

Figure B.16. Large displacement response of Type II 13a, longitudinal orientation.

B.4 LARGE DISPLACEMENT RESPONSE WITH SIGNIFICANT MIDDLE PLATE ROTATION

Force-displacement data are presented in Figure B.17 corresponding to the friction-ESS data shown in the report for large displacement response of a Type II 7c bearing in a longitudinal orientation.

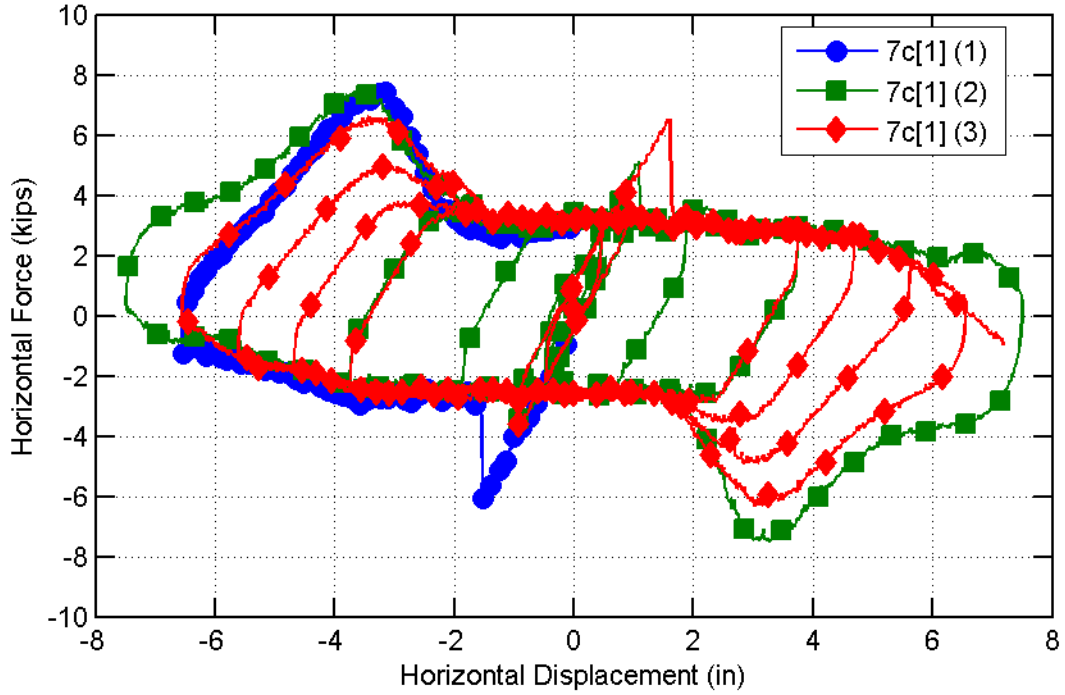

Figure B.17. Force versus displacement response for Type II elastomeric bearings, longitudinal orientation.

APPENDIX C SUPPLEMENTARY LOW-PROFILE FIXED BEARINGS EXPERIMENTAL RESULTS

C.1 GENERAL FORCE-DISPLACEMENT RESPONSE

C.1.1 Weak Anchor Tests

This section contains plots of individual bearing response corresponding to the data presented in the weak anchor testing section of Chapter 5. Plots of the force-displacement response for the fixed bearings with capacities limited by weak anchors are shown in Figure C.1 through Figure C.4 for the initial cycles prior to fusing of anchors, and then for large displacement cycles post-fusing. Figure C.5 and Figure C.6 show that same data, normalized by vertical force on the vertical axis. Although minor, there is a visible difference between the longitudinal and transverse orientations at the maximum negative displacements in Figure C.3 and Figure C.4. The difference develops as a result of the geometric difference between the orientations. In the transverse direction, when the bearing is shifted to large displacements, most of the bearing is still supported on a 1/8 in. elastomeric leveling pad placed between the masonry (bottom) plate and the concrete surface. For the longitudinal direction, however, the edge of the steel masonry plate begins to drop downward and dive slightly into the concrete when the imposed bearing displacement is almost equal to the width of the elastomeric leveling pad. This phenomenon appears in the constitutive response with a slight initial decrease in the shear resistance, reflecting the reduced bearing contact area and concomitant increase in normal stress between the steel and elastomeric pad, and the associated reduction in friction resistance of rubber with increasing normal stress. As the steel continues to slide off of the elastomeric pad and the leading edge dives into the top of the concrete, the load begins to increase, but only for the first cycle. Afterward, the bearing is returning to a position occupied in a previous cycle, so the concrete does not offer resistance.

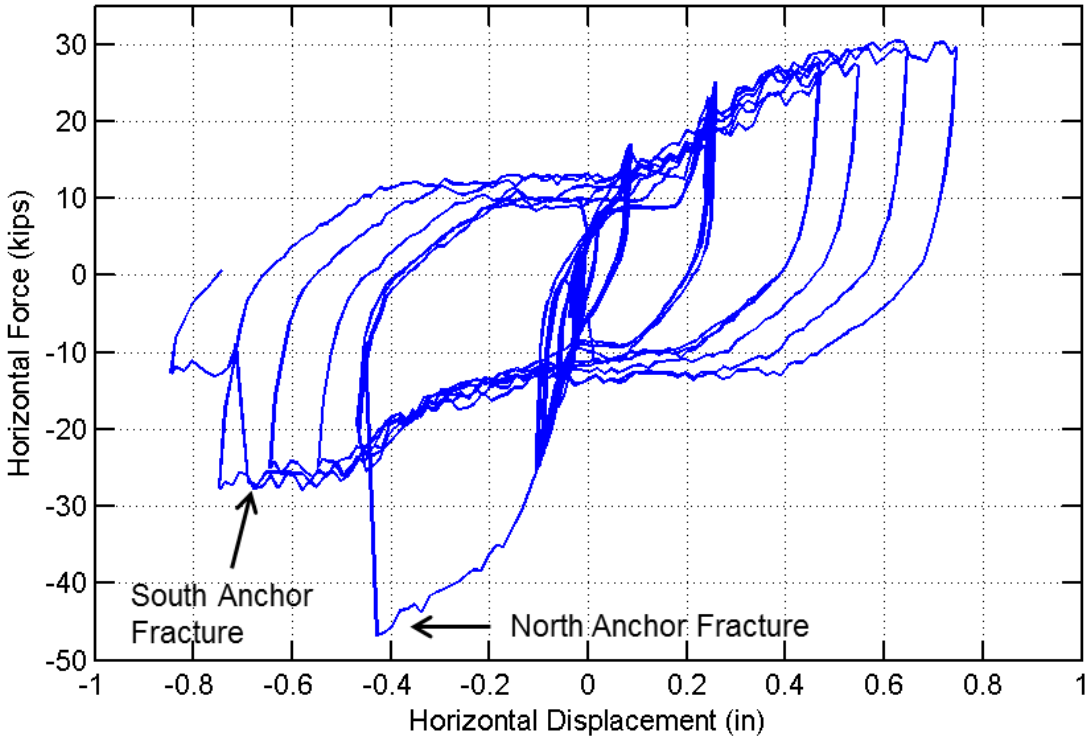

Figure C.1. Force versus displacement response to fully fused state for weak anchor LPF test, longitudinal orientation.

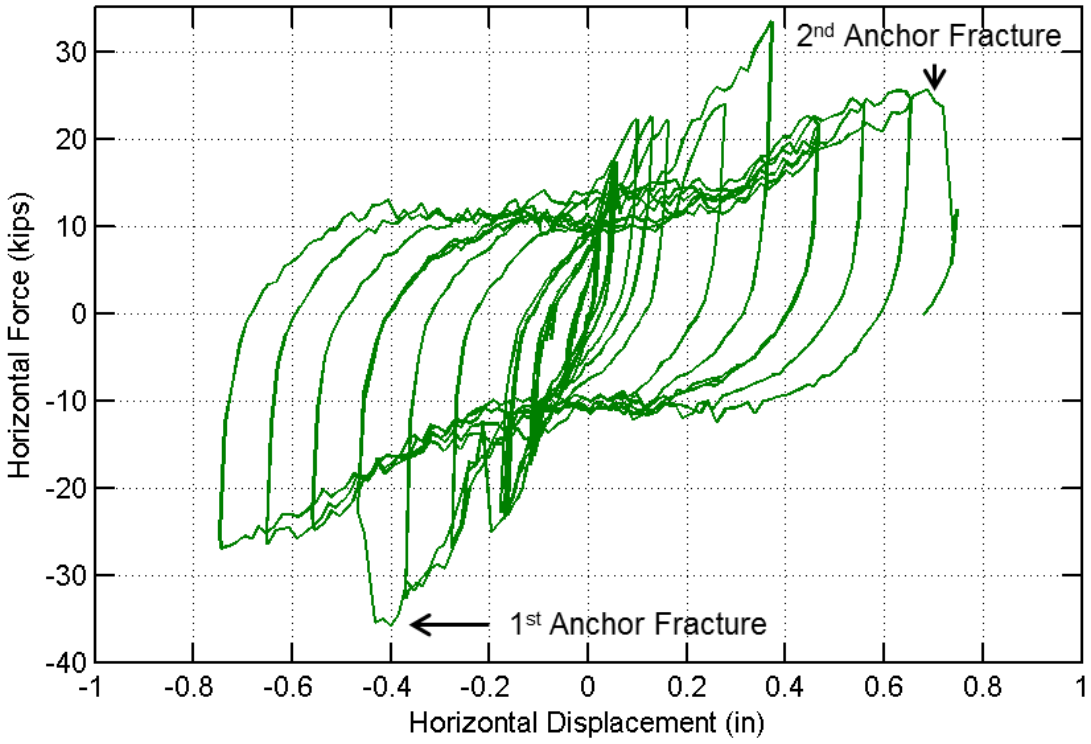

Figure C.2. Force versus displacement response to fully fused state for weak anchor LPF test, transverse orientation.

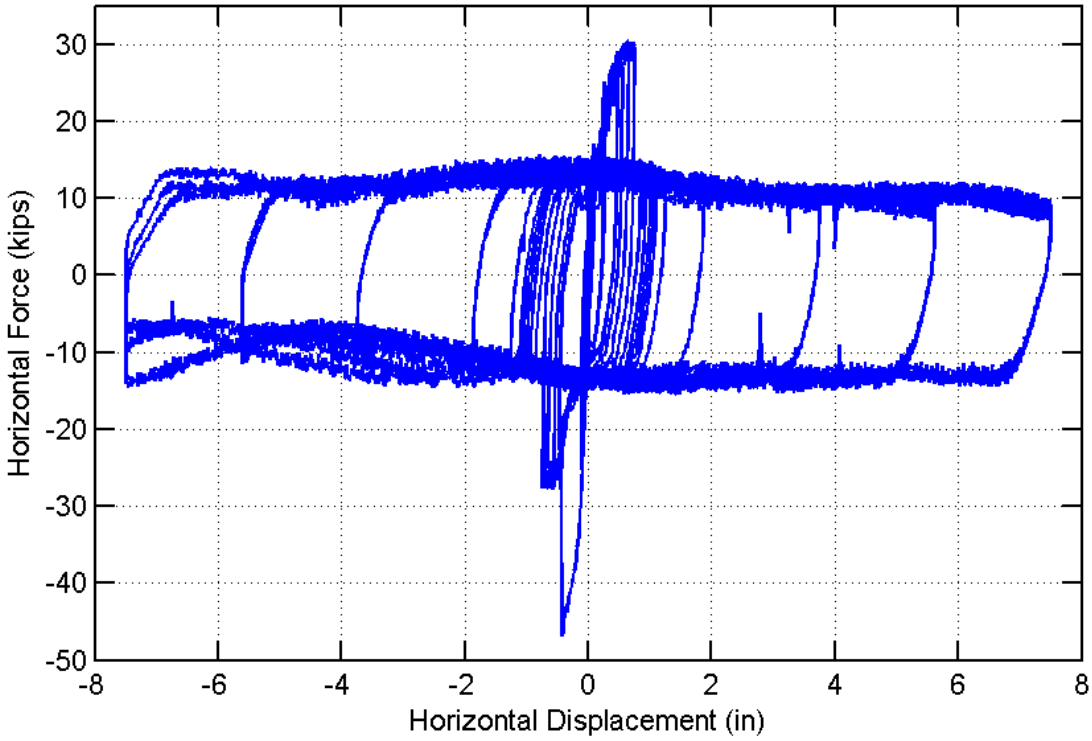

Figure C.3. Force versus displacement response for complete weak anchor LPF test, longitudinal orientation.

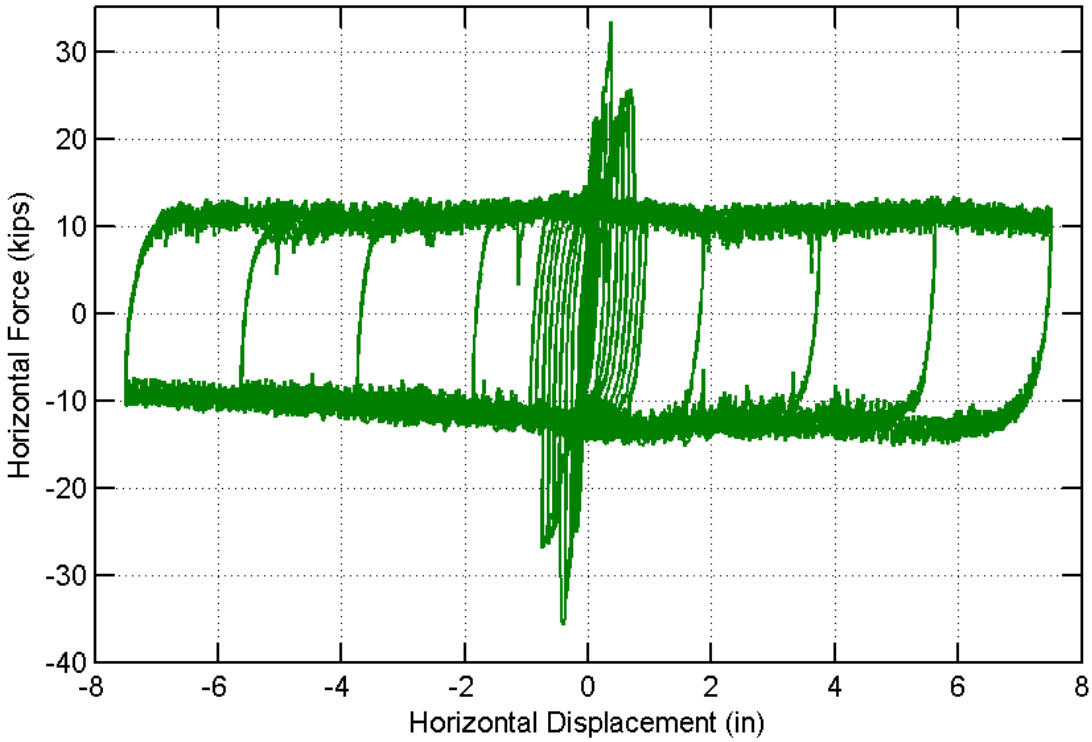

Figure C.4. Force versus displacement response for complete weak anchor LPF test, transverse orientation.

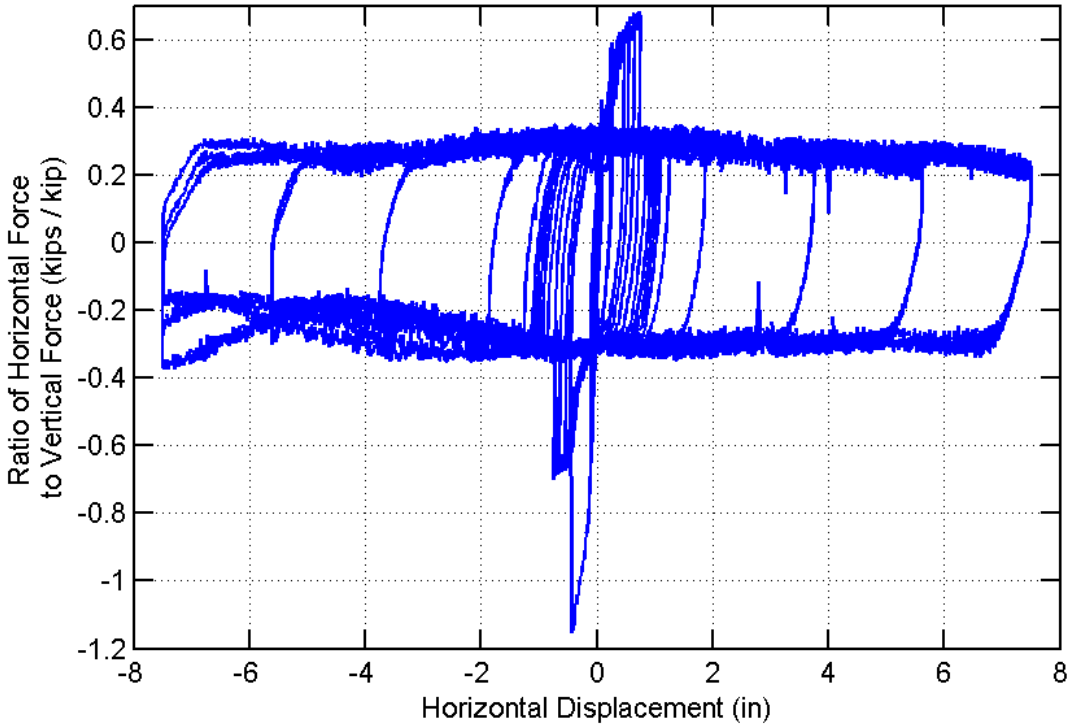

Figure C.5. Ratio of horizontal to vertical force versus displacement response for complete weak anchor LPF test.

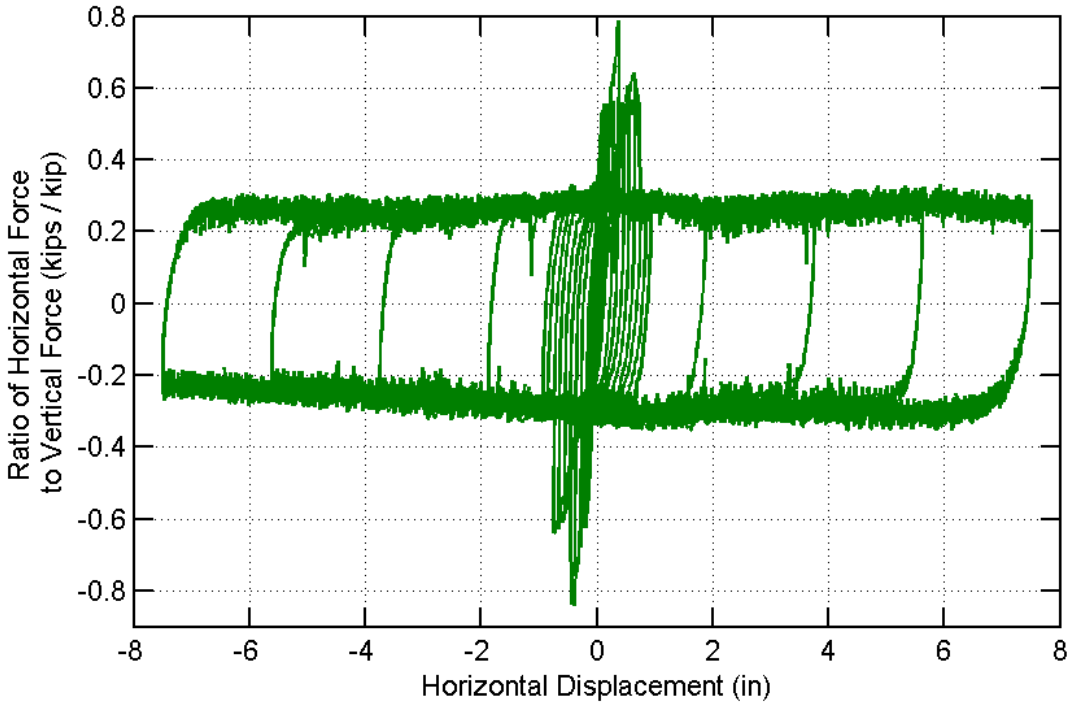

Figure C.6. Ratio of horizontal to vertical force versus displacement response for complete weak anchor LPF test.

C.1.2 Weak Pintle Tests

Two tests, one each in the longitudinal and the transverse direction, were performed on fixed bearings for which the pintles were intended to be the ultimate fuse component. Similar to the previous section, plots are provided in Figure C.7 through Figure C.10 to illustrate the force-displacement characteristics of the bearings observed during the experiments for the initial cycles and then separately for large displacement cycles. Figure C.11 and Figure C.12 show similar data, with the horizontal force normalized by vertical force on the vertical axis.

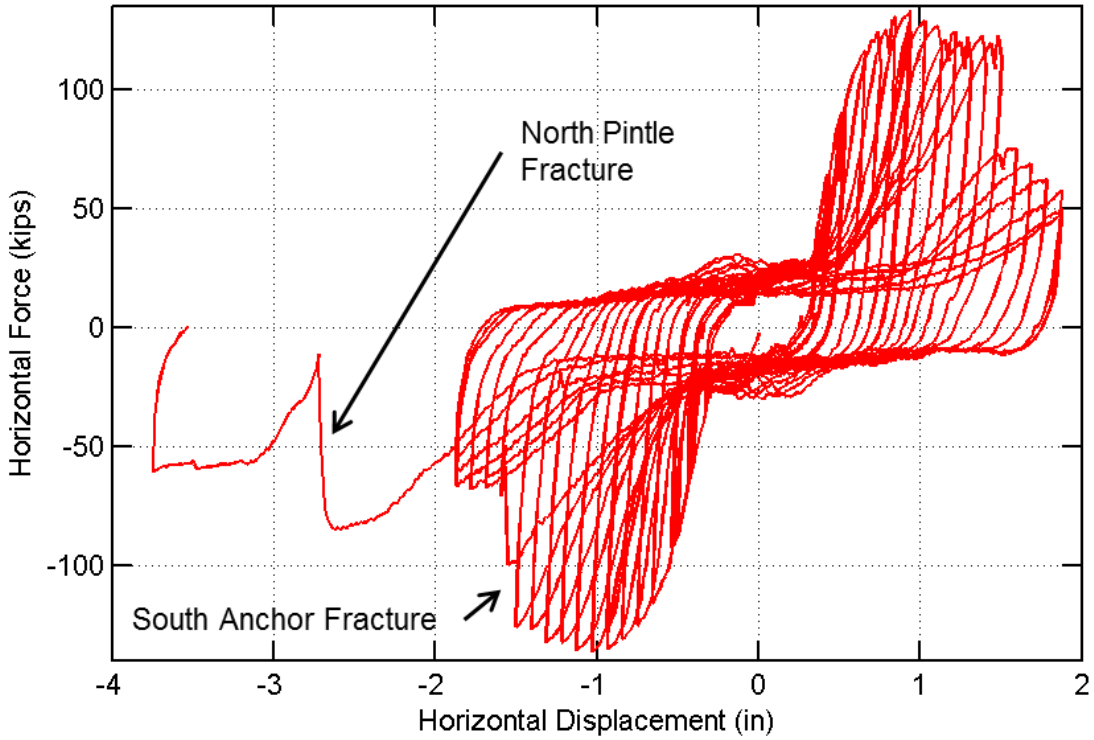

Figure C.7. Force versus displacement response to fully fused state for pintle-controlled LPF test, longitudinal orientation.

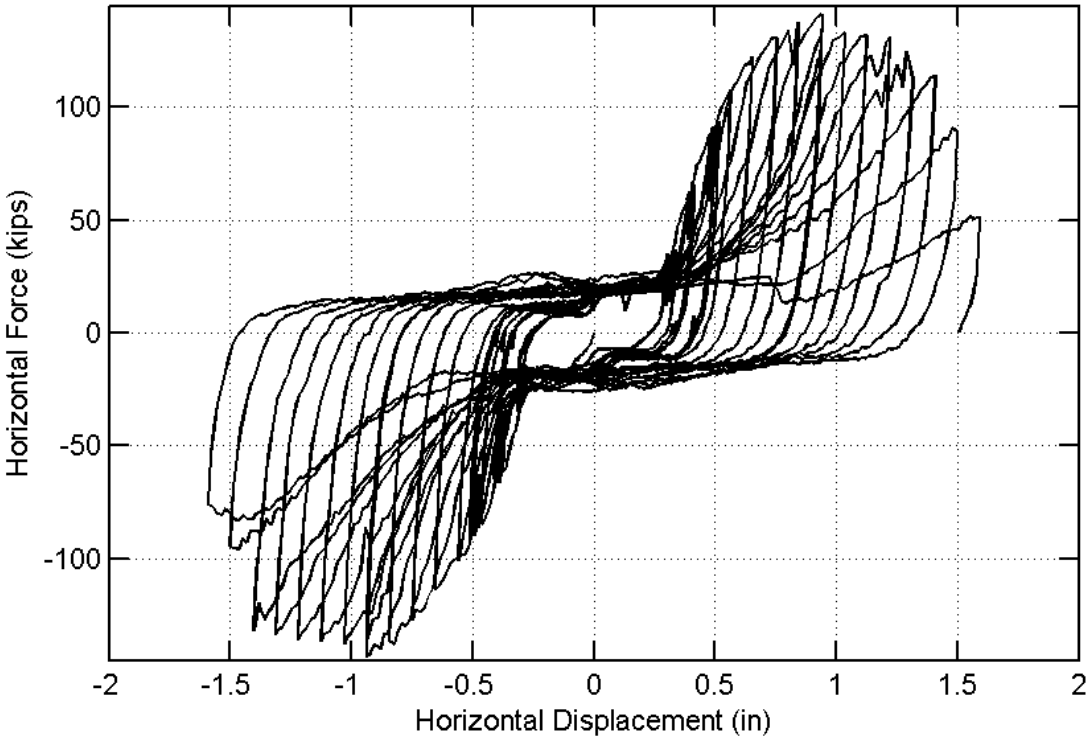

Figure C.8. Force versus displacement response to fully fused state for pintle-controlled LPF test, transverse orientation.

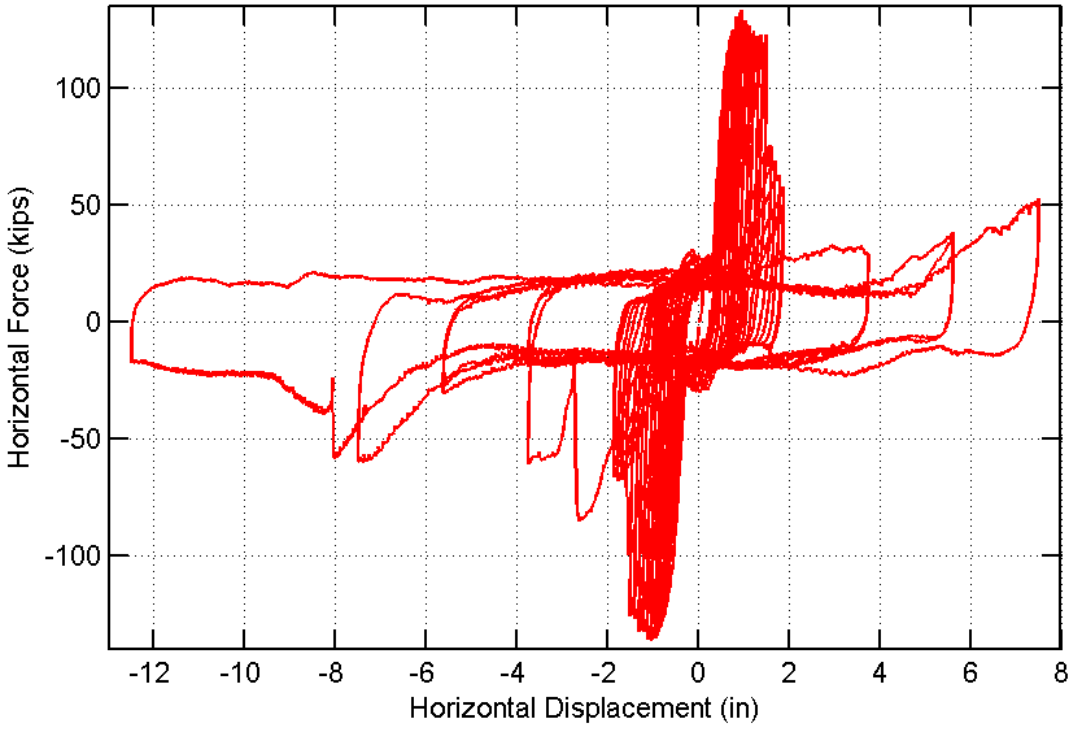

Figure C.9. Force versus displacement response for complete pintle-controlled LPF test, longitudinal orientation.

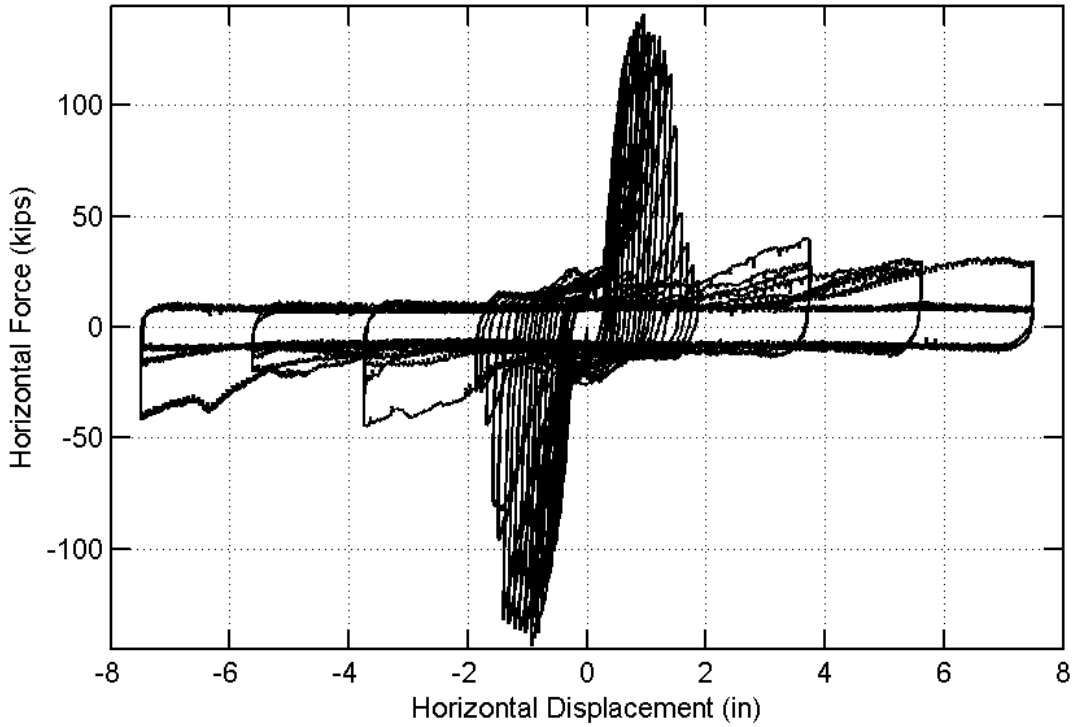

Figure C.10. Force versus displacement response for complete pintle-controlled LPF test, transverse orientation.

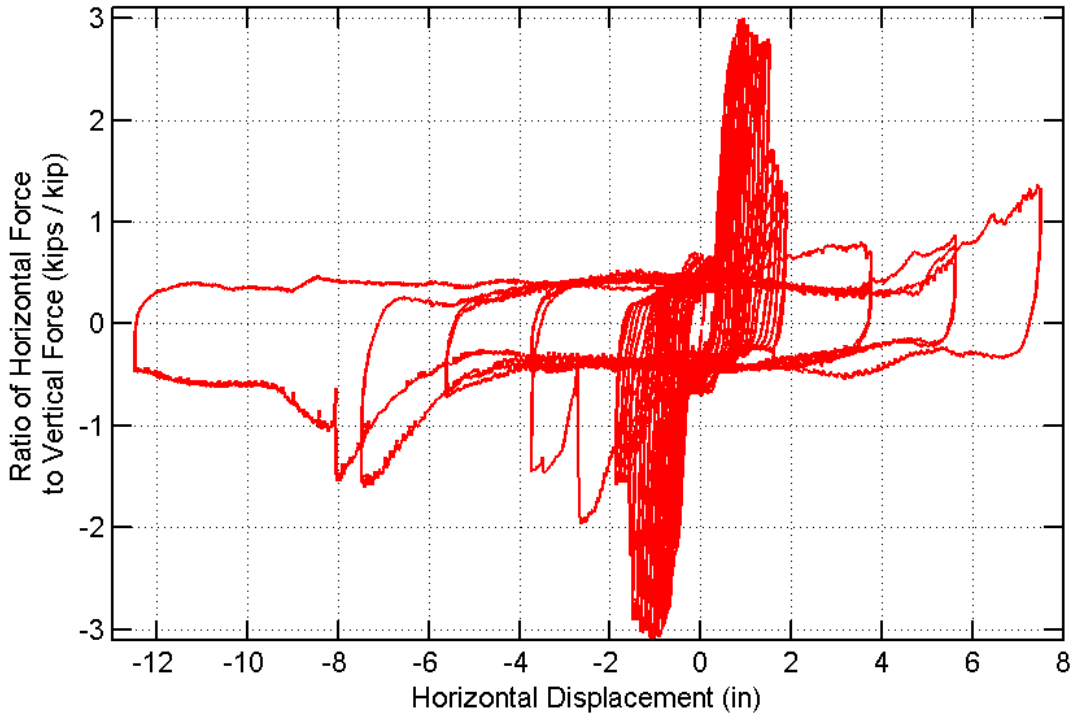

Figure C.11. Ratio of horizontal to vertical force versus displacement response for complete pintle-controlled LPF test, longitudinal orientation.

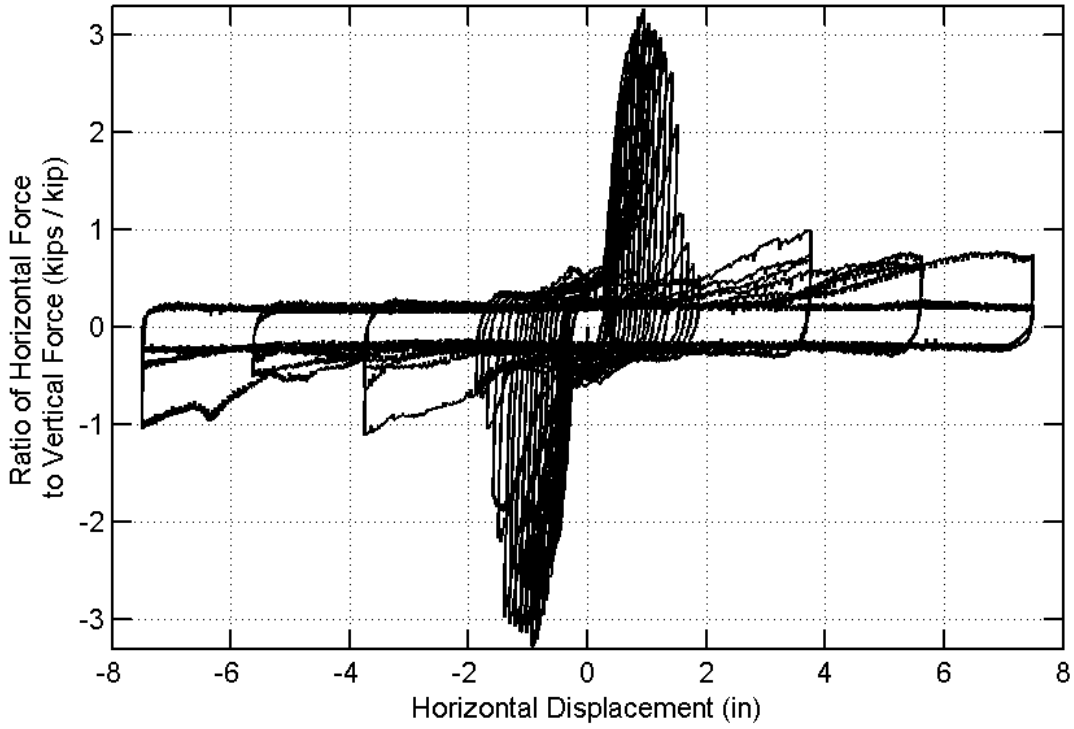

Figure C.12. Ratio of horizontal to vertical force versus displacement response for complete pintle-controlled LPF test, transverse orientation.

APPENDIX D ALTERNATE FUSE DESIGN

D.1 INTRODUCTION

The alternate fuse assembly described in this appendix is the third alternate investigated in the experimental program. The first two alternates were minor adjustments to typical retainer designs used by IDOT, with increased base width in the transverse bridge direction to reduce the influence of concrete crushing at the retainer toe. Both of the modified retainer designs were intended to maintain the general behavioral characteristics generally targeted by IDOT, i.e., rupture of a steel anchor element at a relatively low level of horizontal load. The third alternate departs significantly in design and response from typical retainers and the two previous alternates.

The design was conceived as a modification of shear fuse links studied by Ma et al. (2011). Ma et al. used steel plates with openings cut to reduce the plate to a set of parallel shear-flexure elements, as shown in Figure D.1, and demonstrated that “butterfly” fuses provided superior response, compared to “slitted” fuses. The primary benefit of the non-prismatic butterfly configuration is that the plastic hinge location is shifted away from regions with abrupt changes in geometry. Ma et al. (2011) targeted a 1:3 ratio for the a:b dimensions, which should concentrate the plastic hinging behavior of the links at the quarter points of the link span, L.

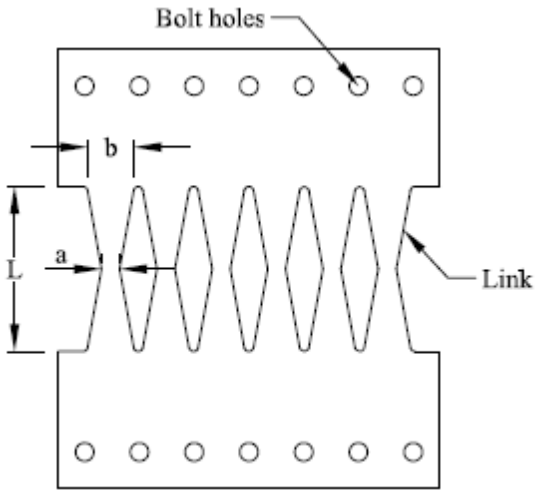

Figure D.1. Typical butterfly fuse.

D.2 DESIGN

D.2.1 Fabrication Drawings

The third alternate fuse design, herein referred to as Alt Fuse 3, was designed with the intent of mimicking the behavior of butterfly fuses, to an extent. In Ma et al. (2011) and in research performed incorporating butterfly fuses as energy dissipating fuse elements in a coupled rocking frame system (Deierlein et al., 2011; Eatherton and Hajjar, 2010), the fuses are symmetric. The previously-employed configuration described in these research programs incorporated a boundary condition that provides full flexural fixity on each side of

the fuse. The configuration selected for Alt Fuse 3, on the other hand, assumes that a diaphragm will transfer the accumulated shear load tributary to a substructure unit, but does not require the diaphragm to provide flexural fixity at the top of the fuse element.

Alt Fuse 3 was designed to represent one half of a butterfly fuse. Rather than use a flat plate, a WT 5x22.5 section was selected so that the flanges could be anchored to the concrete substructure. Portions of the stem were selectively cut-out to create a section similar to a half fuse, as shown in Figure D.2. Effective full butterfly fuse dimensions are shown in Figure D.3.

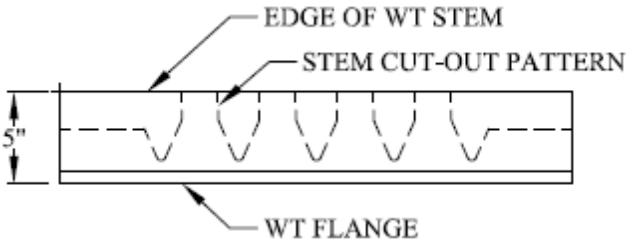

Figure D.2. WT Cut-out elevation.

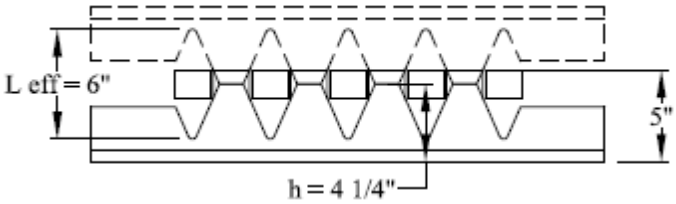

Figure D.3. Effective butterfly fuse dimensions.

The shear load is transmitted by 1-1/2 in. x 2 in. sections of rectangular steel bar spanning 4 in. between the faces of parallel steel angles. The effective height of the fuse, *h*, is offset by 3/4 in. from the top of the WT, half the height of the bars, to correspond to the centroid of the bars and connecting bolts at the angles, yielding an effective height of 4-3/4 in. The tops of the cut-out fins are held to a constant width (2 in., as shown in Figure D.5) to provide a parallel face upon which the bars can impose shear loading on the test specimen. Fabrication drawings for the Alt Fuse 3 assembly and components are shown in Figure D.4 through Figure D.7.

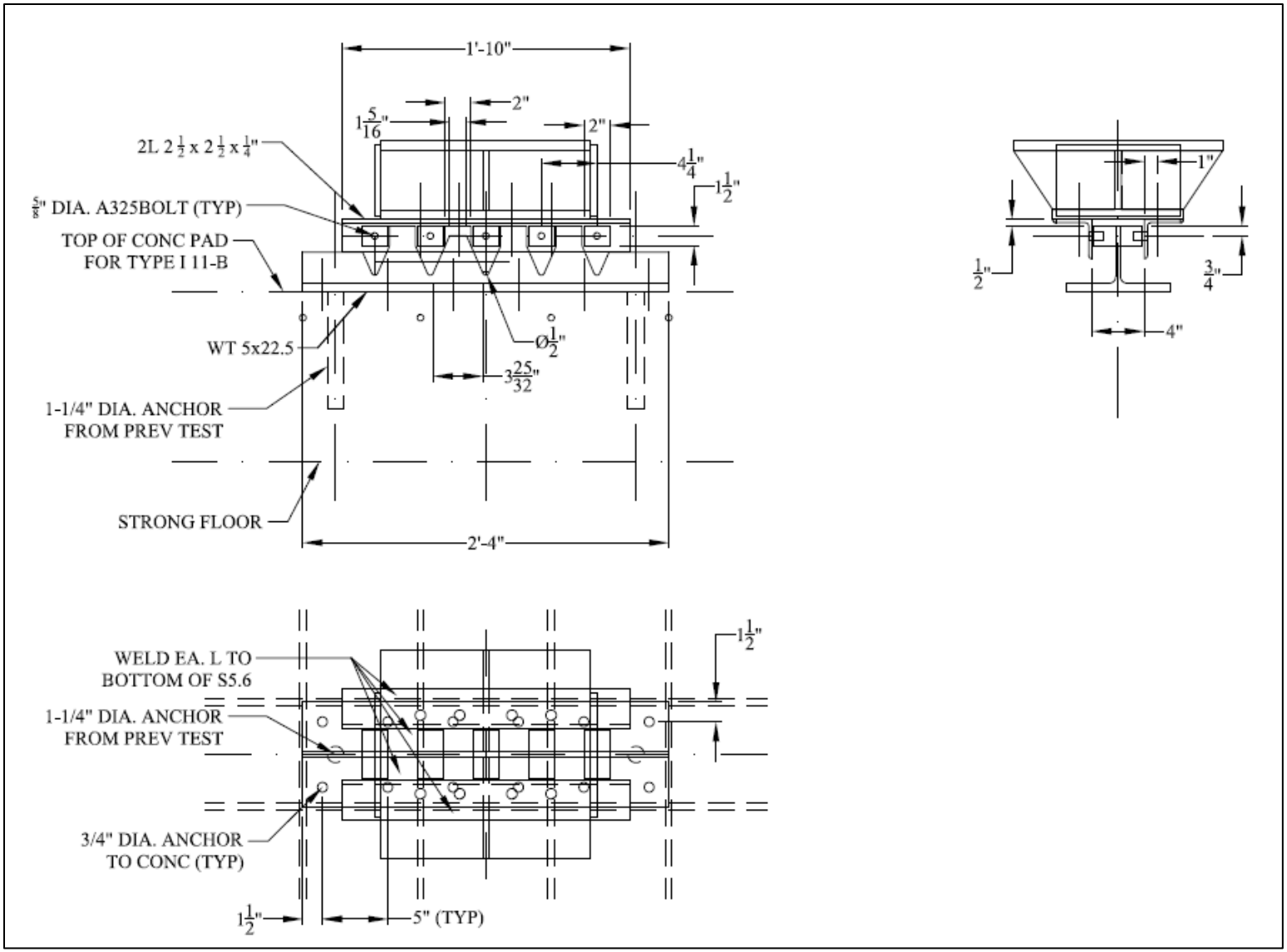

Figure D.4. Alt Fuse 3 assembly.

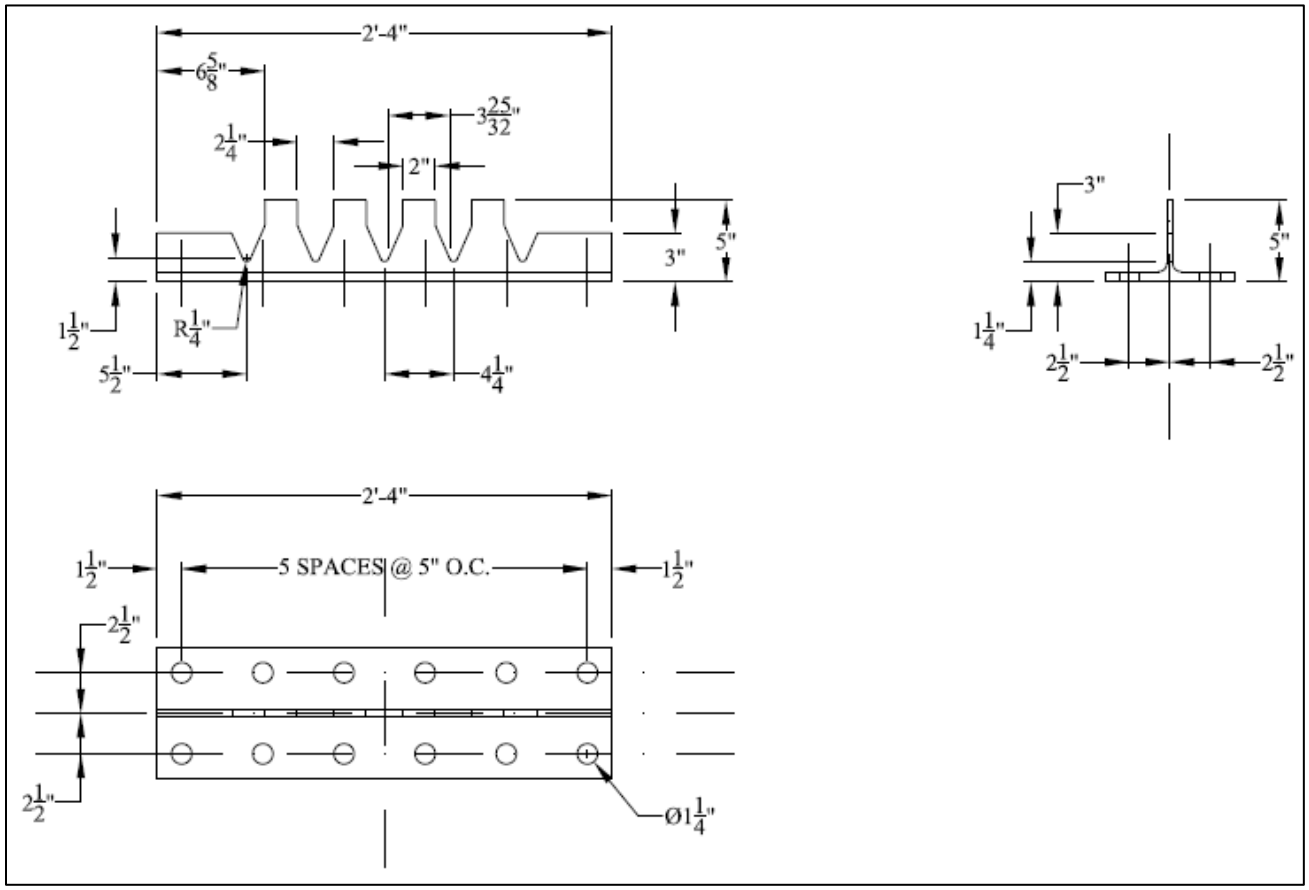

Figure D.5. Alt Fuse 3 WT fuse component.

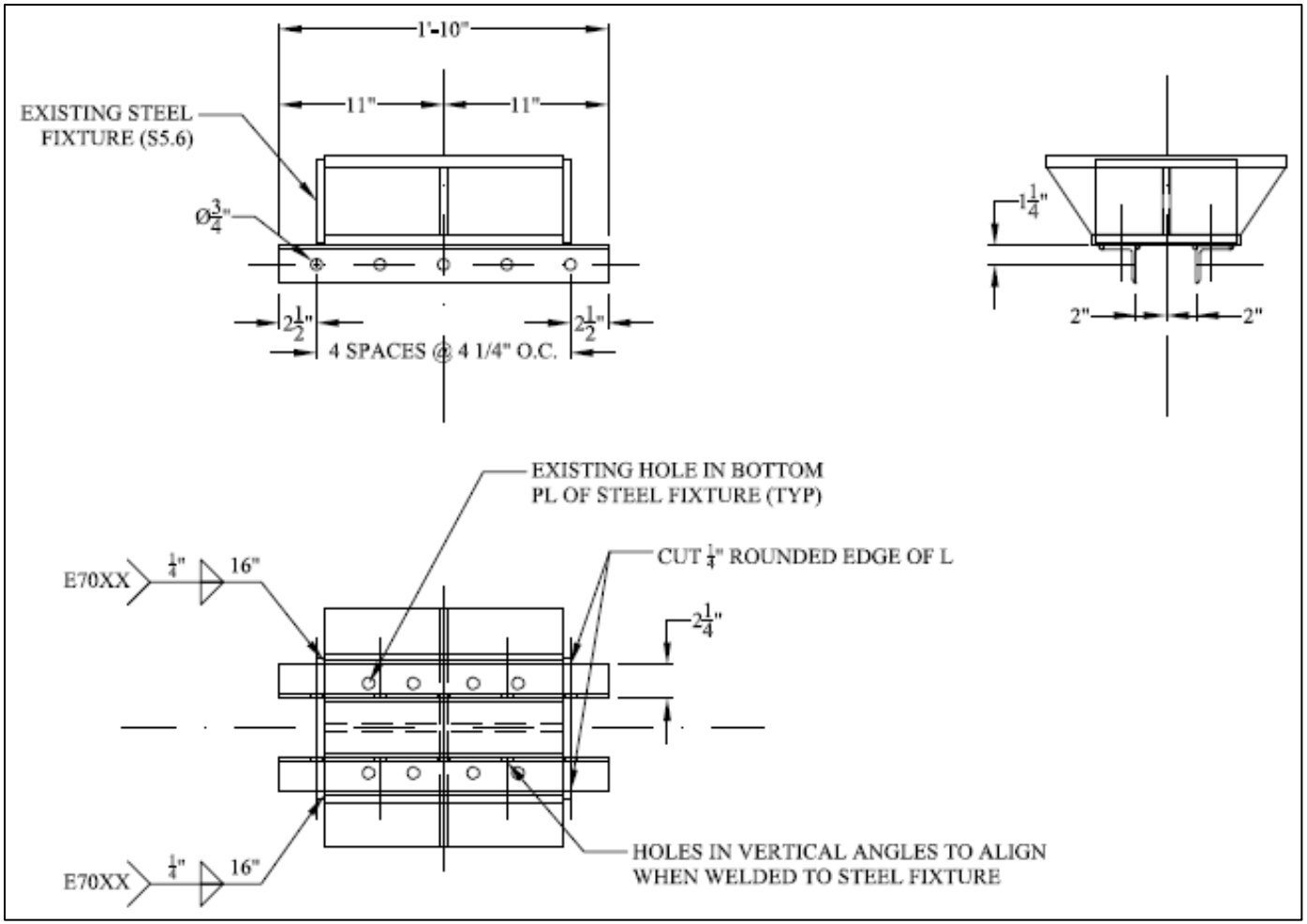

Figure D.6. Alt Fuse 3 steel fixture with welded angles.

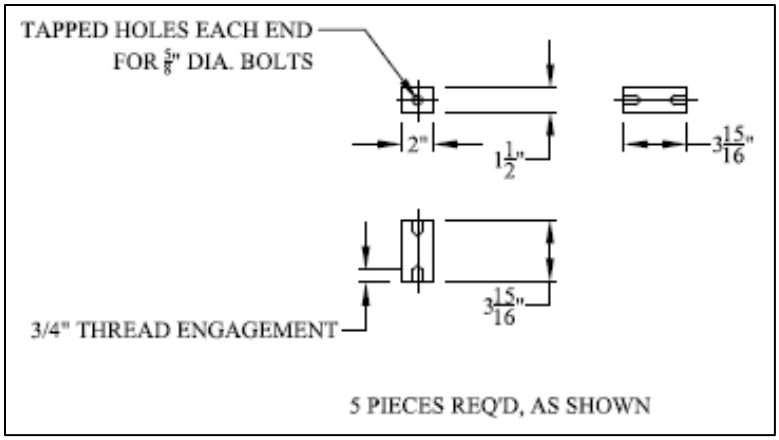

Figure D.7. Alt Fuse 3 loading bars.

D.2.2 Predicted Capacity Calculations

The force capacity of the fuse assembly was estimated according to equations presented in Ma et al. (2011). With an a:b ratio of 1:3, the predicted location of maximum flexural strain is at ½ of the height from the centerline of the loading bars to the bottom of the cut-outs. Accounting for the varying section modulus and moment, the load to reach first yield is determined by

$$Q_y = \frac{8}{27}\frac{nb^2 t\sigma_y}{L_{eff}} \qquad \text{(Eq. D-1)}$$

where

n = Number of links (fins)

b = Width of fin at base (in.)

t = Thickness of plate (in.)

σ_y = Yield strength of steel (ksi)

L_{eff} = Effective length of link

For Alt Fuse 3, the values of n and b are 4 and 3-25/32 in., respectively, as shown in Figure D.5. The value of t corresponds to the stem thickness of the WT, which is 0.350 in. for a WT 5x22.5. The yield strength of the steel is assumed to be 50 ksi for A992 steel, and the effective length is 6 in., as shown in Figure D.6. The resulting value of Q_y is 49.4 kips.

Plastic moment capacity is 3/2 times yield moment capacity for a rectangular cross-section, so the load corresponding to full plastic flexure is

$$Q_p = \frac{3}{2}Q_y = \frac{4}{9}\frac{nb^2 t\sigma_y}{L_{eff}} \qquad \text{(Eq. D-2)}$$

Accordingly, the estimated ultimate load, Q_p, is 74.1 kips.

Evaluating the threaded steel anchor rods into the concrete as pure shear elements,

$$V_{n,anc} = 0.6\ n_{anc}\left(0.8\frac{\pi d^2}{4}\right)\sigma_{y,anc} \qquad \text{(Eq. D-3)}$$

where

n_{anc} = Number of anchors

d = Nominal anchor diameter (in.)

$\sigma_{y,anc}$ = Yield strength of steel (ksi)

Discounting the total number of anchors by 2 to allow for a localized uplift, the total number of anchors effective in resisting shear, n_{anc}, is 10. The 0.6 coefficient accounts for the relation of shear to tensile strength, and the 0.8 factor accounts for the reduction of area at a cross-section including threads. The nominal diameter of the steel anchors is ¾ in. Based on tests performed on samples of the anchors, the yield strength of the steel is approximately 45 ksi. The nominal shear yield capacity of the anchor group is 95.4 kips.

Similarly, the nominal tension capacity of two anchors may be estimated using (Eq. D-3), except without applying the 0.6 factor. The nominal tension yield capacity of two anchors (n_{anc} = 2) is 31.8 kips. The tension and compression developed in flexure of adjacent fins should equilibrate, and so only the anchors located near the outside edges of the outer fins should experience tension. The anticipated tension load is estimated from the stress distribution on the critical section when subjected to Q_p. With a linear variation of section depth between “a” and “b”, a 1:3 ratio of a:b, and a critical section at the mid-point between “a” and “b”, the depth of the critical section is 2/3 of “b”. Taking half of this depth as the portion of the fin subjected to tension when experiencing plastic moment, the tension demand is estimated to be 22.1 kips.

D.3 EXPERIMENT PROCEDURE

D.3.1 Instrumentation

Displacement is measured at three levels of the Alt Fuse 3 assembly with string potentiometers. The two 50 in. stroke string potentiometers normally attached to the center of the top bearing plate are attached to brackets at the welded angles, and so provide a representative measurement of the transverse translation for a bridge superstructure. The four 25 in. stroke string potentiometers normally attached near the corners at the base of Type I bearing are attached to brackets near the corners of the WT flange, and so provide a measure of slip for the WT on the simulated substructure. The third level of displacement was measured near the top of two separate fins (west side interior, east side exterior) using 10 in. stroke string potentiometers. Additionally, strain gage rosettes were attached at the expected critical section of the two fins with 10 in. string potentiometers. Instrumentation components and locations are shown in Figure D.8 through Figure D.10.

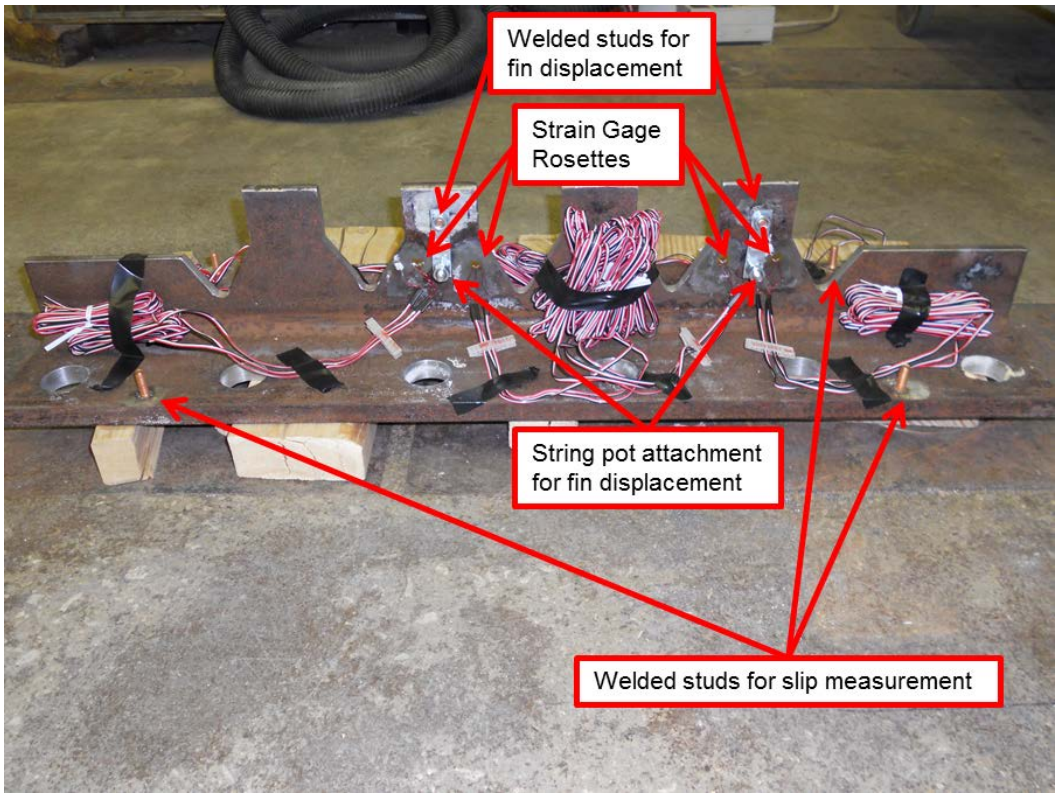

Figure D.8. Alt Fuse 3 WT instrumentation.

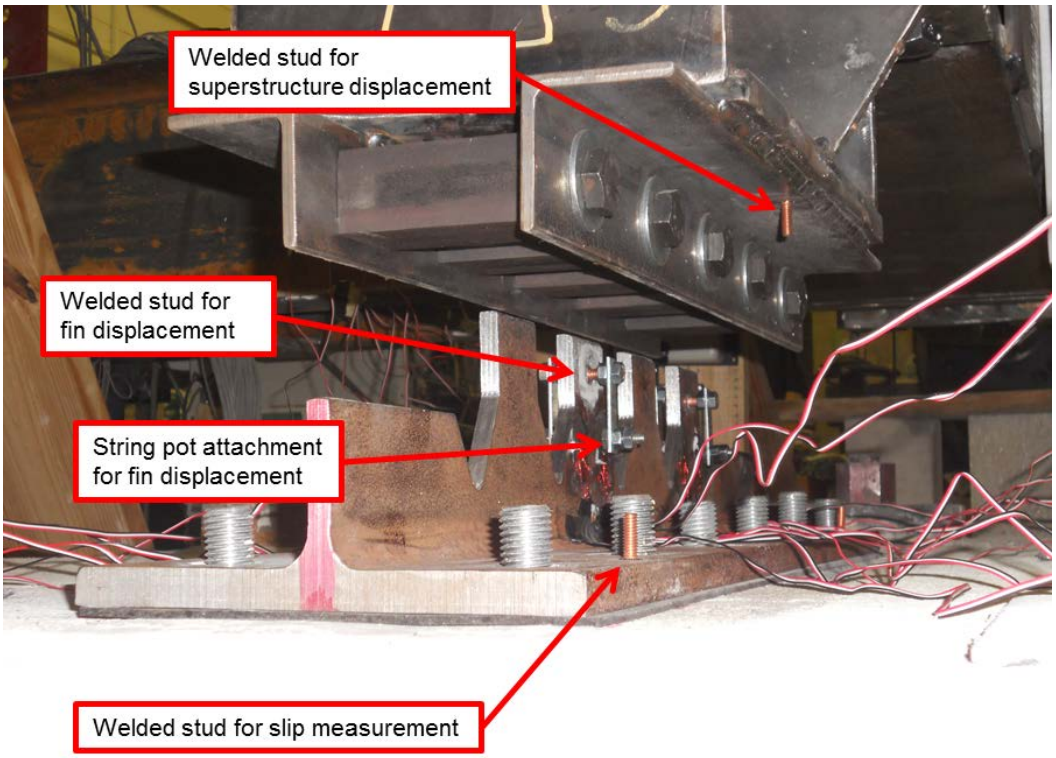

Figure D.9. Alt Fuse 3 string potentiometer attachment locations.

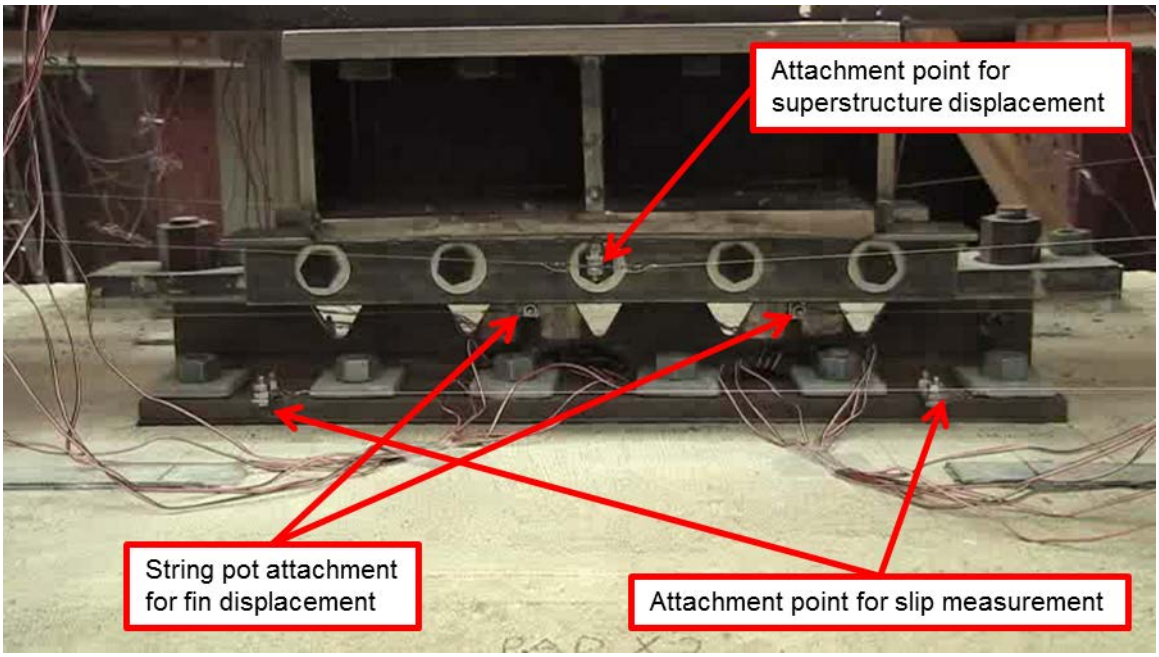

Figure D.10. Alt Fuse 3 with all instrumentation attached.

D.3.2 Protocol and Control

The testing protocol for Alt Fuse 3 generally followed the protocol described in Ma et al. (2011) for shear strain cyclic amplitudes and strain rates. Ma et al. (2011), in turn, had based their testing protocol on AISC Seismic guidelines for eccentrically braced frames. Shear strains for control were calculated according to (Eq. D-4) as the ratio of the difference between the average displacement of the top portion of the assembly, determined from the 50 in. string potentiometers, and the average slip displacement of the WT portion of the assembly, determined from the 25 in. string potentiometers, relative to the effective height, *h*, of the WT fuse, as shown in Figure D.3. Figure D.11 shows the locations were each of these components is determined during the test.

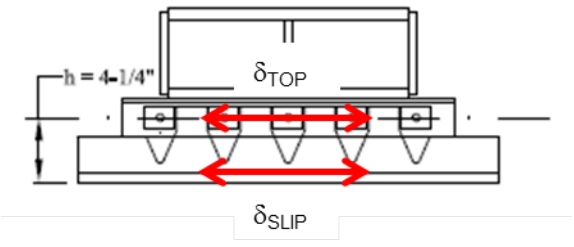

Figure D.11. Alt Fuse 3 control calculation references.

$$\gamma_{control} = \frac{\delta_{top} - \delta_{slip}}{h} \quad \text{(Eq. D-4)}$$

where

δ_{top} = Mean displacement of welded angles determined from 50 in. string pots (in.)

δ_{slip} = Mean displacement of WT determined from 25 in. string pots (in.)

h = Effective height of WT fuse (in.)

There were two notable differences between the protocol used for Alt Fuse 3 and that used by Ma et al. (2011). First, the number of cycles was reduced to avoid the possibility of low-cycle fatigue. No more than two cycles were performed at any amplitude level. The protocol transitioned to single cycles at larger amplitudes (greater than 3% nominal shear strain), and reached a nominal peak shear strain cyclic amplitude of 29%, as in Ma et al. (2011). Second, the nominal shear strain targets were increased to account for 1/8 in. gaps provided on each side of the loading bars between the faces of the bars and the edges of the fins. With a value of 4-1/4 in. for *h*, the adjustment to target shear strains was 2.94%. The base (used in Ma et al. (2011)) and adjusted values are shown versus the anticipated time to perform the test in Figure D.12, based on strain rates indicated in Ma et al. (2011).

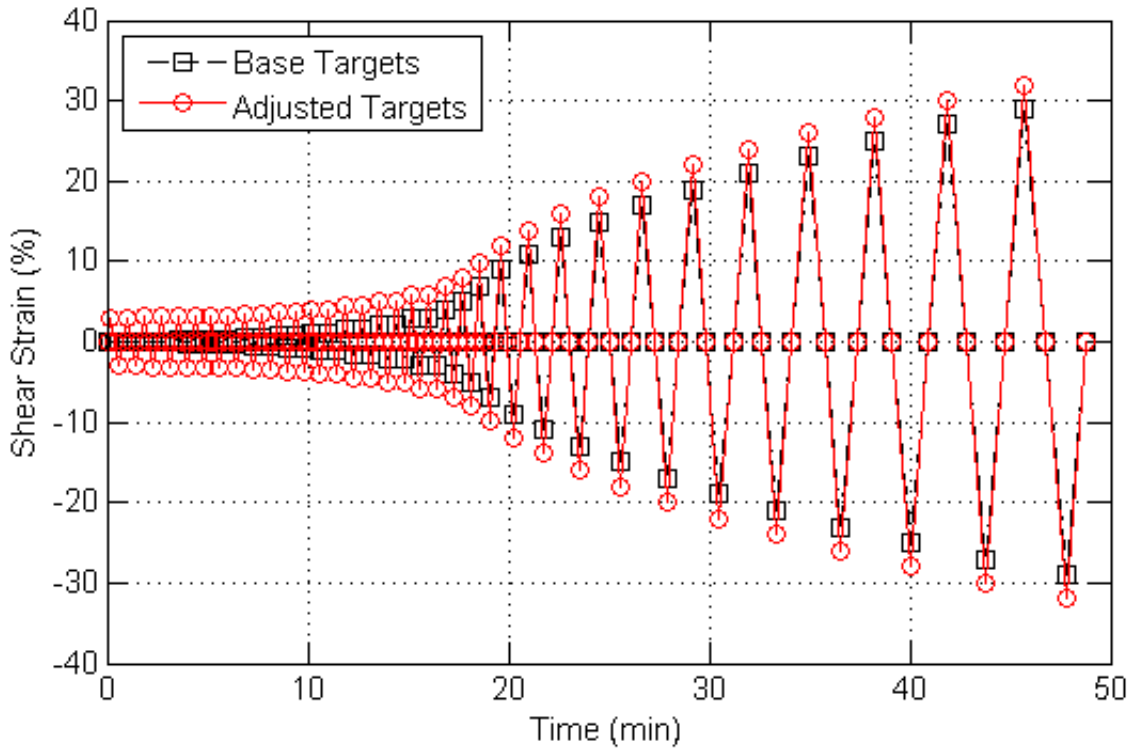

Figure D.12. Alt Fuse 3 shear strain protocol.

The control program was modified to calculate the slip displacement of the WT, deduct the slip from the top plate displacement, and evaluate the strain as the ratio of the relative displacement to the effective height, *h*, of the fuse. This approximate shear strain was used as the control feedback for the horizontal actuator control. Additionally, the test was not intended to impose a vertical load, but the bars were to maintain a constant elevation while travelling horizontally. Therefore, the control code was modified to output a control signal to the vertical actuators, based on the current horizontal actuator command.

D.3.3 Preparation and Installation

Alt Fuse 3 was tested by mounting the specimen on the same pad, and overlapping the footprint for a previous test conducted with the Type I 11b bearing specimen. The remnants of the anchors from the Type I retainers extended slightly above the surrounding concrete, and the concrete had also experienced minor localized crushing at the toes of the retainers, as shown in Figure D.13.

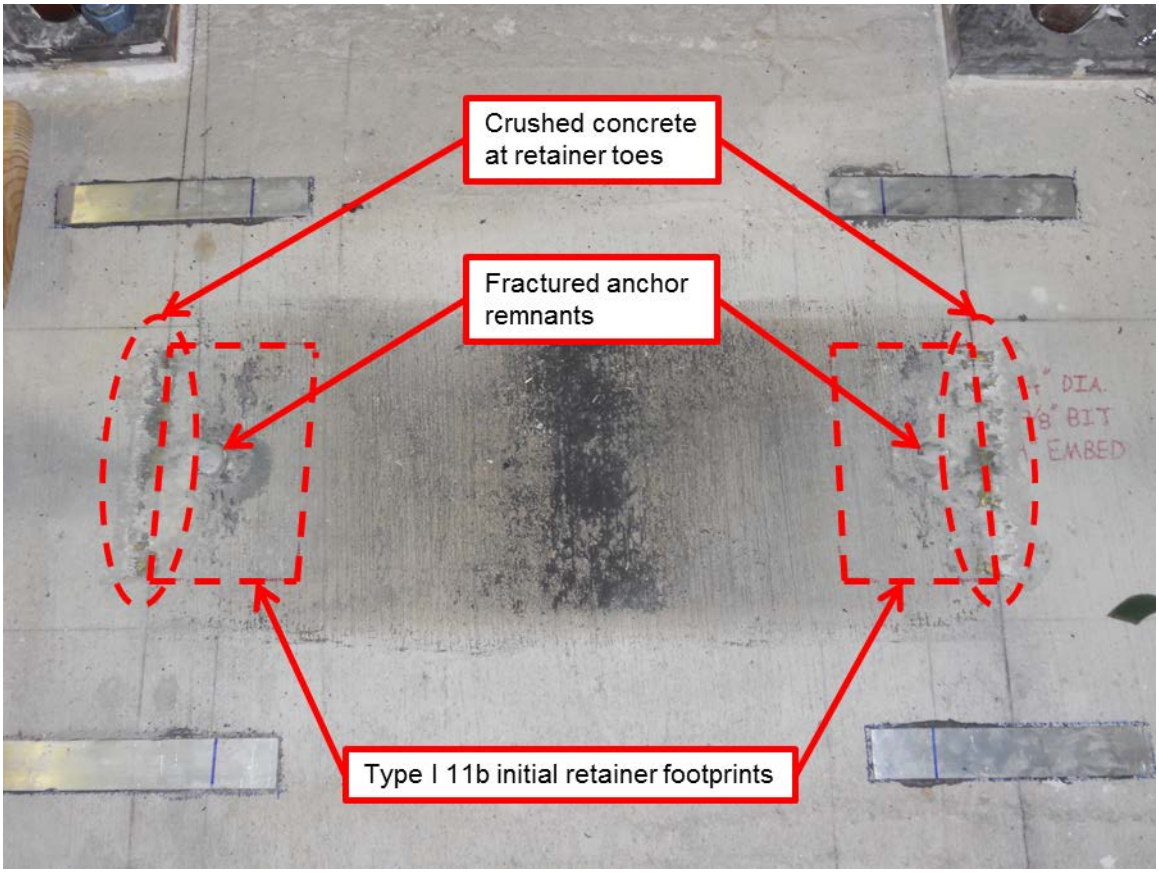

Figure D.13. Initial concrete pad condition.

Loose concrete debris was cleaned off from the damaged regions where retainers had been located. The anchor remnants were cut off at the concrete surface, and the concrete was patched with a high strength, low shrinkage cementitious concrete repair paste. The footprint for the WT on the concrete surface was located to ensure that the WT would be centered under the loading beam in the direction perpendicular to the direction of travel, and

so that the concrete anchors would be installed in the spaces between the rebar in the concrete. The WT and elastomeric leveling pad were then placed on the concrete surface, and concrete anchors were installed into the concrete through the holes in the WT flange, as shown in Figure D.14.

Figure D.14. Concrete anchors installed.

After the WT had been used as a template for positioning of concrete anchors, the WT was removed from the concrete pad, some welded studs were removed and replaced, and strain gage rosettes were installed at two of the fins as described previously. The WT was then returned to the concrete pad, the strain gages were connected to the DAQ wiring, and washers and nuts were installed at each anchor. The nuts were tightened with a torque wrench to 100 ft-lb.

D.4 EXPERIMENT RESULTS

D.4.1 Horizontal Force vs. Horizontal Displacement

The resultant horizontal force acting on the WT is plotted versus the displacement of the welded angles in Figure D.15 and Figure D.16. The total displacement is influenced by slip of the bolts connecting the rectangular bars to the angle legs, deformation of the WT fins, sliding of the WT on the elastomeric leveling pad, and deformation of the concrete anchors. The peak load was 119 kips in the positive direction at a displacement of 0.97 inches, but

the load was also maintained at 114 kips up to a displacement of 1.07 in. The response was similar in the negative direction, with a peak load of 118 kips at 1.07 in. Strength degraded rapidly beyond these displacements, as the fins began to exhibit a torsional buckling response. In the range of 1.25 in. to 1.5 in., the fins began to rupture at a height near the bottom of the rectangular loading bars. Figure D.16 shows the response for one final excursion to +/- 10 in., after all fins have ruptured. The resistance increases temporarily in short segments of the displacement range when the rectangular bars are sliding across the top of the remnants of the fins, but is generally negligible, especially when compared to the capacity of the intact fins.

D.4.2 Horizontal Force vs. Shear Strain

Shear strain for the WT fins can be estimated from two sets of data. Direct measurement of fin displacement is available from 10 in. string potentiometers, with attachments mounted to each side of two fins. Figure D.17 shows the measured shear strain at each of the two instrumented fins up to the appearance of twist in the measured data, determined from a nontrivial discrepancy in the measured displacement for two string potentiometers attached to opposite sides of the same fin. The plot shows that the fins experienced plastic response and reached peak shear strains of approximately 1.2% to 1.4% prior to significant twist. Figure D.18 shows data from the same instruments, with the plotted data truncated when the first welded stud attachment failed at each fin. The data becomes less reliable at higher ranges, as the deforming test components may interfere with the string extension. Additionally, the string is attached to a bracket extending down from the stud mounted near the top of the fin. The stud was welded to the fin to correspond with the centroid of the applied force, but the bars that imparted the shear load to the fin presented an obstacle to direct attachment of a string potentiometer line. The physical arrangement of components necessitated the use of the bracket to provide an attachment point for the string, but as the fin experienced plastic flexure deformations, the bracket was also followed the rotation of the top of the fin, in addition to the translation. Because the bracket extended downward from the stud, the influence of fin rotation on string potentiometer measurements was counter to the translation direction. For large deformations, an approximate shear strain determined from the motion of the welded angles, which was used for control, and is shown in Figure D.19, is likely to be more reliable than the measurements for the direct attachments to the fins. To approximate the true shear strain, the shear strain used for control must be reduced to account for the gaps between the loading bars and the fins, equal to about 3% shear strain, and also slip of the bolts at the angle legs, equal to about 1.5% shear strain. Prior to accounting for these influences, the maximum shear strain available from the WT fuse is estimated to be about 12% to 14%. With the reductions for gaps and slip, the actual shear strain available from the fuse was about 7.5% to 9.5%.

D.4.3 Vertical Force vs. Horizontal Force

Although vertical force was not intentionally imposed on the specimen during the test, vertical loads developed nonetheless, as shown in Figure D.20. As the bars drove against the fins, the initial response appears to have been to “ride up” the sides of the fins, creating tension as the fins were pulled upward. As the bars continued to press into the fins, the fins became pinched under the bars, and the induced vertical load reversed from tension to compression. The response was symmetric, with a maximum tension of about 12 kips, and a maximum compression of about 32 kips.

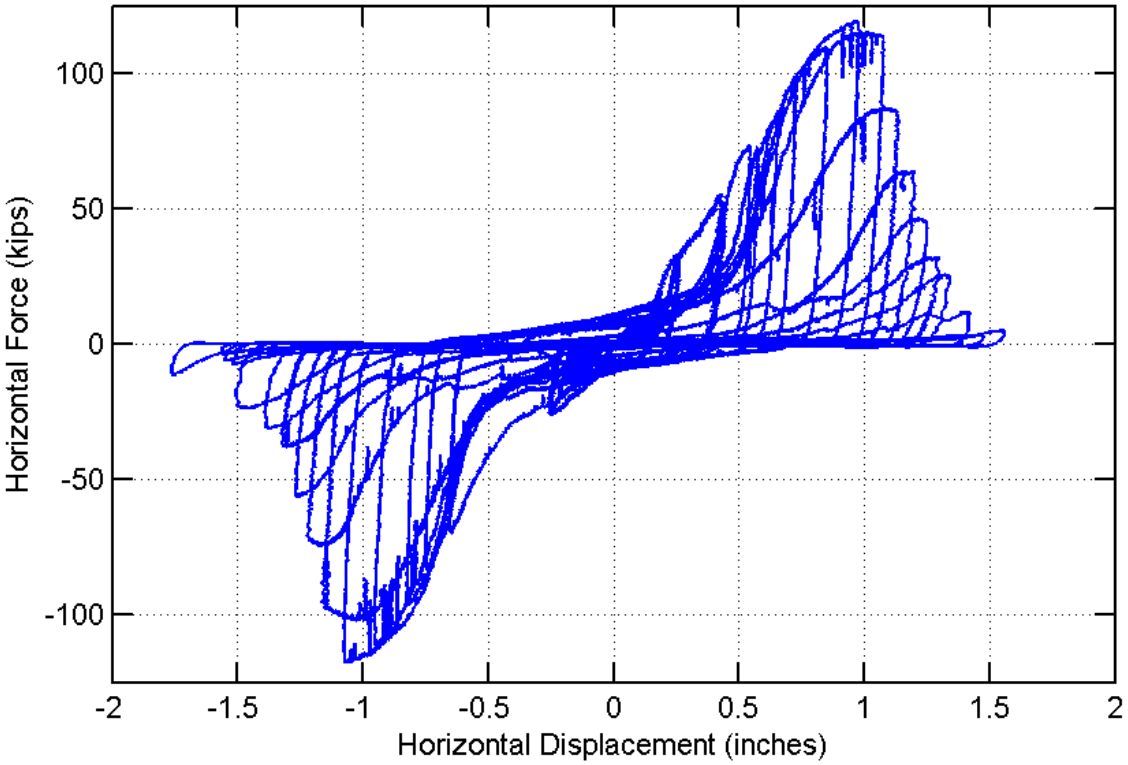

Figure D.15. Horizontal force versus angle displacement to fusing.

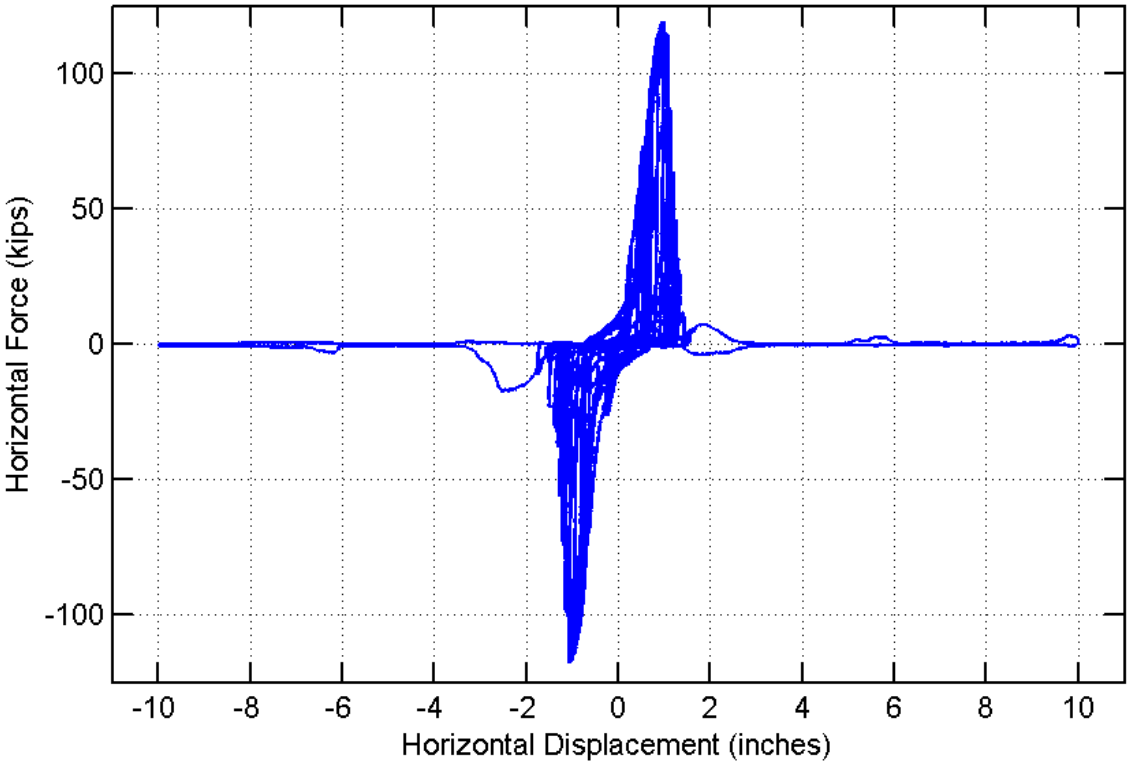

Figure D.16. Horizontal force versus angle displacement with large excursion.

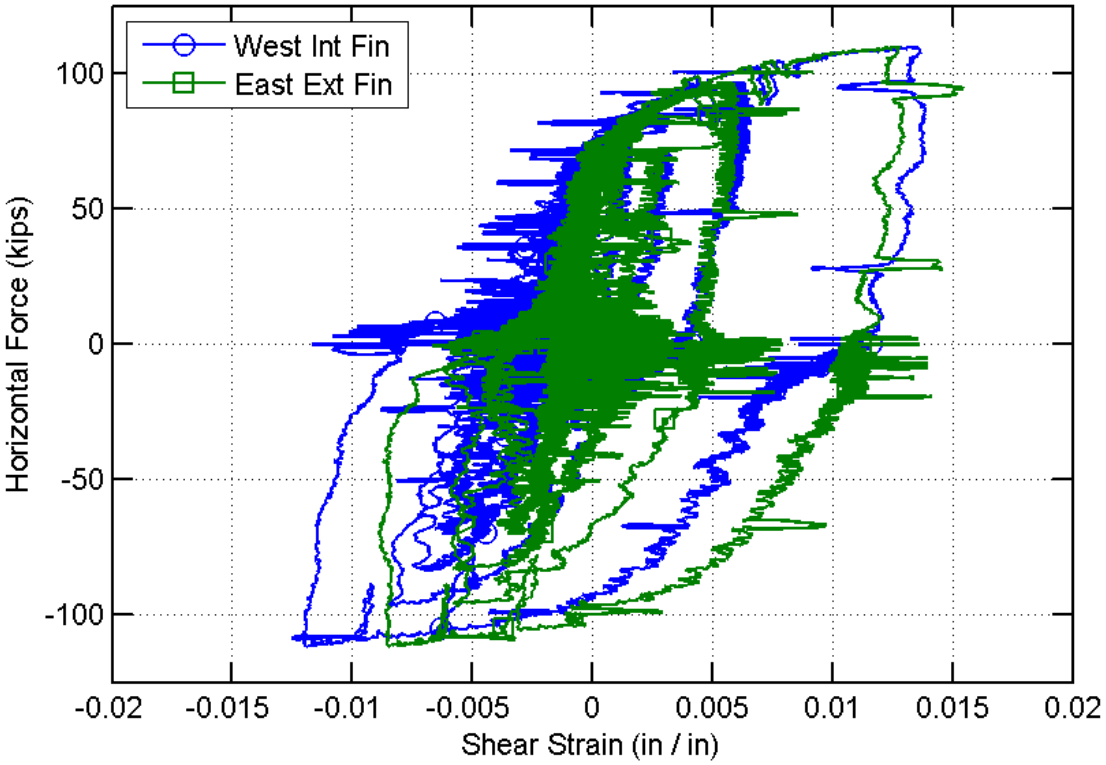

Figure D.17. Horizontal force versus fin shear strain prior to twist.

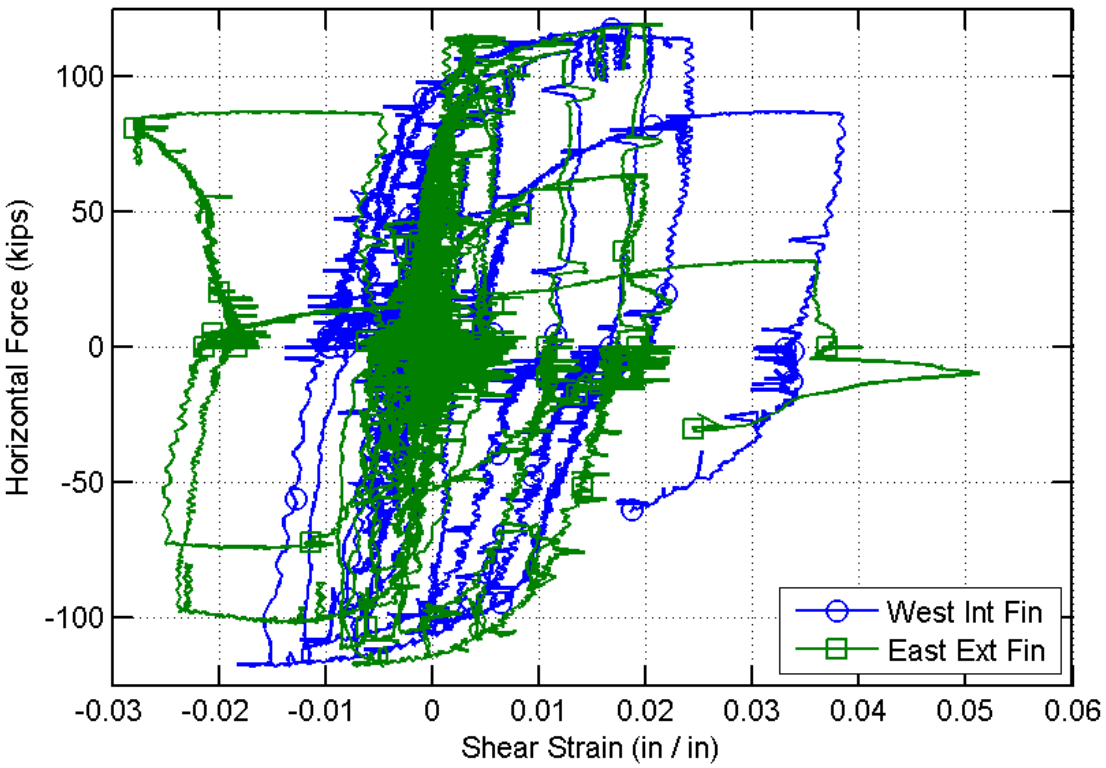

Figure D.18. Horizontal force versus fin shear strain prior to stud weld failures.

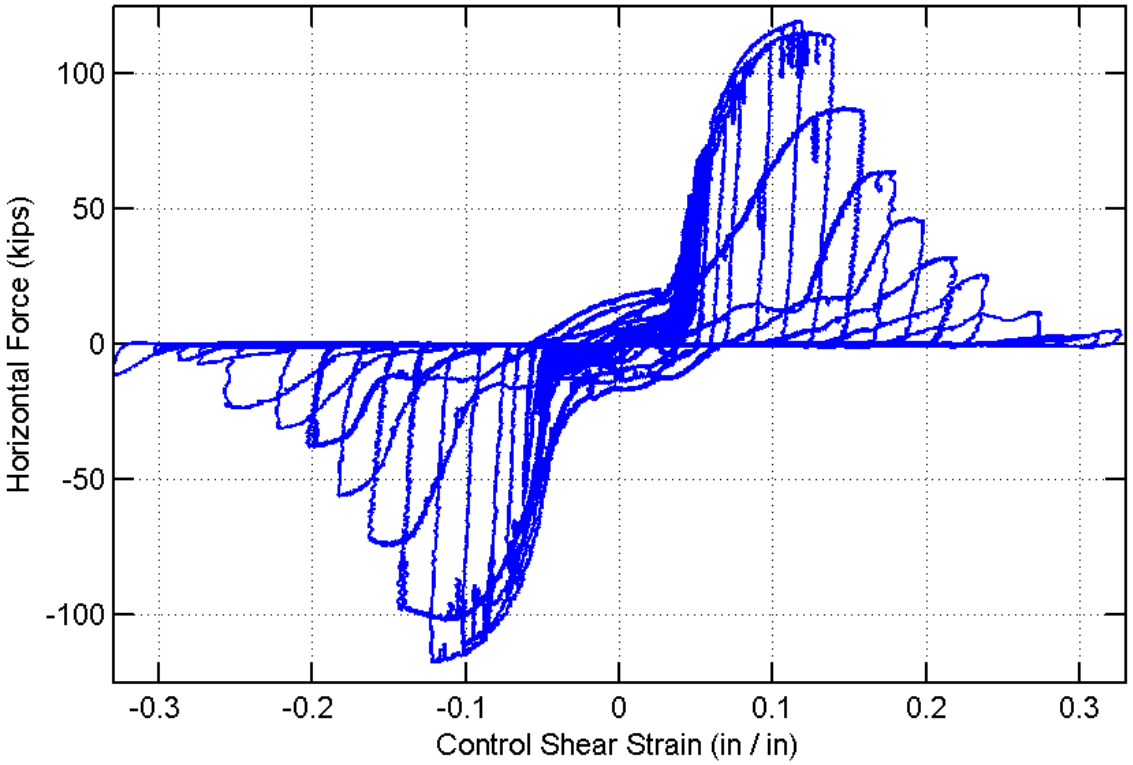

Figure D.19. Horizontal force versus control shear strain to fusing.

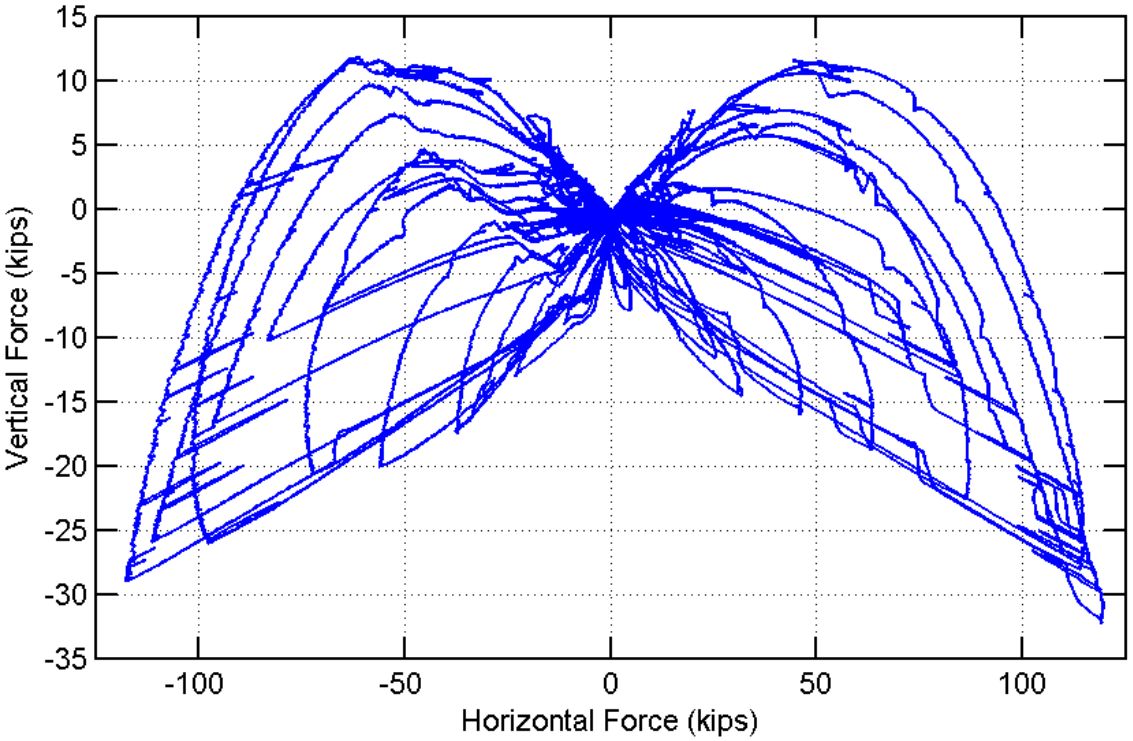

Figure D.20. Vertical force versus horizontal force.

D.5 DISCUSSION

D.5.1 As-Built Dimensions

The dimensions of the fabricated specimen did not conform to the design drawings. The top fin width and fin spacing were accurate, but the depth of the cut-outs was not as intended. With a total depth of 5 in., 1-1/2 in. to the center of the rounded cut-out, and a ¼ in. radius, as shown in Figure D.5, the total distance from the top of the stem to the deepest extent of the cut-out should be 3-3/4 in. However, checking the actual dimension showed that the depth was actually 3-1/4 in., as shown in Figure D.21.

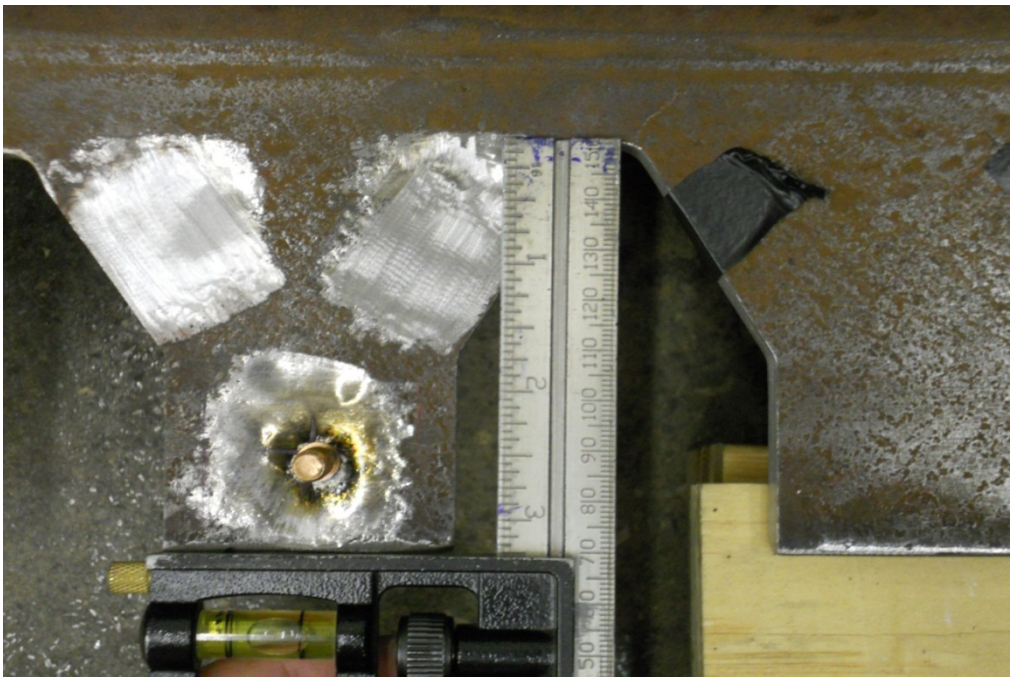

Figure D.21. Measured cut-out depth as-built.

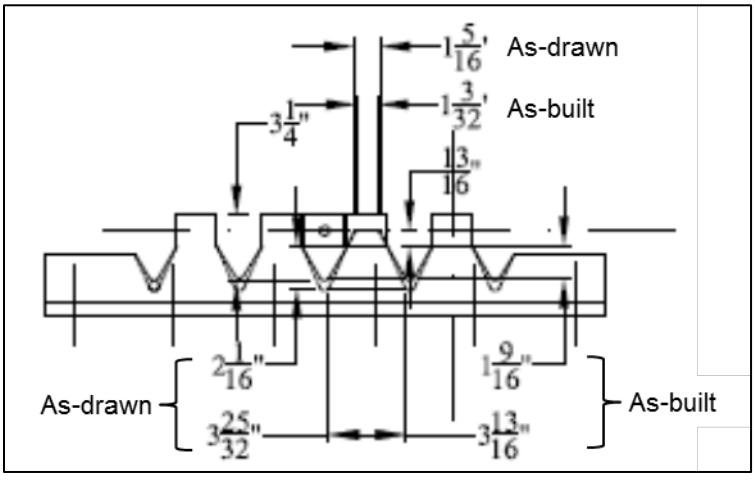

Figure D.22. As-drawn (design) and as-built dimensions.

The cut-outs were made to a circle with the correct center and radius, as indicated in the design drawings, but the cut-outs were made to the top of the circle, rather than the bottom. Dimensions for the design and as-built configurations are shown in Figure D.22. Projecting the sloped faces up to the line of force for the loading bars, the original design drawing would provide fins with effective dimensions of 1-5/16 in., 3-25/32 in., and 6 in. for a, b, and L, respectively. As-built, the dimensions became approximately 1-3/32 in., 3-13/16 in., and 5 in., respectively. To determine the influence of the geometric discrepancy between design and as-built conditions, the location of first yield must be determined. Treating the fin as a cantilever, the demand moment is

$$M = Q\,y \qquad \text{(Eq. D-5)}$$

where

Q = Applied shear load (kips)

y = Distance measured vertically from the centroid of the applied force, positive downward (in.)

The section modulus for the non-prismatic fin is

$$S = \frac{t\left(a + my\right)^2}{6} \qquad \text{(Eq. D-6)}$$

where

t = WT stem thickness (in.)

a = Effective minimum fin width (in.)

m = Change in fin width per unit height (in./in.)

Maximum stress as a function of height is

$$\sigma = \frac{6Q\,y}{t\left(a + my\right)^2} \qquad \text{(Eq. D-7)}$$

The value of y at which $d\sigma / dy = 0$ must be evaluated to determine the maximum stress.

$$\frac{d\sigma}{dy} = \frac{d}{dy}\left[\frac{6Q}{t}\left(\frac{y}{\left(a + my\right)^2}\right)\right] = 0$$

$$\frac{d\sigma}{dy} = \frac{6Q}{t}\left(\frac{\left(a + my\right) - 2my}{\left(a + my\right)^3}\right) = 0 \qquad \text{(Eq. D-8)}$$

This expression will be satisfied when

$$\left(a + my\right) - 2my = 0 \qquad \text{(Eq. D-9)}$$

So that the location of the maximum stress due to strong-axis flexure of the fin is

$$y = \frac{a}{m} \qquad \text{(Eq. D-10)}$$

For the dimensions in the as-built configuration, the value of *y* at which maximum flexural stress occurs is 0.955 in. below the centroid of the loading bars. Rearranging (Eq. D-7) to solve for the load corresponding to flexural yield strength, substituting (Eq. D-10), and rearranging terms results in

$$Q_y = \frac{2\sigma tamn}{3} \qquad \text{(Eq. D-11)}$$

An *n* term has been included in the equation to account for the presence of multiple fins, where *n* = 4 for the tested specimen. Scaling this value to account for the increase from elastic to plastic section modulus in flexure, the estimated peak load capacity becomes

$$Q_p = \sigma tamn \qquad \text{(Eq. D-12)}$$

Assuming a yield strength for the WT A992 steel, as before, the revised strength of the WT fuse increases from 74.1 kips to 87.6 kips, or about 18%. This is a noticeable difference, but is well short of the observed discrepancy of about 60% between the experimental data and the initially estimated strength.

D.5.2 Component Coupon Tests

The purchased length of the WT section was longer than required to fabricate the fuse component, so that coupons could be cut and tested to establish material strength for the critical component of the fuse assembly. Standard specimens conforming to ASTM E8 (2008) were fabricated and tested, providing the data shown in Figure D.23. The mean static yield strength was 55.4 ksi, and the mean ultimate strength was 70.7 ksi. Scaling the revised strength that accounted for the geometric as-built dimensions, the full plastic moment strength of the fins is 97.1 kips. To achieve the shear capacity observed in the experiments, the plastic moment strength would need to strain harden to a uniform plastic stress distribution of 67.6 ksi.

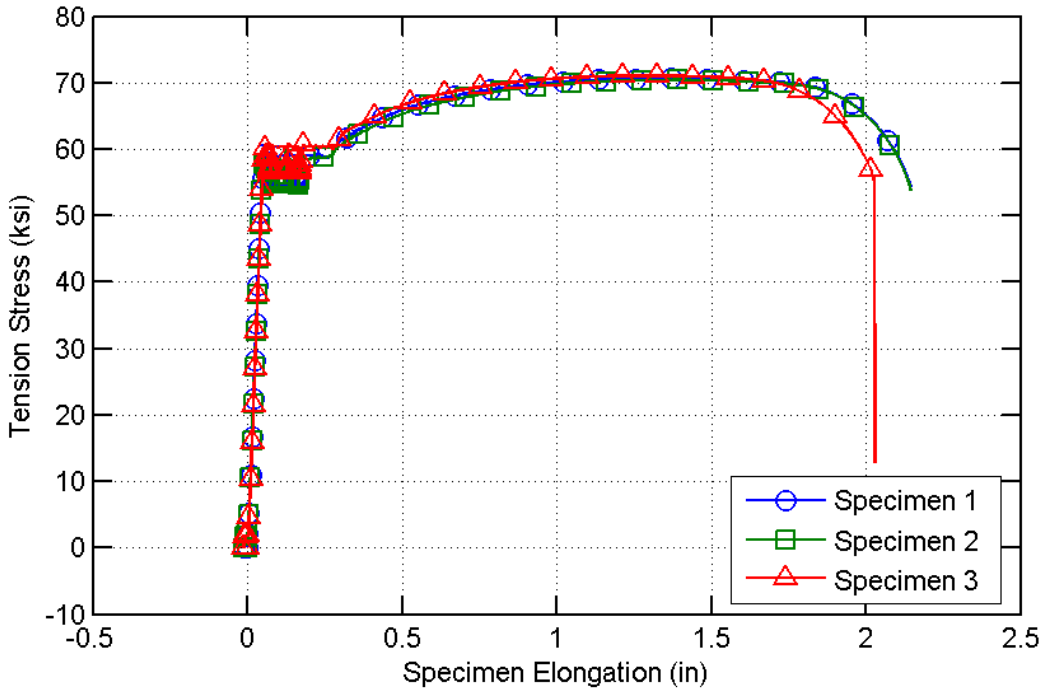

Figure D.23. Tension coupon test data for WT 5x22.5 stem.

D.5.3 Influence of Vertical Reaction

As seen in Figure D.20, a significant vertical reaction developed as the rectangular bars drove against the WT fins. The downward load imposed on the contact surface acted counter to the moment induced by the shear load. A vertical compression of about 7.5 kips (average of 30 kips distributed to 4 fins) would reduce the available plastic moment capacity to about 22.5 k-in at the critical section, compared to the nominal plastic moment capacity of 23.2 k-in in the absence of axial compression. The vertical moment acting at the face of the fin would also provide a counter-balancing moment of 7.5 k-in, so that the applied shear load would need to generate a total moment of 30 k-in to develop a plastic hinge at the critical section. This moment corresponds to an applied shear of 31.4 kips, or 125.5 kips total acting on 4 fins. This seems a likely mechanical interaction and response, so that the fins would experience some limited plasticity, but would ultimately twist prior to reaching full plastic moment strength (at approximately 94% of the estimated shear load required to counteract the vertical reaction-induced moment and develop a plastic hinge.)

D.5.4 Behavior Characterization and Comparison with Prior Research

The tests reported in Ma et al. (2011) included four variations on butterfly fuses, with b/t ratios ranging from 2 to 10, and L/t ratios ranging from 14 to 56. The effective dimensions of the fuse component tested as an alternate to the retainers had an effective b/t ratio of about 10.9 and an L/t ratio of about 13.6. Ma et al. indicate that the b/t ratio is the more influential of the two parameters. The closest comparison is for the Ma et al. specimen with b/t of 10 and L/t of 36. Ma et al. appear to have directly incorporated material strength in Q_p. Even so, the test data indicate that the specimen had a capacity exceeding the predicted shear to develop a plastic hinge by about 35% before exhibiting a pinched response. Interestingly, the observed strength for the alternate fuse is also about 35% higher than the revised estimate determined accounting for as-built geometry and static yield stress observed from

coupon tests. It may be that some limited strain hardening contributed to the results obtained by Ma et al., and that the counter-acting moment induced for the alternate fuse, together with the loss of flexural capacity with imposed compression, coincidentally led to similar capacities. If so, the similarity in the results between the alternate fuse and Ma et al. (2011) suggest that a similar degree of overstrength may be expected for the alternate fuse, even if the loading apparatus provided in the field is not sufficiently stiff to induce the same vertical load observed during the alternate fuse experiment.

D.6 CONCLUSIONS

The alternate fuse test results show that the alternate design can provide fusing restraint with strength and stiffness similar to retainers used with elastomeric bearings. A rapid strength degradation was observed at a displacement of about 1 in. of simulated superstructure displacement, and the fins experienced failure at about a displacement of about 1.5 in. In comparison, the Type I 7c retainer anchors ruptured at bearing displacements of about 1 to 1.7 inches, and the Type I 11b retainer anchors ruptured similarly, at about 1.6 to 1.75 inches. The length of the alternate fuse can be increased or decreased to modify the number of fins and thereby calibrate the fuse peak strength according to project requirements. Additionally, the fusing mechanism for the alternate configuration is minimally influenced by concrete strength, whereas the retainers must be carefully designed to avoid crushing of the concrete at the toe resulting from overturning. The alternate fuse also offers the benefit of replacement following a major seismic event. Because the anchors into the concrete do not rupture, a damaged WT can be removed from the anchors and replaced with a new part after an earthquake, whereas reinstalling retainers at bearings may be problematic with remnants of failed anchors embedded in the substructure. A potential drawback of the alternate fuse is that a specialized diaphragm would need to be designed and fabricated to interact with the WT component. The test data also suggest that a vertical reaction developed at the contact surface of the WT fins may have a significant influence on the fuse capacity. Therefore, the stiffness of the specialized diaphragm may also need to be a design consideration. Further testing will be required to verify to what extent the fuse capacity is dependent on the vertical reaction.


Illinois Department
of Transportation


ILLINOIS
UNIVERSITY OF ILLINOIS AT URBANA-CHAMPAIGN